

Decarbonizing the Electricity Sector in Qatar

Ibraheam Ali Y M Al-Aali

Submitted in partial fulfillment of the  
requirements for the degree of  
Doctor of Philosophy  
under the Executive Committee  
of the Graduate School of Arts and Sciences

COLUMBIA UNIVERSITY

2023

© 2023

Ibraheam Ali Y M Al-Aali

All Rights Reserved

# **Abstract**

## **Decarbonizing the Electricity Sector in Qatar**

**Ibraheam Ali Y M Al-Aali**

Limiting global warming to 1.5°C requires transitioning to low-carbon electricity grids. In Qatar, high and predictable insolation synergetic with demand makes exploiting solar energy particularly attractive to decarbonize the electricity sector. With a hot desert climate, space-cooling drives demand, accounting for nearly half of annual electricity use. This dissertation analyzes a decarbonization pathway by exploiting solar PV generation combined with ice storage for cooling load shifting and battery storage for electric load shifting in a top-down approach by (i) assessing the potential for large-scale deployment, (ii) examining the subsequent problem of distributed energy resources capacity sizing, and (iii) proposing a solution to the arising demand side management problem. A carbon tax is examined to oppose cheap and plentiful natural gas.

The analysis outcomes using a linear program show a strong potential for decarbonizing using PV-enabled solutions. While they cannot displace gas generations, their role is reduced to aid in meeting summer demands. Although buildings are well suited for distributed PV, Qatar is a better fit for utility-scale implementation because of reduced costs and higher output from solar tracking technology, and accessibility for cleaning as soiling on PV is a concern.

Under the current gas price of \$3.3/MMBtu, PV with ice storage could reduce emissions by 43% while cutting annual costs by 20%. Carbon pricing at \$60/ton of CO<sub>2</sub> reduces emissions by 60%. Further reduction is difficult due to the misalignment of the summer electricity demand peak with the solar insolation peak, and ice storage cannot outcompete existing gas generation for a seasonal cooling load. Ice storage is fit to utilize the large idle chiller capacity in the shoulder season, particularly in less efficient systems, because an equal tank volume corresponds

to a greater electric load shifting. Battery storage becomes economical with a carbon tax above \$100/ton of CO<sub>2</sub> to manage non-cooling loads and is unsuitable for seasonal loads. Without a feed-in tariff, battery storage is better suited for utility-scale applications due to a reliable aggregate non-cooling load. Supported by battery storage, emissions could be reduced by 92% at \$140/ton of CO<sub>2</sub> carbon tax. However, peak gas generation demand was only lowered by 66%.

Linear models are useful to describe large systems, but they cannot be applied to an individual system. Instead, hybrid models combining models from first principles with data-driven parameters are developed. The distributed-scale capacity sizing problem is formulated in a bi-level optimization. The upper-level decided equipment capacities using particle swarm are passed down to solve the scheduling problem to estimate electricity charges in a mixed-integer linear program with piecewise linearization. The distributed-scale analysis affirmed the suitability of the decarbonization pathway. Buildings with dominant day-time demand, such as commercial buildings, are well positioned to benefit from exploiting distributed PV generation.

Demand-side management for cooling systems becomes essential in transitioning to low-carbon power grids since intermittent renewable generations cannot be dispatched or perfectly predicted. An optimization strategy is developed to schedule and dispatch chiller systems with ice storage. The strategy decomposes the problem into a bi-level formulation solved using the genetic algorithm. The upper level decides the storage dispatch amount, and the lower level solves the scheduling problem at each time step. The penalty function method handles the scheduling problem's constraints, and with penalty factor tuning, premature convergence is eliminated. Compared to commonly used heuristic strategies, optimal control reduced cost by 11-33%. The gains are augmented with a more complex tariff structure like demand charge.



# Table of Contents

List of Figures .....	iv
List of Tables .....	xiii
Nomenclature .....	xiv
Acknowledgments .....	xxxii
Chapter 1: Introduction .....	1
Chapter 2: Assessing large-scale deployment from a utility-scale perspective .....	11
2.1 Introduction .....	11
2.2 Methodology .....	13
2.2.1 Cooling systems performance estimation .....	16
2.2.2 Cooling load estimation .....	19
2.2.3 Problem formulation .....	28
2.3 Results and discussion .....	37
2.3.1 Current cost structure .....	37
2.3.2 Effects of carbon pricing .....	43
2.3.3 Decarbonized system with \$140/ton of CO <sub>2</sub> carbon tax .....	48
2.3.4 Impact of BESS capacity cost .....	53
2.4 Conclusion .....	56
Chapter 3: Modeling of WC CWS with I-TES .....	58
3.1 Introduction .....	58
3.2 Components modeling .....	63
3.2.1 Electric chillers .....	63
3.2.2 Pumps .....	73

3.2.3 Cooling towers .....	75
3.2.4 Cooling and dehumidifying coils .....	78
3.2.5 I-TES .....	82
3.3 Conclusion .....	87
Chapter 4: Design of an integrated WC CWS with I-TES, BESS, and on-site PV .....	89
4.1 Introduction .....	89
4.2 Methodology .....	92
4.2.1 Simulation of building cooling and electric loads .....	93
4.2.2 Optimization strategy .....	97
4.2.3 Problem formulation .....	110
4.2.4 Model parameters .....	113
4.2.5 Chillers performance data .....	115
4.2.6 Scenarios selection .....	117
4.3 Results and discussion .....	121
4.3.1 Commercial building .....	121
4.3.2 Residential building .....	129
4.4 Conclusion .....	135
Chapter 5: Optimal equipment scheduling and dispatch of WC CWS with I-TES .....	137
5.1 Introduction .....	137
5.2 Methodology .....	139
5.2.1 Problem formulation .....	139
5.2.2 Optimization strategy .....	145
5.3 Results and discussion .....	152

5.4 Conclusion .....	162
Chapter 6: Conclusions and recommendations for future works.....	164
6.1 Main Conclusion.....	164
6.2 Recommendations for future work .....	169
6.2.1 Examining the cost of retrofitting DXS .....	169
6.2.2 Alternative energy storage technologies .....	169
6.2.3 Alternative decarbonization pathway.....	170
6.2.4 Determining the ideal electricity tariffs structure .....	170
6.2.5 Incorporate BESS in the I-TES dispatch problem .....	170
6.2.6 Inclusion of seawater desalination in the model.....	171
6.2.7 Modeling the impact of electrifying the transportation sector.....	171
References .....	172
Appendix A: Simulation of buildings' cooling and electric loads .....	186
A.1 Occupant load .....	188
A.2 Electric load .....	189
A.3 Infiltration and ventilation .....	190
A.4 Solar gain .....	191
A.5 Shell heat gain.....	192
A.6 Total heat gain .....	193
Appendix B: Chapter 4 Models Parameters.....	196
Appendix C: Chapter 5 Models Parameters.....	200

## List of Figures

### Chapter 1

Figure 1.1: Qatar's 2016 electricity demand in the winter, spring, and summer for three days on the left y-axis and the ambient conditions, dry and wet-bulb temperatures, on the right y-axis. ... 3

Figure 1.2: Qatar 2016's weekly mean electric demand and solar output over 19 km<sup>2</sup> in MW on the left y-axis, and the weekly mean heat index and dry-bulb temperature in degrees Celsius on the right y-axis. Yearly solar output over 19 km<sup>2</sup> is equivalent to 2016's total electricity use of 42 TWh. .... 6

### Chapter 2

Figure 2.1: An illustration of the considered power grid. Central grid PV and gas generation can be used for all loads, including BESS charging. Buildings are classified based on their cooling system type: DXS, AC CWS, and WC CWS. To account for emissions reduction from cooling, the cooling load is assumed to be met in the following order using: (i) PV generation, (ii) BESS, and (iii) gas generation..... 14

Figure 2.2: Pathways to satisfying the cooling demand in the three cooling systems types. While AC and WC CWS can make ice, additional AC ice chillers can be installed. Additional ice chillers must be installed with the I-TES for the DXS. .... 15

Figure 2.3: System COP for (a) WC systems v. wet-bulb temperature and (b) AC CWS v. dry-bulb temperature in refrigeration and ice-making modes. AC systems include AC CWS and DXS..... 18

Figure 2.4: Qatar's 2016 electric demand vs. (a) dry-bulb temperature, (b) wet-bulb temperature, and (c) heat index. Data points highlighted in red are warm and humid hours with a humidity

ratio ( $HRp, t$ ) $\geq 0.02$ , and in yellow are warm and dry hours with $HRp, t \leq 0.02$ and $Tp, tdb \geq 40^{\circ}\text{C}$ .....	21
Figure 2.5: Qatar 2016 electric demand v. heat index at every hour of the day starting from 00:00 (12 AM) to 23:00 (11 PM). A sigmoid function is fitted with 4 data points: peak and base demand, slope, and heat index mid-point. ....	24
Figure 2.6: The four fitted parameters: (a) base load $Bp, t$ , (b) peak demand $Pp, t$ , (c) slope $kp, t$ , and (d) heat index midpoint $HIp, t0$ at the hour of the day for the 2016 scenario. ....	25
Figure 2.7: Actual electric load $Dp, t$ , estimated electric load $Bp, t + Cp, t$ on the left y-axis and electric cooling load $Cp, t$ on the right y-axis from the logistic curve regression for the 2016 scenario. The estimated load generally agrees with the actual load, with an average percent difference of 3.5%.....	27
Figure 2.8: 2016 scenario cost-optimal system under current cost structure with a breakdown of contribution to supplying (a) electric demand and (b) electric cooling load with percent load shifted by I-TES (% met by I-TES), directly met by PV (%D met by PV), and met by gas (% met by Gas) on the left y-axis and the average weekly load on the right y-axis. ....	40
Figure 2.9: Cost-optimal system hourly load profile with D (demand) met by I-TES, DD (demand directly) met from PV, D (demand) met by gas, and on the left y-axis and the ambient temperatures on the right y-axis for three days in winter, spring, and summer. I-TES charge rate is shown in negative.....	42
Figure 2.10: Cost-optimal system as carbon price increases. Power generations and BESS capacities are normalized to the 2016 yearly average electric demand of 4.7 GW. I-TES capacity is normalized to the average aggregate cooling demand of 1.4 $\text{GW}_{\text{th}}$ for DXS, 2.3 $\text{GW}_{\text{th}}$ for AC	

CWS, and 2.2 GW <sub>th</sub> for WC CWS. Ice chiller capacity is normalized to the aggregate cooling system capacity of 3.1 GW <sub>th</sub> for DXS, 6.1 GW <sub>th</sub> for AC CWS, and 5.7 GW <sub>th</sub> for WC CWS. ....	44
Figure 2.11: As carbon price increases: (a) overall system characteristics, (b) cooling system characteristics, (c) average generation cost and total CO <sub>2</sub> emissions, and (d) annual system cost, Capex, and revenue from the carbon tax (carbon pricing).....	45
Figure 2.12: As carbon price increases, carbon abatement costs on the left y-axis and abated CO <sub>2</sub> emissions on the right y-axis, relative to the current system of all gas-based generations.....	47
Figure 2.13: Cost-optimal system with a carbon price at \$140/ton of CO <sub>2</sub> and BESS capacity cost at \$250/kWh with a breakdown of contribution to supplying (a) the electric demand and (b) the electric cooling load. The electric cooling load is assumed to be met first by PV generation before BESS is used, and the remaining load is met using gas generation. ....	51
Figure 2.14: Cost-optimal system hourly load profile with a carbon price at \$140/ton of CO <sub>2</sub> and BESS capacity cost at \$250/kWh with contributions from PV generation and load shifting using I-TES and BESS to meet the electric demand for three days in winter, spring, and summer. I-TES and BESS charge rates are shown as negative loads. ....	52
Figure 2.15: Impact of BESS capacity cost and carbon pricing on the cost-optimal system with (a) emissions reduction, (b) average generation cost, (c) total PV capacity (fixed-tilt and single-axis tracking), and (d) BESS capacity. PV and BESS capacity is normalized to the 2016 yearly average electric demand of 4.7 GW.....	54
Figure 2.16: Impact of BESS capacity cost and carbon pricing on the cost-optimal system. I-TES capacity is normalized to the average aggregate cooling demand of 1.4 GW <sub>th</sub> for DXS, 2.3 GW <sub>th</sub> for AC CWS, and 2.2 GW <sub>th</sub> for WC CWS. Ice chillers' capacity is normalized to the	

aggregate cooling capacity of 3.1 GW <sub>th</sub> for DXS, 6.1 GW <sub>th</sub> for AC CWS, and 5.7 GW <sub>th</sub> for WC CWS.....	55
---	----

### Chapter 3

Figure 3.1: CWS in a simple constant-flow configuration. Each chiller operates with its fixed-speed pumps. Excess water is diverted back using a three-way valve .....	59
--	----

Figure 3.2: CWS in a primary-secondary flow configuration. Chillers operate with their fixed-speed pumps in the primary loop, and two-way valves and variable-speed pumps regulate the flowrate received by the building's coils in the secondary loop. Excess water returns to the chiller in the bypass blending with the coils' return water. ....	60
---	----

Figure 3.3: CWS in a variable primary flow configuration. A bypass control valve is required to maintain proper chiller flow.....	61
---	----

Figure 3.4: Considered CWS in a primary-secondary configuration with multiple WC chillers, two shared cooling towers, and an I-TES downstream of the chillers. The building is represented in a single coil with the respective building aggregate cooling load. ....	62
---	----

Figure 3.5: A schematic of the internals of an electric chiller running on a vapor-compression cycle. Water-glycol mixture is used in the evaporator to prevent freezing when operating near or at sub-freezing temperatures. ....	63
--	----

Figure 3.6: The COP as predicted using the reformulated Gordon-Ng model compared to the COP from EnergyPlus given in a DOE-2 model for 383-tons Carrier 19XR with VSD-equipped centrifugal compressor.....	69
--	----

Figure 3.7: Pressure-enthalpy diagram of vapor compression cycle demonstrating the impact of evaporator and condenser temperatures on refrigerant evaporator thermal capacity. An increase	
--	--

in condenser temperature or a decrease in evaporator temperature reduces the refrigerant evaporator vapor quality, reducing the heat capacity ( $\Delta h > \Delta h^*$ and $\Delta h > \Delta h_0$ ).....	70
Figure 3.8: Estimated cooling capacity ratio from refrigerant thermal capacity versus EnergyPlus for 383-tons Carrier 19XR with VSD-equipped centrifugal compressor at water supply temperature setpoints of 5 and 8°C.....	72
Figure 3.9: Exaggerated illustration of the assumption of linear saturation enthalpy line with respect to temperature. $\Delta T_w$ is the tower water temperature difference, $\Delta h_s$ is the tower air enthalpy difference, $h_s$ is air saturation enthalpy, and $T_{wb}$ is the wet-bulb temperature.....	76
Figure 3.10: An illustration of a modular internal-melt I-TES. Multiple parallel spiral circuits are submerged in water inside the tank, and a water-glycol mixture is circulated through the circuits to build and melt the ice around the tubes. ....	82
Figure 3.11: An illustration of the charging and discharging process along the heat rate curve is shown in a cross-sectional view of the parallel tubes inside the 83-TR-hr internal melt I-TES tank. The intersection of ice formations in charging and water formations in discharging reduces the heat transfer area. Charging is at -6°C and 4 kg/s, and discharging is at 8°C and 4 kg/s. ....	85
Figure 3.12: Simulation of I-TES operation under different inlet conditions for charge mode with (a) charging rate and (b) charging effectiveness, and discharge mode with (c) discharge rate and (d) discharging effectiveness. I-TES is fully charged at an SoC of 1 and fully discharged at 0. .	87

## Chapter 4

Figure 4.1: A schematic of an integrated WC CWS with I-TES, BESS, and on-site PV generation.....	92
--	----



Figure 4.2: Simulated residential building cooling load for three days in winter, spring, and summer using the 2016 meteorological data. Electric and thermal loads are correlated with higher building occupancy in the evening. ....	95
Figure 4.3: Simulated commercial building cooling load for three days in winter, spring, and summer using the 2016 meteorological data. Electric and thermal loads are correlated with higher building occupancy during the day. ....	96
Figure 4.4: Bi-level optimization formulation. The upper level minimizes annual system costs and decides the installed capacities, and the lower level solves the equipment scheduling and dispatch problem in a mixed-integer linear programming formulation and returns the electricity charges. ....	98
Figure 4.5: Illustration of piece-wise linearization for the 383-tons Carrier 19XR chiller with VSD-equipped centrifugal compressor in (a) ice-making mode with a setpoint temperature of -6°C and (b) refrigeration mode with a setpoint temperature of 7°C, at three ambient wet-bulb temperatures. ....	101
Figure 4.6: Piece-wise linearization applied to I-TES maximum charge and discharge rates. ..	107
Figure 4.7: The five scenarios for the commercial building with (a) building thermal cooling demand, (b) solar insolation, (c) non-cooling load, and (d) ambient wet-bulb temperature. ....	118
Figure 4.8: The five representative days for the residential building with (a) building thermal cooling demand, (b) solar insolation, (c) non-cooling load, and (d) ambient wet-bulb temperature. ....	120
Figure 4.9: Effect of carbon pricing on the cost-optimal system installed capacities of (a) PV, (b) BESS, (c) I-TES, and (d) chillers for the commercial building. PV and BESS are normalized to the average electric demand of 515 kW, I-TES is normalized to the average cooling load of 2213	

kW <sub>th</sub> , and the total capacity of chillers is normalized to the peak cooling demand of 7160 kW <sub>th</sub> .	
Peak electricity demand is the maximum power drawn from the electricity grid. ....	122
Figure 4.10: Effect of the carbon price increases on (a) contribution to meeting the electric demand and (b) breakdown of annual system cost for the commercial building. ....	123
Figure 4.11: Carbon abatement cost and abated CO <sub>2</sub> for the commercial building. ....	124
Figure 4.12: Cost-optimal system with (a) chillers loading and (b) hourly load profile for the commercial building without carbon pricing. ....	127
Figure 4.13: Cost-optimal system with (a) chillers loading and (b) hourly load profile for the commercial building with carbon pricing at \$100/ton of CO <sub>2</sub> . ....	128
Figure 4.14: Effect of carbon pricing on the cost-optimal system installed capacities of (a) PV, (b) BESS, (c) I-TES, and (d) chillers for the residential building. PV and BESS are normalized to the average electric demand of 515 kW, I-TES is normalized to the average cooling load of 2213 kW <sub>th</sub> , and the total capacity of chillers is normalized to the peak cooling demand of 7160 kW <sub>th</sub> . ....	129
Figure 4.15: Effect of the carbon price increases on (a) contribution to meeting the electric demand and (b) breakdown of annual system cost for the residential building. ....	130
Figure 4.16: Carbon abatement cost and abated CO <sub>2</sub> for the residential building. ....	131
Figure 4.17: Cost-optimal system with (a) chillers loading and (b) hourly load profile for the residential building without carbon pricing. ....	133
Figure 4.18: Cost-optimal system with (a) chillers loading and (b) hourly load profile for the residential building with carbon pricing at \$100/ton of CO <sub>2</sub> . ....	134

## Chapter 5

Figure 5.1: The considered CWS in a primary-secondary configuration with three WC chillers (two 212-tons Carrier 19XR chillers with VSD and one 153-tons Trane RTHB chiller), two shared cooling towers (360 tons each), and I-TES (1600 TR-hr). The building is represented in a single coil with the respective aggregate cooling load. ....	139
Figure 5.2: The considered CWS with decision variables highlighted in orange and variables in black are consequences of the decision variables. ....	141
Figure 5.3: The developed bi-level optimization strategy. The upper-level decided dispatch is passed down to the lower-level optimizer to solve the equipment scheduling problem sequentially. Infeasible storage dispatch at a given hour is rejected and penalized. The upper-level optimizer input is the TOU rates, and lower-level optimizer inputs are the sensible and latent cooling load and ambient wet-bulb temperature. The genetic algorithm is applied to both levels. ....	146
Figure 5.4: Manufactured Training data with (a) cooling demand v. wet-bulb temperature and (b) storage dispatch amount and SoC. This set has 237 unique data points, each an independent input condition for the scheduling problem. A sensible heat ratio of 0.7 is assumed.....	150
Figure 5.5: System COP for a range of cooling loads at a wet-bulb temperature of 25°C when (a) charging at a rate of 160 tons, (b) discharging at a rate of 160 tons, and (c) idle I-TES. The total load includes the cooling load and the storage charge amount.....	151
Figure 5.6: Optimization problem input for three scenarios with hourly (a) cooling demand, (b) TOU rates, and (c) ambient wet-bulb temperature. A sensible heat ratio of 0.7 is assumed.....	154
Figure 5.7: Cooling demand contribution breakdown from each chiller and storage for the three considered control strategies. From left to right: chiller priority control, storage priority control,	

and optimal storage control. The system comprises two 212-tons chillers with a VSD-equipped centrifugal compressor (Carrier 19XR) and one 153-tons screw chiller without VSD (Trane RTHB)..... 158

Figure 5.8: For the three control strategies, hourly systems profiles with (a) system operation cost; (b) total system electric energy use; (c) total energy use by all chillers excluding auxiliary equipment; (d) auxiliary equipment energy use which includes primary, secondary and condenser pumps, and towers and coil fans. .... 159

Figure 5.9: For the three control strategies, hourly system: (a) COP, (b) blended chillers supply temperature, (c) storage dispatch amount curve, and (d) flowrate to I-TES. System COP is the ratio of total chiller loading to the system's electric load. .... 160

Figure 5.10: Applying a demand charge of \$20/kW to Scenario 1 with (a) a breakdown of cooling contribution from each chiller and storage and (b) system electric energy use. .... 161

## List of Tables

### Chapter 2

Table 2.1: Characteristics parameters in the model .....	35
Table 2.2: Financial parameters in the model .....	36
Table 2.3: Cost-optimal system capacities under the current cost structure .....	38
Table 2.4: Cost-optimal system characteristics under the current cost structure .....	39
Table 2.5: Cost-optimal system at \$140/ton of CO <sub>2</sub> carbon price .....	48
Table 2.6: Cost-optimal system characteristics at \$140/ton of CO <sub>2</sub> carbon price .....	49

### Chapter 4

Table 4.1: Assumed characteristics parameters .....	113
Table 4.2: Assumed financial parameters .....	114
Table 4.3: Qatar electricity tariffs for bulk customers .....	115
Table 4.4: Scenarios for the commercial building .....	117
Table 4.5: Scenario for the residential building .....	119
Table 4.6: Optimal-cost cooling system capacities for the commercial building .....	125
Table 4.7: Optimal-cost cooling system capacities for the residential building .....	132

### Chapter 5

Table 5.1: Daily cost, energy use, and storage utilization for all scenarios .....	155
--	-----

## Nomenclature

### Abbreviations

Symbol	Meaning
AC	Air-Cooled
AC CWS	Air-Cooled Chilled Water System
BESS	Battery Energy Storage System
Capex	Capital Expenditure
COP	Coefficient of Performance
CWS	Chilled Water System
D	Demand
DD	Demand Directly
DXS	Direct Expansion System
I-TES	Ice Thermal Energy Storage
OpEx	Operation Expenditure
PV	Photovoltaics
SoC	State of Charge
TOU	Time-of-Use
TR	Ton of Refrigeration
WC	Water-Cooled
WC CWS	Water-Cooled Chilled Water System

## Chapter 2

### Parameters

Symbol	Meaning
$HR_{p,t}$	Humidity ratio at time $t$ and scenario $p$ , [kg of water/kg of air]
$B_{p,t}$	Logistic curve non-cooling load at time $t$ and scenario $p$ , [MW]
$C_{p,t}^{DX}$	Hourly aggregate thermal cooling demand from direct expansion systems at time $t$ and scenario $p$ , [MW <sub>th</sub> ]
$C_{p,t}^{AC}$	Hourly aggregate thermal cooling demand from air-cooled chilled water systems at time $t$ and scenario $p$ , [MW <sub>th</sub> ]
$C_{p,t}^{WC}$	Hourly aggregate thermal cooling demand from water-cooled chilled water systems at time $t$ and scenario $p$ , [MW <sub>th</sub> ]
$C^{AC}$	Existing aggregate cooling capacity of air-cooled chilled water systems in refrigeration mode, [MW <sub>th</sub> ]
$C^{WC}$	Existing aggregate cooling capacity of water-cooled chilled water systems in refrigeration mode, [MW <sub>th</sub> ]
$C^{AC,ice}$	Existing aggregate cooling capacity of air-cooled chilled water systems in ice-making mode, [MW <sub>th</sub> ]
$C^{WC,ice}$	Existing aggregate cooling capacity of water-cooled chilled water systems in ice-making mode, [MW <sub>th</sub> ]
$C^{DX,des}$	Design aggregate cooling capacity of direct expansion cooling systems, [MW <sub>th</sub> ]
$C^{AC,des}$	Design aggregate cooling capacity of air-cooled chilled water systems, [MW <sub>th</sub> ]
$C^{WC,des}$	Design aggregate cooling capacity of water-cooled chilled water systems, [MW <sub>th</sub> ]

$COP_{p,t}^{ac}$	Air-cooled systems coefficient of performance in refrigeration mode at time $t$ and scenario $p$ , dimensionless
$COP_{p,t}^{wc}$	Water-cooled systems coefficient of performance in refrigeration mode at time $t$ and scenario $p$ , dimensionless
$COP_{p,t}^{ac,ice}$	Air-cooled systems coefficient of performance in ice-making mode at time $t$ and scenario $p$ , dimensionless
$COP_{p,t}^{wc,ice}$	Water-cooled systems coefficient of performance in ice-making mode at time $t$ and scenario $p$ , dimensionless
$COP_{p,t,i}^{ac,des}$	Air-cooled systems design coefficient of performance at time $t$ and scenario $p$ , dimensionless
$COP_{p,t}^{wc,des}$	Water-cooled systems design coefficient of performance at time $t$ and scenario $p$ , dimensionless
$c^{BESS}$	Capital cost of installed battery capacity, [\$/MWh]
$c_s^{PV,C}$	Capital cost of installed PV capacity with solar tracking technology $s$ , [\$/MW <sub>p,dc</sub> ]
$c^{ITES}$	Capital cost of installed ice storage capacity, [\$/MWh <sub>th</sub> ]
$c^{IceChl,C}$	Capital cost of additionally installed ice chillers capacity, [\$/MW <sub>th</sub> ]
$c_s^{PV,O}$	Operating cost of installed PV capacity with solar tracking technology $s$ , [\$/MW <sub>p,dc</sub> /yr.]
$c^{IceChl,O}$	Operating cost of additionally installed ice chillers, [\$/MW <sub>th</sub> /yr.]
$c^{GT}$	Cost of electricity produced by gas-fired generations, [\$/MWh]
$c^{PGT}$	Peak gas-fired generations demand price, [\$/MW <sub>p</sub> ]
$D_{p,t}$	Hourly aggregate total electric demand at time $t$ and scenario $p$ , [MW]



$\mathcal{D}_{p,t}^{\mathcal{N}}$	Hourly aggregate non-cooling electric demand at time $t$ and scenario $p$ , [MW]
$\mathcal{D}_{p,t}^{\mathcal{C}}$	Hourly aggregate total electric cooling load at time $t$ and scenario $p$ , [MW]
$\mathcal{D}_{p,t}^{DX}$	Hourly aggregate electric cooling load from direct expansion systems at time $t$ and scenario $p$ , [MW]
$\mathcal{D}_{p,t}^{AC}$	Hourly aggregate electric cooling load from air-cooled chilled water systems at time $t$ and scenario $p$ , [MW]
$\mathcal{D}_{p,t}^{WC}$	Hourly aggregate electric cooling load from water-cooled chilled water systems at time $t$ and scenario $p$ , [MW]
$E^{DX}$	Maximum aggregate electric load from direct expansion cooling systems, [MW]
$E^{AC}$	Maximum aggregate electric load from air-cooled chilled water systems, [MW]
$E^{WC}$	Maximum aggregate electric load from water-cooled chilled water systems, [MW]
$f^{ITES,chs}$	Ice storage maximum charge power to energy ratio, [ $\text{h}^{-1}$ ]
$f^{ITES,dis}$	Ice storage maximum discharge power to energy ratio, [ $\text{h}^{-1}$ ]
$HI_{p,t}^0$	Logistic curve heat index midpoint at time $t$ and scenario $p$ , [ $^{\circ}\text{C}$ ]
$HI_{p,t}$	Heat index at time $t$ and scenario $p$ , [ $^{\circ}\text{C}$ ]
$I_{p,t,s}$	Hourly solar insolation with a solar tracking technology $s$ at time $t$ and scenario $p$ , dimensionless by peak sun hour, [ $\text{MW}/\text{MW}_p$ ]
$ir$	Interest rate, dimensionless
$k_{p,t}$	Logistic curve slope at time $t$ and scenario $p$ , [ $^{\circ}\text{C}^{-1}$ ]
$P_{p,t}$	Logistic curve peak demand at time $t$ and scenario $p$ , [MW]
$T_{p,t}^{db}$	Ambient dry-bulb temperature at time $t$ and scenario $p$ , [ $^{\circ}\text{C}$ ]
$T_{p,t}^{wb}$	Ambient wet-bulb temperature at time $t$ and scenario $p$ , [ $^{\circ}\text{C}$ ]

$yr$	Service life of PV, ice chillers, and ice storage, [yrs.]
$yr_b$	Battery service life, [yrs.]
$\eta^{ITES,sdis}$	Ice storage self-discharge efficiency, dimensionless
$\eta^{BESS,chs}$	Battery charge efficiency, dimensionless
$\eta^{BESS,dis}$	Battery discharge efficiency, dimensionless
$\eta^{BESS,sdis}$	Battery self-discharge efficiency, dimensionless
$\eta^I$	Inverter efficiency, dimensionless
$\psi^{ice}$	Depressed chiller capacity factor in ice-making mode, dimensionless
$\varphi^{ice}$	Depressed chiller performance factor in ice-making mode, dimensionless

#### Decision variables

Symbol	Meaning
$\mathcal{B}_{p,t}^{dis}$	Battery discharge rate at time $t$ and scenario $p$ , [MW]
$\mathcal{B}_{p,t}^{chs}$	Battery charge rate at time $t$ and scenario $p$ , [MW]
$\mathcal{B}_{p,t}^s$	Stored electric energy at time $t$ and scenario $p$ , [MWh]
$\mathcal{C}^{BESS}$	Installed electric battery capacity, [MWh]
$\mathcal{C}_s^{PV}$	Installed PV capacity with solar tracking technology $s$ , [MW <sub>p,dc</sub> ]
$\mathcal{C}_i^{ITES}$	Installed ice storage thermal capacity for cooling system $i$ , [MWh <sub>th</sub> ]
$\mathcal{C}_i^{IceChl}$	Additionally installed ice chiller capacity for cooling system $i$ , [MW <sub>th</sub> ]
$GT_{p,t}$	Electricity generated from gas at time $t$ and scenario $p$ , [MW]
$GT^P$	Peak gas generation demand, [MW]
$PV_{p,t}^{curt}$	Curtailed PV generation at time $t$ and scenario $p$ , [MW]
$\mathcal{S}_{p,t,i}^{dis}$	Ice storage discharge rate for cooling system $i$ at time $t$ and scenario $p$ , [MW <sub>th</sub> ]

$S_{p,t,i}^{ac,chs}$	Ice storage charge rate using air-cooled chillers for cooling system $i$ at time $t$ and scenario $p$ , [MW <sub>th</sub> ]
$S_{p,t,i}^{wc,chs}$	Ice storage charge rate using water-cooled chillers for cooling system $i$ at time $t$ and scenario $p$ , [MW <sub>th</sub> ]
$S_{p,t}^S$	Stored thermal energy in ice storage for cooling system $i$ at time $t$ and scenario $p$ , [MWh <sub>th</sub> ]

#### Index sets

Symbol	Meaning
$i$	Cooling system type index set $\{1, 2, 3\}$ denoted by $\mathcal{I}$
$p$	Scenario index set $\{1, 2, 3, 4\}$ denoted by $\mathcal{P}$
$s$	PV orientation and tracking technology index set $\{1, 2, 3\}$ denoted by $\mathcal{S}$
$t$	Time step index set $\{1, 2, 3, \dots, 8760\}$ denoted by $\mathcal{T}$

#### Chapter 3

##### Parameters

Symbol	Meaning
$A$	Area, [m <sup>2</sup> ]
$c^p$	Specific heat, [kJ/kg · K]
$COP$	Coefficient of Performance, dimensionless
$\dot{E}$	Rate of change of energy, [kW]
$f$	Fraction, dimensionless
$\dot{H}$	Rate of change of enthalpy, [kW]
$h$	Specific enthalpy, [kJ/kg]

$k$	Pumps/fans constant, [kW]
$\dot{m}$	Flowrate, [kg/s]
$N^{row}$	Number of rows in coils, dimensionless
$NTU$	Number of transfer units, dimensionless
$P$	Power, [kW]
$p$	Pressure, [kPa]
$PLR$	Part-load ratio, dimensionless
$\dot{Q}$	Heat transfer rate, [kW]
$R$	Chiller effective thermal resistance, [K/kW]
$\Delta\dot{S}$	Entropy generation rate, [kW/K]
$SoC$	State of charge, dimensionless
$T$	Temperature, [°C]
$V$	Fluid face velocity, [m/s]
$VSD$	Angular speed, [% of maximum speed]
$x$	Evaporator refrigerant quality, dimensionless
$Y$	Cooling tower height, [m]
$\varepsilon$	Effectiveness, dimensionless
$\eta$	Efficiency, dimensionless
$\rho$	Density, [kg/m <sup>3</sup> ]

#### Superscripts

Symbol	Meaning
$a$	Air
$ae$	Coil leaving air

<i>ai</i>	Coil entering air
<i>atwr</i>	Cooling tower air
<i>chl</i>	Chiller
<i>cc</i>	Cooling coil
<i>cca</i>	Cooling coil air
<i>ccw</i>	Cooling coil water
<i>ccrw</i>	Cooling coil return water
<i>ccsw</i>	Cooling coil supply water
<i>cf</i>	Coil fan
<i>comp</i>	Compressor
<i>cond</i>	Condenser
<i>cp</i>	Condenser pump
<i>crw</i>	Leaving condenser water
<i>csw</i>	Entering condenser water
<i>cw</i>	Chiller condenser water
<i>des</i>	Design conditions
<i>dp</i>	Dew-point
<i>dry</i>	Dry section of the coil
<i>evap</i>	Evaporator
<i>ext</i>	External
<i>fg</i>	Latent heat of evaporation
<i>ice</i>	Ice
<i>int</i>	Internal

<i>iw</i>	Ice storage water
<i>irw</i>	Ice storage return water
<i>isw</i>	Ice storage supply water
<i>ITES</i>	Ice storage
<i>leak</i>	Leak
<i>lim</i>	Limit
<i>m</i>	Motor
<i>max</i>	Maximum
<i>pp</i>	Primary pump
<i>ref</i>	Reference
<i>refg</i>	Refrigerant
<i>rw</i>	Return water
<i>s</i>	Saturated
<i>s</i>	Sensible
<i>sf</i>	Latent heat of fusion
<i>sp</i>	Secondary pump
<i>sw</i>	Chiller evaporator leaving water
<i>twr</i>	Cooling Tower
<i>VSD</i>	Variable speed drive
<i>w</i>	Water
<i>wb</i>	Ambient air wet-bulb
<i>wet</i>	Wet section of the coil
<i>wtwr</i>	Cooling tower water

## Chapter 4

### Parameters

Symbol	Meaning
$a_{f,m}^S$	Storage heat rate curve slope for piecewise linear segment $f$ and mode of operation $m$ , [kW <sub>th</sub> ]
$a_{x,j,m,e}^{chl}$	Chiller power curve slope for piecewise linear segment $f$ and mode of operation $m$ , [kW <sub>th</sub> ]
$b_{f,m}^S$	Storage heat rate curve y-intercept for piecewise linear segment $f$ and mode of operation $m$ , [kW <sub>th</sub> ]
$b_{x,j,m,e}^{chl}$	Chiller power curve y-intercept for piecewise linear segment $f$ and mode of operation $m$ , [kW <sub>th</sub> ]
$c^{BESS}$	Capital cost of installed battery capacity, [\$/kWh]
$c^{PV,C}$	Capital cost of installed fixed-tilt PV capacity, [\$/kW <sub>p,dc</sub> ]
$c^{ITES}$	Capital cost of installed ice storage capacity, [\$/kWh <sub>th</sub> ]
$c_x^{chl}$	Capital cost of installed chiller capacity with compressor technology $x$ , [\$/kW <sub>th</sub> ]
$c^{P,FS}$	Capital cost of installed chiller pumps, [\$/kW]
$c^{P,VSD}$	Capital cost of installed secondary pump, [\$/kW]
$c^{twr}$	Capital cost of installed cooling tower, [\$/kW <sub>th</sub> ]
$c_s^{PV,O}$	Operating cost of installed fixed-tilt PV capacity, [\$/kW <sub>p,dc</sub> /yr.]
$c^e$	Cost of electricity from the power grid, [\$/kWh]
$c^P$	Demand charge, [\$/kW <sub>p</sub> ]
$C^{Calmac}$	Usable capacity of modular ice storage tank (83-TR-hr nominal), [kWh <sub>th</sub> ]

$\mathcal{L}^{Elec}$	Hourly electric load, [kW]
$\dot{m}$	Flowrate, [kg/s]
$M$	Arbitrarily large number (Big M)
$N^{chl}$	Number of chillers, dimensionless
$N^{ITES}$	Number of modular ice tanks, dimensionless
$N_p^{days}$	Number of days represented by scenario $p$ , dimensionless
$N_p^{mos}$	Number of months represented by scenario $p$ , dimensionless
$P$	Power, [kW]
$PLR$	Part-load ratio, dimensionless
$\dot{Q}_{p,t}^D$	Building cooling demand at time $t$ and scenario $p$ , [kW <sub>th</sub> ]
$\overline{Q^{chl,des}}$	Upper limit for design chiller cooling capacity, [kW <sub>th</sub> ]
$\underline{Q^{chl,des}}$	Lower limit for design chiller cooling capacity, [kW <sub>th</sub> ]
$SoC$	State of charge, dimensionless
$yr$	Service life of PV, ice chillers, and ice storage, [yrs.]
$yr_b$	Battery service life, [yrs.]
$\eta^{BESS,chs}$	Battery charge efficiency, dimensionless
$\eta^{BESS,dis}$	Battery discharge efficiency, dimensionless
$\eta^{BESS,sdis}$	Battery self-discharge efficiency, dimensionless
$\eta^I$	Inverter efficiency, dimensionless
Superscripts	
Symbol	Meaning
$adj$	Adjusted



<i>Aux</i>	Auxiliary
<i>base</i>	Base
<i>chl</i>	Chiller
<i>cf</i>	Coil fan
<i>cp</i>	Condenser pump
<i>csw</i>	Entering condenser water
<i>cw</i>	Condenser water
<i>D</i>	Demand
<i>des</i>	Design conditions
<i>evap</i>	Evaporator
<i>ice</i>	Ice-making
<i>ITES</i>	Ice storage
<i>iw</i>	Ice storage water
<i>lim</i>	Limit
<i>ll</i>	Lower-limit
<i>max</i>	Maximum
<i>pp</i>	Primary pump
<i>ref</i>	Reference
<i>refg</i>	Refrigerant
<i>rw</i>	Return water
<i>sp</i>	Secondary pump
<i>sw</i>	Supply water
<i>twr</i>	Cooling Tower

$ul$	Upper-limit
$VSD$	Variable speed drive

### Decision variables

Symbol	Meaning
$\mathcal{B}_{p,t}^{chs}$	Battery charging rate at time $t$ and scenario $p$ , [kW]
$\mathcal{B}_{p,t}^{dis}$	Battery discharging rate at time $t$ and scenario $p$ , [kW]
$\mathcal{B}_{p,t}^s$	Stored electric energy at time $t$ and scenario $p$ , [kWh]
$B_{p,t,x,j,m,e}^{chl}$	Binary variable to toggle on chiller power curve piecewise linear segment $e$ in operation mode $m$ for chiller $j$ with compressor technology $x$ at time $t$ and scenario $p$ , binary
$B_{p,t}^{ice}$	Binary variable to activate ice-making mode at time $t$ and scenario $p$ , binary
$B_{p,t,m,f}^{ITES}$	Binary variable to toggle on ice storage heat rate curve piecewise linear segment $f$ in operation mode $m$ at time $t$ and scenario $p$ , binary
$C^{BESS}$	Installed BESS capacity, [kWh]
$C^{PV}$	Installed on-site fixed-tilt PV capacity, [kW <sub>p,dc</sub> ]
$C^p$	Installed chiller pumps capacity, [kW]
$C^{sp}$	Installed secondary pump capacity, [kW]
$C^{twr}$	Installed cooling tower capacity, [kW <sub>th</sub> ]
$Q_{x,j}^{chl,des}$	Installed nominal cooling capacity of chiller $j$ with compressor technology $x$ , [kW <sub>th</sub> ]
$GT^P$	Peak gas generation demand, [kW]
$GT_{p,t}$	Power delivered by the electricity grid at time $t$ and scenario $p$ , [kW]

$N^{ITES}$	Number of modular ice storage tanks, $N^{ITES} \in \mathbb{R}$
$\dot{Q}_{p,t,x,j}^{chl}$	Load for chiller $j$ with compressor technology $x$ at time $t$ and scenario $p$ , [ $\text{kW}_{th}$ ]
$S_{p,t}^{chs}$	Ice storage charge rate at time $t$ and scenario $p$ , [ $\text{kW}_{th}$ ]
$S_{p,t}^{dis}$	Ice storage discharge rate at time $t$ and scenario $p$ , [ $\text{kW}_{th}$ ]
$S_{p,t}^s$	Stored thermal energy at time $t$ and scenario $p$ , [ $\text{kWh}_{th}$ ]
$ON_{p,t,x,j}^{chl}$	Power switch for chiller $j$ with compressor technology $x$ at time $t$ and scenario $p$ , binary
$PV_{p,t}^{curt}$	Curtailed PV generation at time $t$ and scenario $p$ , [ $\text{kW}$ ]
$\Delta T^{cw,des}$	Design chillers condenser temperature differential, [ $^{\circ}\text{C}$ ]
$\Delta T^{sw,des}$	Design chillers evaporator temperature differential, [ $^{\circ}\text{C}$ ]

#### Index sets

Symbol	Meaning
$e$	Chiller piecewise linear segment index set $\{1, 2\}$ denoted by $\mathcal{E}$
$f$	Storage piecewise linear segment index set $\{1, 2, 3, 4\}$ denoted by $\mathcal{F}$
$j$	Chiller index set $\{1, 2, 3, \dots\}$ such that $j \in \mathbb{N}$
$m$	Operation mode index set $\{1, 2\}$ denoted by $\mathcal{M}$
$p$	Scenario index set $\{1, 2, 3, 4, 5\}$ denoted by $\mathcal{P}$
$t$	Time step index set $\{1, 2, 3, 4, \dots, 24\}$ denoted by $\mathcal{T}$
$x$	Chiller compressor technology index set $\{1, 2, 3\}$ denoted by $\mathcal{X}$

## Chapter 5

### Parameters

Symbol	Meaning
$c^e$	Time-of-use electricity rates
$f$	Fraction, dimensionless
$h$	Specific enthalpy, [kJ/kg]
$\dot{m}$	Flowrate, [kg/s]
$m$	Mass, [kg]
$P$	Power, [kW]
$PLR$	Part-load ratio, dimensionless
$SoC$	State of charge, dimensionless
$T$	Temperature, [°C]
$\dot{Q}$	Heat transfer rate, [kW <sub>th</sub> ]
$VSD$	Angular speed normalized to maximum speed, dimensionless

### Superscripts

Symbol	Meaning
$ae$	Coil exit air
$ai$	Coil inlet air
$atwr$	Cooling tower air
$bcw$	Blended chillers condenser water
$bsw$	Blended chillers evaporator water
$chl$	Chiller
$cca$	Cooling coil air

<i>ccrw</i>	Cooling coil return water
<i>ccsw</i>	Cooling coil supply water
<i>ccw</i>	Cooling coil water
<i>cf</i>	Coil fan
<i>cp</i>	Condenser pump
<i>crw</i>	Blended leaving chillers condenser water
<i>csw</i>	Blended entering chillers condenser water
<i>cw</i>	Chiller condenser water
<i>D</i>	Demand
<i>des</i>	Design conditions
<i>dry</i>	Dry section of the coil
<i>ITES</i>	Ice storage
<i>isw</i>	Ice storage supply water
<i>irw</i>	Ice storage return water
<i>iw</i>	Ice storage water
<i>ℓ</i>	Latent
<i>max</i>	Maximum
<i>min</i>	Minimum
<i>pp</i>	Primary pump
<i>rw</i>	Blended chillers evaporator returning water
<i>s</i>	Saturated
<i>s</i>	Sensible
<i>sp</i>	Secondary pump

$sw$	Chiller evaporator water
$Sys$	System
$twr$	Cooling Tower
$VSD$	Variable speed drive
$wtwr$	Cooling tower water

#### Decision variables

Symbol	Meaning
$\dot{m}_t^{tw}$	Storage water flowrate at time $t$ , [kg/s]
$T_{t,j}^{sw}$	Leaving chilled water temperature setpoint for chiller $j$ at time $t$ , [°C]
$T_t^{cws}$	Entering condenser water temperature for chillers at time $t$ , [°C]
$\Delta SoC_t$	Ice thermal storage dispatch amount at time $t$ , dimensionless
$ON_{t,j}^{chl}$	Power switch for chiller $j$ at time $t$ , binary
$ON_{t,n}^{twr}$	Power switch for cooling tower $n$ at time $t$ , binary
$VSD_t^{cf}$	Cooling coil fan motor speed normalized to the maximum speed at time $t$ , dimensionless
$VSD_t^{sp}$	Secondary pump motor speed normalized to the maximum speed at time $t$ , dimensionless
$VSD_t^{twr}$	Cooling tower fan motor speed normalized to the maximum speed at time $t$ , dimensionless

## Index sets

Symbol	Meaning
$g$	Secondary pump index set $\{1, 2\}$ denoted by $\mathcal{G}$
$j$	Chiller index set $\{1, 2, 3\}$ denoted by $\mathcal{J}$
$n$	Cooling tower index set $\{1, 2\}$ denoted by $\mathcal{N}$
$t$	Time step index set $\{1, 2, 3, 4, \dots, 24\}$ denoted by $\mathcal{T}$
$z$	Training data index set $\{1, 2, 3, 4, \dots, 237\}$ denoted by $\mathcal{Z}$

## **Acknowledgments**

First and foremost, I need to acknowledge the people who shaped this work through their immense knowledge and invaluable insight. I express my sincere gratitude and appreciation to my advisor, Professor Vijay Modi, for his support, guidance, and understanding throughout the stages of this project. I am grateful for his patience with me in my academic life and especially during challenges in my daily life. I extend my gratitude and appreciation to Professor Arvind Narayanaswamy for his invaluable insights, support, and advice during my studies. I further extend my gratitude to everyone who contributed to my Ph.D. experience.

I could not have embarked on this challenging project without the support of my family and friends. I want to thank them for their encouragement and patience on this journey. I sincerely apologize for the missed events and celebrations while I was absent in New York City. I apologize to my adorable niece, Al-Dana, for missing many milestones.

Last but not least, I want to thank Qatar National Research Fund for sponsoring this project with grant number QRLP10-G-1803028. Last, I need to acknowledge Qatar General Electricity and Water Corporation (Kahramaa) for providing the necessary power generation data and Qatar Environment and Energy Institute (QEERI) for providing the necessary solar irradiance and meteorological data used in this work.



## Chapter 1: Introduction

The world's use of fossil fuels as an on-demand energy source is increasing the concentration of greenhouse gas emissions in our atmosphere [1], [2] that continues to accelerate as many parts of the world develop and industrialize [3], [4]. It became evident that anthropogenic greenhouse gas emissions, primarily CO<sub>2</sub> (carbon dioxide), drive climate change by trapping heat in the atmosphere and increasing the global temperature [5]–[8]. If not mitigated, climate change threatens rising sea levels, coastal flooding, food and fresh water shortages, and higher frequency and intensity of extreme weather events [9]–[11]. The International Panel on Climate Change's special report finds that the risk of irreversible ecological damages can be reduced by limiting global warming to 1.5°C above the pre-industrial era [12]. World energy use is responsible for two-thirds of yearly anthropogenic carbon emissions [13], which can be classified into three end-use sectors: transportation, industrial, and buildings. Building energy use accounts for 30% of total energy end-use and 55% of electricity use worldwide [14], dominated by space-cooling and heating and domestic hot water needs [15]–[17].

Qatar is a small country along the Arabian Gulf with a population of 2.7 million and a total land area of 11,600 km<sup>2</sup>. The climate can be described as dry-arid with mild winter months (average daily temperature of 20-25°C) and hot summer months (average daily temperature of 35-40°C). Qatar ranks highest for per capita carbon emissions [18]. Although largely propelled by carbon emissions from producing and exporting liquefied natural gas, it displaces dirtier and more emission-producing fuels elsewhere. Still, the electricity sector is responsible for one-fourth of total carbon emissions, of which buildings account for 60% of total electricity use [18],

[19]. The high electricity demands in buildings are dominated by near year-round energy-intensive space-cooling [20], [21].

Qatar's electricity and water demands are met by gas-fired integrated water and power plants, combining electricity production and water desalination. In 2016, the total electricity and desalinated water consumption were 42 TWh and 560 million m<sup>3</sup>, respectively, produced using 452 million MMBtu of natural gas at an average thermal efficiency of 31%, emitting 24 Mt of CO<sub>2</sub> [19].

Electricity is subsidized based on sector and consumption bracket [22]. For non-bulk consumers with a peak demand of less than 5 MW and a monthly consumption bracket of less than 4 MWh, the rate is flat at \$36/MWh. For bulk customers with a peak demand greater than 5 MW, the tariff is \$58/MWh during the low-demand seasons and rises to \$93/MWh during peak hours in the hotter months (May to October) from 12 to 6 PM [22]. The on-peak pricing is motivated by the growing peak demand, which grew at an average rate of 6% per year since 2010 to 7.33 GW in 2016. This led to expanding gas generation capacity only to supplement the yearly marginal increase in demand in the hotter summer months. Also, the high ambient temperatures in the summer significantly depress their power capacity and thermal efficiency relative to their design condition, leading to further upsizing them.

Figure 1.1 shows Qatar's 2016 daily electricity demand and ambient temperatures for three days in the winter (Jan 5-7), spring (April 10-12), and summer (Sept 2-4), where Hour 0 corresponds to 12 AM in all subsequent figures. Meteorological and solar insolation data were collected from a station in Doha, where most of the population lives. Daily demand variations are minor relative to seasonal variations driven by high electricity demand from space cooling. In the summer, diurnal demand from space-cooling is synergetic with dry-bulb temperatures, and in

the winter, the electricity demand is largely from non-cooling loads. Average daily dry-bulb temperature variations can be as high as 10°C compared to 5°C for wet-bulb temperature.

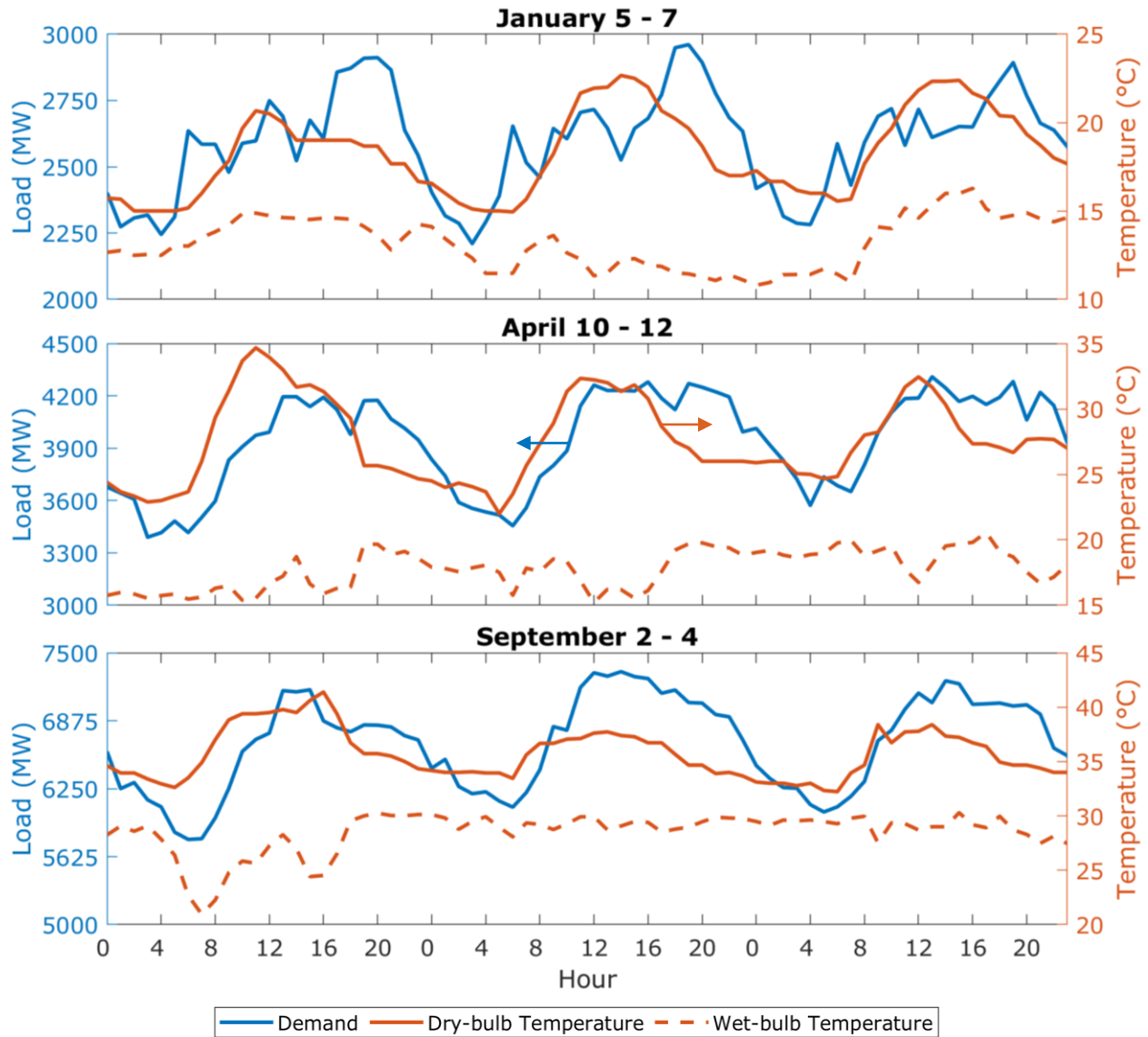


**Figure 1.1: Qatar’s 2016 electricity demand in the winter, spring, and summer for three days on the left y-axis and the ambient conditions, dry and wet-bulb temperatures, on the right y-axis.**

Threatened by rising sea levels and extreme inhospitable temperatures due to climate change [23], Qatar, alongside the world, needs to adopt more sustainable approaches to meet increasing energy and cooling demand. While considerations are made for renewable-based

energy sources and demand-side management [24]–[28], which could reduce emissions by 20–25% by 2035, Qatar does not have a net zero or a deep decarbonization plan. Pathways to decarbonizing the electricity sector in Qatar have been investigated by scholars for large-scale renewables deployment [29]–[33] and from a distributed building-scale perspective with an emphasis on demand side management [34]–[41].

In a comprehensive examination of renewable energy sources in Qatar, Okonkwo et al. [32] explored wind turbines, PV (photovoltaic), concentrated solar power, and biofuels combined with energy storage technologies, including thermal and pump-hydro storage. Okonkwo identified several potential decarbonization pathways with PV and wind generation. However, energy storage systems such as pump hydro were determined to be essential for deep decarbonization, but Qatar's geography lacks favorable topography. Bohra and Shah [30] and Martinez-Plaza et al. [31] analyzed the long-term potential of solar energy in Qatar. The studies agree on the large potential for grid-scale PV generation. Martinez-Plaza also identified concentrated solar power with large thermal storage as an alternative solution. An investigation of wind turbine potential by Marafia and Ashour [33] reveals promising wind speeds reaching 6.5 m/s at 10 m above ground. The research finds off-shore wind energy suitable for off-grid connection for islands in Qatar and promising for a grid-connected generation. However, unlike solar insolation, wind speed is highly spatially sensitive. Furthermore, obtained meteorological data demonstrate correlated wind speed with intra-annual and diurnal PV generation, which makes wind turbines less able to reduce the required energy storage capacity.

Alrawi et al. [36] and Elbeheiry et al. [35] examined the economic viability of distributed-scale rooftop PV generation with battery energy storage systems in Qatar. The studies find the examined system economically infeasible, constrained by subsidized tariffs and a lack of

economic incentives. In another work, Alrawi et al. [36] investigated factors influencing residential rooftop PV adoption using surveys. They establish subsidized electricity tariffs as a challenge to PV adoption and propose lifting subsidies and promoting energy conservation awareness. Teshnizi et al. [37] analyzed grid-connected household-scale wind turbines in Qatar, and their analysis found limited suitability and emissions reduction potential in certain areas.

Demand-side management can be categorized into energy efficiency and demand response. Energy efficiency reduces energy use from higher efficiency building standards, appliances, and cooling technologies. Conversely, demand response exploits electricity tariffs to motivate demand adjustments to match supply, which is essential for intermittent renewable generation. Bayram and Koc [38] investigated demand-side management practices in Qatar. The study finds energy efficiency to be most explored. Although the demand response is gaining attention, the current tariff structure does not motivate demand adjustment. They propose adjusting the air-conditioning set point for unoccupied buildings to reduce peak electricity demand in summer through demand load control programs. Krarti et al. [39] analyzed the macroeconomic benefit of large-scale building energy efficiency programs in Qatar. They find that higher buildings' energy efficiency standards can significantly reduce energy consumption and peak energy demand even when retroactively implemented. Kamal et al. [41] recommend a policy pathway of building codes and standards to reduce building energy consumption with special emphasis on new constructions considering Qatar's unique rapid urban development pace. However, the analysis determines that subsidized electricity tariffs do not encourage energy savings.

Prior works in the literature identified that the subsidized electricity sector is challenging to decarbonize but affirm Qatar's particular attractiveness for exploiting solar PV. Qatar has a

high and predictable solar insolation with a global horizontal irradiance of 2200 kWh/m<sup>2</sup>/yr. with few rainy or cloudy days that are synergetic with electricity demand. This is further complemented by access to low-interest capital and abundant suitable land area. Figure 1.2 illustrates the synergistic relationship between the weekly average electric load, solar output, mean heat index, and ambient dry-bulb temperature in degrees Celsius. The heat index is a metric for the human perception of the ambient temperature combining the ambient dry-bulb temperature and the humidity level. High humidity between July and September is responsible for the increased electricity demand from space cooling.

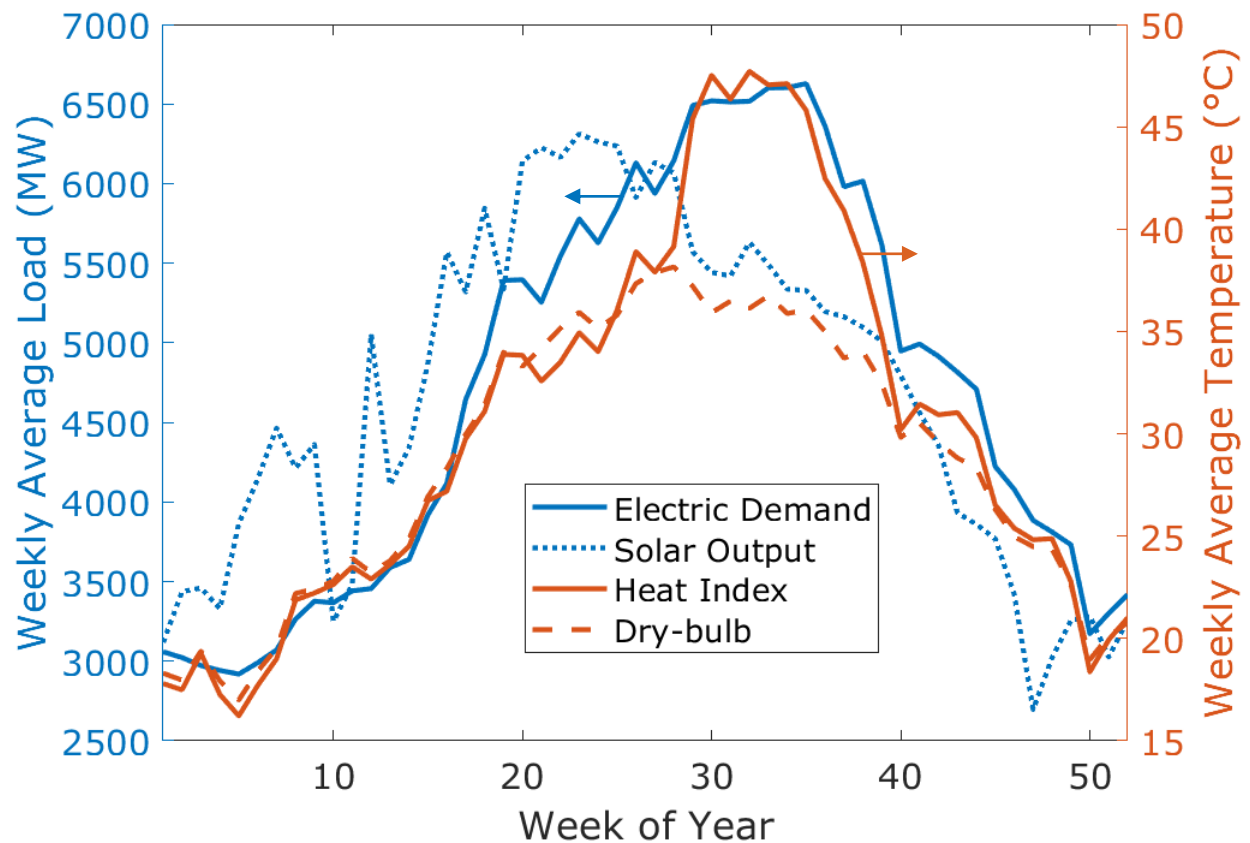


**Figure 1.2: Qatar 2016's weekly mean electric demand and solar output over 19 km<sup>2</sup> in MW on the left y-axis, and the weekly mean heat index and dry-bulb temperature in degrees Celsius on the right y-axis. Yearly solar output over 19 km<sup>2</sup> is equivalent to 2016's total electricity use of 42 TWh.**

In the past, a high fraction of airborne dust hindered large-scale PV deployment in Qatar. However, ongoing research investigates procedures to evaluate and reduce the degradation due to soiling. Abdallah et al. [42] found that fouling can drop panels yield by 15% if not cleaned monthly. A study by Martinez-Plaza et al. [43] determined anti-soiling coating to be ineffective in limiting yield drop but allowed for easier cleaning of the panels. Tahir et al. [44] theoretically analyzed the impact of climate change on mono and bi-facial PV panels in Qatar. The study predicts rising air temp in the years 2050 and 2080 with a reduction in solar insolation by 5-8%. Bi-facial panels are determined to be better suited due to their high energy output and reduced cell temperature. In early 2020, a deal was signed to build an 800 MW solar PV plant in Qatar with a record levelized cost of electricity of \$15/MWh [45], which was commissioned in October 2022. Another deal was signed in August 2022 to build two additional solar PV plants with a combined capacity of 875 MW [46].

Still, cooling demand that continues through the night cannot be met with diurnal solar PV generation. I-TES (ice thermal energy storage) is examined as a low-cost means, as opposed to current BESS (battery energy storage system) technologies, to store excess PV generation for subsequent cooling. I-TES requires a chiller to produce cooling to convert liquid water into ice. It allows as much as 0.4 MJ/kg of cooling compared to 0.04 MJ/kg for cold water storage since it takes advantage of both the sensible and latent heat from the phase change of liquid water to ice.

Carbon pricing is examined as a state policy tool to accelerate the adoption of energy storage and renewable energy resources as a viable competitor with cheap natural gas in Qatar. Carbon pricing is an instrument to increase the cost of generations from carbon-based energy sources to reflect better the environmental damage caused by CO<sub>2</sub> emissions. By shifting the burden back to the energy consumers, carbon pricing enables renewable energy to compete with

carbon-based energy sources and mobilize investments [47], [48]. While there are many forms of carbon pricing, the examined carbon pricing tool is the carbon tax, which adds a cost to gas generation per ton of CO<sub>2</sub> emitted.

Moving to low-carbon electricity grids while satisfying the world's growing energy needs remains humanity's greatest challenge. This work is a subset of a large body of literature that attempts to examine, analyze, and develop alternative decarbonization pathways. This dissertation aims to examine and analyze a decarbonization pathway for the cooling-driven electricity sector in Qatar using PV generation combined with I-TES for cooling load shifting and BESS for electric load shifting from multiple perspectives in a top-down approach. The dissertation is organized into the following chapters:

## **Chapter 2: Assessing large-scale deployment from a utility-scale perspective**

PV generation already out-competes gas generation at current prices. However, large-scale deployment of PV generation cannot be supported without the widespread adoption of costly energy storage. This chapter assesses the potential of utility-scale PV generation combined with I-TES and BESS. The problem is formulated in a two-stage stochastic linear program solved at a given gas price. Linear programming is extensively used for large-scale energy problems when describing aggregate systems' performance and behavior. Statistical tools are applied to estimate electric demand from space cooling. To combat low energy prices in Qatar, carbon pricing is examined as a policy tool in order to boost the adoption of energy storage and facilitate the transition to sustainable renewable energy sources.

## **Chapter 3: Modeling of WC CWS with I-TES**

The conventional way to cool medium to large buildings in Qatar is using a WC CWS (water-cooled chilled water system). Using water to transport heat over large distances reduces



energy losses in air distribution and refrigeration systems. However, the behavior and control of CWSs (chilled water systems) tend to be more complex than cooling systems used in smaller buildings. While simpler models can describe the aggregate behavior of the systems, as done in Chapter 2, they cannot be applied to individual systems. This chapter develops hybrid models combining first principles with data-driven parameters to capture the complex behavior of the major power-consuming components in CWS with I-TES used for building-scale analysis in Chapters 4 and 5.

#### **Chapter 4: Design of an integrated WC CWS with I-TES, BESS, and on-site PV**

The decarbonization pathway examined for large-scale deployment in Chapter 2 must eventually be applied to individual buildings with distinct envelope construction and electricity and cooling needs. This chapter examines the design and equipment capacity sizing problem of CWS with I-TES and BESS for better integration with on-site PV generation. A problem confronted when deciding equipment capacity is estimating their energy, which requires solving the scheduling and dispatch problem that is highly non-linear and involves many decision variables at each time step. A bi-level optimization formulation is developed to decouple the capacity sizing from the scheduling and dispatch problem. The upper level minimizes yearly total system costs and decides the installed capacities and design parameters using particle swarm optimization. The decided parameters are passed down to solve the scheduling and dispatch problem in a mixed-integer linear program with piece-wise linearization and return the estimated yearly electricity charges. Two buildings are examined with dissimilar demand profiles: a residential building with dominant night-time electricity needs and a commercial building with diurnal cooling and electricity needs. This chapter restresses the role of carbon pricing in adopting energy storage and highlights the impact of demand-side management.

## **Chapter 5: Optimal equipment scheduling and dispatch of WC CWS with I-TES**

Intermittent renewable generations cannot be dispatched or perfectly predicted. A low-carbon power grid must be accompanied by demand-side management through load shifting using energy storage and demand adjustments communicated by the central grid via a pricing signal. Cooling is responsible for nearly half of the electricity demand in Qatar, thereby making cooling systems a crucial target for demand-side management. However, operating CWS to maximize savings can be challenging. This challenge arises from operating the system outside its design conditions, which requires careful consideration of chillers' part-load performances and the performances of associated auxiliary equipment. This chapter develops an optimization strategy for optimal scheduling and dispatch of WC CWS with I-TES to reduce operating costs. A bi-level optimization formulation is developed that minimizes the daily electricity charge, which is solved using the genetic algorithm at both levels. The upper level decides the I-TES dispatch amount fed to the lower-level optimizer to solve the WC CWS equipment scheduling problem sequentially at each hour and returns the corresponding system power consumption to update the guess for the next iteration. This approach negates the need for simplistic system models for complex space cooling and heating applications. The developed strategy is contrasted against two commonly used heuristic strategies: chiller priority and storage priority control.

## **Chapter 6: Conclusions and recommendations for future works**

The proposed decarbonization pathway is analyzed from different perspectives in a top-down approach in the earlier chapters. This chapter ties in the different perspectives to build a complete picture of the challenges and prospects of the considered pathway. Recommendations are made to address current and future urban development needs. Last, future research questions are provided to expand the scope of the study.

## **Chapter 2: Assessing large-scale deployment from a utility-scale perspective**

### **2.1 Introduction**

The solution to sustainably meet the world's growing energy demand will not be universal. Instead, each region must tailor a plan specific to its energy needs, climate, and geology. Nevertheless, any approach will combine renewable energy sources with energy storage technologies and demand-side management. Individuals' actions to reduce energy consumption or consider alternative energy sources can only have a limited impact on the overall electricity sector's carbon emissions, and any far-reaching impact requires government intervention via direct actions or policy enactments.

This chapter assesses the potential for large-scale deployment of utility-scale PV generation combined with I-TES and BESS for decarbonizing cooling and electric loads. The planning problem is solved to estimate the required aggregate capacities and annual system cost. In addition to the literature, more sophisticated models are developed to examine I-TES for cooling load shifting. The developed models account for the impact of ambient conditions on the performance of cooling systems and evaluate existing idle chillers' cooling capacity that could be used for I-TES charging.

The utility-scale perspective provides insight into the renewable penetration potential, overall emissions reduction, and the impact on power grid operation. Linear programming is extensively employed in utility-scale analyses because it can solve large problems with thousands of continuous and binary variables commonly confronted in large-scale deployment of renewables with energy storage [49]–[51]. It is also useful for describing the aggregate behavior and performance of its constituent systems, which tend to exhibit simpler behavior.

In the literature, thermal energy storage has been examined to increase the flexibility of the power grid by responding to the electricity demand and intermittent renewables generations [52]–[55]. More commonly, in regions with variable electricity rates or demand charges, thermal storage is examined to reduce the required chiller cooling capacity, demand charges, and electricity use charges from load shifting [56]–[59]. For that mode of operation, the storage is charged during the off-peak period, typically at night, and discharged during the on-peak period, typically in the afternoon, making it suitable for use in schools, offices, and other buildings with dominant diurnal cooling needs. Deetjen et al. [60] considered thermal storage for grid-wide efficiency improvements by taking advantage of the higher cooling efficiency achieved when running chillers at capacity, countering the narrative of thermal storage as net energy consumers. Ruan et al. [56] performed a linear programming analysis to improve the efficiency and economics of building combined cooling, heating, and power using I-TES. They found that gas and electricity charges are the main factors in determining the economic feasibility of I-TES.

The roles and use of BESS in decarbonization are extensively studied [61]–[69]. Unlike I-TES, BESS can be used to decarbonize all electric loads, but it suffers from capacity degradation, high cost of capacity, and shorter service life. However, the rate at which the cost is falling [70] enables BESS to be cost-competitive with other energy storage technologies. Several studies have stressed the role of utility-scale BESS with PV in reducing carbon emissions and carbon abatement costs compared to PV alone [62]–[64]. Arbabzadeh et al. [65] examined various energy technologies to reduce the curtailment of variable renewable energy sources and carbon emissions in California and Texas. The results showed that BESSs have a limited role at the current capacity cost. However, a modest decrease in capacity cost can make BESS economically viable.

Chapter 2 is organized as follows: the methodology is presented in Section 2.2. First, the performance of cooling systems as a function of the ambient temperatures is estimated from generic chillers' performance data; second, statistical tools are applied to determine the aggregate cooling load from hourly electric demand; third, the problem formulation is laid out. Section 2.3 first presents and discusses the cost-optimal system under current cost structures and then examines the role of carbon pricing as a state policy to reduce carbon emissions. Next, a deeply decarbonized system realized with a carbon pricing policy is analyzed in more detail. Last, the impact of declining BESS costs on the cost-optimal system is investigated. The chapter is concluded in Section 2.4.

## **2.2 Methodology**

The overall framework utilizes central grid PV and gas generation to distribute electricity via the grid, which can be used for all loads, including BESS charging. The centralized BESS delivers power to the electric grid when needed. I-TES is installed on the customer side as an addition to an already existing cooling system and can be charged using existing idle chillers and/or additional ice chillers for a cost. Additional ice chillers are particularly important due to the overlap of solar insolation with daytime cooling loads, reducing idle chillers' capacity that could be used for storage charging. Solutions are sought that minimize overall annual system costs from Capex (capital expenditures) and OpEx (operation expenditures) at a given gas price. In accounting for emissions reduction from cooling, the electric cooling load is assumed to be met in the following order using: (i) PV generation, (ii) BESS, and (iii) gas generation.

Cooling systems can be classified into three types: DXS (direct expansion system), AC CWS (air-cooled chilled water system), and WC CWS. DXS, which includes rooftop units, split and ductless mini-split systems, and window units, provide cooling directly from the expansion

of the refrigerant. In CWS (chilled water system), water is used as an intermediary fluid to transport heat over larger distances and in large buildings. An illustration of the analyzed problem is shown below in Figure 2.1.

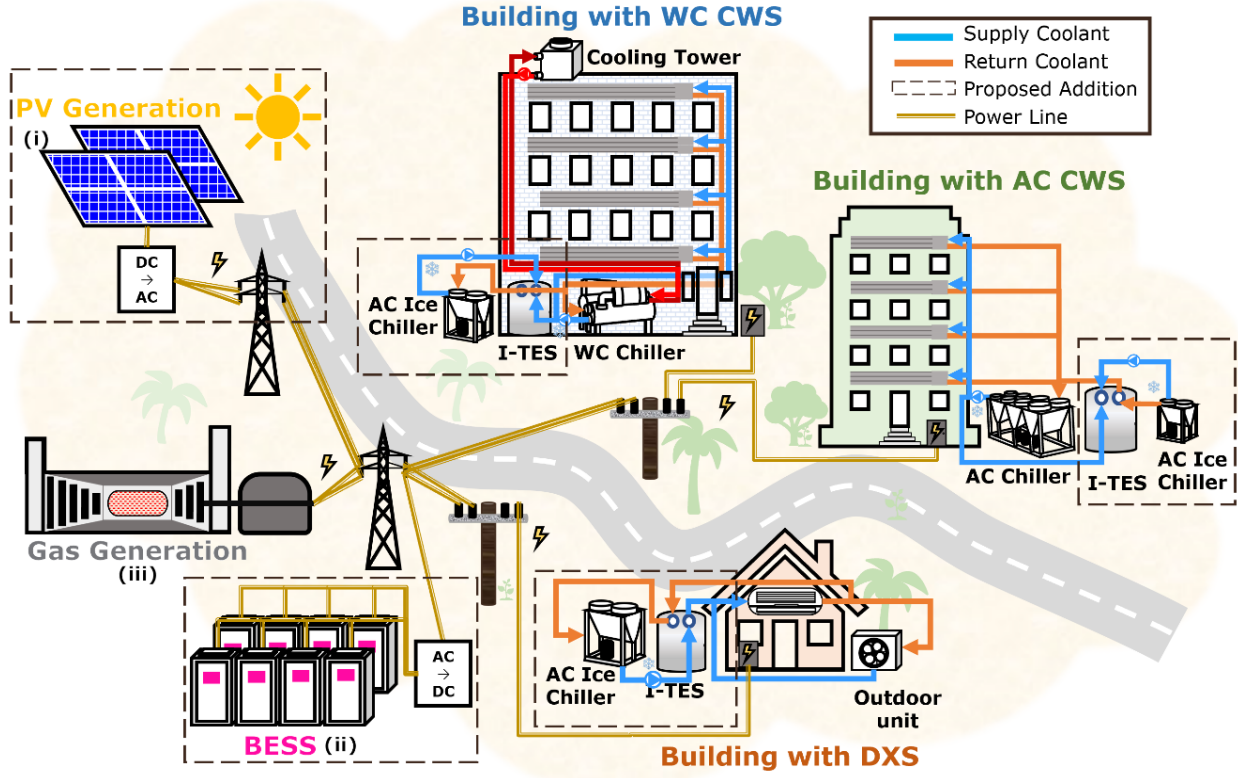


**Figure 2.1: An illustration of the considered power grid. Central grid PV and gas generation can be used for all loads, including BESS charging. Buildings are classified based on their cooling system type: DXS, AC CWS, and WC CWS. To account for emissions reduction from cooling, the cooling load is assumed to be met in the following order using: (i) PV generation, (ii) BESS, and (iii) gas generation.**

I-TES stores thermal energy mainly in the form of latent heat. The considered I-TES type in this study is internal melt, a modularized tank favored for its predictable charge and discharge rates. Inside the tank, multiple parallel loops of tubes are submerged in water, and a secondary water-glycol mixture is circulated through the inner loops to freeze or melt the water inside the tank. The heat rate of internal melt I-TES is a function of the SoC (State of Charge) and inlet water-glycol mixture temperature and flowrate [71]–[73]. The charge rate is highest during

sensible charging due to a greater temperature difference between the entering water-glycol mixture and the tank water temperature. Once the tank is brought to freezing temperature, the charge rate reduces as the thermal resistance increases due to ice formations. Similarly, discharging of I-TES is initially higher when the water in the tank is completely frozen, and the rate reduces as the ice around the tube melts.

DXS and AC CWS are AC (air-cooled) systems, and their COP (coefficient of performance) is associated with the ambient dry-bulb temperature. WC CWS utilizes WC (water-cooled) condensers, and their COP is associated with the wet-bulb temperature as heat is ultimately rejected using evaporative cooling in a cooling tower. WC systems run more efficiently, benefiting from lower condensing temperatures, especially in dry seasons. The current approach to meet the cooling demand in Qatar, which lacks thermal storage, uses a mix of DXS, AC CWS, and WC CWS. The considered pathway of load shifting using I-TES for each cooling system type is illustrated in Figure 2.2.

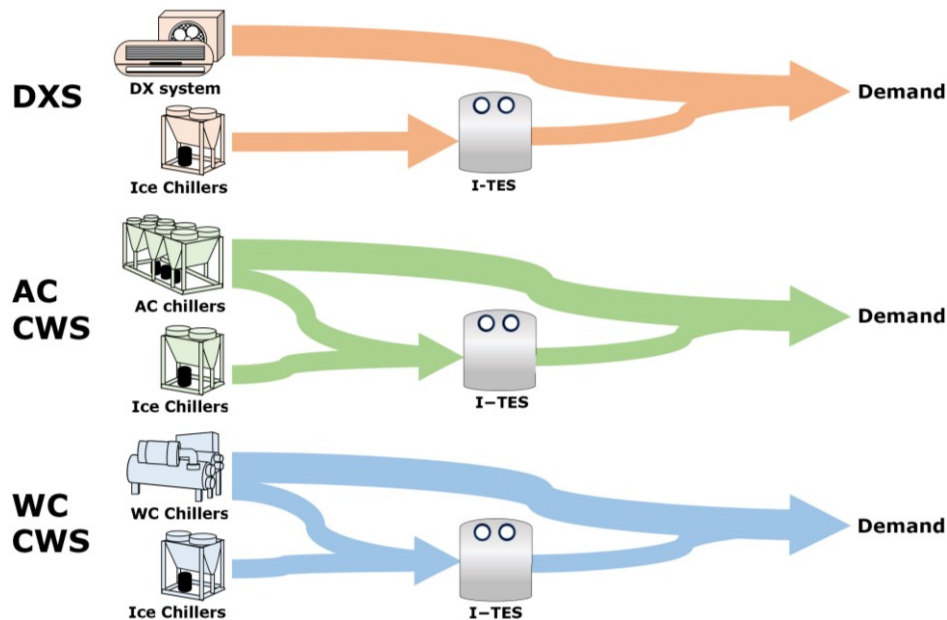


**Figure 2.2: Pathways to satisfying the cooling demand in the three cooling systems types. While AC and WC CWS can make ice, additional AC ice chillers can be installed. Additional ice chillers must be installed with the I-TES for the DXS.**

The DXS' I-TES can only be charged using additionally installed ice chillers as currently installed standard systems are incompatible with ice-making. For AC and WC CWS, I-TES can be charged using idle and additionally installed chillers capacities. All additional ice chillers are lower-cost AC chillers, provided they utilize low-cost excess generation for I-TES charging.

The analysis is performed with four scenarios, each with one year of hourly solar insolation (private station in Doha), electric demand, and meteorological data (collected from Doha International Airport Station) from 2013 to 2016. However, as the demand has been growing yearly, the demands from 2013 to 2015 are normalized to the peak demand of 2016. The aggregate cooling load is determined using the normalized hourly electric demand and its respective year's meteorological data set. The 2016 scenario was taken as the reference scenario in all produced figures.

### **2.2.1 Cooling systems performance estimation**

The COP of cooling systems is affected by the refrigerant condensing temperatures influenced by the ambient conditions. The dry-bulb temperature influences AC systems condensing temperature as they depend on dry cooling to reject heat to the ambient. The condensing temperature of WC systems is influenced by the wet-bulb temperature as they rely on evaporative cooling. The fundamentally lower wet-bulb temperature reduces the condensing temperature and improves system performance.

The COP of AC and WC systems as a function of ambient conditions is derived from the behavior of generic system performance analogous to Deetjen et al. work [60], [74]. Although less significant, the performance of cooling systems is also a function of their loading. Chillers' performance data are taken from the library of chillers in EnergyPlus at the typical design water supply temperature of 7°C and the ideal part-load ratio of 80%. The data are extracted and used



with Gordon-Ng model to predict chiller performance across a broader range of ambient temperatures than permitted by the DOE-2 model in EnergyPlus. Details of the methodology used are explained in Section 3.2.1 in Chapter 3.

Two AC chillers with typical performance are selected: Carrier 19XA and McQuay AGZ, and two WC chillers: Trane RTHB and Carrier 19XR. Auxiliary equipment, such as water pumps and tower fans, consumes on the order of 10% of total system energy in AC CWS and about 20% in WC CWS [75]. The entering condenser temperature for WC CWS is taken at a standard 3°C above the wet-bulb temperature. A power curve is fitted to the estimated system COP for AC systems in refrigeration and ice-making (I-TES charging) mode, which are given by:

$$COP_{p,t}^{ac} = 14.44(T_{p,t}^{db})^{-0.5}, \quad [^{\circ}\text{C}] \quad (T_{p,t}^{db} > 0^{\circ}\text{C}) \quad (2.1)$$

$$COP_{p,t}^{ac,ice} = COP_{p,t}^{ac} \times \varphi^{ice}, \quad [^{\circ}\text{C}] \quad (T_{p,t}^{db} > 0^{\circ}\text{C}) \quad (2.2)$$

and for WC systems:

$$COP_{p,t}^{wc} = 25.25(T_{p,t}^{wb})^{-0.56}, \quad [^{\circ}\text{C}] \quad (T_{p,t}^{wb} > 0^{\circ}\text{C}) \quad (2.3)$$

$$COP_{p,t}^{wc,ice} = COP_{p,t}^{wc} \times \varphi^{ice}, \quad [^{\circ}\text{C}] \quad (T_{p,t}^{wb} > 0^{\circ}\text{C}) \quad (2.4)$$

where the subscripts  $p$  is the scenario index set  $\{1, 2, 3, 4\}$  denoted by  $\mathcal{P}$  and refers to years 2013-2016, and  $t$  is the time step index set  $\{1, 2, 3, \dots, 8760\}$  denoted by  $\mathcal{T}$  that refers to the hour of the year,  $\varphi^{ice}$  is the depressed chiller performance factor in ice-making mode and is 0.8, and  $T_{p,t}^{db}$  and  $T_{p,t}^{wb}$  are the dry and wet-bulb temperatures, respectively, in degrees celsius. Running the

chillers in ice-making mode reduces the COP due to decreased refrigerant vapor quality [76]–[78]. Figure 2.3 visualizes the developed relation between system COP and the wet-bulb temperature for WC systems and dry-bulb temperatures for the AC systems in refrigeration and ice-making mode.

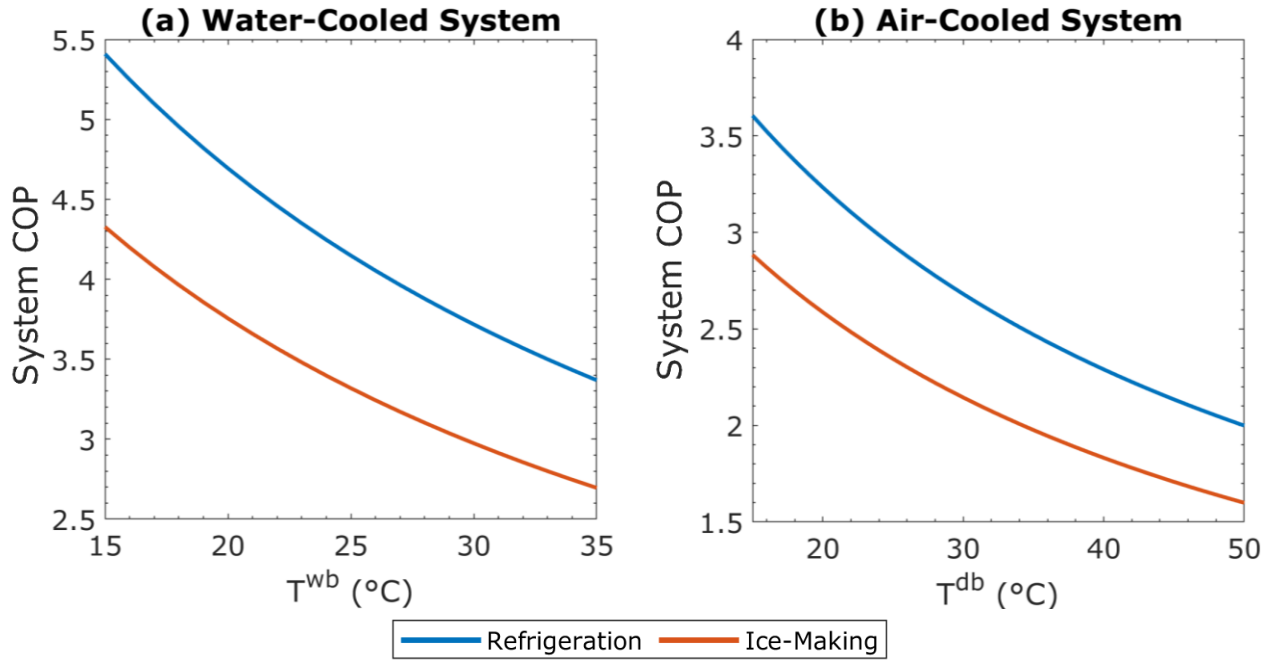


**Figure 2.3: System COP for (a) WC systems v. wet-bulb temperature and (b) AC CWS v. dry-bulb temperature in refrigeration and ice-making modes. AC systems include AC CWS and DXS.**

An exponential improvement in COP is realized with reduced temperatures. Design system COP, which dictates the installed nominal cooling capacities and performance, for WC systems of 4.2 is evaluated at the standard design wet-bulb temperature of 25°C, and for the AC system of 2.4 is evaluated at the standard design dry-bulb temperature of 35°C in refrigeration mode. The developed COP relation allows for the conversion between electric and thermal loads necessary for thermal energy storage analysis.

Ambient conditions also impact the cooling capacity of cooling systems. The cooling capacity of a cooling system in refrigeration mode is associated with the COP. In ice-making mode, the cooling capacity is associated with both the COP and evaporator refrigerant saturation density captured in the depressed chiller capacity factor,  $\psi^{ice}$ . The factor accounts for the loss in refrigerant thermal capacity in the evaporator due to a reduced refrigerant vapor saturation, and is 0.75. Running the chillers in ice-making mode can depress their cooling capacity by 30-40% relative to their nominal capacities [79]. For AC chillers, the cooling capacity relation in both modes is given by:

$$C^{AC} \propto COP_{p,t}^{ac} \quad (\text{Refrigeration mode}) \quad (2.5)$$

$$C^{AC,ice} \propto COP_{p,t}^{ac,ice} \psi^{ice} \quad (\text{Ice-making mode}) \quad (2.6)$$

and for WC chillers:

$$C^{WC} \propto COP_{p,t}^{wc} \quad (\text{Refrigeration mode}) \quad (2.7)$$

$$C^{WC,ice} \propto COP_{p,t}^{wc,ice} \psi^{ice} \quad (\text{Ice-making mode}) \quad (2.8)$$

### 2.2.2 Cooling load estimation

Qatar's electric demand varies with meteorological conditions and the time of day, influenced by daily social routines and building occupancy. There are several methods to estimate the aggregate electric demand from space cooling. The methods can be classified into bottom-up and top-down approaches [80]. In the bottom-up approach, simulation tools are used

to predict the cooling demand of building stock; they require knowledge of building construction, orientation, and use and are computationally demanding. Statistical analysis aggregates the estimated cooling demand for the entire building stock. In top-down approaches, statistical methods are used to isolate demand from space cooling from the total electric demand. A way to isolate the cooling load is by subtracting the total electric demand from the base load (days with no cooling needs). This method assumes that all intra-annual variations in electric demand from the reference base load are due to space cooling. Bayram et al. [21] employed this method to estimate Qatar's cooling load. Another top-down approach estimates the electric demand based on correlation with meteorological parameters, such as linear regression of demand with ambient temperature. This method was used by Saffouri et al. [20] to estimate Qatar's cooling load, which produced a similar estimate to the former approach used by Bayram.

A slightly more sophisticated method is considered in this work. The cooling load is estimated as the change in electric demand due to the change in ambient conditions at every hour of the day using least-squares regression. In Qatar, the time of the day and ambient conditions are found to be excellent predictors of electric demand. In contrast, wind speed was poorly correlated with electric demand, with a correlation coefficient of 4%. Furthermore, the day of the week had an insignificant effect on the estimated cooling load and was not considered. Three ambient conditions metrics were considered: dry-bulb temperature, wet-bulb temperature, and heat index. The heat index, which is the human perception of ambient conditions, was found to be a better indicator of demand, with a correlation coefficient of 96% compared to 93% with dry-bulb temperature and 83% with wet-bulb temperature. A plot of the metrics against the electric demand is in Figure 2.4.

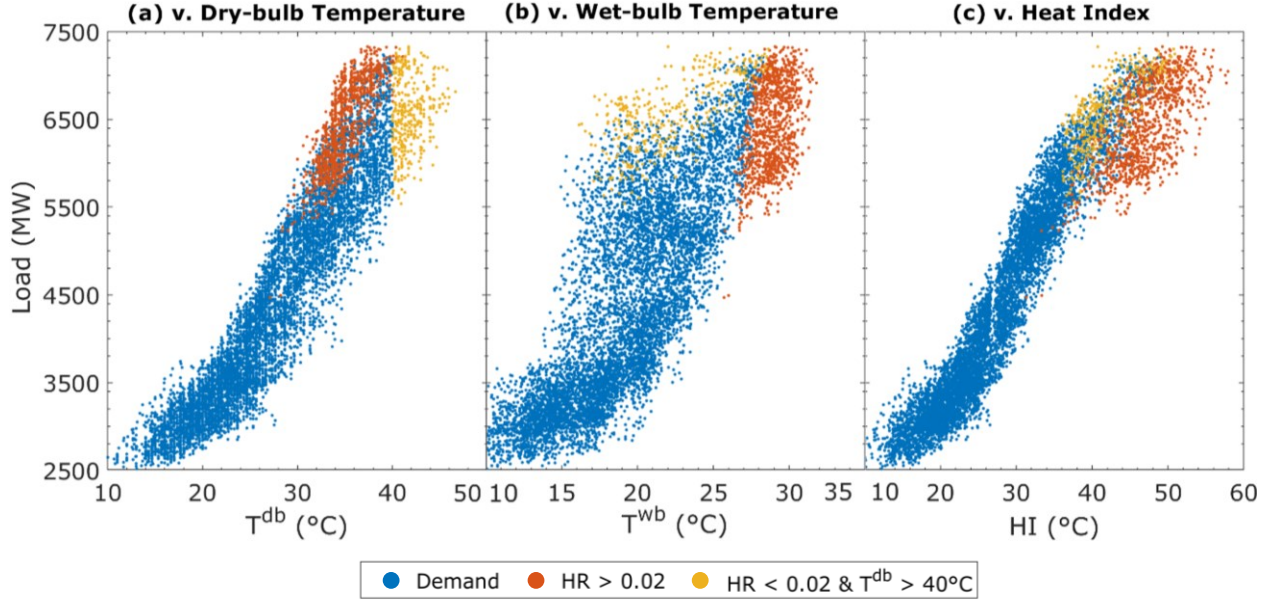


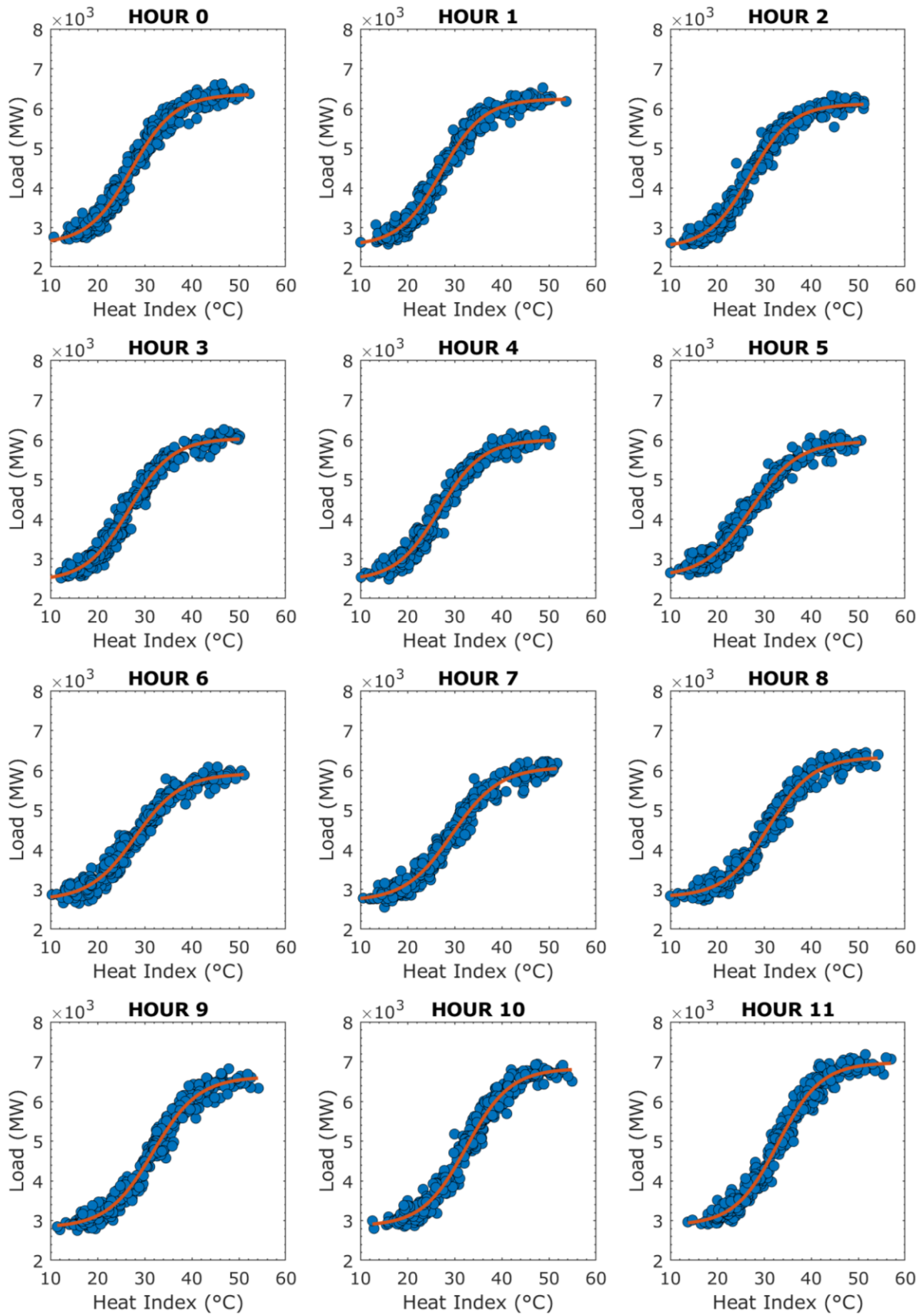
**Figure 2.4: Qatar's 2016 electric demand vs. (a) dry-bulb temperature, (b) wet-bulb temperature, and (c) heat index. Data points highlighted in red are warm and humid hours with a humidity ratio ( $HR_{p,t}$ )  $\geq 0.02$ , and in yellow are warm and dry hours with  $HR_{p,t} \leq 0.02$  and  $T_{p,t}^{db} \geq 40^\circ\text{C}$ .**

The use of dry-bulb temperature as a metric underpredicts the load on warm and humid days with a humidity ratio ( $HR_{p,t}$ ) greater than 0.02 in July-August, whereas the use of wet-bulb temperatures underpredicts the load on dry and warm days ( $HR_{p,t} < 0.02$  and  $T_{p,t}^{db} > 40^\circ\text{C}$ ) in June-July. On the other hand, using the heat index well-predicted the demand under both dry and humid conditions. This can be observed with higher electric demands associated with a higher heat index compared to lower dry and wet-bulb temperatures. The higher prediction power is attributed to the compounding effect of humidity level and dry-bulb temperature on the heat index, which drives cooling loads. A sigmoid function is fitted to the exhibited sigmoid relation between electricity demand and the heat index at each hour of the day, as illustrated in Figure 2.5. The aggregate electric cooling load from the sigmoid function fit is as follows:

$$D_{p,t}^C = \frac{P_{p,t} - B_{p,t}}{1 + e^{-k_{p,t}(HI - HI_{p,t}^0)}} \quad (2.9)$$

where  $k_{p,t}$  is the slope,  $B_{p,t}$  is the non-cooling load,  $P_{p,t}$  is the peak load, and  $HI_{p,t}^0$  is the heat index midpoint, all shown in Figure 2.6 at each hour.  $B_{p,t}$  peaks in the evening and troughs in the morning suggestive of correlation with buildings occupancy;  $P_{p,t}$  peaks midday and is driven by cooling needs;  $k_{p,t}$  is the slope (curve's steepness) and is time-insensitive;  $HI_{p,t}^0$  is influenced by the yearly temperature range at each hour of the day. The non-cooling portion of the electric demand is determined by deducting the estimated electric cooling load from the total electric demand,  $\mathcal{D}_{p,t}$ , as follows:

$$\mathcal{D}_{p,t}^{\mathcal{N}} = \mathcal{D}_{p,t} - \mathcal{D}_{p,t}^{\mathcal{C}} \quad (2.10)$$



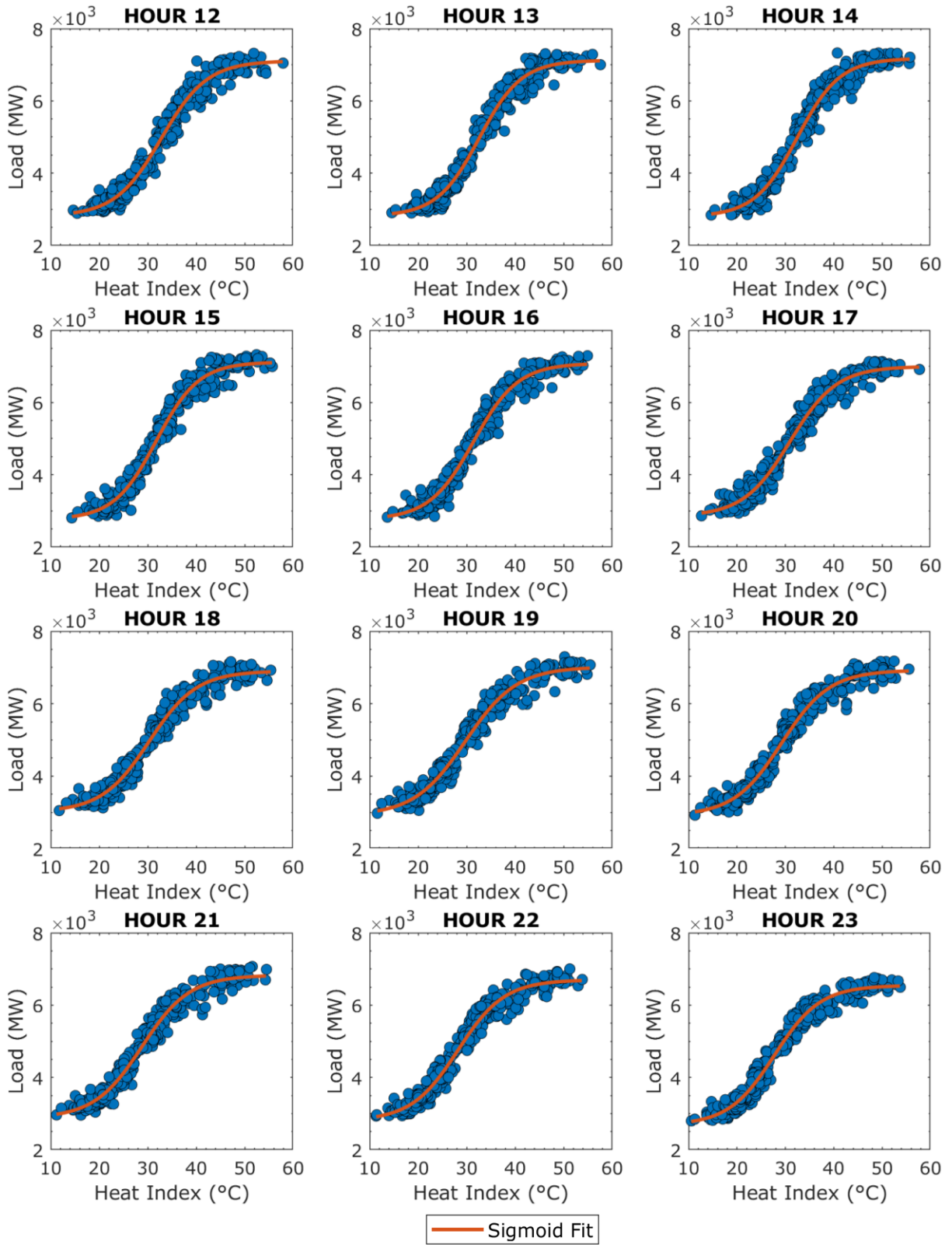


**Figure 2.5: Qatar 2016 electric demand v. heat index at every hour of the day starting from 00:00 (12 AM) to 23:00 (11 PM). A sigmoid function is fitted with 4 data points: peak and base demand, slope, and heat index mid-point.**



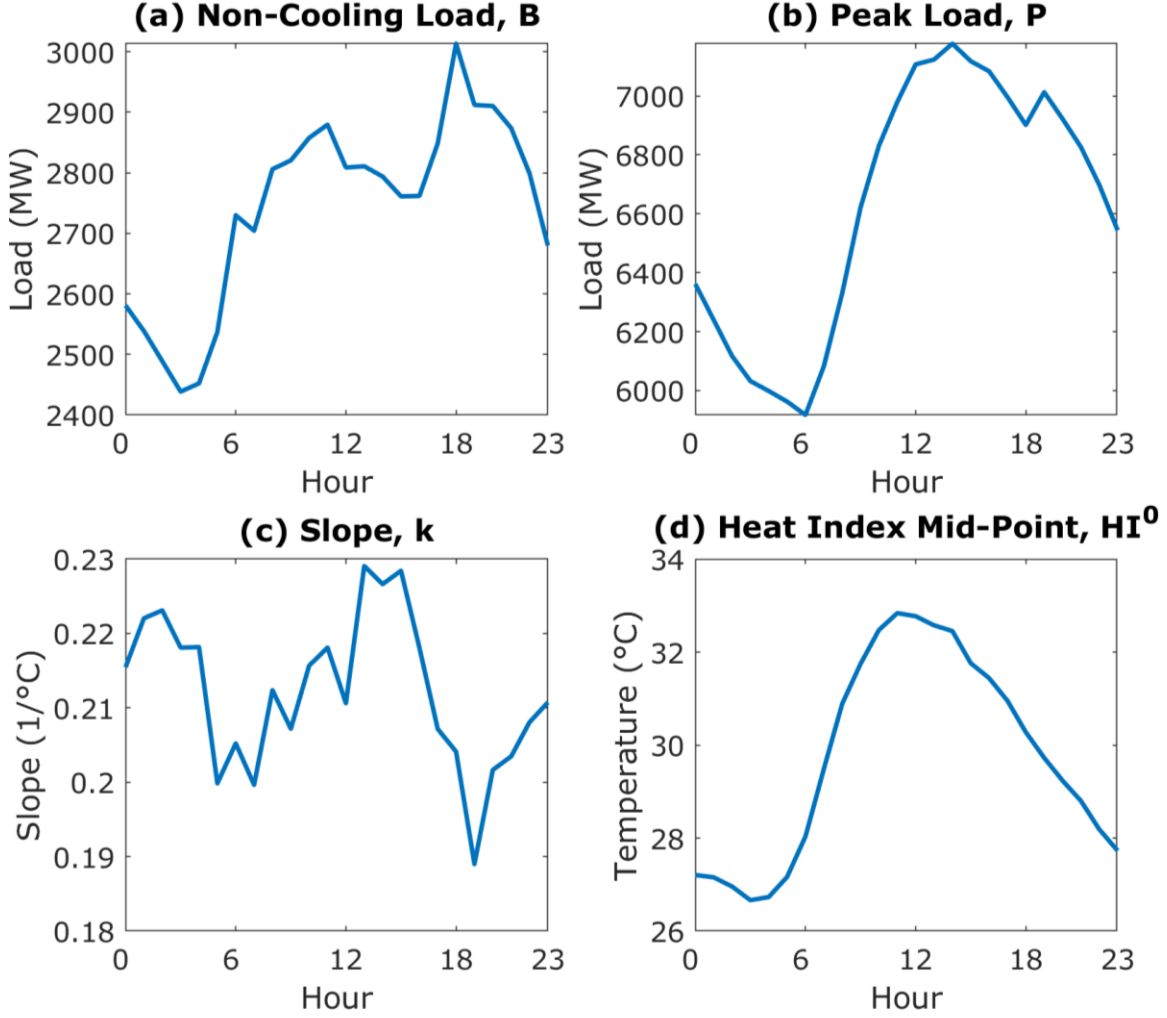


**Figure 2.6: The four fitted parameters: (a) base load  $B_{p,t}$ , (b) peak demand  $P_{p,t}$ , (c) slope  $k_{p,t}$ , and (d) heat index midpoint  $HI_{p,t}^0$  at the hour of the day for the 2016 scenario.**

Ambient condition-insensitive cooling demand in large buildings such as malls and airports cannot be distinguished from the non-cooling baseload using statistical methods and thus was not unaccounted for in the cooling load. This method estimates that space-cooling in Qatar was responsible for 42% of electric demand in 2016, slightly higher than Saffouri et al. [20] and Bayram et al. [21] estimate of approximately 35%. The difference is credited to a more accurate estimate of the cooling load in the low cooling periods. The estimated aggregate cooling load is divided proportionally to the installed cooling capacities of DXS, AC CWS, and WC CWS and

is converted to thermal cooling demand using the developed COP relation in Section 2.2.1 as follows:

$$\mathcal{C}_{p,t}^{DX} = \frac{\mathcal{D}_{p,t}^c}{\max_{p \in \mathcal{P}, t \in \mathcal{T}} [\mathcal{D}_{p,t}^c]} E^{DX} COP_{p,t}^{ac} \quad (2.11)$$

$$\mathcal{C}_{p,t}^{AC} = \frac{\mathcal{D}_{p,t}^c}{\max_{p \in \mathcal{P}, t \in \mathcal{T}} [\mathcal{D}_{p,t}^c]} E^{AC} COP_{p,t}^{ac} \quad (2.12)$$

$$\mathcal{C}_{p,t}^{WC} = \frac{\mathcal{D}_{p,t}^c}{\max_{p \in \mathcal{P}, t \in \mathcal{T}} [\mathcal{D}_{p,t}^c]} E^{WC} COP_{p,t}^{wc} \quad (2.13)$$

where  $E^{DX}$ ,  $E^{AC}$ , and  $E^{WC}$  are the maximum electric load of existing DXS, AC CWS, and WC CWS, respectively. As reported by the utility, the maximum electric loads from AC CWS and WC CWS were 2 and 1.1 GW in 2016, respectively [81]. DXS is responsible for the remaining cooling loads with an estimated maximum aggregate electric load of 1.3 GW. Because of data deficiency, it is reasonably assumed that the three cooling systems are similarly represented in different sectors. It should be noted that WC and AC cooling systems' electric loads are unlikely to be perfectly correlated, as the estimated aggregate cooling demand suggests, since their performance is affected by two different atmospheric parameters: the wet and dry-bulb temperatures. Nevertheless, the ambient dry-bulb and wet-bulb temperatures are generally well-correlated with correlation coefficients of 0.72, 0.81, and 0.85 for average hourly, daily, and weekly temperatures, respectively, which are unlikely to produce significant errors.

The electric demand,  $\mathcal{D}_{p,t}$ , estimated electric demand from non-cooling and cooling loads,  $B_{p,t} + \mathcal{D}_{p,t}^c$ , and the hourly estimated aggregate cooling load,  $\mathcal{D}_{p,t}^c$ , are shown in Figure 2.7 for three consecutive days in the winter, spring, and summer.

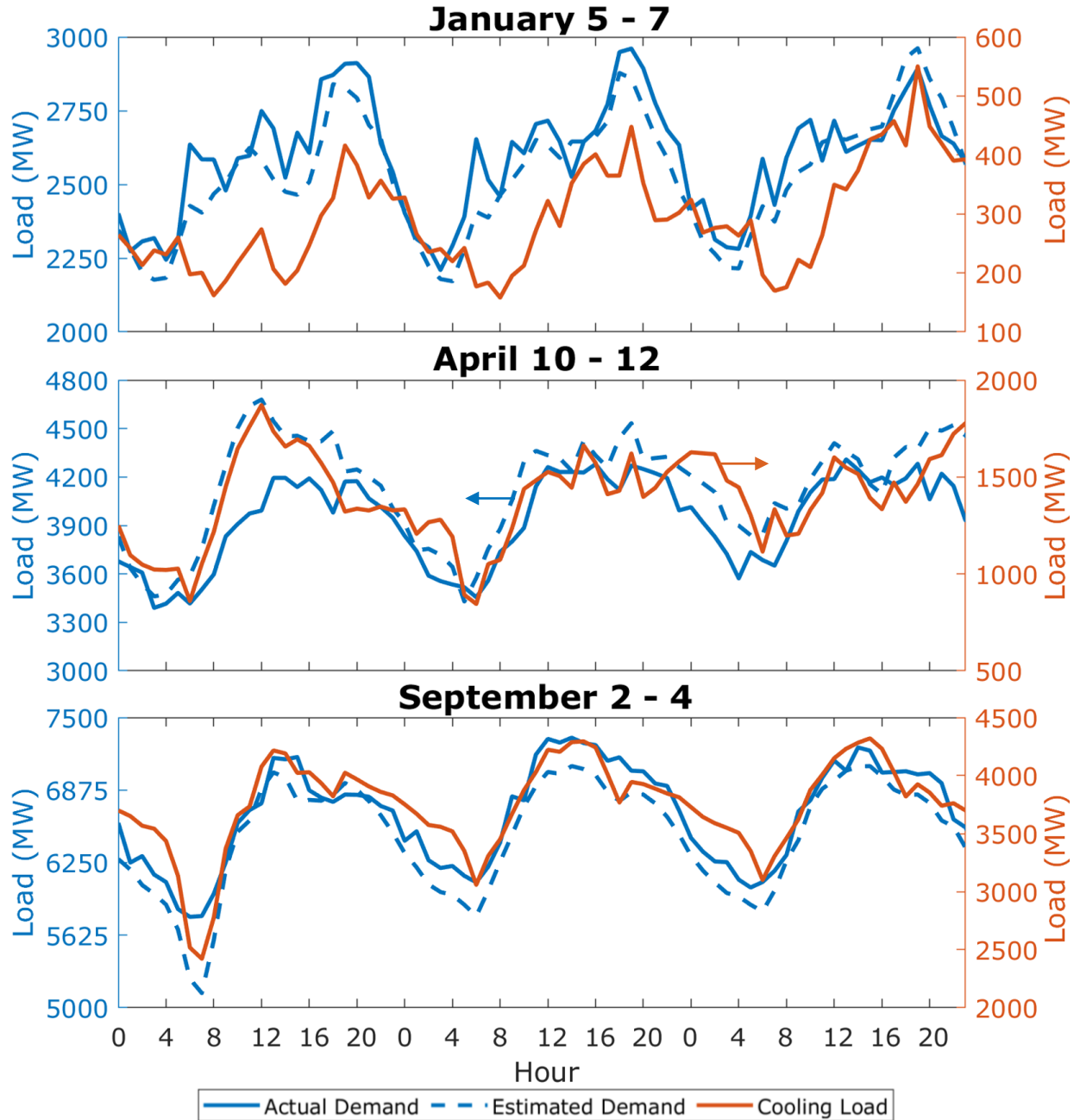


**Figure 2.7: Actual electric load  $\mathcal{D}_{p,t}$ , estimated electric load  $B_{p,t} + \mathcal{D}_{p,t}^c$  on the left y-axis and electric cooling load  $\mathcal{D}_{p,t}^c$  on the right y-axis from the logistic curve regression for the 2016 scenario. The estimated load generally agrees with the actual load, with an average percent difference of 3.5%.**

The estimated demand generally agrees with the actual electric demand with an average percent difference of 3.5%. In the warmer seasons, the cooling load peaks in the afternoon between 11 AM and 3 PM, and troughs in the early morning between 3 and 6 AM, as expected, are well-correlated with the electric demand and ambient heat index. During the peak cooling demand season, the contribution to electric load from space cooling can be as high as two-thirds of the electric demand. In the winter, counter to expected trends, there is a higher cooling load in the evening, mostly attributed to higher building occupancy and cooling footprint.

### 2.2.3 Problem formulation

The problem is modeled in a two-stage stochastic linear programming that minimizes the expected annual system cost across four scenarios of demand, ambient dry and wet-bulb temperatures, and solar insolation. The intention is to account for annual variations in the ambient conditions, which influence the electric demand due to space cooling and PV generation power output. The first stage decision variables are the capacities, and the second stage decision variable is the consumed gas. The objective function that is to be minimized is as follows:

$$\begin{aligned}
\min Cost = & \left( \sum_{s \in \mathcal{S}} c_s^{PV,C} C_s^{PV} + \sum_{i \in \mathcal{I}} [c^{ITES} C_i^{ITES} + c^{IceChl,C} C_i^{IceChl}] \right) \frac{ir(ir+1)^{yr}}{(1+ir)^{yr}-1} + \\
& c^{BESS} C^{BESS} \frac{ir(ir+1)^{yrb}}{(1+ir)^{yrb}-1} + \sum_{s \in \mathcal{S}} c_s^{PV,O} C_s^{PV} + \sum_{i \in \mathcal{I}} [c^{IceChl,O} C_i^{IceChl}] + \mathbb{E}_{p \in \mathcal{P}} [c^{GT} \sum_{t \in \mathcal{T}} GT_{p,t}] + \\
& c^{PGT} GT^P
\end{aligned} \tag{2.14}$$

The objective function contains the annualized Capex and associated annual OpEx from installed capacities of PV, I-TES, BESS, and additional ice chillers and the expected annual OpEx of existing gas generation from gas use. The subscript  $i$  is the cooling system technology index set  $\{1, 2, 3\}$  denoted by  $\mathcal{I}$  that corresponds to 1) DXS, 2) AC CWS, and 3) WC CWS,  $s$  is PV

orientation and tracking technology index set  $\{1, 2, 3\}$  denoted by  $\mathcal{S}$  that corresponds to 1) optimal fixed-tilt angle at Qatar latitude of  $25^\circ$  [82], 2) single-axis tracking, and 3) dual-axis tracking PV systems.  $C_s^{PV}$ ,  $C_i^{ITES}$ ,  $C_i^{IceChl}$ , and  $C^{BESS}$  are installed capacities of PV, I-TES, ice chillers, and BESS, respectively.  $c_s^{PV,C}$  and  $c_s^{PV,O}$  are installed PV Capex and OpEx.  $c^{IceChl,C}$  and  $c^{IceChl,O}$  are installed ice chillers Capex and OpEx.  $c^{ITES}$  and  $c^{BESS}$  are the installed I-TES and BESS Capex, respectively.  $ir$  is the interest rate,  $yr$  is the service life for PV, I-TES, and ice chillers, and  $yrb$  is the BESS service life.  $c^{GT}$  is the yearly average cost of produced energy using gas-fired generation,  $GT_{t,p}$  is power delivered from gas generation, and  $GT^P$  is peak gas generation demand.  $c^{PGT}$  is a small cost of  $\$5/\text{MW}_p$  that is assigned to the peak gas generation demand to find a unique solution that minimizes peak gas generation demand without impacting the cost-optimal system. The term  $\mathbb{E}_{p \in \mathcal{P}}[c^{GT} \sum_{t \in \mathcal{T}} GT_{p,t}]$  is the expected annual cost from gas use across 4 scenarios (2012-2016), each with an assumed equal likelihood of occurrence (25%).

The first constraint balances the supply and demand of power in the grid as follows:

$$GT_{p,t} + \mathcal{B}_{p,t}^{dis} - \mathcal{B}_{p,t}^{chs} + \eta^I \sum_{s \in \mathcal{S}} I_{p,t,s} C_s^{PV} - PV_{p,t}^{curt} = \mathcal{D}_{p,t}^{\mathcal{N}} + \mathcal{D}_{p,t}^{DX} + \mathcal{D}_{p,t}^{AC} + \mathcal{D}_{p,t}^{WC}, \forall p \in \mathcal{P}, \forall t \in \mathcal{T} \quad (2.15)$$

The right-hand side of the equation is the electric demand, which comprises the non-cooling,  $\mathcal{D}_{p,t}^{\mathcal{N}}$ , and the aggregate electric cooling loads:  $\mathcal{D}_{p,t}^{DX}$  from the DXS,  $\mathcal{D}_{p,t}^{AC}$  from AC CWS, and  $\mathcal{D}_{p,t}^{WC}$  from WC CWS.  $\mathcal{B}_{p,t}^{chs}$  and  $\mathcal{B}_{p,t}^{dis}$  are BESS charge and discharge rates, respectively.  $I_{p,t,j}$  is solar insolation normalized by peak sun hour, and  $\eta^I$  is the inverter efficiency. The terms  $\eta^I \sum_{s \in \mathcal{S}} I_{p,t,s} C_s^{PV}$  and  $PV_{p,t}^{curt}$  are the supplied and curtailed power from PV generation, respectively. Only excess PV generation can be used for energy storage charging in a cost-optimal system. Other uses are sub-optimal due to the performance loss associated with the

charging and dispatch processes. Gas-fired generations were modeled as a single equivalent power generation plant, and minimum part load and up/down-times for the individual generation were not considered. Since gas-fired generations can ramp up to capacity in less than an hour and the analysis was done hourly, ramping constraints were disregarded. Peak gas generation demand in all scenarios is captured in the following constraint and penalized by the objective function:

$$GT^P - GT_{p,t} \geq 0, \quad \forall p \in \mathcal{P}, \quad \forall t \in \mathcal{T} \quad (2.16)$$

### 2.2.3.1 I-TES model

While the behavior of individual I-TES tanks is a non-linear function of the SoC, inlet temperature, and flowrate, the aggregate behavior of thousands of I-TES tanks is approximated by a simple linear function of chiller loading. As seen by the electricity grid, the electric cooling load is altered because of load shifting from using I-TES. The electric load increases when forming ice and decreases when I-TES is dispatched. The dispatch of I-TES reduces the load on cooling systems proportional to the dispatched amounts and systems COP. The cooling load balance for each system is described by:

$$\mathcal{D}_{p,t}^{DX} = \left( \frac{1}{COP_{p,t}^{ac}} \right) [\mathcal{C}_{p,t}^{DX} - S_{p,t,i}^{dis}] + \left( \frac{S_{p,t,i}^{ac,chs}}{COP_{p,t}^{ac,ice}} \right), \quad \forall p \in \mathcal{P}, \quad \forall t \in \mathcal{T}, \quad i = 1 \quad (2.17)$$

$$\mathcal{D}_{p,t}^{AC} = \left( \frac{1}{COP_{p,t}^{ac}} \right) [\mathcal{C}_{p,t}^{AC} - S_{p,t,i}^{dis}] + \left( \frac{S_{p,t,i}^{ac,chs}}{COP_{p,t}^{ac,ice}} \right), \quad \forall p \in \mathcal{P}, \quad \forall t \in \mathcal{T}, \quad i = 2 \quad (2.18)$$

$$\mathcal{D}_{p,t}^{WC} = \left( \frac{1}{COP_{p,t}^{wc}} \right) [\mathcal{C}_{p,t}^{WC} - S_{p,t,i}^{dis}] + \left( \frac{S_{p,t,i}^{ac,chs}}{COP_{p,t}^{ac,ice}} \right) + \left( \frac{S_{p,t,i}^{wc,chs}}{COP_{p,t}^{wc,ice}} \right), \quad \forall p \in \mathcal{P}, \quad \forall t \in \mathcal{T}, \quad i = 3 \quad (2.19)$$

where  $C_{p,t}^{DX}$ ,  $C_{p,t}^{AC}$ , and  $C_{p,t}^{WC}$  is the aggregate thermal cooling demand for the DXS, AC CWS, and WC CWS, as estimated in Section 2.2.2. The COP of AC and WC systems is  $COP_{p,t}^{ac}$  and  $COP_{p,t}^{wc}$  in refrigeration mode, and  $COP_{p,t}^{ac,ice}$  and  $COP_{p,t}^{wc,ice}$  in ice-making mode, respectively, as estimated in Section 2.2.1.  $S_{p,t,i}^{ac,chs}$  and  $S_{p,t,i}^{wc,chs}$  are I-TES charging rates using AC and WC chillers, respectively, and  $S_{p,t,i}^{dis}$  is the ice melt rate of I-TES. The stored thermal energy in the ice is balanced via the following two constraints:

$$S_{p,t,i}^s - \eta^{ITES,sdis} S_{p,t-1,i}^s = S_{p,t,i}^{ac,chs} + S_{p,t,i}^{wc,chs} - S_{p,t,i}^{dis}, \quad \forall p \in \mathcal{P}, \quad \forall t \in \mathcal{T}, \quad \forall i \in \mathcal{I} \quad (2.20)$$

$$S_{p,t,i}^s \leq C_i^{ITES}, \quad \forall p \in \mathcal{P}, \quad \forall t \in \mathcal{T}, \quad \forall i \in \mathcal{I} \quad (2.21)$$

where  $S_{p,t,i}^s$  is the amount of thermal energy stored in ice and  $\eta^{ITES,sdis}$  is the self-discharge efficiency from thermal losses. The amount of dispatchable stored thermal energy is restricted to the available thermal cooling demands:

$$S_{p,t,i}^{dis} \leq C_{p,t}^{DX}, \quad \forall p \in \mathcal{P}, \quad \forall t \in \mathcal{T}, \quad i = 1 \quad (2.22)$$

$$S_{p,t,i}^{dis} \leq C_{p,t}^{AC}, \quad \forall p \in \mathcal{P}, \quad \forall t \in \mathcal{T}, \quad i = 2 \quad (2.23)$$

$$S_{p,t,i}^{dis} \leq C_{p,t}^{WC}, \quad \forall p \in \mathcal{P}, \quad \forall t \in \mathcal{T}, \quad i = 3 \quad (2.24)$$

and due to physical limitations associated with the maximum melt rate:

$$S_{p,t,i}^{dis} \leq f^{ITES,dis} C_i^{ITES}, \quad \forall p \in \mathcal{P}, \quad \forall t \in \mathcal{T}, \quad \forall i \in \mathcal{I} \quad (2.25)$$

where  $f^{ITES,dis}$  is the maximum discharge rate per unit capacity in  $\text{h}^{-1}$ . Similarly, I-TES charge rate is bounded by physical limitations associated with the maximum ice build rate as follows:

$$S_{p,t,i}^{wc,chs} + S_{p,t,i}^{ac,chs} \leq f^{ITES,chs} C_i^{ITES}, \forall p \in \mathcal{P}, \forall t \in \mathcal{T}, \forall i \in \mathcal{I} \quad (2.26)$$

and to available chillers cooling capacities in the respective cooling system:

$$S_{p,t,i}^{ac,chs} \leq C_i^{IceChl} \frac{COP_{p,t}^{ac,ice}}{COP_{p,t}^{ac,des}} \psi^{ice}, \forall p \in \mathcal{P}, \forall t \in \mathcal{T}, \forall i \in \{1, 3\} \quad (2.27)$$

$$S_{p,t,i}^{ac,chs} \leq [C^{AC} - C_{p,t}^{AC}] \frac{COP_{p,t}^{ac,ice}}{COP_{p,t}^{ac}} \psi^{ice} + C_i^{IceChl} \frac{COP_{p,t}^{ac,ice}}{COP_{p,t}^{ac,des}} \psi^{ice}, \forall p \in \mathcal{P}, \forall t \in \mathcal{T}, i = 2 \quad (2.28)$$

$$S_{p,t,i}^{wc,chs} \leq [C^{WC} - C_{p,t}^{WC}] \frac{COP_{p,t}^{wc,ice}}{COP_{p,t}^{wc}} \psi^{ice} \psi^{ice}, \forall p \in \mathcal{P}, \forall t \in \mathcal{T}, i = 3 \quad (2.29)$$

where  $f^{ITES,chs}$  is the maximum charge rate per unity capacity in  $\text{h}^{-1}$ ,  $COP_{p,t}^{ac,des}$  and  $COP_{p,t}^{wc,des}$  are design COP of AC and WC systems, and  $\psi^{ice}$  is the depressed chiller capacity factor, which accounts for the loss in chiller cooling capacities from the reduced refrigerant saturation density in ice-making mode. The DXS charge rate is limited by the additionally installed ice chiller capacity. For AC and WC CWS, the charge rate is limited by the combined cooling capacity of idle and additional ice chillers. The first term in Equations (2.28) and (2.29) is the aggregate cooling capacities of the existing AC and WC chiller, respectively, which are given by:

$$C^{AC} = C^{AC,des} COP_{p,t}^{ac} / COP_{p,t}^{ac,des} \quad (2.30)$$



$$C^{WC} = C^{WC,des} COP_{p,t}^{wc} / COP_{p,t}^{wc,des} \quad (2.31)$$

where  $C^{AC,des}$  and  $C^{WC,des}$  are the nominal aggregate existing capacities of AC and WC chillers. The two terms in Equations (2.28) and (2.29) thus determine the idle chillers' capacity that could be utilized to make ice.

### 2.2.3.2 BESS model

Modeling of BESS is less complex than I-TES due to both storing electric energy and the nature of their performance. No consideration is made for the depth of discharge as  $C^{BESS}$  is taken to represent the usable capacity. Charge and discharge rates are limited to a 4-hour electric battery (power-to-energy capacity ratio of  $\frac{1}{4}$ ), a standard market product. The following constraints balance the stored energy and restrict charge and discharge rates:

$$\mathcal{B}_{p,t}^s - \eta^{BESS,sdis} \mathcal{B}_{p,t-1}^s = \eta^{BESS,chs} \mathcal{B}_{p,t}^{chs} - \frac{1}{\eta^{BESS,dis}} \mathcal{B}_{p,t}^{dis}, \quad \forall p \in \mathcal{P}, \quad \forall t \in \mathcal{T} \quad (2.32)$$

$$\mathcal{B}_{p,t}^s \leq C^{BESS}, \quad \forall p \in \mathcal{P}, \quad \forall t \in \mathcal{T} \quad (2.33)$$

$$\mathcal{B}_{p,t}^{dis} + \mathcal{B}_{p,t}^{chs} \leq \left(\frac{1}{4}\right) \times C^{BESS}, \quad \forall p \in \mathcal{P}, \quad \forall t \in \mathcal{T} \quad (2.34)$$

where  $\mathcal{B}_{p,t}^s$  is the stored electric energy and  $\eta^{BESS,sdis}$ ,  $\eta^{BESS,chs}$ , and  $\eta^{BESS,dis}$  are the self-discharge, charge, and discharge efficiencies, respectively. To eliminate solutions with simultaneous BESS charging and discharging without the use of a more complex and computationally intensive mixed integer linear programming, a negligibly small cost in the order

of  $10^{-3}$  \$/MW is applied to  $\mathcal{B}_{p,t}^{chs}$  in the objective function, which does not impact the cost-optimal system.

### 2.2.3.3 Model parameters

The considered characteristics parameters in the model are tabulated in Table 2.1. An efficient inverter with 98% efficiency was assumed for the PV system [83]. A 4-hour BESS was considered with charging and discharging efficiencies of 92% and a self-discharge efficiency of 99.9% [84], [85]. The charge and discharge efficiencies also account for inverter losses. The modeled I-TES is an internal melt type with a maximum charge rate of  $1/6 \text{ h}^{-1}$  and discharge rate of  $1/3 \text{ h}^{-1}$  from performance data taken from CALMAC, a prominent internal melt I-TES manufacturer. Measurements taken from I-TES demonstrate a high self-discharge efficiency of 99.9% [86].

Peak electric loads from existing AC CWS and WC CWS of 2 and 1.1 GW are utility estimates [81] used to predict the corresponding existing cooling systems' capacities. The design cooling capacities are conservatively assumed to be oversized by 20% above the utility's peak load estimate; this corresponds to AC CWS and WC CWS's maximum electric load of 2.5 and 1.4 GW, respectively. DXS are responsible for the remaining cooling loads with an estimated maximum aggregate load of 1.3 GW. At design WC and AC systems COP of 4.2 and 2.4, respectively, the estimated aggregate nominal cooling capacities are  $3.1 \text{ GW}_{\text{th}}$  for DXS,  $6.1 \text{ GW}_{\text{th}}$  for AC CWS, and  $5.7 \text{ GW}_{\text{th}}$  for WC CWS. The subscript "th" is used to differentiate thermal and electric capacities. I-TES and BESS are assumed to be initially fully charged at the first hour of each scenario (January 1<sup>st</sup> at midnight) in order not to impede the minimization of peak gas generation demand.

**Table 2.1: Characteristics parameters in the model**

Item	Parameter	Symbol	Value
PV	Inverter efficiency	$\eta^I$	98%
	Initially charge	$\mathcal{B}_{p,t=0}^S$	100%
BESS	Charge efficiency	$\eta^{BESS,chs}$	92%
	Discharge efficiency	$\eta^{BESS,dis}$	92%
	Self-discharge efficiency	$\eta^{BESS,sdis}$	99.9%
	Charge capacity	$f^{ITES,chs}$	1/6 hr <sup>-1</sup>
I-TES	Discharge capacity	$f^{ITES,dis}$	1/3 hr <sup>-1</sup>
	Initially charge	$S_{p,t=0,i}^S$	100%
	Self-discharge efficiency	$\eta^{ITES,sdis}$	99.9%
	Existing DXS cooling capacity	$C^{DX,des}$	3100 MW <sub>th</sub>
Chiller	Existing AC CWS cooling capacity	$C^{AC,des}$	6100 MW <sub>th</sub>
	Existing WC CWS cooling capacity	$C^{WC,des}$	5700 MW <sub>th</sub>
	Depressed chiller capacity factor	$\psi^{ice}$	0.75
	Design WC systems COP	$COP^{wc,des}$	4.2
	Designed AC systems COP	$COP^{ac,des}$	2.4

The assumed financial parameters in the model are tabulated in Table 2.2. All capital costs are installed costs and are taken on the lower side [45], [77], [85], [87]–[91], benefiting from the economy of scale. OpEx was valued per unit capacity per year and not based on consumption [92]–[94]. Based on utility-scale prices in Qatar [45], installed PV is at \$450/kW<sub>p,dc</sub> for fixed-tilt, \$550/kW<sub>p,dc</sub> for single-axis tracking, and \$700/kW<sub>p,dc</sub> for dual-axis tracking. OpEx for installed PV was at \$10/kW<sub>p,dc</sub>/yr. for fixed-tilt, \$15/kW<sub>p,dc</sub>/yr. for single-axis tracking, and \$20/kW<sub>p,dc</sub>/yr. for dual-axis tracking. The cost of I-TES was taken to be \$50/TR-hr (\$14/kWh<sub>th</sub>) [87] and ice chillers at \$200/TR (\$57/kW<sub>th</sub>) [88], [89]. 4-hour BESS was taken at \$250/kWh, of which is \$200/kW for power and \$200/kWh for energy components [85], [91]. The yearly average gas generation cost of \$37/MWh covers all OpEx. Benefiting from access to cheap

capital in the region, finances are done at a 3.5% interest rate. A service life of 25 years was assumed for I-TES, ice chillers, and PV and 10 years for the BESS [90], [95], [96].

**Table 2.2: Financial parameters in the model**

Item	Unit	Expense	Symbol	Value
PV	Fixed-tilt	Capex	$c_1^{PV,C}$	\$450/kWp,dc
		OpEx	$c_1^{PV,O}$	\$10/kWp,dc/yr.
	Single-axis tracking	Capex	$c_2^{PV,C}$	\$550/kWp,dc
		OpEx	$c_2^{PV,O}$	\$15/kWp,dc/yr.
	Dual-axis tracking	Capex	$c_3^{PV,C}$	\$700/kWp,dc
		OpEx	$c_3^{PV,O}$	\$20/kWp,dc/yr.
I-TES	Internal melt	Capex	$c^{ITES}$	\$14/kWhth (\$50/TR-hr)
BESS	4-Hour Li-ion	Capex	$c^{BESS}$	\$250/kWh
Chiller	Ice chillers for charging	Capex	$c^{IceChl,C}$	\$57/kWhth (\$200/TR)
		OpEx	$c^{IceChl,O}$	\$3/kWhth/yr. (\$20/TR)
Misc.	Gas generation cost	OpEx	$c^{GT}$	\$37/MWh
	Gas price	OpEx	-	\$3.33/MMBtu
	Capital	Interest rate	$ir$	3.5%
		Service life	$yr$	25 years
		BESS service life	$yrb$	10 years
	Peak gas generation cost	OpEx	$c^{PGT}$	\$5/MWp

## 2.3 Results and discussion

First, the formulated problem is solved at the current cost structure to determine the penetration of PV, I-TES, and BESS. Second, the impact of the carbon pricing policy on the decarbonization pathway is examined. Third, a deeply decarbonized system supported by carbon pricing is analyzed in detail. Last, the impact of the continual decline in the cost of BESS on the cost-optimal system is investigated. For all considered cases, dual-axis tracking PV was not economically feasible and was omitted from the results.

### 2.3.1 Current cost structure

The formulated problem is solved at the current cost structure tabulated in Table 2.2. The results suggest that BESS is not cost-effective under current conditions. The cost-optimal system, as tabulated in Table 2.3, comprises 8.1 GW<sub>p,dc</sub> of PV capacity (5.9 GW<sub>p,dc</sub> for fixed-tilt and 2.2 GW<sub>p,dc</sub> for single-axis tracking), 28 GWh<sub>th</sub> of aggregate I-TES capacity (3 GWh<sub>th</sub> for DXS, 15 GWh<sub>th</sub> for AC CWS, and 10 GWh<sub>th</sub> for WC CWS), and 0.7 GW<sub>th</sub> of aggregate ice chillers capacity for the DXS. For AC CWS and WC CWS, I-TES is charged using the existing idle chillers' capacity. Benefiting from optimized load shifting using I-TES during the summer months, peak gas generation demand is reduced by 18% (7.33 to 6.0 GW).

The cost-optimal system stipulates investing \$326 million/yr. in PV capacity, \$25 million/yr. in I-TES capacity, and \$4 million/yr. in additional ice chillers capacity. This investment brings about a 20% reduction in both the average cost of produced energy (\$37/MWh to \$29/MWh) and total annual system expenditures (\$1.5 billion/yr. to \$1.2 billion/yr.) relative to the current approach of all gas-fired generations by utilizing low-cost energy produced by PV generation.

**Table 2.3: Cost-optimal system capacities under the current cost structure**

Parameter	Value	Notes
Solar PV capacity	8.1 GW <sub>p,dc</sub>	5.9 GW <sub>p,dc</sub> fixed-tilt 2.2 GW <sub>p,dc</sub> single-axis tracking
I-TES thermal capacity	28 GWh <sub>th</sub>	3 GWh <sub>th</sub> DXS 15 GWh <sub>th</sub> AC CWS 10 GWh <sub>th</sub> WC CWS
Additional ice chiller capacity	0.7 GW <sub>th</sub>	DXS
Peak gas generation demand	6.0 GW	Across all scenarios

A PV capacity of 8.1 GW<sub>p,dc</sub> is slightly higher than the current peak electricity demand of 7.33 GW, producing low-cost electricity to displace gas generation during the day and year-round excess generation for I-TES use. About half of the excess generation is used to store ice, and the remaining half is curtailed. The mismatch between PV generation, which peaks in June, and the cooling load, which peaks in August, is the primary reason for curtailment. The cost-optimal system's preference for fixed-tilt PV generation is due to its lower costs and the lack of energy storage capacity to utilize the higher surplus generation generated with solar tracking technology.

The cost-optimal system characteristics averaged over the four scenarios (2013-2016) are tabulated in Table 2.4. 38% of the electric demand was directly met by PV generation, and 5% in-directly from load shifting using I-TES. Since power generations in Qatar exclusively use gas generation with collective CO<sub>2</sub> emissions of 24 Mt/yr., the electric demand met by PV and load shifted by I-TES is directly proportional to gas consumption and CO<sub>2</sub> emissions reduction. Gas generation use and CO<sub>2</sub> emissions are reduced by 43%, of which PV alone contributes almost 90% of these emissions reductions.

**Table 2.4: Cost-optimal system characteristics under the current cost structure**

Parameter	Value	Notes
Cost	\$1239 million/yr.	Annual cost from Capex and OpEx
Average power generation cost	\$29/MWh	From gas and PV generation
Demand met by gas generation	57%	-
Demand met by PV generation	38%	Directly
Electric load shifted by I-TES	5%	All cooling systems
Cooling demand met by PV generation	41%	Directly
Cooling demand met by I-TES	13%	All cooling systems
Solar capacity factor	25%	After curtailment
Curtailment	10%	Of total PV generation
I-TES average charge residency	17 hrs	Based on first-in, first-out
I-TES average capacity utilization	70%	Equivalent full cycles per day

Figure 2.8 shows the weekly average percent contribution of the I-TES, PV, and gas generation in meeting the electric demand in (a) and the electric cooling load in (b). Note that the load met by I-TES corresponds to the electric load shifted. The highest utilization of I-TES is in the low cooling demand season is enabled by a higher amount of surplus PV generation and idle chillers capacity. It reduces the nighttime cooling load by 40-60%, which equates to about load shifting 10% of the nighttime electric demand. Higher electricity and cooling demand in the warmer season produces less surplus PV generation coupled with a lack of idle chillers capacity constrained and diminished I-TES use. Nonetheless, sole PV generation consistently and reliably met 40% of the cooling load and electric demand. This system decarbonizes 54% of the electric cooling load, of which PV directly contributes 41%, and I-TES contributes 13% from load shifting.

## Current Cost Structure

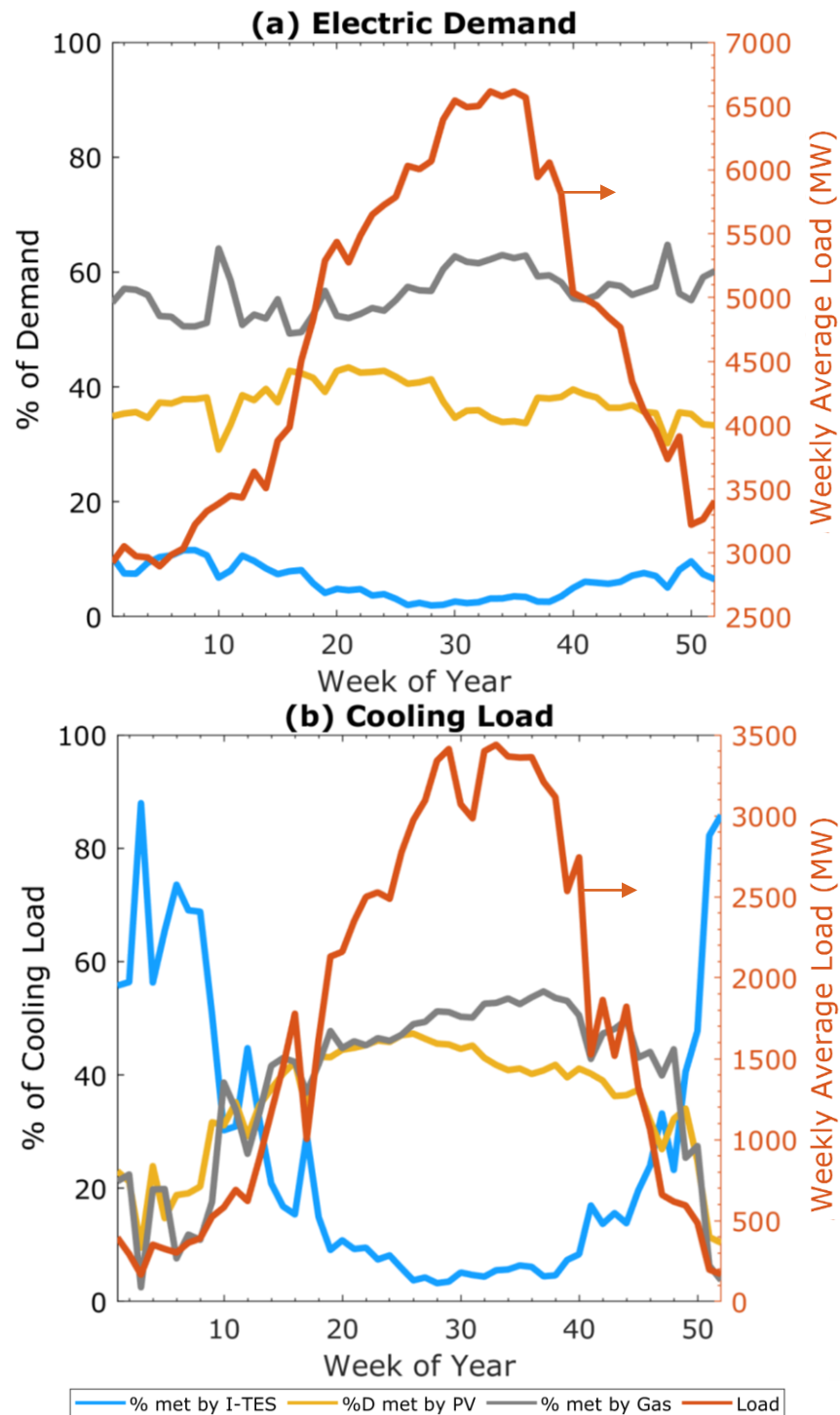


**Figure 2.8: 2016 scenario cost-optimal system under current cost structure with a breakdown of contribution to supplying (a) electric demand and (b) electric cooling load with percent load shifted by I-TES (% met by I-TES), directly met by PV (%D met by PV), and met by gas (% met by Gas) on the left y-axis and the average weekly load on the right y-axis.**



The load profile for three consecutive days in the winter, spring, and summer are shown in Figure 2.9 for the 2016 scenario, with DD (demand directly) met from PV and D (demand) met by I-TES. In the winter, I-TES is continuously dispatched, restricted by the absence of cooling demand. When the cooling demand has increased in the spring, I-TES is dispatched to displace cooling systems operating at reduced efficiency due to relatively higher dry-bulb temperatures in the AC systems or wet-bulb temperatures in WC CWS. This can be seen from the correlation between the I-TES dispatch amount and higher ambient temperatures. In the summer, I-TES use was limited due to multiple adverse factors: (i) limited idle chillers' capacity for charging due to higher cooling demand, (ii) chillers' cooling capacities degradation from higher ambient temperatures, and (iii) limited amount and duration of surplus PV generation. Still, a smaller amount of stored ice is dispatched in the early evening hours to reduce the peak gas-fired generation demand.

Gas generation, which has to cover intermittent PV generation and lack of storage, sees a high ramp rate of 3.5-5 GW/hr (50-70% of the current peak electricity demand) for less than 100 hours of the year caused by the early evening peak in the summer. The ramp rates do not exceed 2.5 GW/hr for the remaining time. On average, 70% of I-TES capacity is utilized daily, with an average charge residency of 17 hours, counterintuitively depressed by lower utilization in the high cooling demand season. Storage is charged in 2500 hours, restricted by the narrow charging window, equivalent to the number of hours PV produces surplus power. I-TES is dispatched over 4450 hours to reduce gas generation use and peak demand.

## Current Cost Structure

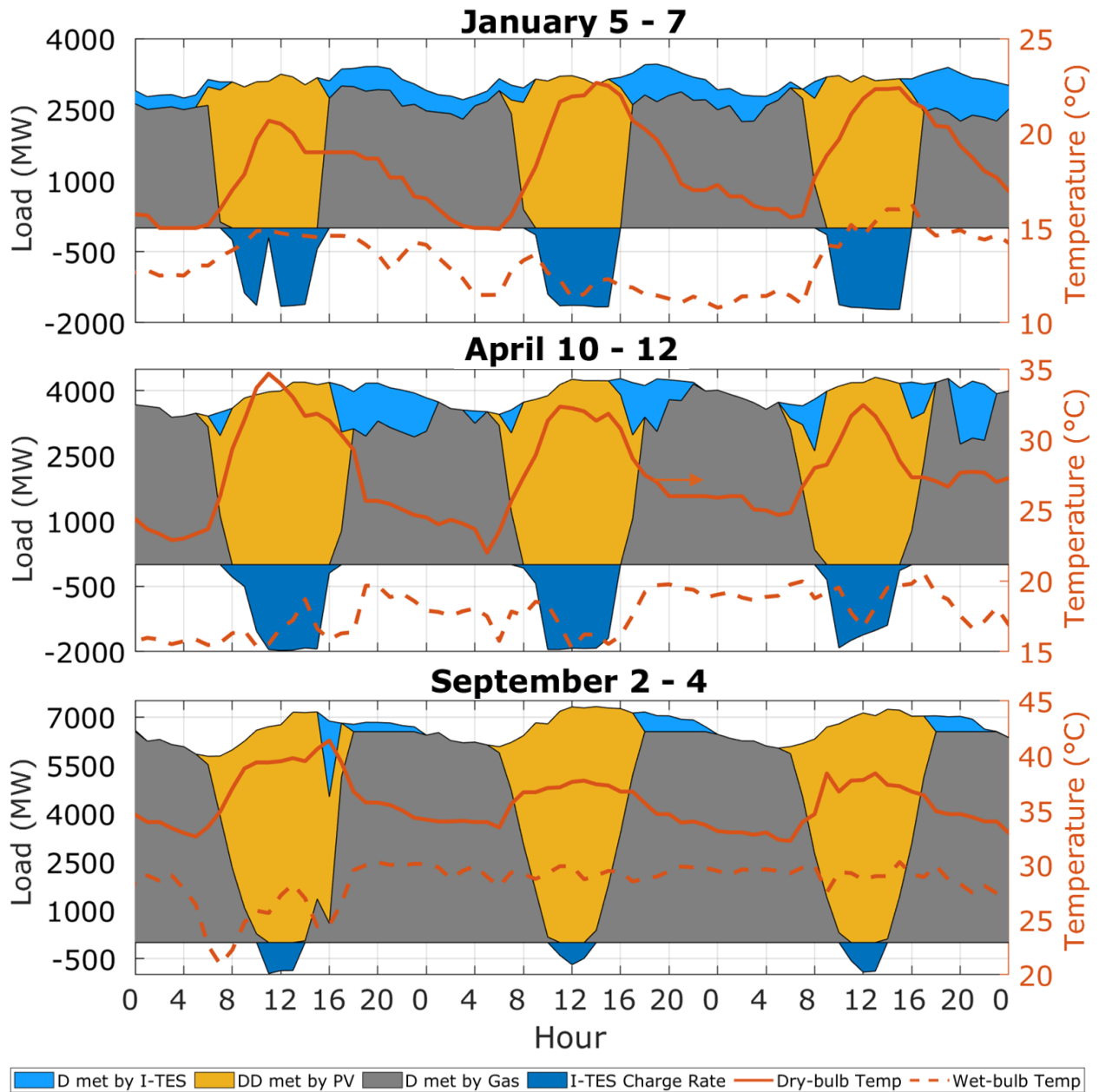


**Figure 2.9: Cost-optimal system hourly load profile with D (demand) met by I-TES, DD (demand directly) met from PV, D (demand) met by gas, and on the left y-axis and the ambient temperatures on the right y-axis for three days in winter, spring, and summer. I-TES charge rate is shown in negative.**

### 2.3.2 Effects of carbon pricing

Plentiful and easily accessible natural gas provided low-cost fuel to gas generation in Qatar, instigating a cost structure that lacks the appropriate economic incentives to reduce carbon emissions. This section assesses carbon pricing policy to promote energy and environmental sustainability. The cost-optimal system with a carbon pricing from 0 to \$200/ton of CO<sub>2</sub> is shown in Figure 2.10 with capacities of power generators in (a), BESS in (b), I-TES in (c), (e), and (g), and ice chillers in (d), (f), and (h) for DXS, AC CWS, and WC CWS, respectively. Figure 2.11 (a)-(d) shows the corresponding cost-optimal system characteristics.

The cost-optimal system with carbon pricing below \$20/ton of CO<sub>2</sub> is dominated by PV generation and limited I-TES. That is because I-TES cannot outcompete already existing gas generation for highly seasonal cooling needs. This system nearly displaces all daytime gas generation directly using lower-cost PV generation and exploits surplus generation to reduce the nighttime cooling load in the shoulder seasons using I-TES for load shifting. While fixed-tilt PV generation is initially preferred, fixed-tilt is swapped for single-axis tracking with a net positive gain as the carbon price increases, accompanied by an increase in additional ice chillers and I-TES capacity. PV generation with I-TES for electric and cooling loads decarbonization reaches a plateau at carbon pricing of \$100/ton of CO<sub>2</sub>. For this system, about 88% of cooling needs are met using PV generation during the daytime and I-TES during the nighttime. The remaining 12% is in days with reduced solar output and during the high cooling load season between July and September. Optimized I-TES dispatch could reduce peak demand from gas generation by 35% (7.33 to 4.8 GW); further decrease is limited by the non-cooling portion of the electric demand and challenges of using I-TES in the high cooling load season.

### Battery at \$250/kWh

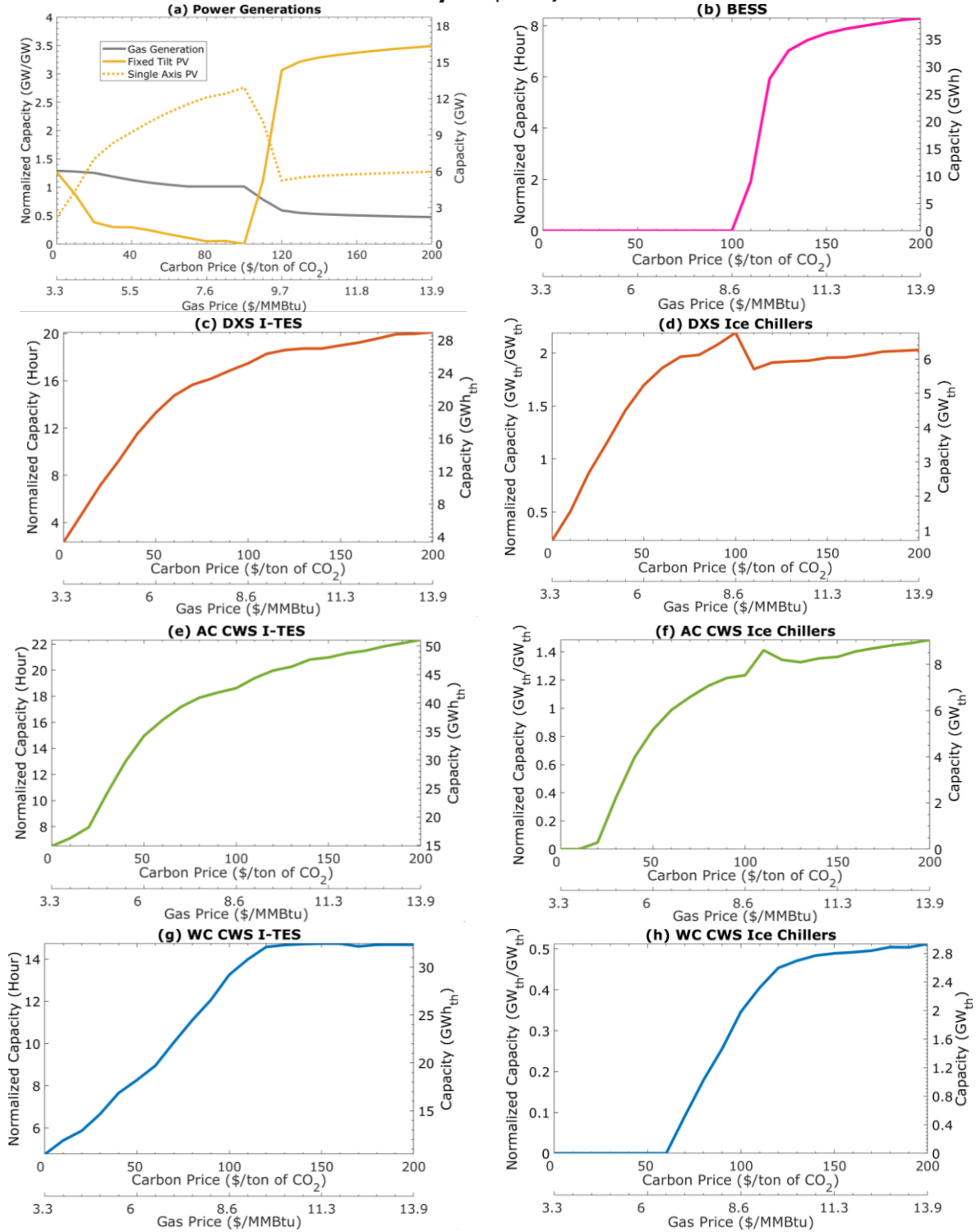


**Figure 2.10: Cost-optimal system as carbon price increases. Power generations and BESS capacities are normalized to the 2016 yearly average electric demand of 4.7 GW. I-TES capacity is normalized to the average aggregate cooling demand of 1.4 GW<sub>th</sub> for DXS, 2.3 GW<sub>th</sub> for AC CWS, and 2.2 GW<sub>th</sub> for WC CWS. Ice chiller capacity is normalized to the aggregate cooling system capacity of 3.1 GW<sub>th</sub> for DXS, 6.1 GW<sub>th</sub> for AC CWS, and 5.7 GW<sub>th</sub> for WC CWS.**

## Battery at \$250/kWh

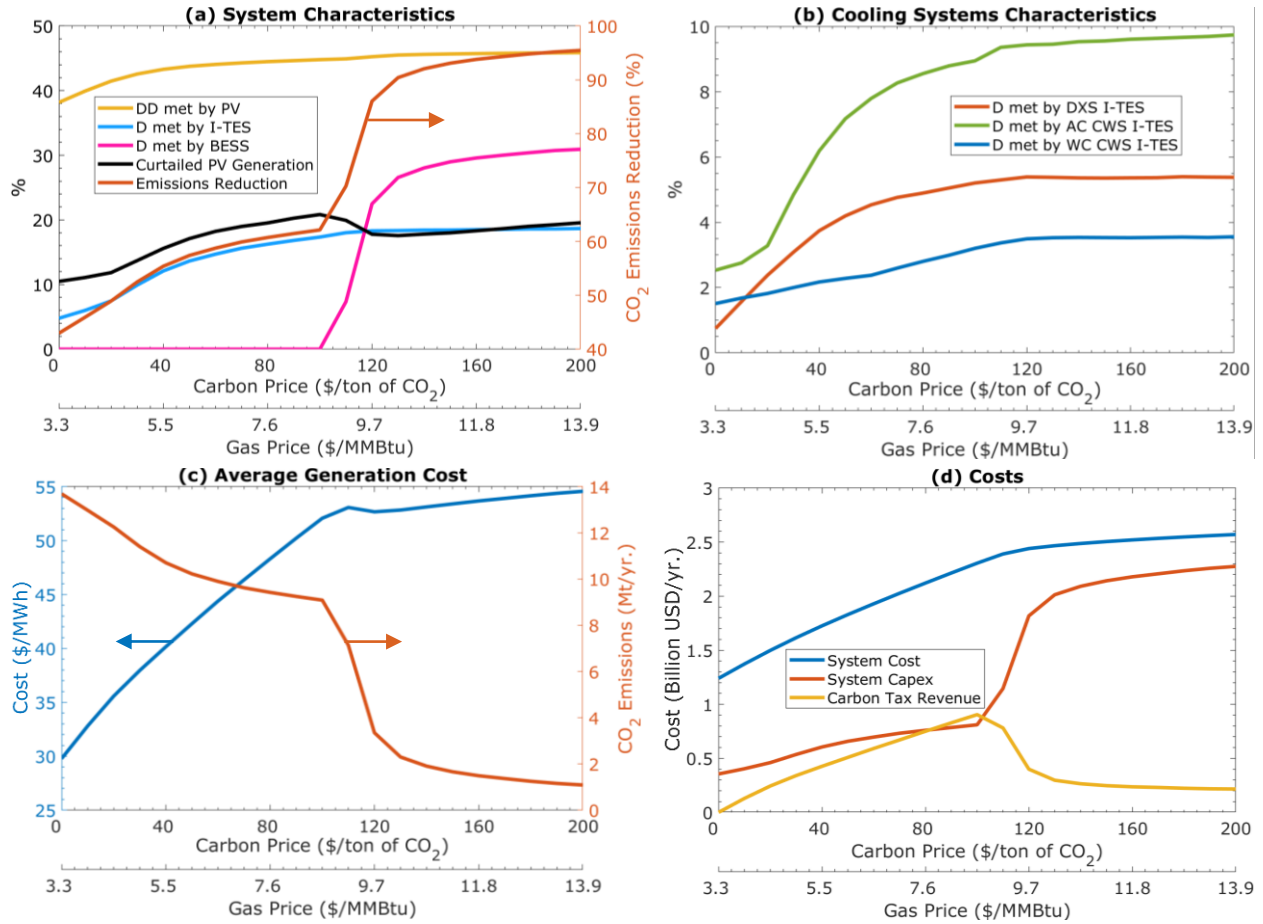


**Figure 2.11: As carbon price increases: (a) overall system characteristics, (b) cooling system characteristics, (c) average generation cost and total CO<sub>2</sub> emissions, and (d) annual system cost, Capex, and revenue from the carbon tax (carbon pricing).**

Different cooling system technologies respond differently to carbon pricing. AC systems are favored over WC CWS for I-TES use due to a lower system COP; this means an equal amount of thermal energy corresponds to a greater electric load shifting in AC systems. An additional advantage for AC CWS is utilizing the idle capacity to make ice, allowing for greater penetration of I-TES at reduced costs compared to DXS. To decarbonize nighttime cooling needs, the additional installed ice chillers' capacity is 2, 1.4, and 0.5 times the existing nominal capacities of DXS, AC CWS, and WC CWS, respectively. This large additional capacity is needed because of the capacity loss in ice-making mode and the necessity to store nighttime

cooling needs during daylight hours of no more than 6-8 hours. Less additional ice chillers are needed in CWS by utilizing the existing idle capacity to make ice. Furthermore, the pronounced difference between AC and WC CWS is due to more minor intra-annual and diurnal variations in ambient wet-bulb than dry-bulb temperatures, corresponding to less capacity degradation and a more consistent cooling system performance.

Curtailment remains modest, between 10 to 20% of total PV generation. Unless long-duration energy storage is considered, surplus PV generation produced from the mismatch between electric and cooling loads, which peaks in August, and PV generation, which peaks in June, is curtailed. As carbon pricing increases from 0 to \$200/ton of CO<sub>2</sub>, the average cost of power generation increases by about a factor of 2 in the cost-optimal systems. Simultaneously, emissions sharply declined by a factor of 7 relative to the cost-optimal system and 12 relative to the current system structure. Furthermore, the higher annual system cost is increasingly from Capex, driven by installed PV generation and BESS, as opposed to OpEx from carbon tax revenue.

BESS becomes cost-effective above carbon pricing of \$100/ton of CO<sub>2</sub>. The analysis suggests that BESS does not displace I-TES for cooling load shifting and is primarily used to manage the diurnal behavior of non-cooling loads. BESS requires a high daily average capacity utilization rate of around 90% to be economical, which is unsuitable for a seasonal cooling load. The model suggests a rapid increase in installed BESS capacity with carbon prices up to \$140/ton of CO<sub>2</sub>. This system achieves a decarbonization rate exceeding 90%, which vastly diminishes the role of gas generation. With a net positive increase in PV generation capacity, the cost-optimal system shifts to a preference for fixed-tilt PV generation over single-axis tracking enabled by BESS's naturally higher charging rate, which reduces system cost and curtailment.

The carbon abatement cost, defined as the yearly cost of mitigating carbon emissions from gas generation, for the cost-optimal system as carbon pricing increases is shown in Figure 2.12. The negative abatement cost at low carbon pricing indicates that a more sustainable solution can be achieved at a reduced annual cost. Otherwise, the abatement cost does not exceed \$55 per ton of CO<sub>2</sub> up to a decarbonization rate of nearly 95%, supported by low-cost PV generation and I-TES and reliable non-cooling load for BESS.

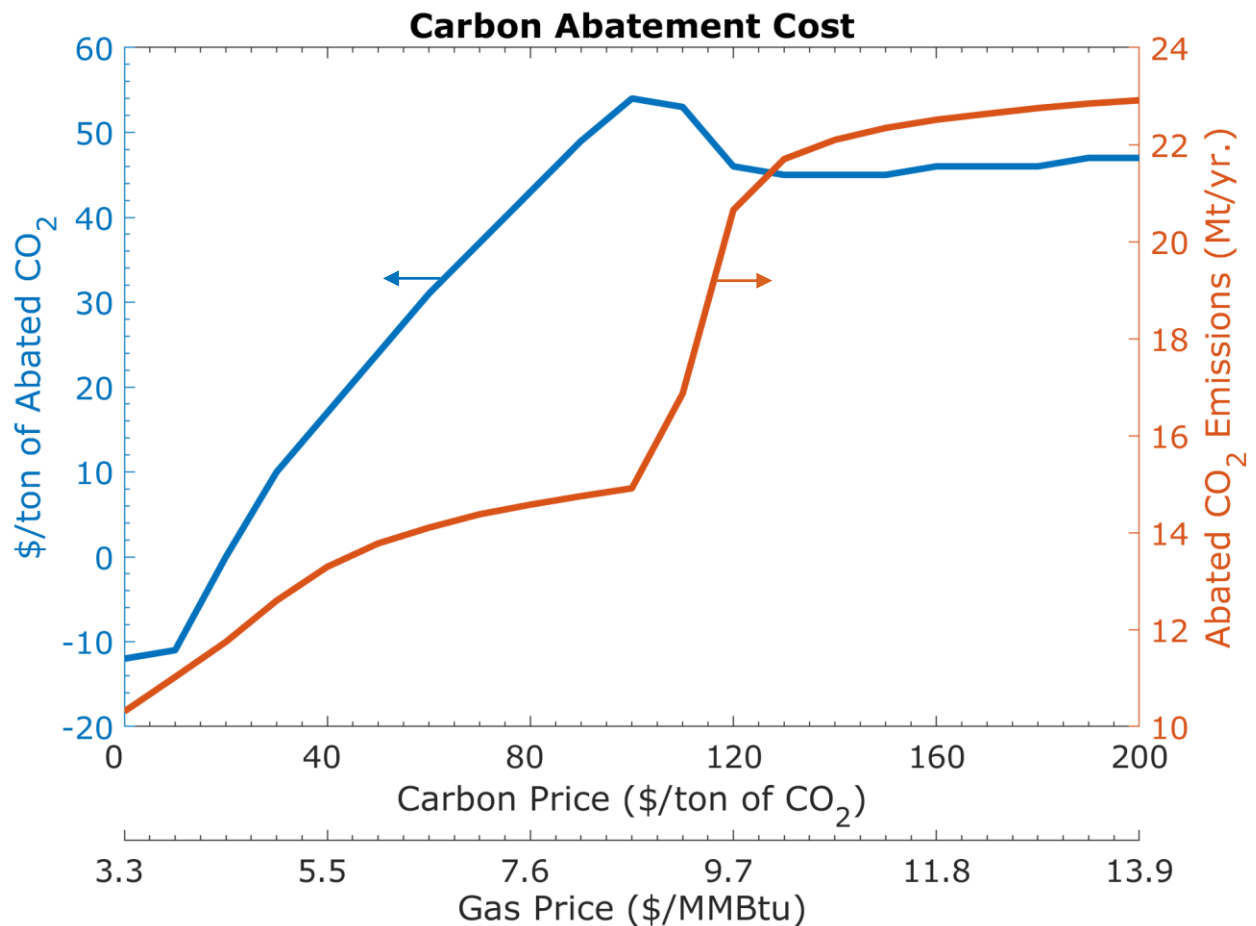


**Figure 2.12: As carbon price increases, carbon abatement costs on the left y-axis and abated CO<sub>2</sub> emissions on the right y-axis, relative to the current system of all gas-based generations.**

### 2.3.3 Decarbonized system with \$140/ton of CO<sub>2</sub> carbon tax

This section examines a deeply decarbonized system supported by carbon pricing at \$140/ton of CO<sub>2</sub> at the current BESS capacity cost of \$250/kWh. Limited carbon emissions reduction can be realized beyond a carbon price of \$140/ton of CO<sub>2</sub> using the examined pathway, as shown in Figure 2.12. PV generation combined with BESS and I-TES cannot compete with existing gas generation for highly seasonal cooling between mid-July and mid-September. This deeply decarbonized system utilizes PV generation for daytime electric loads, I-TES for nighttime cooling, and BESS for non-cooling electricity needs, achieving a 92% percent reduction in emissions from the current approach of all gas generation. As tabulated in Table 2.5, the cost-optimal system comprises 21 GW<sub>p,dc</sub> of PV (15 GW<sub>p,dc</sub> for fixed-tilt and 6 GW<sub>p,dc</sub> for single-axis tracking), 107 GWh<sub>th</sub> of I-TES (27 GWh<sub>th</sub> for DXS, 48 GWh<sub>th</sub> for AC CWS, and 32 GWh<sub>th</sub> for WC CWS), 17 GW<sub>th</sub> of additional ice chillers (6 GW<sub>th</sub> for DXS, 8 GW<sub>th</sub> for AC CWS, and 3 GW<sub>th</sub> for WC CWS), and 35 GWh of usable BESS capacity. In AC CWS and WC CWS, I-TES also benefits from utilizing existing idle chillers' capacity for ice-making. Since PV with BESS and I-TES cannot displace gas generation during the peak demand season between mid-July to mid-September, peak demand from gas generation was only reduced by 66% to 2.5 GW.

**Table 2.5: Cost-optimal system at \$140/ton of CO<sub>2</sub> carbon price**

Parameter	Value	Notes
Solar PV capacity	21 GW <sub>p,dc</sub>	15 GW <sub>p,dc</sub> fixed-tilt 6 GW <sub>p,dc</sub> single-axis tracking
I-TES capacity	107 GWh <sub>th</sub>	27 GWh <sub>th</sub> DXS 48 GWh <sub>th</sub> AC CWS 32 GWh <sub>th</sub> WC CWS
Additional ice chiller capacity	17 GW <sub>th</sub>	6 GW <sub>th</sub> DX systems 8 GW <sub>th</sub> AC CWS 3 GW <sub>th</sub> WC CWS
BESS capacity	35 GWh	Net usable capacity
Peak gas generation demand	2.5 GW	Across all scenarios



The cost-optimal system characteristics averaged over the four scenarios are tabulated in Table 2.6. 40% of the electric demand was directly met by PV generation, and 23% and 29% indirectly from load shifting using I-TES and BESS, respectively. The remaining 8% of the electric demand is met using gas generation with less than 1300 hrs of operation on days with reduced solar output and during the peak cooling season. Further decarbonization using PV generation might require long-duration energy storage. Furthermore, due to reliable nighttime cooling and electricity demands, the required PV capacity to decarbonize the system is about three times the current peak electricity demand. Governed by the seasonality of cooling demand, I-TES average daily capacity utilization rate remains around 70%. On the other hand, the capacity factor for BESS is higher at 92%, suggesting continual year-round use for managing the non-cooling loads.

**Table 2.6: Cost-optimal system characteristics at \$140/ton of CO<sub>2</sub> carbon price**

Parameter	Value	Notes
Cost	\$2487 million/yr.	Annual cost from Capex and OpEx
Average power generation cost	\$52/MWh	From gas and PV generation
Demand met by gas generation	8%	Mostly In the high-demand season
Demand met by PV generation	40%	Directly
Load shifted by I-TES	23%	All cooling systems
Load met by the BESS	29%	Primarily non-cooling loads
Cooling demand met by PV generation	34%	Directly
Cooling demand met by I-TES	57%	All cooling systems
Cooling demand met by BESS	9%	Mostly In the high-demand season
Solar capacity factor	20%	After curtailment
Curtailment	16%	Of total PV generation
I-TES average capacity utilization	73%	Equivalent full cycle per day
BESS average capacity utilization	92%	Equivalent full cycle per day

The cost-optimal system increases the average cost of produced energy by 41% (\$37/MWh to \$52/MWh) and total annual system cost by 65% (\$1.5 billion/yr. to \$2.5 billion/yr.) relative to the current approach of all gas-fired generation. The cost-optimal system incurs \$845 million/yr. from installed PV, \$92 million/yr. from installed I-TES, \$107 million/yr. from additional ice chillers, and \$1047 million/yr. from installed BESS capacity. Annual gas generation expenditure was reduced to \$383 million/yr.

Figure 2.13 shows the percent contribution of PV, I-TES, BESS, and gas generation to meet the electric demand in (a) and the electric cooling load in (b). I-TES became a prominent year-round contributor to meeting the electric demand, especially during the high cooling season. BESS, on the other hand, contributes to meeting cooling loads in the high-demand season. However, BESS contributes a steady amount of energy to the electricity grid year-round to meet the baseload.

## Carbon Price at \$140/ton of CO<sub>2</sub>; Battery at \$250/kWh

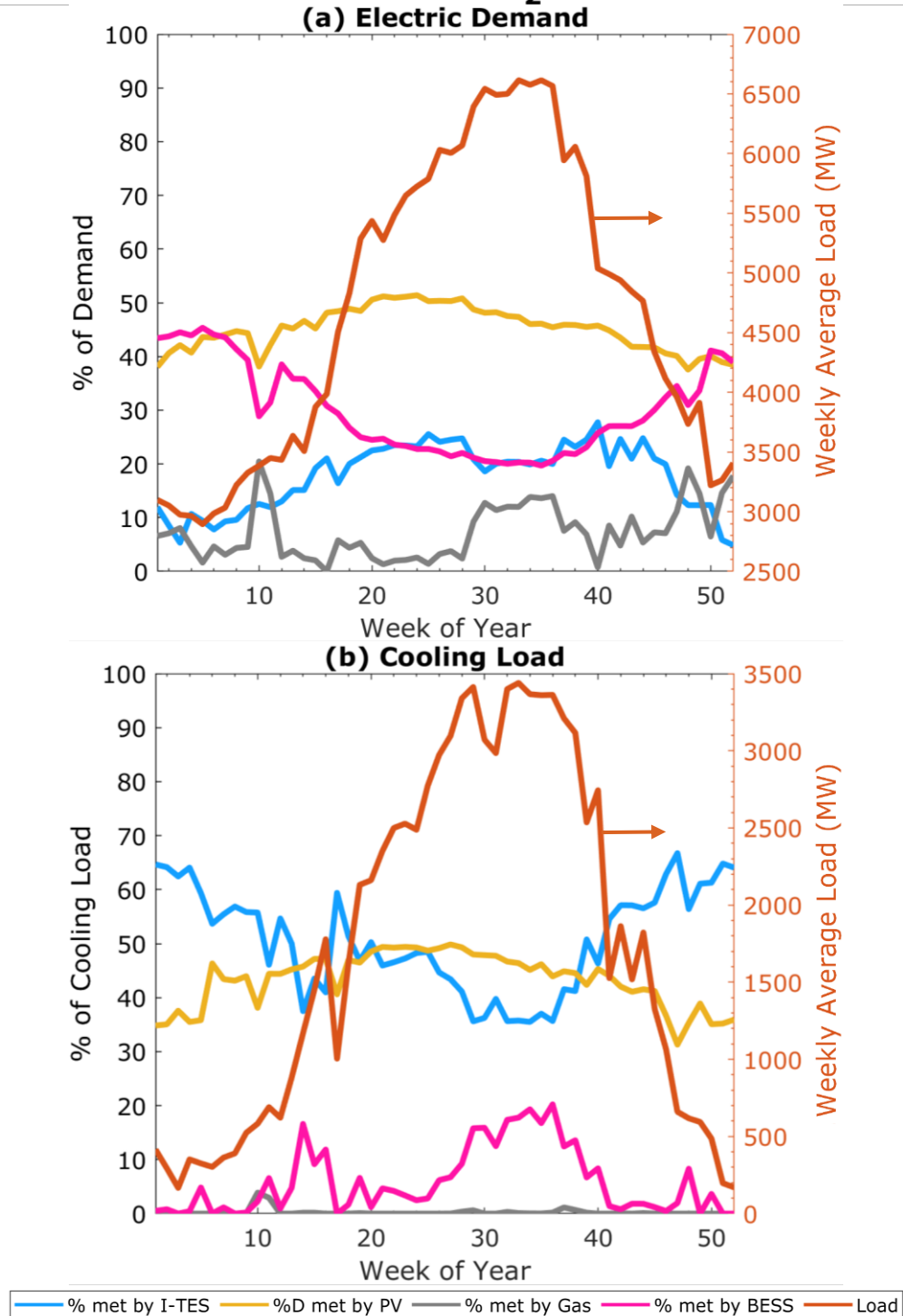


**Figure 2.13: Cost-optimal system with a carbon price at \$140/ton of CO<sub>2</sub> and BESS capacity cost at \$250/kWh with a breakdown of contribution to supplying (a) the electric demand and (b) the electric cooling load. The electric cooling load is assumed to be met first by PV generation before BESS is used, and the remaining load is met using gas generation.**

Hourly system loads for three consecutive days in the winter, spring, and summer are shown in Figure 2.14. BESS is dispatched overnight to manage the non-cooling load. In the peak season, I-TES and BESS are dispatched to minimize gas generation use and peak demand. The sole use of PV generation for energy storage charging in the deeply decarbonized system soars the daytime electric load to 15-20 GW compared to the current daytime load of 5-7 GW.

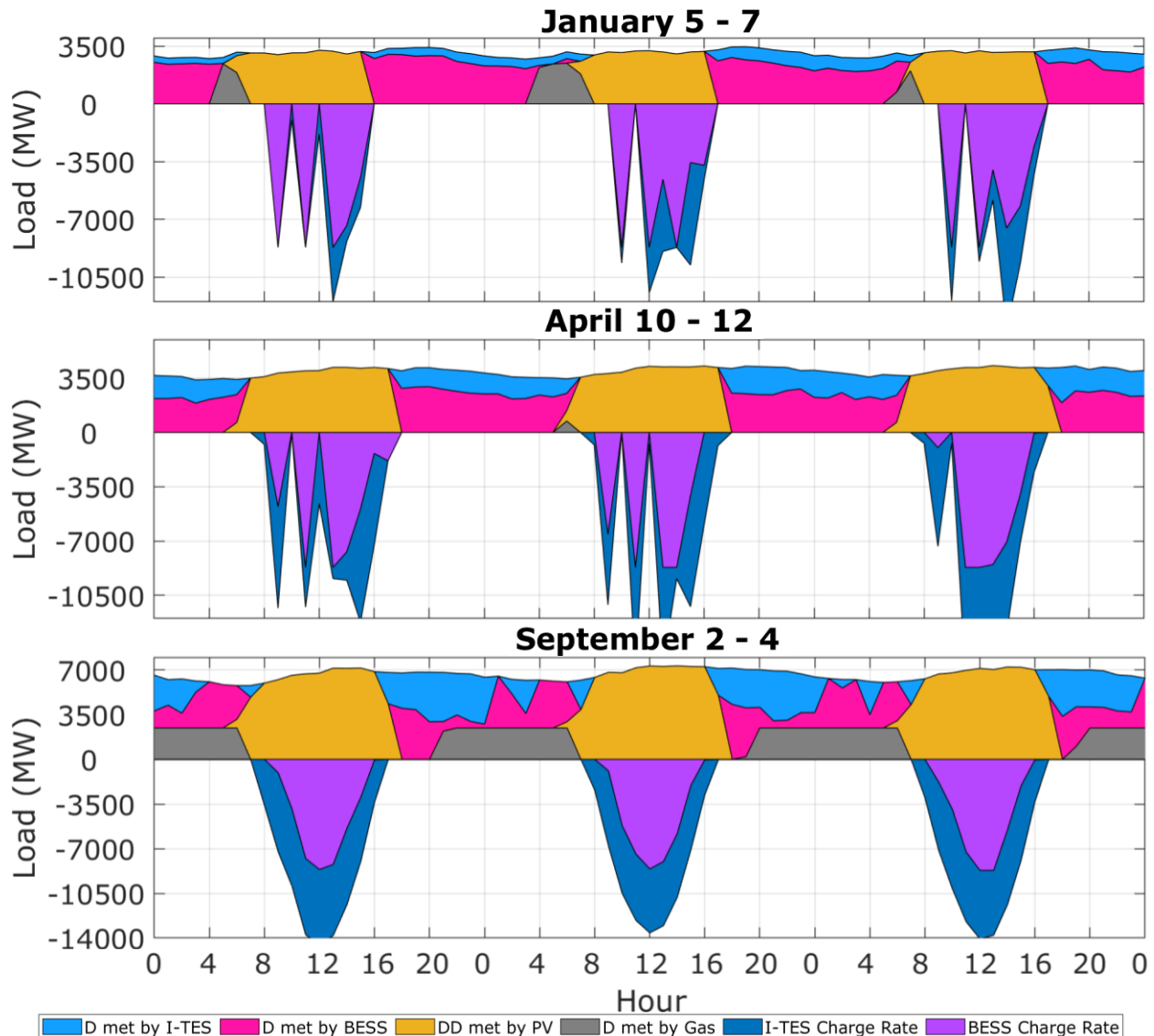


**Figure 2.14: Cost-optimal system hourly load profile with a carbon price at \$140/ton of CO<sub>2</sub> and BESS capacity cost at \$250/kWh with contributions from PV generation and load shifting using I-TES and BESS to meet the electric demand for three days in winter, spring, and summer. I-TES and BESS charge rates are shown as negative loads.**

### 2.3.4 Impact of BESS capacity cost

BESS remains cost-prohibitive at the capacity cost of \$250/kWh without economic incentives. The continual decline in the capacity cost can enable BESS to be cost-effective at a reduced carbon price. This section investigates the impact of the BESS capacity cost and carbon pricing on the cost-optimal system. The cost-optimal system for a BESS capacity cost ranging from \$100/kWh to \$300/kWh and carbon pricing between 0 and \$200/ton of CO<sub>2</sub> is shown in Figure 2.15 with (a) emissions reduction, (b) generation cost, (c) total PV capacity, and (d) BESS capacity. Cooling systems characteristics are shown in Figure 2.16 with I-TES and chillers capacities for DXS, AC CWS, and WC CWS, respectively.

Similar to the outcome from the analysis with carbon pricing, the model suggests that a declining BESS capacity cost will not displace the use of I-TES for cooling load shifting even as the capacity cost is considerably dropped to \$100/kWh but will increasingly utilize BESS to supplement seasonal cooling needs. This is seen as a drop in I-TES and chillers capacities in Figure 2.16 and is necessary to maintain a cost-effective BESS with a larger capacity. In CWS, more idle chiller capacities are utilized for I-TES charging in the shoulder season, supported by the higher availability of surplus PV generation without additional ice chiller capacities. As BESS cost declines, WC CWS sees a more significant drop in I-TES and chillers capacity than AC CWS and DXS. As indicated earlier, stored thermal energy corresponds to less electric load shifting in WC systems due to a higher system COP, enabling BESS to be more cost-competitive.

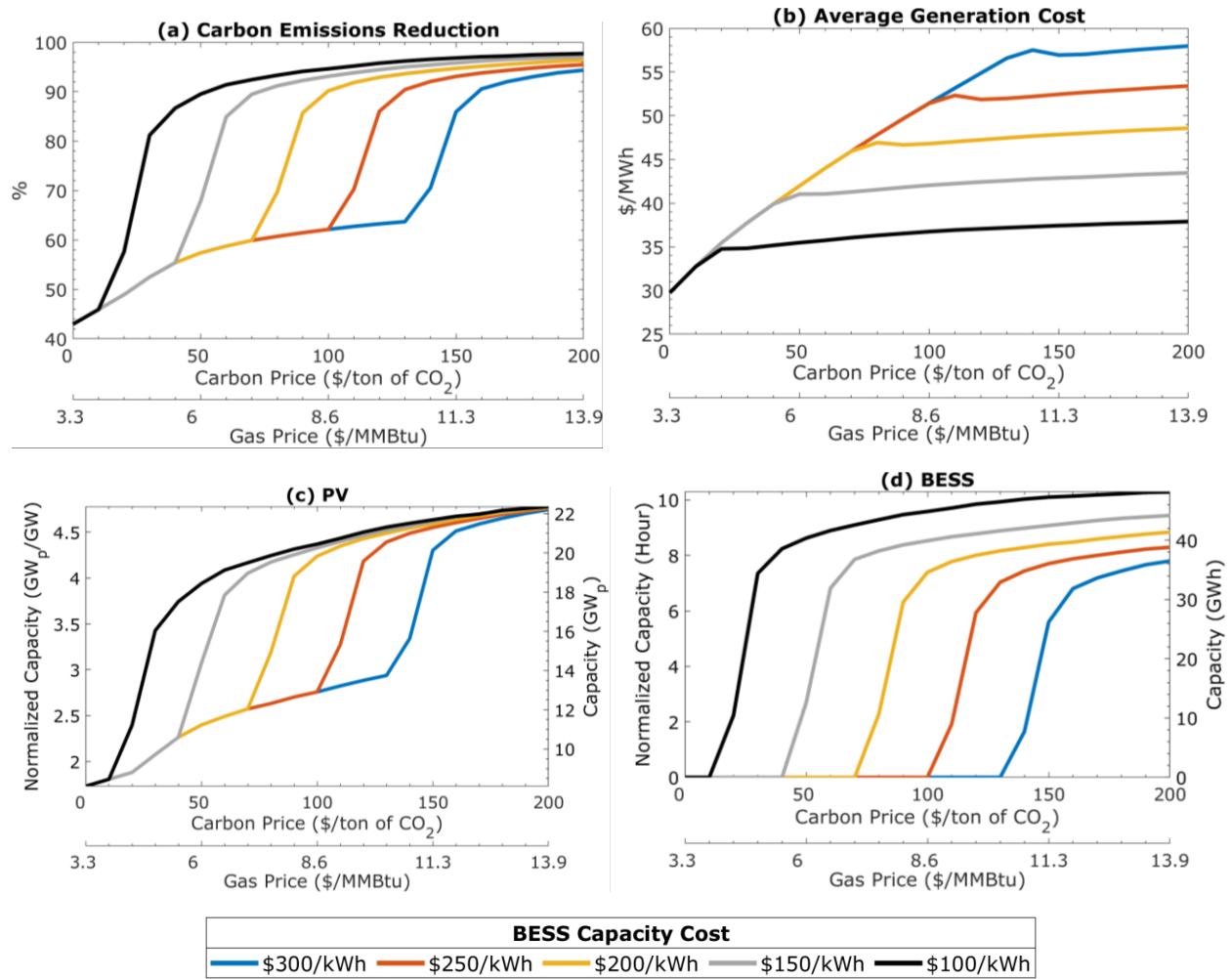


**Figure 2.15: Impact of BESS capacity cost and carbon pricing on the cost-optimal system with (a) emissions reduction, (b) average generation cost, (c) total PV capacity (fixed-tilt and single-axis tracking), and (d) BESS capacity. PV and BESS capacity is normalized to the 2016 yearly average electric demand of 4.7 GW.**

Reducing BESS capacity costs promotes using more BESS with a limited need for an additional PV capacity. The BESS partly substitutes I-TES in the high-demand season with a higher round trip efficiency of about 85% compared to 60-70% in I-TES. Furthermore, as the capacity cost is reduced to \$100/kWh, the average cost of produced energy in a deeply decarbonized system could approach that of the current cost of gas generation of \$37/MWh. However, the annual cost remains moderately higher at \$1.8 billion/yr. due to round-trip losses compared to the current system cost of \$1.5 billion/yr.

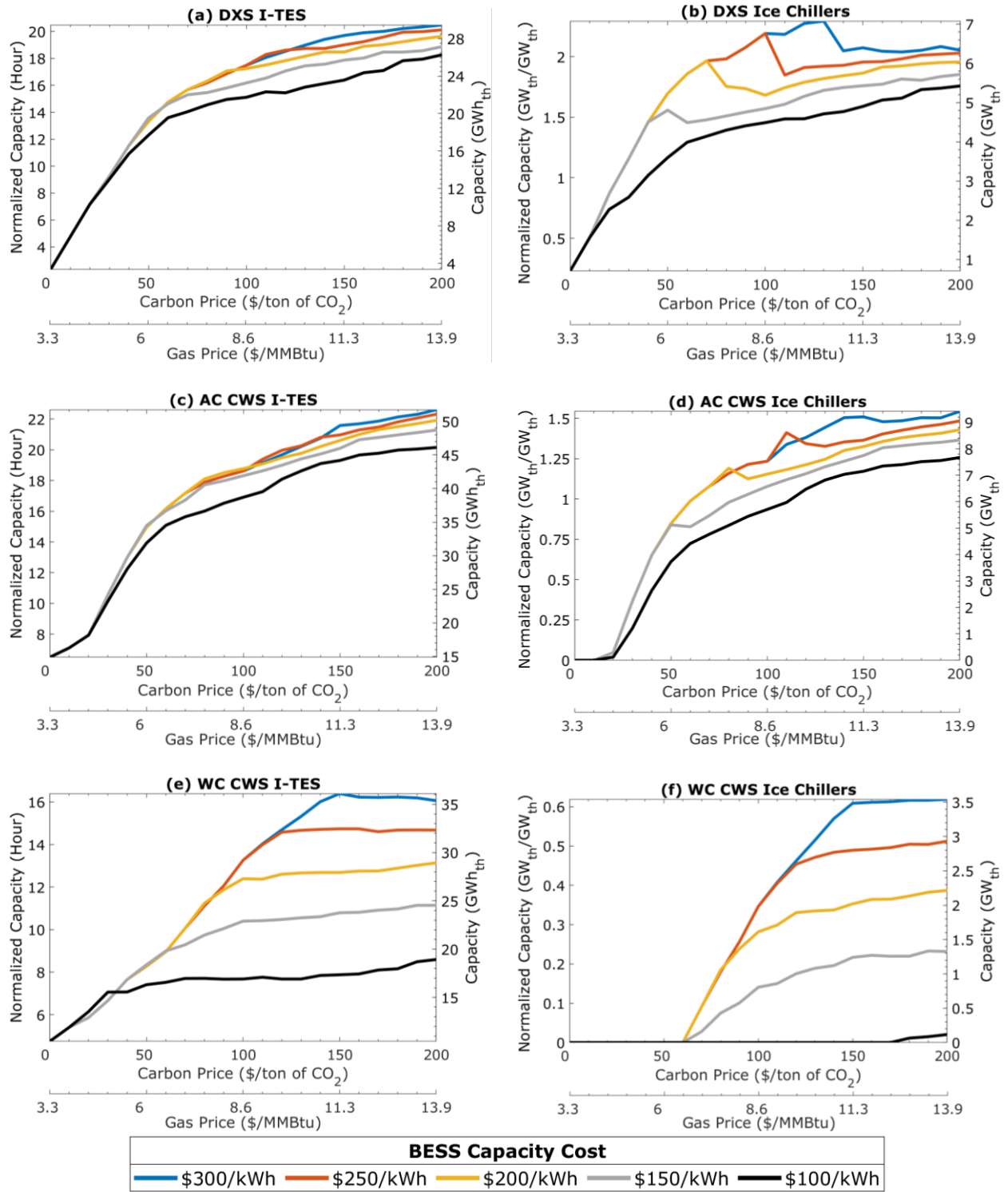


**Figure 2.16: Impact of BESS capacity cost and carbon pricing on the cost-optimal system. I-TES capacity is normalized to the average aggregate cooling demand of 1.4  $\text{GW}_{\text{th}}$  for DXS, 2.3  $\text{GW}_{\text{th}}$  for AC CWS, and 2.2  $\text{GW}_{\text{th}}$  for WC CWS. Ice chillers' capacity is normalized to the aggregate cooling capacity of 3.1  $\text{GW}_{\text{th}}$  for DXS, 6.1  $\text{GW}_{\text{th}}$  for AC CWS, and 5.7  $\text{GW}_{\text{th}}$  for WC CWS.**

## 2.4 Conclusion

The examination of the utility-scale perspective demonstrates strong potential for using PV generation with I-TES and BESS for load shifting. However, BESS is cost-prohibitive under the current gas price of \$3.3/MMBtu and capacity cost of \$250/kWh. Nevertheless, the analysis suggests that 8 GW of PV and 28 GWh<sub>th</sub> of I-TES capacity can reduce CO<sub>2</sub> emissions and peak gas generation demand by 43% and 18%, respectively, and cut annual system costs by 20%. For this system, I-TES is counterintuitively primarily used in low cooling demand seasons constrained by the availability of surplus PV generation and idle chiller capacity for ice-making.

Carbon pricing is determined to be an effective tool to boost energy storage adoption and reduce emissions. However, challenges arise due to (i) electric demands peak in August, whereas PV generation peaks in June, producing less surplus generation when needed, (ii) I-TES and BESS for seasonal loads cannot cost-effectively outcompete already existing gas generation, (iii) reduced idle chiller capacity in the peak cooling demand season, and (iii) chiller cooling capacity degradation due to higher ambient temperatures. Nevertheless, using PV and I-TES, the cost-optimal system with carbon pricing at \$60/ton of CO<sub>2</sub>, could reduce emissions by 60%.

BESS becomes cost-effective above carbon pricing at \$100/ton of CO<sub>2</sub> at the current capacity cost of \$250/kWh. The analysis suggests that BESS does not displace I-TES at higher carbon pricing or a lower capacity cost for cooling load shifting but primarily manages the non-cooling loads. That is because BESS requires a high average daily capacity utilization rate of about 90% to be cost-effective. A system with carbon pricing at \$140/ton of CO<sub>2</sub> could fully decarbonize the cooling load and reduce gas generation use and peak demand by 92% and 66%, respectively. Limited further emissions reduction can be realized with higher carbon pricing using the considered energy storage technologies.



Several simplifications and estimations were made that can impact the estimated optimal PV and energy storage capacities and limit the calculated decarbonization rate, including the estimated cooling loads and COPs and the simplified linear I-TES model. Greater penetration of AC systems, lower COPs, and higher charge/discharges will favor slightly larger I-TES and PV capacities. Otherwise, the cost-optimal system was only minorly sensitive to the assumed PV, I-TES, and ice chiller costs, partly due to their ability to compete with gas generation at the current cost structure. Furthermore, BESS degradation, which was not accounted for, will make BESS slightly less favorable. Lastly, the hourly analysis does not permit an extensive examination of the impact of high penetration of PV capacity on the stability of the national electricity grid.

## Chapter 3: Modeling of WC CWS with I-TES

### 3.1 Introduction

Because of their simpler design and lower installed cost, DXS is the preferred method of cooling small buildings such as homes, offices, schools, and small shopping centers. In DXS, warm air directly exchanges heat with the expanding refrigerant in the evaporator. Using DXS in larger buildings is less favorable due to increased pressure losses in the refrigeration pipeline and air distribution side. For these buildings, water is used as an intermediate fluid to transport heat over a larger distance exchanging heat between the air in the conditioned space and the refrigerant inside the chillers. Chillers can either be AC or WC. WC chillers utilize a cooling tower to reject heat to the ambient and deliver more efficient cooling and are often considered for building with over 20,000 m<sup>2</sup> of cooled space [88]. The improved efficiency is enabled by the reduced compressor lift (pressure differential) in exchange for a higher initial cost compared to AC chillers.

Although WC CWS are far more complex than DXS used in small buildings, they deliver more efficient cooling at a reduced life cycle cost. WC CWS comprises several components: chillers, pumps, valves, cooling towers, and cooling and dehumidification coils. The simplest system configuration, shown in Figure 3.1, is a constant flow system and contains chillers in a single loop that combines chilled water production and distribution. The total chilled water flowrate is dictated by the number of operating chillers. Air temperature in the coil is regulated using a three-way valve by diverting excess flow back to the chillers. A limitation of this configuration is maintaining the air temperature setpoint during off-peak hours, especially in buildings with uneven cooling needs. This limitation arises from the three-way valve's inability to modulate the flowrate it receives, only diverting excess flow, which can starve heavily loaded

coils. This forces CWS operators to sub-optimally operate additional chillers with a reduced temperature differential (commonly referred to as delta T) to satisfy the building's load.

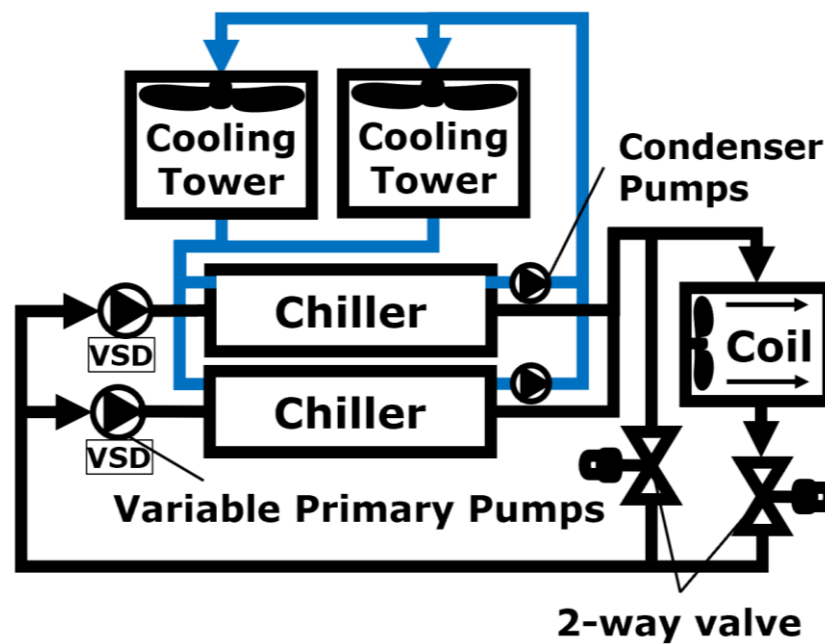


**Figure 3.1: CWS in a simple constant-flow configuration. Each chiller operates with its fixed-speed pumps. Excess water is diverted back using a three-way valve**

A primary-secondary flow configuration is commonly implemented to mitigate the problem of poor chiller sequencing in constant flow systems. The primary-secondary flow configuration, shown in Figure 3.2, is a well-established CWS configuration used on small to large buildings [75], [97], [98]. This configuration decouples the secondary (distribution) loop from the primary (production) loop. The chillers operate with their respective fixed-speed pumps to maintain design flow. In conjunction with two-way valves, variable-speed pumps modulate the water supply to the coil to satisfy the building's load. Surplus chilled water flows back to the chillers through the decoupler and blends with the coils' return water. Although pump energy use for operating chillers is constant, the secondary pumps' energy use is reduced with the building load.

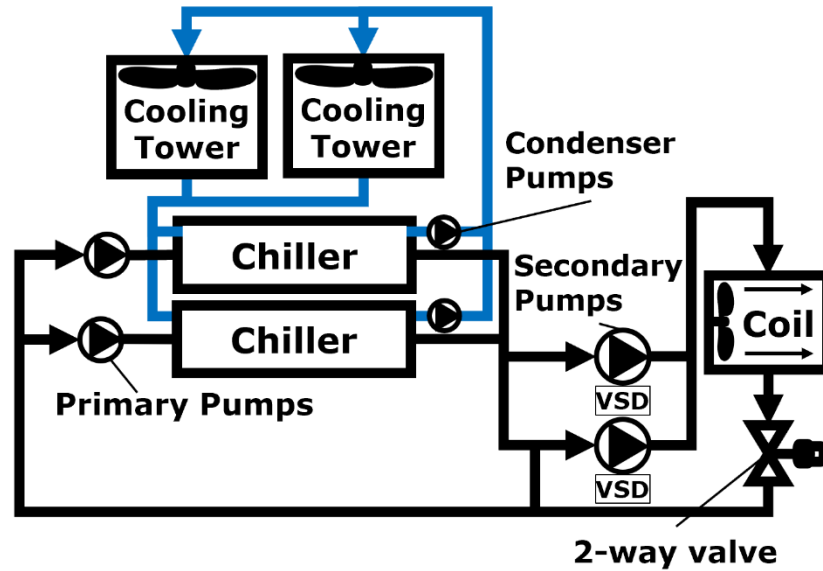


**Figure 3.2: CWS in a primary-secondary flow configuration. Chillers operate with their fixed-speed pumps in the primary loop, and two-way valves and variable-speed pumps regulate the flowrate received by the building's coils in the secondary loop. Excess water returns to the chiller in the bypass blending with the coils' return water.**

A variable chiller flow configuration that does away with the secondary loop has been gaining popularity and attention in recent years due to advancements in control technology [99], [100]. Shown in Figure 3.3, this configuration reduces the initial cost and footprint by eliminating the secondary pumps and associated fittings. This configuration allows for reduced pump energy use and improved overall plant efficiency at the expense of a more complex operation to maintain proper chiller flow and satisfy the building load. The minimum and maximum flowrate of chillers is regulated by modulating a two-way valve in the bypass. An additional advantage for variable primary flow is its resistance to the low temperature differential problem (also known as low delta T syndrome) generally confronted when the building coils are not adequately maintained.

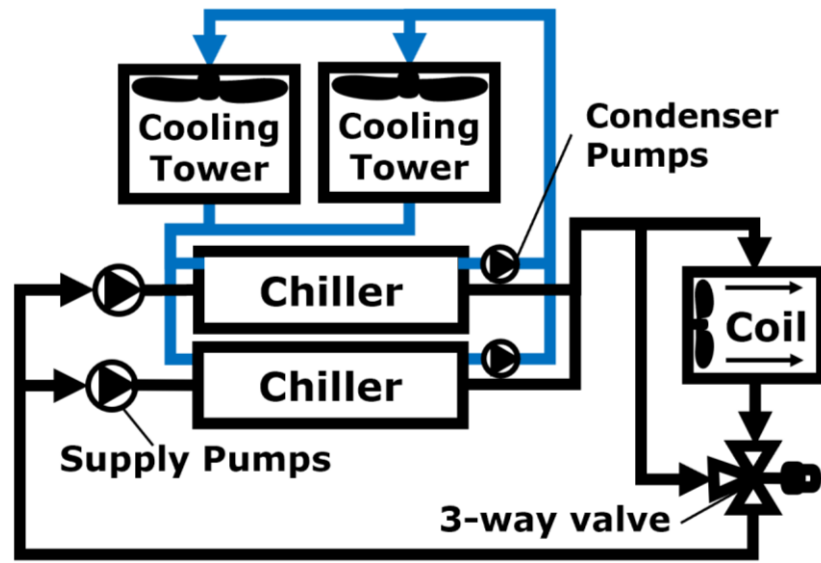


**Figure 3.3: CWS in a variable primary flow configuration. A bypass control valve is required to maintain proper chiller flow.**

CWS components' models in the literature are developed with varying complexity and motivations. Dynamic models are often developed for control and diagnostic problems, detailed models for design and analysis problems, and simpler models for process control and optimization problems. The models considered in this chapter are used to solve optimization problems developed in Chapters 4 and 5. CWS models developed for optimization problems can be classified into physic-based, regression-based or data-driven, and hybrid models [101]. While physics-based models can offer physical insight, they are computationally intensive and suffer from accuracy problems. Regression-based and other machine-learning models are among the most popular models in the literature; they simplify the complex behavior CWS components into a regression model with several input parameters. They are computationally efficient but cannot be generalized and lack the physical insight to explain components' performance characteristics. On the other hand, hybrid models combine the efficiency of data-driven models with the physical insight of physics-based models in a simpler formulation. This simpler formulation is

accomplished with empirically obtained parameters that capture complex behavior that would otherwise be difficult to model physically.

In this chapter, hybrid steady-state models are developed for the major devices in CWS in a primary-secondary configuration illustrated in Figure 3.4. The developed models are laid out in Section 3.2 in the following order: (i) electric chillers, (ii) water pumps, (iii) cooling towers, (iv) cooling and dehumidification coils, and (v) I-TES model. This system can be operated in three modes: charging, discharging, and idle storage while simultaneously satisfying the building cooling requirements. The I-TES is located downstream of the chillers, allowing chillers to receive warmer return water and operate more efficiently.

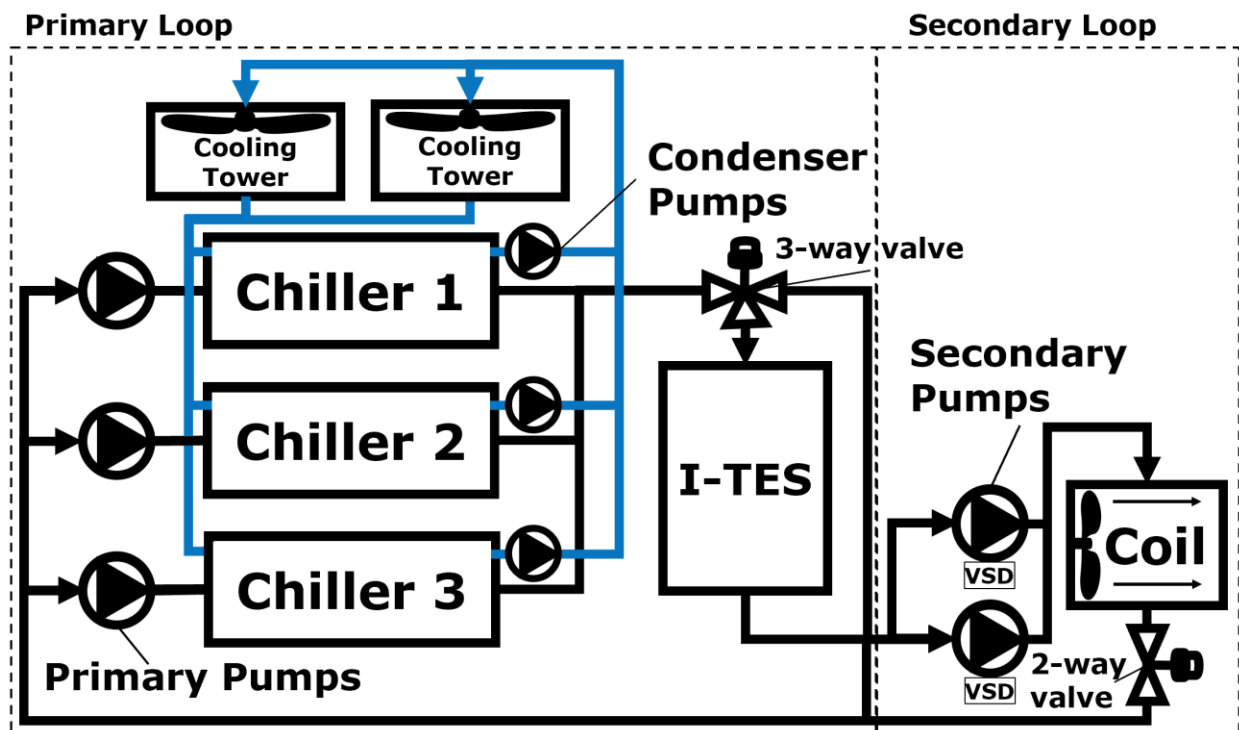


**Figure 3.4: Considered CWS in a primary-secondary configuration with multiple WC chillers, two shared cooling towers, and an I-TES downstream of the chillers. The building is represented in a single coil with the respective building aggregate cooling load.**



In reality, the performance of chillers is a strong function of their loading in addition to evaporator and condenser temperatures influenced by the compressor efficiency. The chiller model described below is a widely used simple model first developed by Gordon-Ng [102]–[105] to predict electric chillers' coefficient of performance using the first and second laws of thermodynamics. Applying the first law of thermodynamics, conservation of energy, to a vapor-compression cycle yields the following expression:

$$\Delta \dot{E} = 0 = \dot{Q}^{cond} + \dot{Q}^{leak,cond} - \dot{Q}^{chl} - \dot{Q}^{leak,evap} + \dot{Q}^{leak,comp} - P^{chl} \quad (3.1)$$

where  $\dot{Q}^{cond}$  is the heat rejected from the condenser,  $\dot{Q}^{chl}$  is the chiller cooling rate,  $\dot{Q}^{leak,cond}$ ,  $\dot{Q}^{leak,evap}$ , and  $\dot{Q}^{leak,comp}$  are the heat leaks into the evaporator, out of the condenser, and out of the compressor, respectively, and  $P^{chl}$  is the electric power consumed by the chiller. Similarly, applying the second law of thermodynamics, entropy balance, yields the following expression:

$$\Delta \dot{S} = 0 = \frac{\dot{Q}^{cond} + \dot{Q}^{leak,cond}}{T^{cond}} - \frac{\dot{Q}^{chl} + \dot{Q}^{leak,evap}}{T^{evap}} - \Delta \dot{S}^{int} \quad (3.2)$$

where all energy flows are defined as positive.  $T^{cond}$  and  $T^{evap}$  are the refrigerant saturation temperatures in the condenser and evaporator, respectively, and  $\Delta \dot{S}^{int}$  is the internal entropy generation rate. Heat leak from the condenser into the ambient is negligible due to comparatively minor temperature differences between the condenser and the ambient temperatures and hence is ignored. Performing energy balance across the evaporator and condenser heat exchangers yields the following two relations:

$$\dot{Q}^{cond} = \dot{m}^{cw} c^{p,cw} \varepsilon^{cond} (T^{cond} - T^{csw}) = \left( \frac{\varepsilon^{cond}}{1 - \varepsilon^{cond}} \right) \dot{m}^{cw} c^{p,cw} (T^{cond} - T^{crw}) \quad (3.3)$$



and,

$$\dot{Q}^{chl} = \dot{m}^{sw} c^{p,sw} \varepsilon^{evap} (T^{rw} - T^{evap}) = \left( \frac{\varepsilon^{evap}}{1 - \varepsilon^{evap}} \right) \dot{m}^{sw} c^{p,sw} (T^{sw} - T^{evap}) \quad (3.4)$$

where  $\varepsilon^{evap}$ ,  $\dot{m}^{sw}$  and  $c^{p,sw}$  are the evaporator heat exchanger effectiveness, water mass flowrate, and water-glycol mixture specific heat, and  $\varepsilon^{cond}$ ,  $\dot{m}^{cw}$  and  $c^{p,cw}$  are the condenser heat exchanger's effectiveness, water mass flowrate, and specific heat, respectively.

$T^{csw}$  and  $T^{crw}$  are entering and leaving condenser water temperature, and  $T^{sw}$  and  $T^{rw}$  are the evaporator leaving (or supply) and entering water-glycol mixture temperature, respectively.

Plugging Equation (3.2) to (3.4) back into Equation (3.1) and using the definition of  $COP$

( $COP = \dot{Q}^{chl} / P^{chl}$ ) has been experimentally shown by Ng et al. [106] to simplify to the Gordon-

Ng general model for electric chillers as follows:

$$\frac{T^{sw}}{T^{csw}} \left[ 1 + \frac{1}{COP} \right] = 1 + \frac{T^{sw} \Delta \dot{S}^{int}}{\dot{Q}^{chl}} + \frac{\dot{Q}^{leak,eqv} (T^{csw} - T^{sw})}{T^{csw} \dot{Q}^{chl}} + \frac{R \dot{Q}^{chl}}{T^{csw}} \left[ 1 + \frac{1}{COP} \right] \quad (3.5)$$

where the chiller load is described by the following equation:

$$\dot{Q}^{chl} = \dot{m}^{sw} c^{p,sw} (T^{rw} - T^{sw}) = PLR \dot{Q}^{chl,des} \quad (3.6)$$

$\dot{Q}^{chl,des}$  is the design (nominal) chiller cooling capacity, and  $PLR$  is the chiller loading defined as  $\dot{Q}^{chl} / \dot{Q}^{chl,des}$ . Parameters in Gordon model:  $\dot{Q}^{leak,eqv}$  is the equivalent heat leak into the evaporator from the ambient and out of the compressor into the ambient;  $R$  is the effective thermal resistance for the evaporator and condenser heat exchangers and dominates the chiller

performance at high chiller loading;  $\Delta\dot{S}^{int}$  is internal entropy generation rate and dominates performance at low loading conditions.  $\Delta\dot{S}^{int}$ ,  $R$  and  $\dot{Q}^{leak,eqv}$  are obtained from known chiller performance data using linear regression.

Jian and Reddy [107] proposed a modification to include a term representing the entropy generation rate due to irreversibility that is dependent on loading ( $\Delta\dot{S}^{intQ} \dot{Q}^{chl} / \dot{Q}^{chl,des}$ ) in addition to a constant entropy generation rate term ( $\Delta\dot{S}^{int}$ ) which slightly improves the model predictions. The modified Gordon-Ng electric chiller model is described by:

$$\frac{T^{sw}}{T^{csw}} \left[ 1 + \frac{1}{COP} \right] = 1 + \frac{T^{sw} \left( \Delta\dot{S}^{int} + \Delta\dot{S}^{intQ} \frac{\dot{Q}^{chl}}{\dot{Q}^{chl,des}} \right)}{\dot{Q}^{chl}} + \frac{\dot{Q}^{leak,eqv} (T^{csw} - T^{sw})}{T^{csw} \dot{Q}^{chl}} + \frac{R \dot{Q}^{chl}}{T^{csw}} \left[ 1 + \frac{1}{COP} \right] \quad (3.7)$$

It is advantageous to reformulate Gordon-Ng model as a function of the leaving condenser water temperature instead of the condenser water entering temperature to decouple the impact of the condenser water flowrate from the chiller performance curves. The leaving condenser and evaporator temperatures serve as a proxy for the refrigerant temperatures, enabling the investigation of reduced condenser water flowrate. The reformulated Gordon-Ng chiller model is given by:

$$\frac{T^{sw}}{T^{crw}} \left[ 1 + \frac{1}{COP} \right] = 1 + \frac{T^{sw} \left( \Delta\dot{S}^{int} + \Delta\dot{S}_i^{intQ} \frac{\dot{Q}^{chl}}{\dot{Q}^{chl,des}} \right)}{\dot{Q}^{chl}} + \frac{\dot{Q}_i^{leak,eqv} (T^{crw} - T^{sw})}{T^{crw} \dot{Q}^{chl}} + \frac{R \dot{Q}^{chl}}{T^{crw}} \left[ 1 + \frac{1}{COP} \right] \quad (3.8)$$

The reformulation of Gordon-Ng's model in terms of condenser leaving temperature introduces challenges as the leaving temperature is generally unknown that relates to the ambient conditions and the respective chiller loading. However, the condenser return temperature can be expressed

as a function of other controlled parameters, including the entering condenser water temperature and water flowrate as follows:

$$T^{crw} = T^{csw} + \frac{\dot{Q}^{chl}}{\dot{m}^{cw}_{cp,cw}} \left( 1 + \frac{1}{COP} \right) \quad (3.9)$$

Plugging Equation (3.9) back into Equation (3.8) yields the desired expression for electric chillers' performance as a function of condenser water flowrate:

$$\frac{1}{COP} = \frac{\dot{Q}^{chl}(\dot{Q}^{chl} + \dot{Q}^{leak,eqv} + \dot{m}^{cw}_{cp,cw}[R \dot{Q}^{chl} - T^{sw}] + T^{sw}[\Delta\dot{S}^{int} + \Delta\dot{S}^{intQPLR}])}{\dot{m}^{cw}_{cp,cw}(\dot{Q}^{chl} T^{csw} + \dot{Q}^{leak,eqv}[T^{csw} - T^{sw}] + T^{csw} T^{sw}[\Delta\dot{S}^{int} + \Delta\dot{S}^{intQPLR}])} \quad (3.10)$$

The chiller power consumption can then be calculated from the definition of COP as follows:

$$p^{chl} = \frac{\dot{Q}^{chl}}{COP} \quad (3.11)$$

Chillers data are extracted from the chillers data library in EnergyPlus given in a regression-based model with three polynomial curves using the DOE-2 model [108], [109]. The first curve (called *CAPFT* in EnergyPlus) describes the influence of entering evaporator and condenser temperatures on the cooling capacity. The second curve (called *EIRFT* in EnergyPlus) describes the influence of entering evaporator and condenser temperatures on electric power consumption. The third curve (called *EIRFPLR* in EnergyPlus) describes the influence of the chiller loading on electric power consumption. However, the given three polynomial curves are only valid within narrow ranges of supply and condenser temperatures. They cannot be used to predict chiller performance at low supply water temperatures associated with thermal energy

storage charging nor at high condenser water temperatures typical in warm climates. The extracted performance chiller data are used to fit the parameters in the Gordon-Ng model to predict chillers' performance outside the given temperature ranges.

EnergyPlus WC chillers data library contains chillers data with three distinct compressor types: centrifugal compressor with guide vanes, centrifugal compressor with variable speed drive (VSD), and screw compressor with slide valve. The performance of the centrifugal chiller with guide vanes (without VSD) strongly depends on chiller loading and is less sensitive to the condenser temperature. Centrifugal chillers generally offer the best full-load performance, while screw chillers tend to have a better part-load performance without using VSD. A centrifugal chiller can be equipped with a VSD for a considerable cost for optimized part-load performance. However, since a centrifugal compressor's pressure head is proportional to the square of the speed and flowrate, the chiller performance tends to be highest when both the condenser temperature and refrigerant flowrate (linearly correlated with loading) are reduced.

The COP, as determined by the three polynomial curves, is sampled within the given range of condenser and water supply temperatures and loading conditions. Least-square linear regression is then applied between the model's predicted COP and sampled COP from EnergyPlus to determine the parameters in Gordon's model:  $\Delta\dot{S}^{int}$ ,  $\Delta\dot{S}^{intQ}$ ,  $R$  and  $Q^{leak,eqv}$ . A comparison of the COP as predicted by the reformulated and modified Gordon-Ng model and as given in the DOE-2 model in EnergyPlus is shown in Figure 3.6 for 383-tons Carrier 19XR with VSD equipped centrifugal compressor. The model produces a minor error difference of less than 5%.

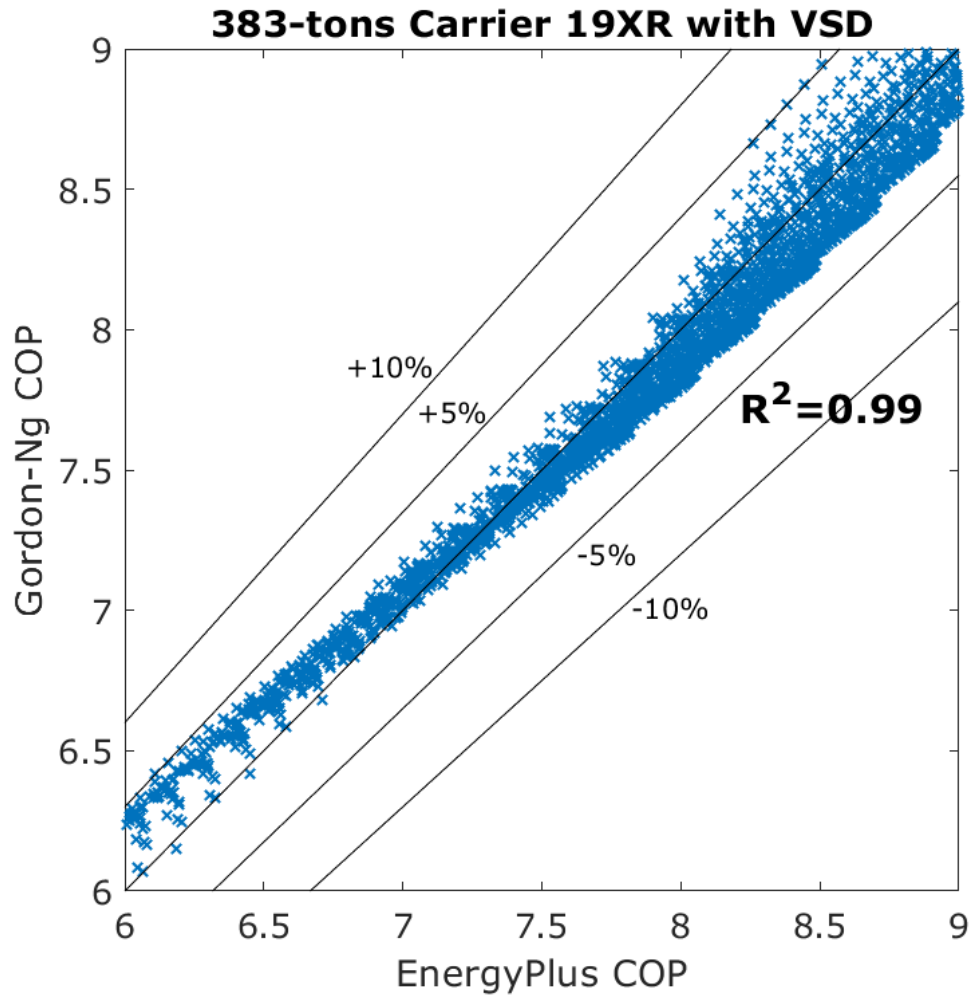


**Figure 3.6: The COP as predicted using the reformulated Gordon-Ng model compared to the COP from EnergyPlus given in a DOE-2 model for 383-tons Carrier 19XR with VSD-equipped centrifugal compressor.**

Operating conditions also influence the refrigerant thermal capacity, which impacts the chillers' cooling capacity. The evaporator refrigerant saturation density and vapor quality affect the refrigerant thermal capacity. Deviations in evaporator and condenser temperature from design conditions impact the refrigerant vapor quality in the evaporator, as illustrated in Figure 3.7 in a pressure-enthalpy diagram of the vapor compression cycle.

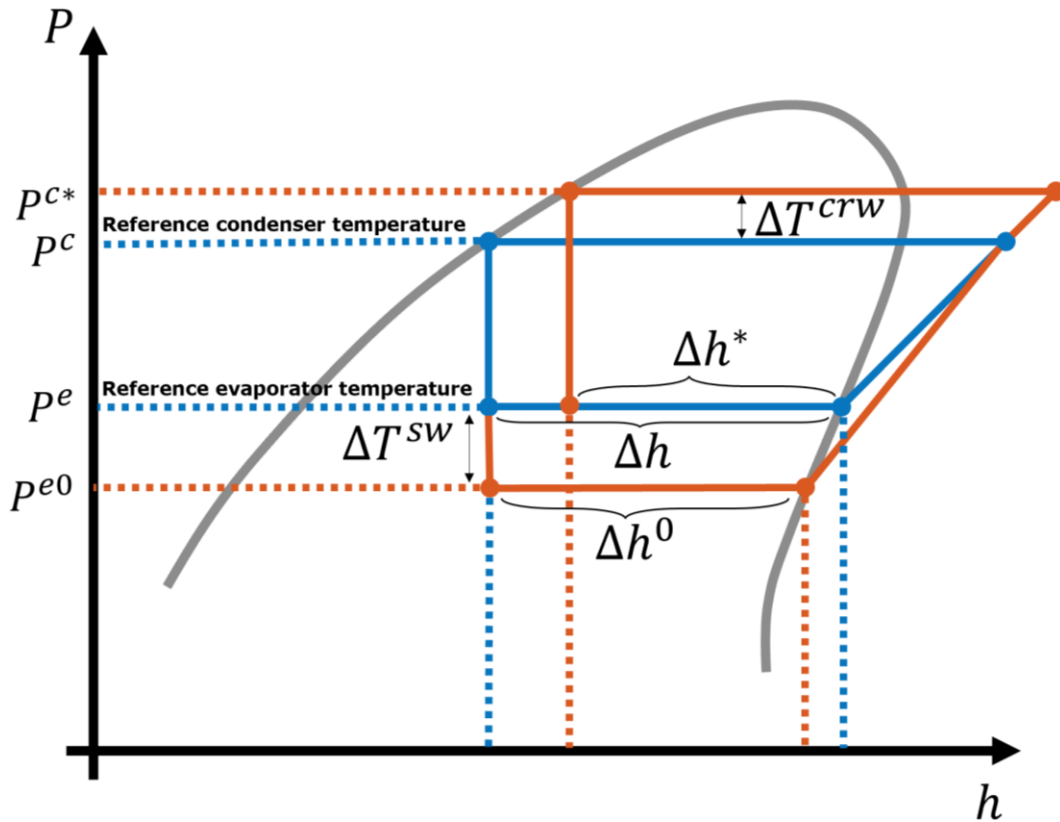


**Figure 3.7: Pressure-enthalpy diagram of vapor compression cycle demonstrating the impact of evaporator and condenser temperatures on refrigerant evaporator thermal capacity. An increase in condenser temperature or a decrease in evaporator temperature reduces the refrigerant evaporator vapor quality, reducing the heat capacity ( $\Delta h > \Delta h^*$  and  $\Delta h > \Delta h^0$ ).**

A reduction in supply temperature or an increase in condenser temperature depresses the refrigerant's thermal capacity. On the contrary, re-setting the supply temperature or reducing the condensing temperature enhances the refrigerant thermal capacity. However, the utility of the increase in evaporator heat transfer capacity is ultimately diminished by the compressor's ability to support the required flow and pressure head. Centrifugal compressors are constant pressure variable flow machines and do not experience significant gain or loss in capacity when the pressure differential is varied. On the other hand, positive displacement compressors are constant flow variable pressure machines and experience dramatic gain or loss in capacity when the pressure differential is varied [110], [111].

The evaporator saturation density, which reduces with the evaporator temperature and affects the mass flowrate, becomes the dominant factor in depressing the chiller cooling capacity in ice-making mode. Modern chillers can lose as much as 30-40% of their nominal cooling capacity when operating in ice-making mode [79]. A simple yet effective approach to estimating the chiller cooling capacity is from the refrigerant thermal capacity under the specified conditions, and the approach is useful when data is unavailable, as is the case here. Otherwise, *CAPFT* from EnergyPlus better predicts the capacity by accounting for changes to refrigerant thermal capacity and turbomachinery limitations. The cooling capacity is expressed as the ratio of available to design (nominal) cooling capacity as follows:

$$\frac{\dot{Q}_{chl,max}}{\dot{Q}_{chl,des}} = \frac{h^{refg,fg}}{h^{refg,fg,des}} \frac{1-x^{refg}}{1-x^{refg,des}} \frac{\rho^{refg}}{\rho^{refg,des}} \quad (3.12)$$

where  $h^{refg,fg}$  is the refrigerant enthalpy of vaporization,  $\rho^{refg}$  is saturated vapor density, and  $x^{refg}$  is the quality of the refrigerant vapor mixture in the evaporator. The superscript *ref* indicates values at reference conditions (reference refrigerant temperatures here). The refrigerant and water temperatures are related by the approach temperature, which is the difference between leaving water and refrigerant temperatures in the evaporator and condenser. It is in the order of 0.5-2°C for modern chillers [112], [113]. While the approach temperatures depend on the load, the variations are too small to significantly impact the chiller cooling capacity. The estimated cooling capacity ratio must not exceed the chiller's compressor capacity, which yields the following expression for the maximum chiller loading:

$$\frac{\dot{Q}_{chl,max}}{\dot{Q}_{chl,des}} = \min \left[ \frac{\dot{Q}_{chl,lim}}{\dot{Q}_{chl,des}}, \frac{h^{refg,fg}}{h^{refg,fg,des}} \frac{1-x^{refg}}{1-x^{refg,des}} \frac{\rho^{refg}}{\rho^{refg,des}} \right] \quad (3.13)$$

$\dot{Q}^{chl,lim}$  is the maximum chiller cooling rate the compressor allows under the given supply and condenser water temperature range from *CAPFT* in EnergyPlus. A comparison of predicted cooling capacity ratios and capacity ratios from EnergyPlus is in Figure 3.8 for 383-tons Carrier 19XR with a VSD-equipped centrifugal compressor. A slight absolute difference in the order of 3% is observed between the estimated and given cooling capacity ratios.

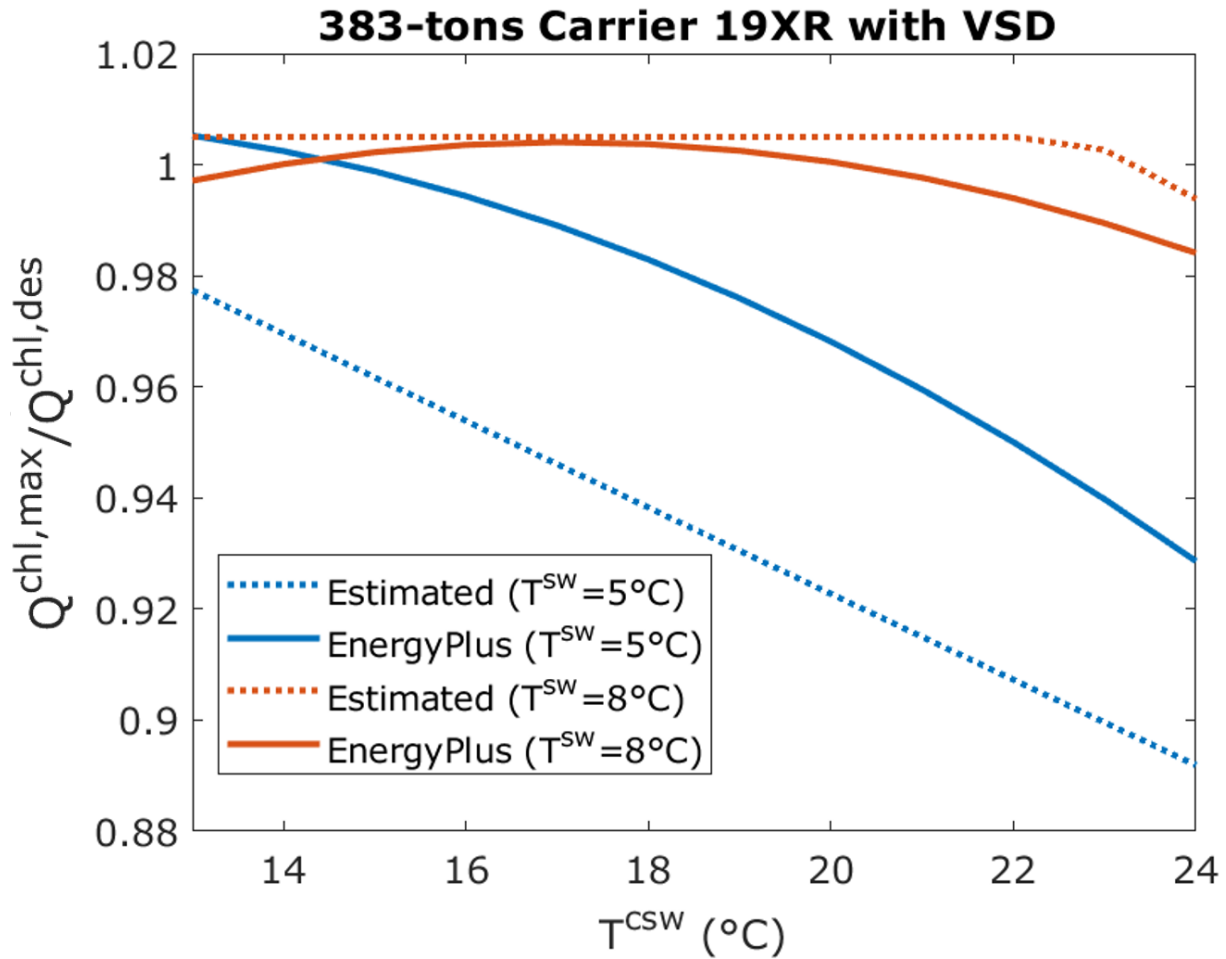


**Figure 3.8: Estimated cooling capacity ratio from refrigerant thermal capacity versus EnergyPlus for 383-tons Carrier 19XR with VSD-equipped centrifugal compressor at water supply temperature setpoints of 5 and 8°C.**



### 3.2.2 Pumps

Pumps continuously transport water to absorb and reject heat to maintain indoor comfort. Chiller pumps (primary and condenser) are fixed-speed pumps controlled to maintain the design water flowrates and only operate with their associated chiller. Conversely, secondary pumps are speed controlled to deliver the required flowrate to satisfy the building cooling load. The power consumed by pumps is a function of the flowrate and the required pressure head; the two parameters are related by affinity laws. The affinity laws express the relation between flowrate, pressure head, and power as follows:

$$\left(\frac{\dot{m}}{\dot{m}^{ref}}\right)^3 = \left(\frac{\Delta T^{ref}}{\Delta T}\right)^3 = \left(\frac{P}{P^{ref}}\right) \quad (3.14)$$

$$\left(\frac{\dot{m}}{\dot{m}^{ref}}\right)^2 = \left(\frac{\Delta T^{ref}}{\Delta T}\right)^2 = \left(\frac{\Delta p}{\Delta p^{ref}}\right) \quad (3.15)$$

where  $\dot{m}$  is flowrate,  $\Delta p$  is the pressure head,  $P$  is the power use, and  $\Delta T$  is the temperature differential which inversely correlates with flowrate. As noted from the affinity laws, a more efficient pumping configuration can be achieved by reducing the flowrate, which has a cubic relation with the power. However, the reduction of flowrates increases the temperature differential, which comes at the expense of increased chiller power as the supply temperature must be reduced to offset reduced flowrates. An analysis by chillers manufacturer Trane finds that reducing pumping power often offsets and compensates for increased chiller energy use [75]. The chiller's primary pump power as a function of temperature differential is given by:

$$P^{pp} = k^{pp,ref} \left(\frac{\Delta T^{evap,ref}}{\Delta T^{evap,des}}\right)^3 \quad (3.16)$$

and condenser pumps power use:

$$P^{cp} = k^{cp,ref} \left( \frac{\Delta T^{cond,ref}}{\Delta T^{cond,des}} \right)^3 \quad (3.17)$$

Superscripts *pp* and *cp* refer to primary and condenser pumps, respectively, and *des* refers to parameters at design conditions, and *k* is the pump constant at the reference temperature differential.  $\left( \frac{\Delta T^{evap,ref}}{\Delta T^{evap,des}} \right)^3$  and  $\left( \frac{\Delta T^{cond,ref}}{\Delta T^{cond,des}} \right)^3$  adjust the evaporator and condenser pumping power for changes in flowrate from reference conditions per the affinity laws, respectively.

The power consumed by the variable speed pumps in the secondary loop is a function of the rotational speed per the affinity laws and the motor and VSD efficiencies:

$$P^{sp} = k^{sp,ref} \left( \frac{\Delta T^{evap,ref}}{\Delta T^{evap,des}} \right)^3 \frac{(VSD^{sp})^3}{\eta^{m,sp} \eta^{VSD,sp}} \quad (3.18)$$

Superscript *sp* refers to the secondary pump, and *VSD* is the non-dimensional rotational speed defined as the actual angular speed normalized by the maximum angular speed. Speed adjustment linearly correlates with the flow and quadratically with the pressure head. Similarly,  $\left( \frac{\Delta T^{evap,ref}}{\Delta T^{evap,des}} \right)^3$  adjust the power for changes in design flowrate. The motor and variable speed drive efficiencies as a function of their speed are from correlations by Bernier and Bernard [114]:

$$\eta^m(VSD) = 0.94187[1 - \exp(-9.04 VSD)] \quad (3.19)$$

$$\eta^{VSD}(VSD) = \frac{1}{100} [50.87 + 128.3 VSD - 142 VSD^2 + 58.34 VSD^3] \quad (3.20)$$

Using a water-glycol mixture in the supply loop to prevent freezing increases pumping power by 15% relative to pure water [115] due to increased viscosity.

### 3.2.3 Cooling towers

Cooling towers reject the heat from the condenser into the atmosphere primarily by evaporative cooling. The first counter-flow cooling tower model in the literature was developed by Merkel [116] using mass and heat transfer balance equations. Merkel simplifies the model into enthalpy balance equations by setting the enthalpy difference as the driving force, neglecting mass transfer, and assuming a Lewis number of unity. The model developed by Merkel for the water and air sides is given by:

$$\frac{dh^a}{dy} = -\frac{NTU}{Y}(h^a - h^{s,w}) \quad (3.21)$$

$$\frac{dT^w}{dy} = \frac{\dot{m}^{atwr} \left( \frac{dh^a}{dy} \right)}{\dot{m}^{wtwr} c_{p,cw}} \quad (3.22)$$

where  $NTU$  is the number of transfer units,  $y$  is the height,  $Y$  is the total height of the tower,  $h^a$  is the enthalpy of moist air and  $h^{s,w}$  is the saturated enthalpy of the air,  $\dot{m}^{atwr}$  and  $\dot{m}^{wtwr}$  are the air and water mass flowrate, respectively, and  $T^w$  is the tower water temperature.

Braun et al. [117] developed a simple and widely used model based on the assumption of linear air saturation enthalpy with respect to the temperature applied to Merkel's model. An exaggerated illustration of the impact of linear saturation assumptions is shown in Figure 3.9.

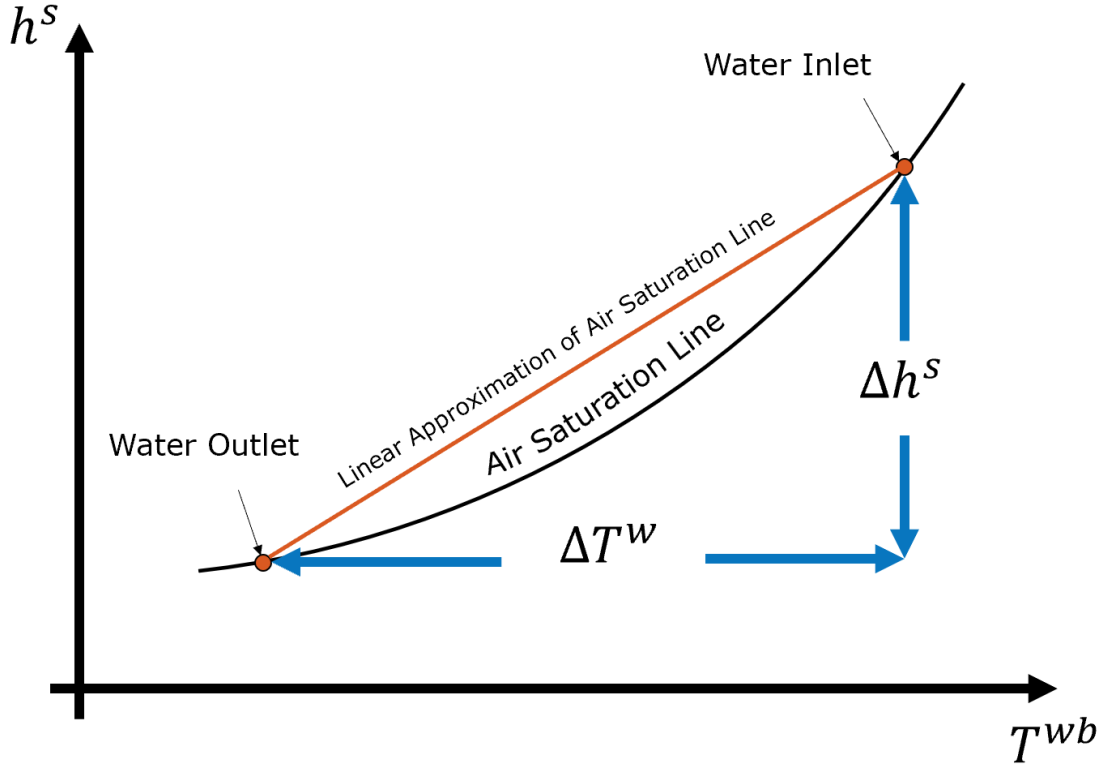


**Figure 3.9: Exaggerated illustration of the assumption of linear saturation enthalpy line with respect to temperature.  $\Delta T^w$  is the tower water temperature difference,  $\Delta h^s$  is the tower air enthalpy difference,  $h^s$  is air saturation enthalpy, and  $T^{wb}$  is the wet-bulb temperature.**

The slope of the saturation line with respect to temperature is defined as the saturation specific heat as follows:

$$c^s = \left[ \frac{dh^s}{dT} \right]_{T=T^w} = \frac{h^{s,crw} - h^{s,csw}}{T^{crw} - T^{csw}} \quad (3.23)$$

where  $T^{csw}$  and  $T^{crw}$  are tower leaving (entering chiller condenser water) and tower entering (leaving chiller condenser water), and  $h^{s,csw}$  and  $h^{s,crw}$  are the enthalpy of saturated air at leaving and entering tower water temperatures, respectively. Plugging Equation (3.23) in Merkel's model in Equation (3.22) allows for an analytical solution to be obtained. Braun derives an effectiveness relationship in terms of saturation specific heat, defined as the ratio of actual to

maximum possible air-side heat transfer that occurs if air leaves saturated at the inlet water temperature. The model uses the NTU-effectiveness approach to predict the heat rejected given inlet air and water mass flowrates and temperatures. The actual heat rejected is given by:

$$\dot{Q}^{twr} = \dot{m}^{atwr} \varepsilon^{twr} (h^{s,crw} - h^{s,wb}) \quad (3.24)$$

$h^{s,wb}$  is the enthalpy of saturated air at the wet-bulb temperature and  $\varepsilon^{twr}$  is the tower's air-side effectiveness. The effectiveness is determined analogously to a dry counter-flow heat exchanger:

$$\varepsilon^{twr} = \frac{1 - \exp(-NTU(1 - C^r))}{1 - C^r \exp(-NTU(1 - C^r))} \quad (3.25)$$

where,

$$C^r = \frac{\dot{m}^{atwr}}{\dot{m}^{wtwr} \left( \frac{c^p, cw}{c^s} \right)} \quad (3.26)$$

The NTU correlation for the cooling tower:

$$NTU = c \left( \frac{\dot{m}^{wtwr}}{\dot{m}^{atwr}} \right)^{1+n} \quad (3.27)$$

where  $c$  and  $n$  are constants for a given cooling tower type. Similar to water pumps, the air flowrate varies linearly with the speed of the fan per the affinity laws, which are given by:

$$\dot{m}^{atwr} = VSD^{twr} \dot{m}^{atwr, des} \quad (3.28)$$

The tower fan is the sole power-consuming device controlled to maintain the condenser water temperature setpoint. The power consumed by the VSD-equipped tower fan is as follows:

$$P^{twr} = k^{twr} \frac{(VSD^{twr})^3}{\eta^{m,twr} \eta^{VSD,twr}} \quad (3.29)$$

where  $k^{twr}$  is the tower fan constant and  $VSD^{twr}$  is the fan's non-dimensional rotational speed.

### 3.2.4 Cooling and dehumidifying coils

Sensible and latent heat from the cooled space is transferred by air to the chilled water in the coils. The developed coil model employs Wang et al. [118] expressions for the overall internal and external heat transfer coefficients. The expressions are converted into an external and internal NTU expression, respectively, as follows:

$$NTU^{ext} = \frac{1}{\dot{m}^{cca} c^{p,a}} \frac{N^{row} A^{face}}{a_1^{cc} (V^a)^{-0.8} + a_3^{cc}} \quad (3.30)$$

$$NTU^{int} = \frac{1}{\dot{m}^{ccw} c^{p,sw}} \frac{N^{row} A^{face}}{a_2^{cc} (V^w)^{-0.8}} \quad (3.31)$$

The denominators of the two expressions are based on Holmes coil's thermal resistance model as a function of air and water face velocities [119].  $a_1^{cc}$ ,  $a_2^{cc}$ , and  $a_3^{cc}$  are experimentally obtained set of coefficients in Holmes's model,  $\dot{m}^{cca}$  and  $\dot{m}^{ccw}$  are the coil air and water flowrate,  $V^a$  and  $V^w$  are the coil air and water face velocities, respectively,  $c^{p,a}$  is air specific heat capacity,  $A^{face}$  is the coil face area, and  $N^{row}$  are the number of coils rows or passes.

Coils maintain the cooled-space humidity and temperature by regulating air and water flowrates using a VSD and a two-way valve. Per the affinity laws, the air and water mass flowrates, respectively, are as follows:

$$\dot{m}^{cca} = VSD^{cf} \dot{m}^{cca,des} \quad (3.32)$$

$$\dot{m}^{ccw} = VSD^{sp} \dot{m}^{ccw,des} \quad (3.33)$$

Similarly, for face air and water velocities, respectively:

$$V^a = VSD^{cf} V^{a,des} \quad (3.34)$$

$$V^w = VSD^{sp} V^{w,des} \quad (3.35)$$

where  $VSD^{cf}$  and  $VSD^{sp}$  are the non-dimensional rotational speed for coil fan and secondary pumps, respectively. The air inlet enthalpy and temperature can then be calculated from the known exit conditions and the cooling load:

$$h^{ai} = \min \left[ h^{ae,des} + \frac{\dot{Q}^D}{\dot{m}^{cca}}, h^{ai,des} \right] \quad (3.36)$$

$$T^{ai} = T^{ae,des} + \frac{\dot{Q}^s}{\dot{m}^{cca}} \quad (3.37)$$

$\dot{Q}^D$  is the building cooling load,  $\dot{Q}^s$  is the sensible cooling load,  $h^{ai,des}$  is the enthalpy of air at the coil inlet under design conditions, and  $h^{ae,des}$  and  $T^{ae,des}$  are the design exit air enthalpy and

temperature, respectively. The conditions at the dry-to-wet transition point can be calculated from the known air and water boundary conditions:

$$h^x = h^{ai} - c^{p,a}(T^{ai} - T^{dp}) \quad (3.38)$$

$$T^{w,x} = \frac{\dot{m}^{cca}}{\dot{m}^{ccw} c^{p,sw}} [h^{ai} - h^{ae,des} - c^{p,a}(T^{ai} - T^{dp})] + T^{ccsw} \quad (3.39)$$

where  $T^{ccsw}$  is the coil entering water temperature and  $T^{dp}$  is the dew-point temperature. The superscript  $x$  represents the point of intersection between dry and wet sections. The air temperature at the dry-to-wet transition is the dew point temperature and is calculated from known parameters.

Models developed by Braun et al. [85] for fully dry and fully wet coils based on the NTU-effectiveness approach are used for the dry and wet section analysis. They utilize a similar approach to the modeling of the cooling tower with the modification of including an additional thermal resistance from the absence of direct contact between air and water streams. The coil is modeled as a counter-flow heat exchanger since the performance of a cross-flow heat exchanger approaches that of a counter-flow when the number of passes increases beyond approximately four. The NTU and effectiveness for the dry section are described by the following two expressions:

$$NTU^{dry} = \frac{1}{c-1} \ln \left( \frac{\varepsilon^{dry}-1}{C\varepsilon^{dry}-1} \right) \quad (3.40)$$

$$\varepsilon^{dry} = \frac{T^{ai}-T^{dp}}{T^{ai}-T^{w,x}} \quad (3.41)$$



where,

$$C = \frac{\dot{m}^{cca} c_{p,a}}{\dot{m}^{ccw} c_{p,sw}} \quad (3.42)$$

Exit water temperature and the fraction of the coil length in the dry section are as follows:

$$T^{ccrw} = T^{w,x} + C(T^{ai} - T^{dp}) \quad (3.43)$$

$$f^{dry} = \frac{NTU^{dry}}{NTU^{ext}} \left( 1 + C \frac{NTU^{ext}}{NTU^{int}} \right) \quad (3.44)$$

The NTU and effectiveness for the wet section are as follows:

$$NTU^{wet} = \frac{NTU^{ext}}{1 + m \left( \frac{NTU^{ext}}{NTU^{int}} \right)} (1 - f^{dry}) \quad (3.45)$$

$$\varepsilon^{wet} = \frac{1 - \exp(-NTU^{wet}(1-m))}{1 - m \exp(-NTU^{wet}(1-m))} \quad (3.46)$$

where,

$$m = \frac{\dot{m}^{cca}}{\dot{m}^{ccw} c_{p,sw}} \left( \frac{h^x - h^{s,ccsw}}{T^{w,x} - T^{ccsw}} \right) \quad (3.47)$$

$h^{s,ccsw}$  is the enthalpy of saturated air at coil supply water temperatures. The actual exit air enthalpy can then be calculated as follows:

$$h^{ae} = h^x - \varepsilon^{wet} (h^x - h^{s,ccsw}) \quad (3.48)$$

A feasible solution necessitates the air leaves at design conditions such that  $h^{ae} \equiv h^{ae,des}$ . The power required by the VSD-equipped cooling coil fan is given by:

$$P^{cf} = k^{cf} \frac{(VSD^{cf})^3}{\eta^{m,cf} \eta^{VSD,cf}} \quad (3.49)$$

where  $k^{cf}$  is the cooling coil fan constant.

### 3.2.5 I-TES

I-TES stores thermal energy mainly in the form of latent heat. The two main types of I-TES are internal and external melt [87]. In external melt, ice comes into direct contact with supply water delivering a rapid discharge rate suitable for specific applications such as providing contingency and for high and short-lasting cooling demands. On the other hand, internal melt I-TES is modularized and prefabricated with predictable charge and discharge behavior. In internal melt, a secondary water-glycol mixture is circulated through inner circuits to freeze or melt the water inside the tank. An illustration of a modular internal melt I-TES is shown in Figure 3.10.

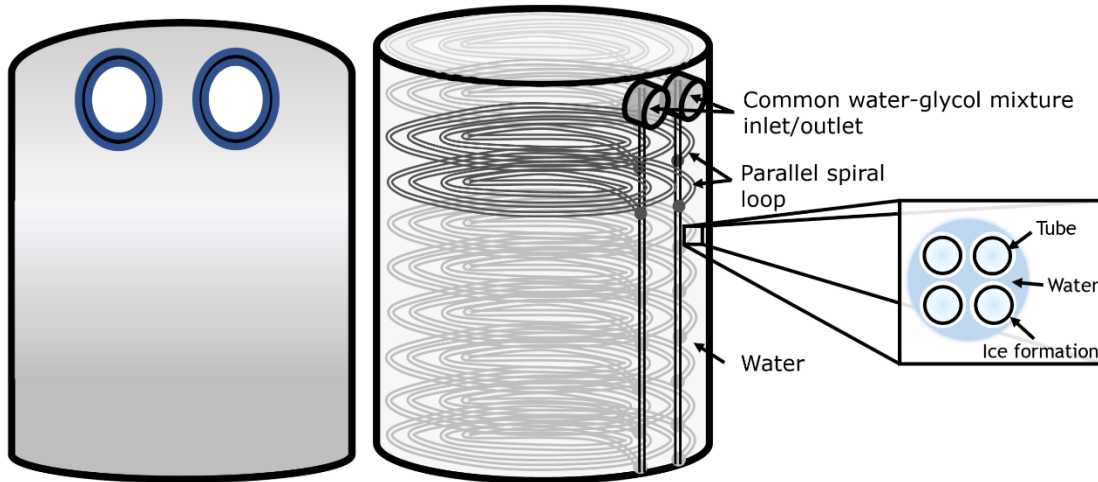


**Figure 3.10: An illustration of a modular internal-melt I-TES. Multiple parallel spiral circuits are submerged in water inside the tank, and a water-glycol mixture is circulated through the circuits to build and melt the ice around the tubes.**

As shown in the figure, multiple parallel spiral circuits are submerged in water inside the tank. Internal melt I-TES can have either fewer circuits with longer tubes or more circuits with shorter ones. I-TES with longer tubes is designed for systems with reduced flowrate to maximize heat transfer, whereas shorter tubes is used for systems with high available flowrate to maximize charge and discharge rates without overburdening the pumps.

The work in this dissertation utilizes the more commonly used internal melt I-TES with fewer circuits and longer tubes. The earliest internal melt I-TES model appears to be developed by Jekel [71] and was later improved by Drees [72], [73]. The work in this dissertation employs the model improved by Drees with specifications based on a product of CALMAC with 83 TR-hr of nominal capacity. Multiple tanks can be balanced and joined in parallel to act as a single tank with an equivalent combined thermal capacity. Control of the ice bank is accomplished by regulating the inlet temperature and flowrate as described by the heat balance equation below:

$$\dot{m}^{iw} c^{p,sw} (T^{irw} - T^{isw}) = \dot{H} = h^{sf} \dot{m}^{ITES,ice} - m^{ITES} c^{p,w} \dot{T}^{ITES} \quad (3.50)$$

where  $\dot{m}^{iw}$  is the circulating water-glycol mix flowrate,  $T^{isw}$  and  $T^{irw}$  is the water-glycol mixture temperature at the inlet and outlet of the storage tank, respectively,  $h^{sf}$  is the enthalpy of fusion of ice,  $\dot{m}^{ITES,ice}$  is the rate of ice formation,  $\dot{T}^{ITES}$  is the rate of change of water temperature in the tank,  $m^{ITES}$  is the total mass of water in the tank, and  $c^{p,w}$  is the specific heat of tank water. The terms  $\dot{m}^{iw} c^{p,sw} (T^{irw} - T^{isw})$  is the heat transfer rate to the circulating water-glycol mixture,  $m^{ITES,w} c^{p,w} \dot{T}^{ITES}$  is the sensible heat rate, and  $h^{sf} \dot{m}^{ITES,ice}$  is the latent heat rate. Sensible heat change of ice can be neglected because of the reduced thermal capacity relative to water and the minor temperature difference between ice and the freezing point of

water. The rate of change of enthalpy,  $\dot{H}$ , can also be obtained from the LMTD method as follows:

$$\dot{H} = \left( \frac{1}{R^{int} + R^{ext}} \right) \left[ \frac{T^{irw} - T^{isw}}{\ln \left( \frac{T^{ITES} - T^{irw}}{T^{ITES} - T^{isw}} \right)} \right] \quad (3.51)$$

$T^{ITES}$  is the average storage water temperature,  $R^{int}$  and  $R^{ext}$  are tubes' internal and external thermal resistance.  $R^{ext}$  depends on both the mode of operation, charging or discharging, and SoC; both  $R^{int}$  and  $R^{ext}$  are obtained from Drees's model [72], [73].

The charging of I-TES is divided into three stages, which are shown in Figure 3.11: sensible, unconstrained latent, and area-constrained latent. In sensible charging, the water temperature in the tank is brought down to freezing temperature without ice formation and constitutes about 10% of capacity. Upon reaching freezing temperature, the unconstrained latent stage initiates with uniform cylindrical ice formation around the tubes up to an SoC of 45%. Once the ice formations intersect, heat transfer becomes increasingly area constrained until all the water around the tubes is frozen. Charging of I-TES terminates once the areas around the tubes are fully frozen, which constitutes about 90% of the total water mass.

Similarly, discharging of I-TES is divided into three stages, also shown in Figure 3.11: unconstrained latent, area-constrained latent, and sensible. In the first stage, the ice closest to the tube is melted. The water-glycol mixture passing through the tubes is cooled down at the expense of (i) warming a layer of liquid water between the outer surface of the tube and the water-ice interface and (ii) a receding liquid water-ice interface. When the ice-liquid water interfaces intersect at an SoC of 60%, heat transfer reduces due to the reduced surface area of ice formations. Once all ice has melted, the storage water temperature is gradually brought to the

circulating water temperature constituting only 5% of the thermal capacity, which ends the discharging process.

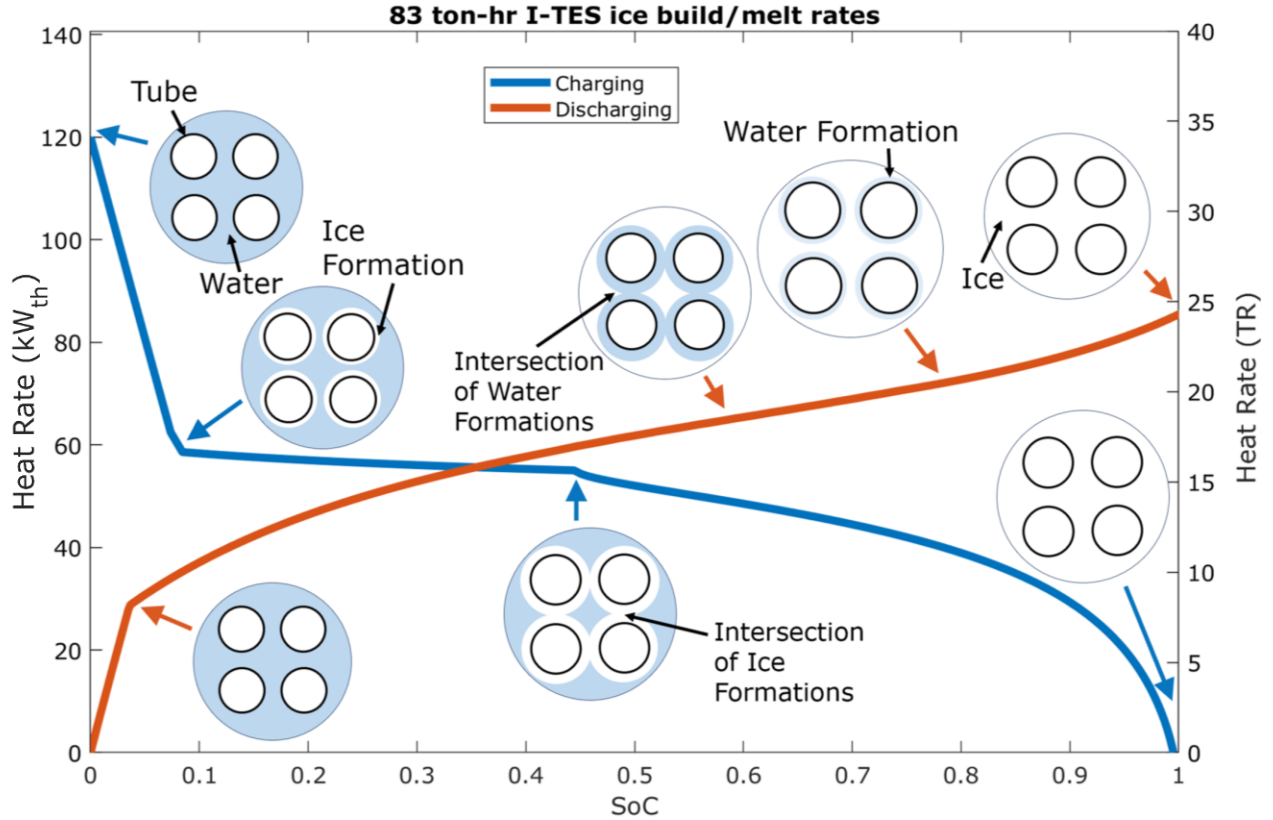


**Figure 3.11: An illustration of the charging and discharging process along the heat rate curve is shown in a cross-sectional view of the parallel tubes inside the 83-TR-hr internal melt I-TES tank. The intersection of ice formations in charging and water formations in discharging reduces the heat transfer area. Charging is at -6°C and 4 kg/s, and discharging is at 8°C and 4 kg/s.**

Drees shows that the effectiveness defined as the ratio of actual to the maximum temperature difference is insensitive to inlet temperature but is a strong function of flowrate and SoC. This is used to reduce the storage model to a function of flowrate and stage of charge. The storage effectiveness is defined as:

$$\varepsilon^{ITES} = \frac{T^{isw} - T^{irw}}{T^{isw} - T^{ITES}} \quad (3.52)$$

where  $T^{ITES}$  is the average storage water temperature in sensible charging mode, otherwise,  $T^{ITES}$  is the freezing temperature of water for all other stages. An effectiveness surface is generated from the simulation of full charge and discharge cycles at multiple increments of flowrates to obtain a function of the form:

$$\varepsilon^{ITES} = f\left(SoC, \dot{m}^{iw}, sgn(\Delta SoC)\right) \quad (3.53)$$

where  $sgn(\Delta SoC)$  is the storage operation mode. The effectiveness for all flowrates in-between the increments is linearly interpolated. Three parameters index the generated surface: the SoC, the inlet water-glycol mixture flowrate, and the mode (charging/discharging). Simulation of I-TES charge and discharge cycles under different water-glycol mixture flowrates and inlet temperatures are shown in Figure 3.12 (a) and (b) for charging and Figure 3.12 (c) and (d) for discharging. Note that the difference in effectiveness due to inlet temperature is negligible. Furthermore, daily storage use requires an inlet temperature close to -6°C, which can significantly depress chiller performance by 20-35% and cooling capacity by 30-40% relative to refrigeration mode.

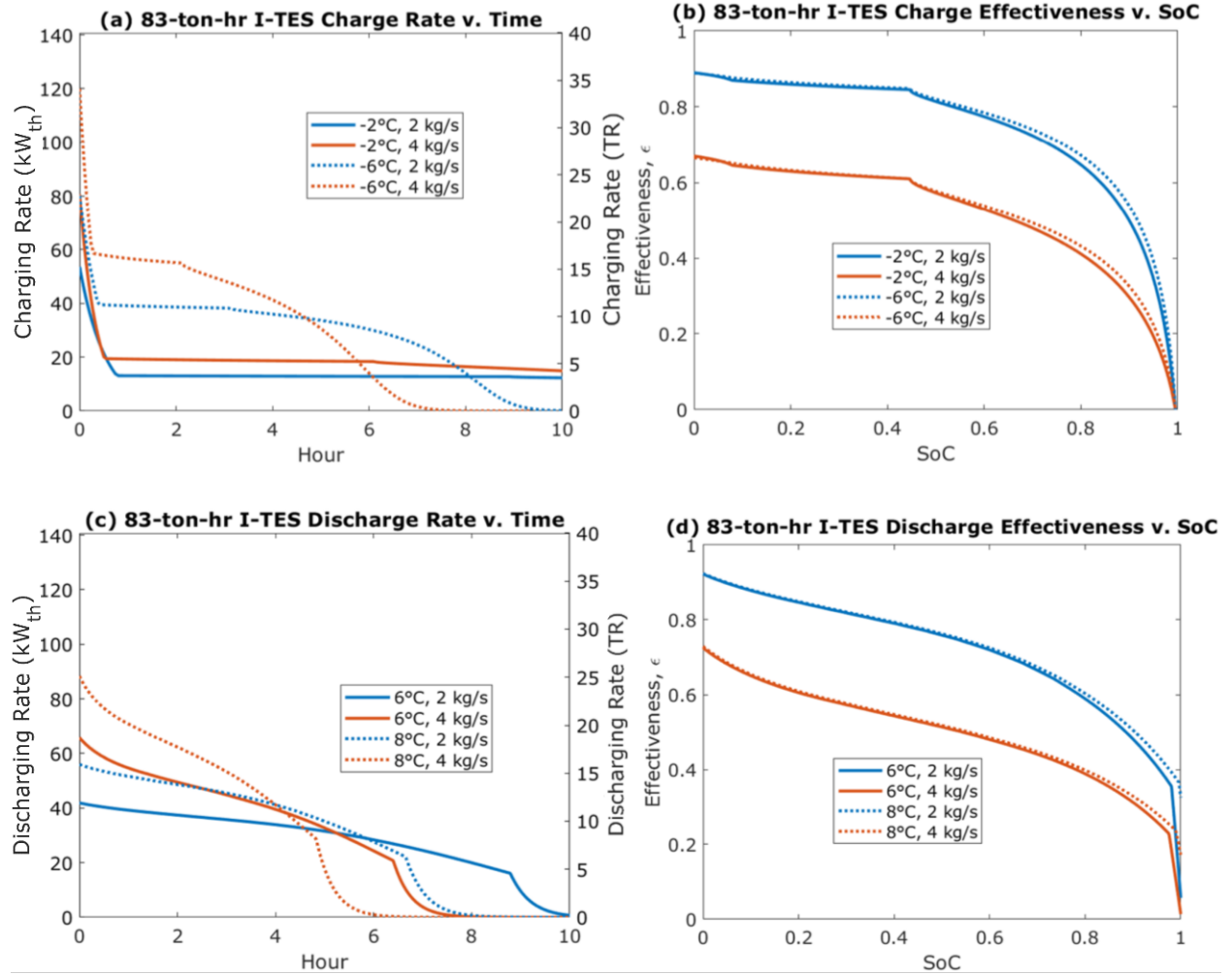


**Figure 3.12: Simulation of I-TES operation under different inlet conditions for charge mode with (a) charging rate and (b) charging effectiveness, and discharge mode with (c) discharge rate and (d) discharging effectiveness. I-TES is fully charged at an SoC of 1 and fully discharged at 0.**

### 3.3 Conclusion

This chapter develops hybrid steady-state models for the major components in CWS in a primary-secondary configuration with WC chillers, cooling towers, and internal melt I-TES.

Hybrid models combine the efficiency of data-driven models with the physical insight of physics-based models in a simpler formulation. This simpler formulation is achieved with empirically attained parameters that capture complex behavior that would otherwise be difficult to model physically accurately. A reformulated Gordon-Ng model was used to predict chillers'

performance, and their cooling capacity is estimated from the evaporator refrigerant thermal capacity. Analogous to the analysis of heat exchangers, the effectiveness approach is used for cooling coils, cooling towers, and I-TES. Fan and pumps are modeled using the simple fan and pump power law equations with pressure and flowrate modulation per the affinity laws. The models thus developed are applied to the equipment capacity sizing and design problem analyzed in Chapter 4 and dispatch and scheduling problems analyzed in Chapter 5.



# **Chapter 4: Design of an integrated WC CWS with I-TES, BESS, and on-site PV**

## **4.1 Introduction**

The decarbonization pathway analyzed in Chapter 2 from a utility-scale perspective must eventually be implemented on buildings with distinct energy needs, either as a part of the large-scale deployment or building-scale solution to reduce emissions and electricity charges. This chapter examines the design problem of an integrated WC CWS with I-TES and BESS for better integration with on-site PV generation for cost and emissions reduction. The objective is to develop an optimization strategy for optimal equipment capacity sizing with greater consideration of the complex behavior and performance of CWS with I-TES than given in the literature, which includes deciding chillers' quantities, capacities, as well as compressor technology. The site analysis also provides insight into the distributed-scale renewable penetration and building emission reduction potential and examines how I-TES and BESS behave on a building scale. The role of carbon pricing policy instrument is re-examined to combat low electricity rates in Qatar.

Two large generic buildings are examined for the optimization problem with dissimilar demand profiles: a residential building with dominant night-time electricity needs and a commercial building with diurnal cooling and electricity needs. These two buildings represent the two most common types of buildings in Qatar. The examination of large buildings serves two purposes, (i) large buildings in Qatar utilize WC CWS, which enables exploring the more complex version of the problem due to additional equipment such as cooling towers; (ii) large systems achieve higher returns and emissions reduction and are a primary target for decarbonization.

The standard approach for designing a cooling system is based on peak cooling demand day (design day) and energy standards [120]. More sophisticated approaches consider the intra-annual variation of cooling load using energy simulation tools [121] and the uncertainty of peak load from internal generation [122]. A more careful examination of part-load performance, intra-annual ambient temperature variations, and pump energy use can significantly reduce CWS's yearly energy consumption [123], [124]. That is partly because CWS are often operated away from the design point due to reduced cooling demands, leading to sub-optimal operations that conventional design methods do not adequately address. This issue can be further propagated when cooling systems are oversized due to parasitic loads.

With hot summer and mild winter, the cooling load in Qatar is highly seasonal. Highly seasonal space-cooling accounts for most energy consumption in buildings in Qatar [20], [21]. Although the high seasonality naturally leads to a large sum of idle chiller capacity in the low cooling demand season, which could be used to store ice, the potential has not been investigated in the literature prior to this work. However, the capacity sizing problem of on-site PV generation with BESS has been examined [34], [35]. The studies find BESS economically unfavorable at the current subsidized electricity tariffs.

Otherwise, the analysis of building-scale PV with BESS and thermal energy storage falls under the smart building energy management systems problem, which is broadly investigated in the literature with varying degrees of complexity [74], [125]–[129]. Many studies recognize the potential of using I-TES for cost reduction but find BESS cost prohibitive. Deetjen et al. [74] developed a mixed-integer linear programming model for optimal dispatch and sizing of a residential central utility plant with a rooftop PV generation, shared I-TES, and BESS. The model accounts for chillers' performance degradation from ambient conditions and in ice-making

mode. Although the study finds cost reduction potential from the examined system, BESS was still determined to be economically unfavorable. Baraa et al. [129] analyzed micro-grid design with BESS and I-TES applied to a commercial building in the UAE, which shares a similar climate as Qatar, using a heuristically developed optimization strategy. The I-TES model was extracted from EnergyPlus, with linearized charge/discharge limits with respect to the storage SoC. Baraa concludes that I-TES further reduces the cost compared to BESS alone. Zhu et al. [130] proposed a bi-level optimization strategy to optimize electric and thermal energy storage capacity in buildings with a chilled water system. The upper level decides the capacities fed to a lower level to solve the dispatch problem and returns the operation cost. The optimization strategy utilizes the genetic algorithm for the upper level and mixed-integer linear programming with a piecewise linearized chiller model for the lower level. The study suggests that energy storage can significantly reduce cost and increase renewable penetration in the grid from load shifting. Xu et al. [131] developed a two-stage stochastic linear model for capacity and dispatch optimization of building-scale PV combined with BESS, I-TES, and heat storage. They consider a simple linear I-TES model with a single chiller. Xu finds TES to be economically favorable whereas BESS is not always feasible due to its higher cost and short life span.

This chapter is structured as follows: Section 4.2 describes the methodology. First, cooling and electric loads are simulated for two generic buildings with dissimilar energy demand profiles. Next, the optimization strategy is developed, followed by the problem formulation. Section 4.3 presents and discusses the model results for the two buildings exposed to a range of carbon pricing. The chapter is summarized and concluded in Section 4.4.

## 4.2 Methodology

The main framework is to design a WC CWS with I-TES and BESS for a building to allow for better integration of on-site PV generation. The on-site PV generation is utilized to meet daytime electricity and cooling needs. Excess generation can be stored in I-TES and BESS to supplement nighttime electricity and cooling needs; unutilized excess generation is curtailed and cannot be sold to the power grid. Figure 4.1 shows a simplified schematic of the design problem. As modeled in Chapter 3, the WC CWS is in a primary-secondary configuration. Due to the overlap of cooling needs with the solar insolation, chillers' cumulative cooling capacity can exceed the building's peak cooling load to allow for ice-making during the day.

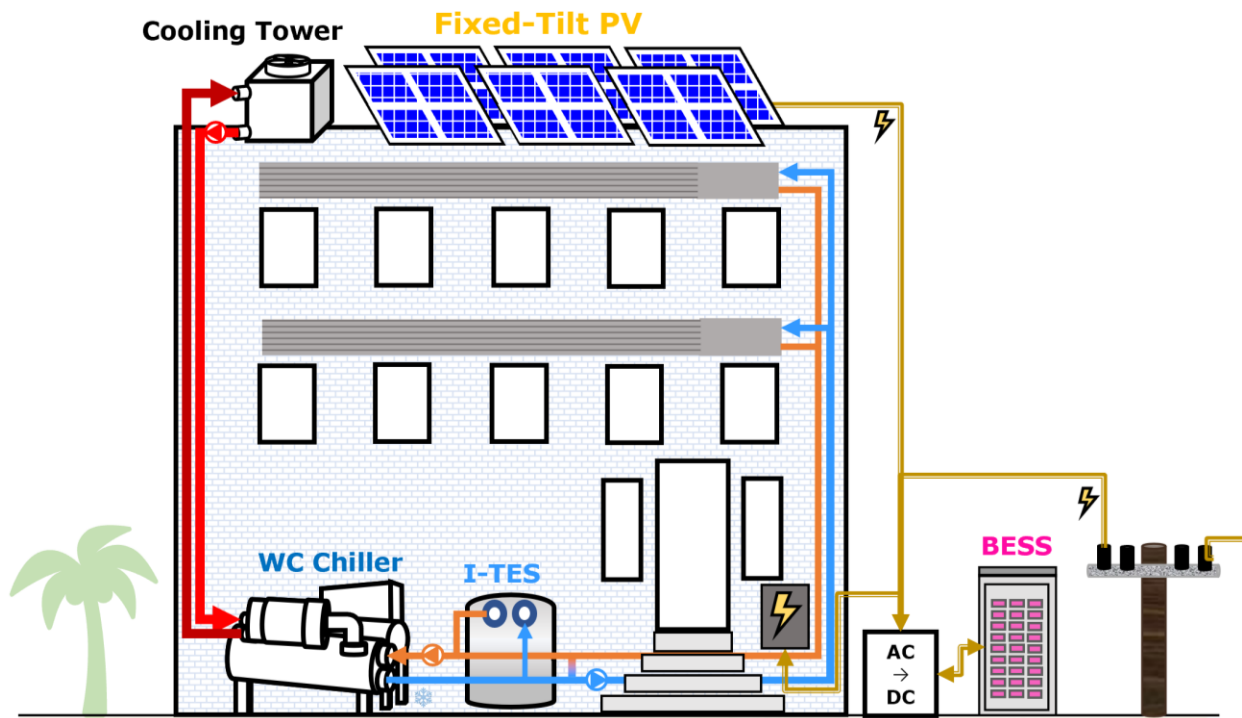


**Figure 4.1: A schematic of an integrated WC CWS with I-TES, BESS, and on-site PV generation.**

### 4.2.1 Simulation of building cooling and electric loads

A Building's cooling load is influenced by the interaction of weather with the building envelope, occupancy and occupants' activity level, and electric loads. The estimated cooling load in Chapter 2 is an aggregate load from all buildings with various uses, occupancy levels, and envelope constructions. Individual building cooling needs can radically deviate from the behavior of the aggregate load.

In the literature, simulation methods of building cooling load can be classified into three categories [132]: (i) energy simulation models, (ii) data-driven models, and (iii) hybrid models. Energy simulation models are performed using software tools such as EnergyPlus, TRANSYS, and eQuest. They require complete knowledge of building envelope construction, orientation, and materials [133], [134]. They are often used for more sophisticated estimations of cooling loads that are not required for the analysis in this chapter. Data-driven models drive patterns from historical data using meteorological and occupancy data [135], [136], which Qatar lacks. Hybrid models, on the other hand, simplify the building description in heat models and are used for optimization problems [137], [138]. The simplification is achieved using (i) parameters that simplify the building description, such as thermal resistance, and (ii) general assumptions are made for building orientation and geometry. The hybrid model approach is used in this dissertation to simulate buildings cooling load profiles. The intention is to capture diurnal and interannual demand profiles for generic buildings in Qatar without explicit knowledge of building interior zoning, orientation, and construction details that would be required with energy simulation software. Nevertheless, the simulated load was validated using EnergyPlus building simulation software with arbitrarily decided building orientation and geometry, producing a comparable estimate.

In this chapter, the cooling load for a high rise (30-stories; gross floor area of 60,000 m<sup>2</sup>) is simulated using heat balance equations for two cases: (i) residential buildings with dominant nighttime electricity needs and (ii) commercial buildings with diurnal cooling and electricity needs. Details of the performed cooling load simulation and electric load estimation can be found in Appendix A. The building's electric load is estimated from the assumed occupancy level for different hours of the day with the typical energy use from appliances and devices. Both simulated residential and commercial buildings have a yearly cooling need of 19.5 GWh<sub>th</sub> (325 kWh<sub>th</sub>/m<sup>2</sup>) using the 2016 meteorological data and electricity use of 4.5 GWh (75 kWh/m<sup>2</sup>). Although meteorological conditions still drive seasonal variations, daily variations can be anti-correlated as people move between the two spaces, from their residences to their places of work and later back to their residences. These daily differences in cooling and electricity needs can influence the storage needed for load shifting. Buildings with more dominant diurnal electricity and cooling needs can benefit from better alignment with PV generation and require less storage capacity. The resultant estimated cooling intensity (cooling load normalized by floor area) agrees with the reported data in the literature when assuming a nominal AC system COP of 2.5-3.

Household electricity consumption in Qatar has only been reported in the literature a few times [20], [139], and they combine electric loads from all appliances and devices. Nevertheless, the electric load from space-cooling can be crudely estimated by deducting the electric load on non-cooling days or days with minimal cooling needs. Driven by space-cooling, about a 5-fold increase in electricity load is observed between winter and summer. Furthermore, demand spikes are observed in the morning between 5 and 7 AM, late afternoon between 3 and 5 PM, and evening between 6 and 9 PM, which correlates with building occupancy. These reported data and demand profiles are used in constructing the building's electric load. Simulated cooling loads for

three days in winter, spring, and summer are shown in Figure 4.2 for the residential building and Figure 4.3 for the commercial building.

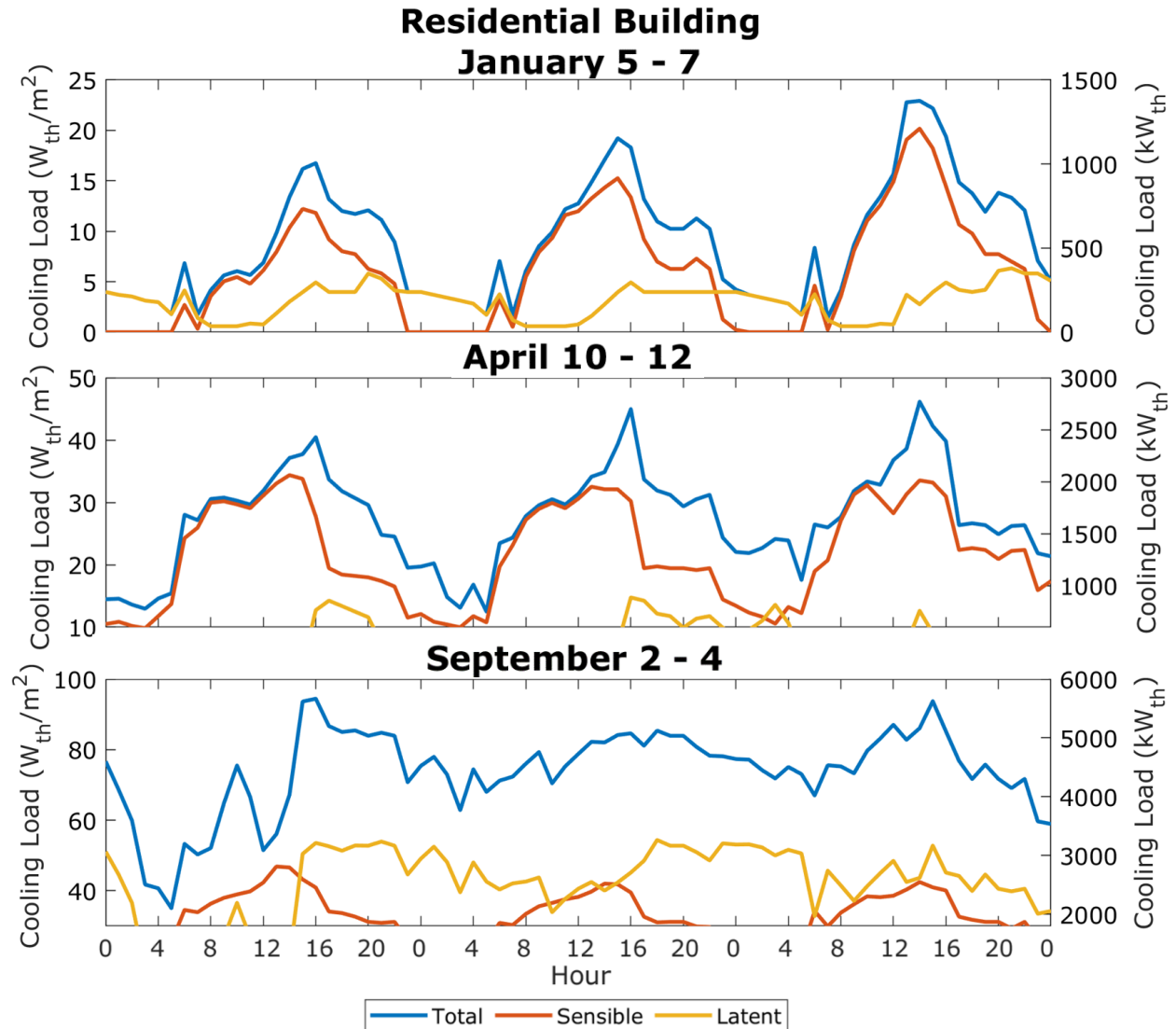


**Figure 4.2: Simulated residential building cooling load for three days in winter, spring, and summer using the 2016 meteorological data. Electric and thermal loads are correlated with higher building occupancy in the evening.**

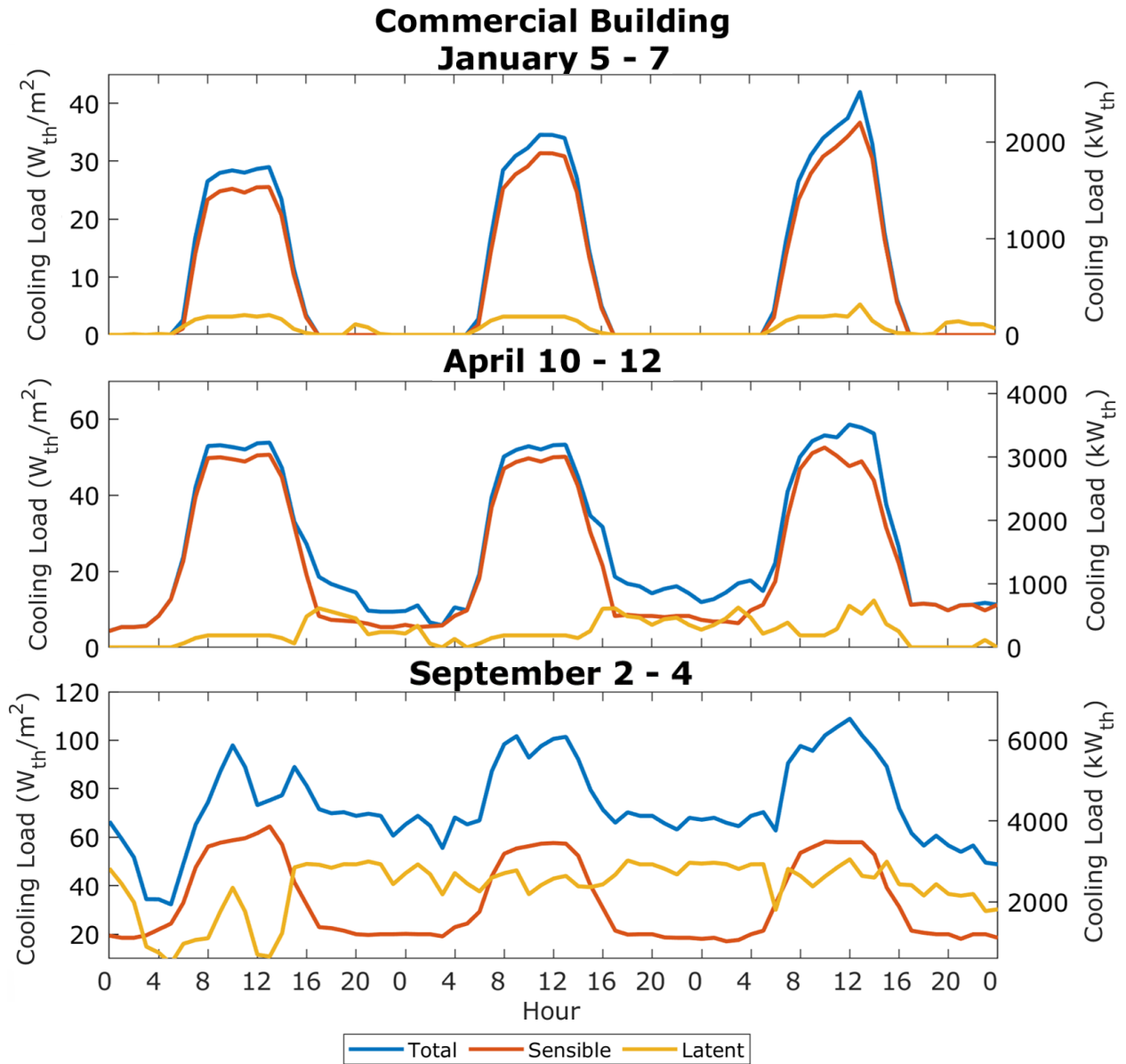


**Figure 4.3: Simulated commercial building cooling load for three days in winter, spring, and summer using the 2016 meteorological data. Electric and thermal loads are correlated with higher building occupancy during the day.**



### 4.2.2 Optimization strategy

The equipment capacity sizing problem entails evaluating equipment performance and estimating their energy use, which requires solving the scheduling and dispatch problem. The scheduling and dispatch problem is highly non-linear, stemming from the interaction of multiple decision variables, and involves many decision variables at each time step. For example, WC chiller power use is a function of 4 parameters at each time step: supply temperature setpoint ( $T^{sw}$ ), entering condenser temperature ( $T^{csw}$ ), loading ( $PLR$ ), and the on/off switch ( $ON^{chl}$ ), in addition to the chiller capacity decision variable ( $Q^{chl,des}$ ). Likewise, I-TES charge and discharge rates are a function of 3 parameters at each time step: the inlet temperature ( $T^{isw}$ ), supply flowrate ( $\dot{m}^{iw}$ ), and the state of charge ( $SoC$ ), in addition to the storage capacity decision variable represented as the number of modular tanks ( $N^{ITES}$ ).

A problem with this level of complexity is extremely computationally demanding to be solved using traditional gradient-based non-linear optimization strategies or more tolerant meta-heuristics optimization algorithms. The approach is to decompose the problem into a bi-level formulation to reduce the problem's complexity and simplify the components model, particularly the chiller and I-TES models. The decomposition of the problem into bi-level formulation enables decoupling the capacity sizing problem from the scheduling and dispatch problem. The scheduling and dispatch problem, used to estimate electricity charges, can be simplified in a mixed-integer linear program with piecewise linearized performance curves. Mixed-integer linear programs are a more complex form of linear programming, and they retain some of their desirable advantages, such as the ability to solve large problems with many variables and the guaranteed optimality.

A flowchart of the developed bi-objective optimization strategy is shown in Figure 4.4. The upper level minimizes annual system expenditures and decides the installed capacities of chillers, BESS, I-TES, and on-site PV using a non-linear optimizer. Piece-wise linearization is applied to the simulated components' performance curves to obtain each segment's slopes and intercepts. The slopes and intercepts of the piece-wise linear segments are then fed to the mixed-integer linear program in the lower level to solve the equipment scheduling and dispatch problem and return electricity charges. The returned electricity charges to the upper-level optimizer are used to update the capacities decision variables for the next iteration.

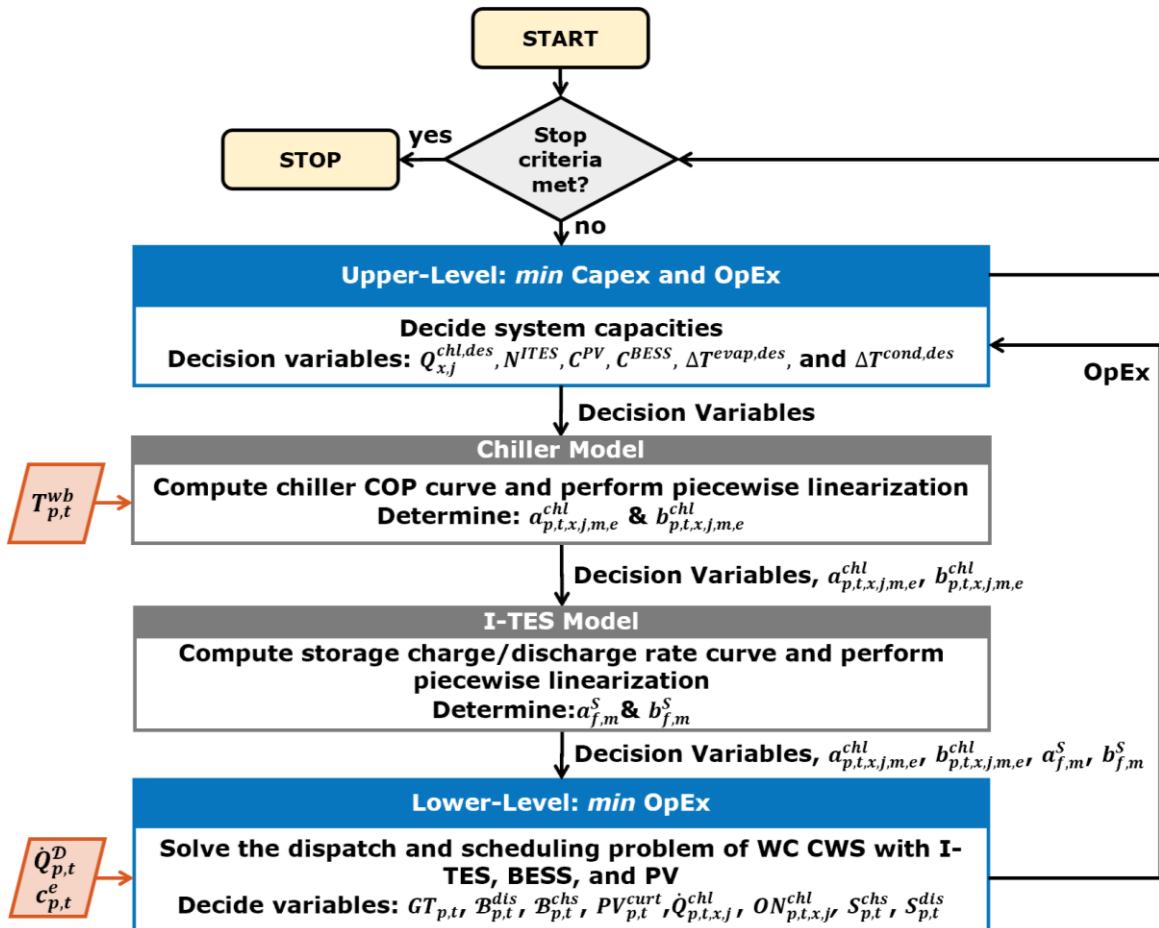


Figure 4.4: Bi-level optimization formulation. The upper level minimizes annual system costs and decides the installed capacities, and the lower level solves the equipment scheduling and dispatch problem in a mixed-integer linear programming formulation and returns the electricity charges.

Meta-heuristic algorithms are commonly used for non-convex and non-linear problems like the confronted equipment capacity sizing problem in the upper level. Meta-heuristic algorithms are broad and work well for many applications. They tend to prop the search space using a population of potential solutions. Examples are particle swarm optimization and genetic algorithm. Particle swarm optimization is better suited for upper-level due to its more efficient use of computational resources [140], [141]. Particle swarm optimization is a search heuristic evolutionary algorithm that relies on a swarm of randomly guessed solutions, termed particles [142]. The location of each particle is guided toward the best-known global positions. Over many iterations, this tends to move the swarm toward the global minimum. Evolutionary algorithms are widely used in air conditioning problems [123], [130] as these problems tend to involve complex models that cannot be reliably solved using traditional gradient-based optimization strategies without over-simplifications.

#### 4.2.2.1 Simplified chiller model

The derived Gordon-Ng chiller's model in Chapter 3 can be simplified to a function of two decision variables: loading and the on/off switch when the supply and entering condenser temperatures are pre-determined, which is often done in the literature in optimal chiller loading problems [143]–[145]. The entering condenser temperature is related to the wet-bulb temperature; a reasonable approximation is to use the design tower approach temperature to infer their relationship, as described below:

$$T_{p,t}^{csw} = T_{p,t}^{wb} + \Delta T^{app,des} \quad (4.1)$$

where subscripts  $p$  is the scenario index set  $\{1, 2, 3, 4, 5\}$  denoted by  $\mathcal{P}$  that corresponds to representative days of the year and  $t$  is the time step index set  $\{1, 2, 3, \dots, 24\}$  denoted by  $\mathcal{T}$  and

represents hours of the day, and  $\Delta T^{app,des}$  is the tower design approach temperature for the cooling tower, typically in the order of 3°C. On the other hand, the supply temperature is set based on the operating mode of the chillers: ice-making or refrigeration. In ice-making, the temperature setpoint is assumed to be at the standard ice-making temperature of -6°C. On the other hand, in refrigeration mode, the temperature depends on the decided evaporator temperature differential and design return temperature. The temperature setpoint in refrigeration mode is as follows:

$$T^{sw} = T^{rw,des} - \Delta T^{evap,des}, \quad (\text{Refrigeration mode}) \quad (4.2)$$

where  $T^{rw,des}$  is the design return temperature established from building requirements and selected coil and  $\Delta T^{evap,des}$  is the decided design evaporator temperature differential. As described by the affinity law, the decided temperature differential is inversely related to the evaporator water flowrate, which impacts pump energy use.

A piecewise linearization is then applied to the simplified model to predict chillers' performance under different loading conditions. For chillers equipped with a VSD, the performance curve is captured by two piecewise segments, whereas for chillers without VSD, a single segment was sufficient. Figure 4.5 shows the performance curves obtained for a 383-tons Carrier 19XR chiller with a VSD-equipped centrifugal compressor using the Gordon-Ng model at different ambient wet-bulb temperatures in both ice-making and refrigeration modes, overlaid with piecewise linear segments. Illustrations of the piece-wise linearization for non-VSD-equipped chillers can be found in Appendix B.

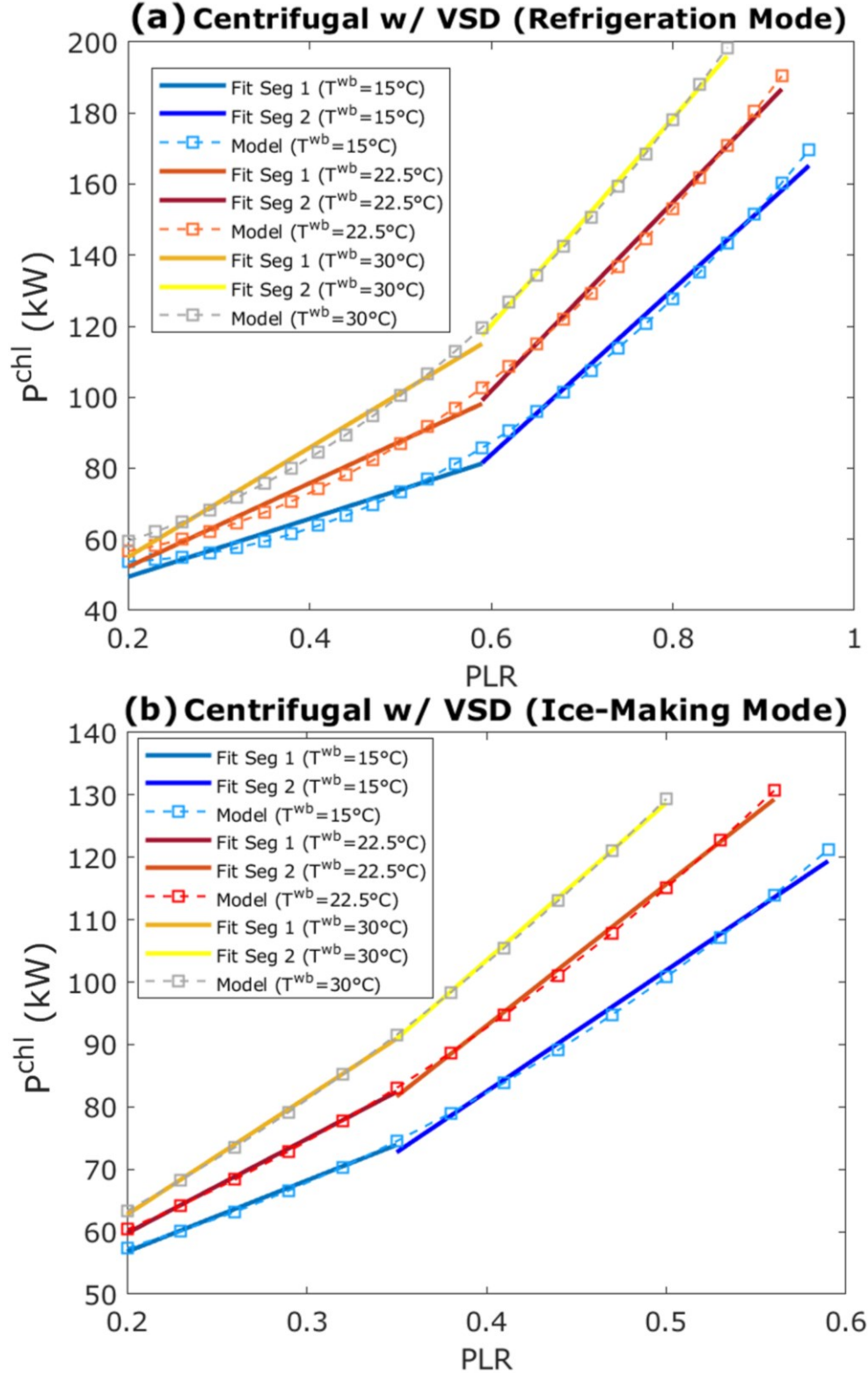


Figure 4.5: Illustration of piece-wise linearization for the 383-ton Carrier 19XR chiller with VSD-equipped centrifugal compressor in (a) ice-making mode with a setpoint temperature of  $-6^{\circ}\text{C}$  and (b) refrigeration mode with a setpoint temperature of  $7^{\circ}\text{C}$ , at three ambient wet-bulb temperatures.

The power consumed by chillers is determined from the piecewise linear slopes and intercepts subject to operating mode as follows:

$$P_{p,t}^{chl} = \sum_{x \in \mathcal{X}, j \in \mathbb{N}, m \in \mathcal{M}, e \in \mathcal{E}} [a_{p,t,x,j,m,e}^{chl} \dot{Q}_{p,t,x,j,m,e}^{chl} + b_{p,t,x,j,m,e}^{chl} B_{p,t,x,j,m,e}^{chl}], \quad \forall p \in \mathcal{P}, \forall t \in \mathcal{T} \quad (4.3)$$

where subscripts  $x$  is the chiller compressor type index set  $\{1, 2, 3\}$  denoted by  $\mathcal{X}$  that corresponds to 1) centrifugal without VSD, 2) centrifugal with VSD, and 3) screw without VSD, and  $j$  is the chiller index set  $\{1, 2, 3, 4, \dots\}$  such that  $j \in \mathbb{N}$ ,  $m$  is the operating mode index set  $\{1, 2\}$  denoted by  $\mathcal{M}$  and corresponds to 1) refrigeration mode and 2) ice-making mode, and  $e$  is the segment index set  $\{1, 2\}$  denoted by  $\mathcal{E}$ .  $\dot{Q}_{p,t,x,j,m,e}^{chl}$  is the chiller load,  $a_{x,j,m,e}^{chl}$  and  $b_{x,j,m,e}^{chl}$  are the piecewise linearization segment slope and intercept, respectively, and  $B_{p,t,x,j,m,e}^{chl}$  is a binary decision variable to toggle on the intercept for the corresponding activated segment. The following constraint restricts the number of activated segments for operating chillers:

$$\sum_{m \in \mathcal{M}, e \in \mathcal{E}} B_{p,t,x,j,m,e}^{chl} \leq ON_{p,t,x,j}^{chl}, \quad \forall p \in \mathcal{P}, \forall t \in \mathcal{T}, \forall x \in \mathcal{X}, j \in \mathbb{N} \quad (4.4)$$

The segment is activated by the decided chiller load, which is constrained within the segment's upper and lower loading bounds as follows:

$$Q_{p,t,x,j,m,e}^{chl} \leq PLR_{p,t,x,j,m,e}^{ul} Q_{x,j,m,e}^{chl,des} B_{p,t,x,j,m,e}^{chl}, \quad \forall p \in \mathcal{P}, \forall t \in \mathcal{T}, \forall x \in \mathcal{X}, j \in \mathbb{N}, m \in \mathcal{M}, e \in \mathcal{E} \quad (4.5)$$

$$Q_{p,t,x,j,m,e}^{chl} \geq PLR_{p,t,x,j,m,e}^{ll} Q_{x,j,m,e}^{chl,des} B_{p,t,x,j,m,e}^{chl}, \quad \forall p \in \mathcal{P}, \forall t \in \mathcal{T}, \forall x \in \mathcal{X}, j \in \mathbb{N}, m \in \mathcal{M}, e \in \mathcal{E} \quad (4.6)$$

$PLR_{p,t,x,j,m,e}^{ul}$  and  $PLR_{p,t,x,j,m,e}^{ll}$  are the upper and lower part-load ratio limit for each piecewise linear segment. For the last segment,  $PLR_{p,t,x,j,m,e}^{ll}$  is the chiller maximum loading estimated from Equation (3.13).

Chillers are restricted to operating in ice-making mode when storing ice and in refrigeration mode otherwise, as described by the following two constraints:

$$\sum_{x \in \mathcal{X}, j \in \mathbb{N}, e \in \mathcal{E}} B_{p,t,x,j,m,e}^{chl} \leq N^{chl} (1 - B_{p,t}^{ice}), \quad \forall p \in \mathcal{P}, \quad \forall t \in \mathcal{T}, \quad m = 1 \quad (4.7)$$

$$\sum_{x \in \mathcal{X}, j \in \mathbb{N}, e \in \mathcal{E}} B_{p,t,x,j,m,e}^{chl} \leq N^{chl} B_{p,t}^{ice}, \quad \forall p \in \mathcal{P}, \quad \forall t \in \mathcal{T}, \quad m = 2 \quad (4.8)$$

$N^{chl}$  is the number of chillers and  $B_{p,t}^{ice}$  is a binary variable that toggles the ice-making mode.

The total cooling provided by operating chillers is a simple summation of all segments and modes as follows:

$$\dot{Q}_{p,t}^{chl} = \sum_{x \in \mathcal{X}, j \in \mathbb{N}, m \in \mathcal{M}, e \in \mathcal{E}} \dot{Q}_{p,t,x,j,m,e}^{chl}, \quad \forall p \in \mathcal{P}, \quad \forall t \in \mathcal{T} \quad (4.9)$$

#### 4.2.2.2 Simplified I-TES model

I-TES charge and discharge rates can be simplified to a function of the SoC when the inlet temperature and flowrates are pre-determined. The chiller operating mode (ice-making/refrigeration) determines the temperature of the water-glycol mixture received by the storage. On the other hand, the flowrate is set to the maximum flowrate. The resultant I-TES charge and discharge rates curves represent the maximum possible heat rates, which are used to constrain decided storage charge and discharge rates. The maximum flowrate is the total flowrate

when all chillers are operating, restricted to the flowrates the storage tank is designed to tolerate, which are given by:

$$\dot{m}_{p,t}^{iw} = \min[\dot{m}^{iw,max}, \sum_{x \in \mathcal{X}, j \in \mathbb{N}} \dot{m}_{p,t,x,j}^{sw}], \forall p \in \mathcal{P}, \forall t \in \mathcal{T} \quad (4.10)$$

$\dot{m}^{iw,max}$  is the maximum flowrate the I-TES tank is designed to tolerate. Similar to the simplified chiller model, piecewise linearization is applied to the yielded performance curve, which is given by:

$$S_{p,t,f,m}^{lim} \leq a_{f,m}^S \left( \frac{S_t}{C^{ITES}} \right) + b_{f,m}^S B_{p,t,f,m}^{ITES} + M(1 - B_{p,t,f,m}^{ITES}), \forall p \in \mathcal{P}, \forall t \in \mathcal{T}, f \in \mathcal{F}, m \in \mathcal{M} \quad (4.11)$$

$$S_{p,t,f,m}^{lim} \leq M B_{p,t,f,m}^{ITES}, \forall p \in \mathcal{P}, \forall t \in \mathcal{T}, f \in \mathcal{F}, m \in \mathcal{M} \quad (4.12)$$

where subscripts  $f$  is the segment index set  $\{1, 2\}$  denoted by  $\mathcal{F}$ ,  $a_{f,m}^S$  and  $b_{f,m}^S$  are the piecewise linear slope and intercept, respectively,  $M$  is an arbitrarily large number (commonly termed Big M), and  $C^{ITES}$  is the installed net usable I-TES capacity. The supply setpoint temperature in refrigeration mode dictates the I-TES sensible stage capacity. The net usable I-TES capacity is thus determined from the number of modular ice tanks and their net usable capacity as follows:

$$C^{ITES} = N^{ITES} \times C^{Calmac} \quad (4.13)$$

where  $N^{ITES}$  is the number of tanks and is not restricted to a whole number and  $C^{Calmac}$  is the net usable capacity of each tank (83-TR-hr nominal).  $B_{p,t,f,m}^{ITES}$  is a binary decision variable to



toggle between the activated relevant segments in each mode depending on the SoC, as described by the following two expressions:

$$S_{p,t} \leq SoC_{f,m}^{ul} C^{ITES} B_{p,t,f,m}^{ITES}, \forall p \in \mathcal{P}, \forall t \in \mathcal{T}, f \in \mathcal{F}, m \in \mathcal{M} \quad (4.14)$$

$$S_{p,t} \geq SoC_{f,m}^{ll} C^{ITES} B_{p,t,f,m}^{ITES}, \forall p \in \mathcal{P}, \forall t \in \mathcal{T}, f \in \mathcal{F}, m \in \mathcal{M} \quad (4.15)$$

where  $SoC_{f,m}^{ul}$  and  $SoC_{f,m}^{ll}$  are the upper and lower limits SoC for each segment. Only one segment can be activated at any given time, as described by the following constraint:

$$\sum_{f \in \mathcal{F}} B_{p,t,f,m}^{ITES} = 1, \forall p \in \mathcal{P}, \forall t \in \mathcal{T}, m \in \mathcal{M} \quad (4.16)$$

The decided storage charge and discharge rates are limited to the computed maximum charge and discharge rates. However, since the analysis is done on an hourly basis in which the storage charge and discharge rates can change considerably, the decided charge and discharge rates are restricted based on the SoC at the current and next time step as follows:

$$S_{p,t}^{chs} \leq \sum_{f \in \mathcal{F}} \left[ \frac{1}{2} (S_{p,t,f,m}^{lim} + S_{p,t+1,f,m}^{lim}) \right], \forall p \in \mathcal{P}, \forall t \in \mathcal{T}, m = 1 \quad (4.17)$$

$$S_{p,t}^{dis} \leq \sum_{f \in \mathcal{F}} \left[ \frac{1}{2} (S_{p,t,f,m}^{lim} + S_{p,t+1,f,m}^{lim}) \right], \forall p \in \mathcal{P}, \forall t \in \mathcal{T}, m = 2 \quad (4.18)$$

$S_{p,t}^{chs}$  and  $S_{p,t}^{dis}$  are the I-TES decided charge and discharge rates, respectively. I-TES is constrained to follow the operating mode of the chillers. The storage receives a sub-freezing inlet

water-glycol mixture when charging and the standard supply water temperature when either discharging or idling as follows:

$$S_{p,t}^{chs} \leq MB_{p,t}^{ice}, \quad \forall p \in \mathcal{P}, \quad \forall t \in \mathcal{T} \quad (4.19)$$

$$S_{p,t}^{dis} \leq M(1 - B_{p,t}^{ice}), \quad \forall p \in \mathcal{P}, \quad \forall t \in \mathcal{T} \quad (4.20)$$

Figure 4.6 shows the I-TES charge rate curve in (a) and the discharge rate curve in (b) overlaid with piecewise linear segments. The discharge rate curve is well captured with three segments compared to the four segments required by the charge rate curve. The segments overlap with the previously discussed three stages of charging and discharging in Chapter 3. The amount of stored thermal energy in I-TES is balanced in the following constraint:

$$S_{p,t} - \eta^{ITES,sdis} S_{p,t-1} = S_{p,t}^{chs} - S_{p,t}^{dis}, \quad \forall p \in \mathcal{P}, \quad \forall t \in \mathcal{T} \quad (4.21)$$

where  $\eta^{ITES,sdis}$  is the I-TES self-discharge efficiency.

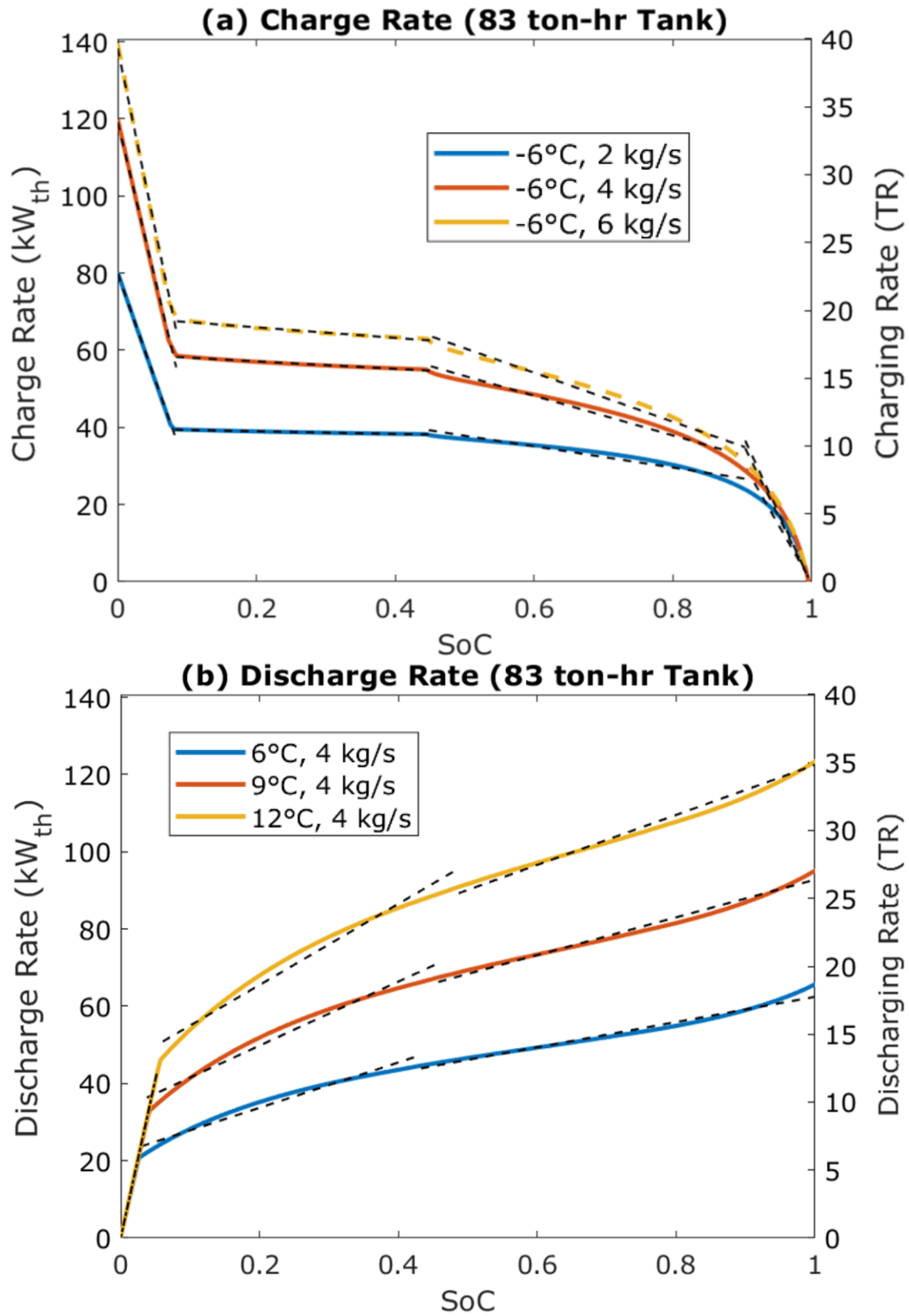


Figure 4.6: Piece-wise linearization applied to I-TES maximum charge and discharge rates.

#### 4.2.2.3 Simplified auxiliary components models

Other simplifications can be made to estimate the power use of auxiliary equipment such as cooling towers, cooling coils, and pumps. The power consumed by the cooling tower fan can be assumed to vary with the chiller load analogous to fixed-speed tower fans and is given by:

$$P_{p,t}^{twr} = P_{twr,des} \frac{\dot{Q}_{p,t}^{chl}}{\dot{Q}_{twr,des}} , \quad \forall p \in \mathcal{P}, \forall t \in \mathcal{T} \quad (4.22)$$

$P_{twr,des}$  is the power consumed by the tower when running at maximum speed ( $VSD^{twr} = 1$ ) in Equation (3.29) in Chapter 3, and  $\dot{Q}_{twr,des}$  is the nominal thermal capacity of the tower.

Although the power consumed by the cooling tower varies cubically with the flowrate, as described by the affinity laws, a simplification of this variability is expected only to produce a small error, given that the cooling power consumption is minor relative to that of the chillers and other auxiliary equipment. The cooling coil and second pumps power use vary with the cooling demand per the affinity laws, which are as follows:

$$P_{p,t}^{dist} = \left( \frac{\dot{Q}_{p,t}^{\mathcal{D}}}{\max_{p \in \mathcal{P}, t \in \mathcal{T}} [\dot{Q}_{p,t}^{\mathcal{D}}]} \right)^3 [P^{sp,des} + P^{cf,des}], \quad \forall p \in \mathcal{P}, \forall t \in \mathcal{T} \quad (4.23)$$

$\dot{Q}_{p,t}^{\mathcal{D}}$  is the cooling demand,  $P^{sp,des}$  and  $P^{cf,des}$  are the rated coil and secondary pump power in Equations (3.18) and (3.49) when running at maximum speed ( $VSD^{sp} = 1$  and  $VSD^{cf} = 1$ ), respectively.

The decided design evaporator and condenser temperature differential adjust the pumps' power use per the affinity laws, as discussed in Section 3.2.2 in Chapter 3. The required power

by the chillers' pumps is a linear function of their constant, as described by the following equation:

$$P_{p,t}^p = \sum_{x \in \mathcal{X}, j \in \mathbb{N}} [P_{p,t,x,j}^{pp,des} + P_{p,t,x,j}^{cp,des}] \cdot ON_{p,t,j,x}^{chl}, \quad \forall p \in \mathcal{P}, \forall t \in \mathcal{T} \quad (4.24)$$

$P_{p,t,x,j}^{pp,des}$  and  $P_{p,t,x,j}^{cp,des}$  are the primary and condenser pump power consumption for each chiller, which are computed from Equations (3.16) and (3.17), respectively, and they only operate with their associated chillers. The following equation computes the total power consumed by auxiliary equipment as follows:

$$P_{p,t}^{Aux} = P_{p,t}^p + P_{p,t}^{dist} + P_{p,t}^{twr}, \quad \forall p \in \mathcal{P}, \forall t \in \mathcal{T} \quad (4.25)$$

#### 4.2.2.4 BESS model

Similar to the utility-scale analysis in Chapter 2, a linear BESS model is developed. Although BESS charge and discharge rates are a function of the SoC and are impacted by degradation, the performance can be well captured in a linear model with fixed charge and discharge efficiencies [74]. No consideration is made for depth of discharge as BESS capacity ( $C^{BESS}$ ) is taken to represent the net usable capacity. Charge and discharge rates are restricted to that of a 4 hours battery (power-to-energy capacity ratio of 1/4). Stored energy in BESS is balanced in the following constraints:

$$\mathcal{B}_{p,t}^s - \eta^{BESS,sdis} \mathcal{B}_{p,t-1}^s = \eta^{BESS,chs} \mathcal{B}_{p,t}^{chs} - \frac{1}{\eta^{BESS,dis}} \mathcal{B}_{p,t}^{dis}, \quad \forall p \in \mathcal{P}, \forall t \in \mathcal{T} \quad (4.26)$$

where  $\mathcal{B}_{p,t}^s$  is the stored electric energy and  $\eta^{BESS,sdis}$ ,  $\eta^{BESS,chs}$ , and  $\eta^{BESS,dis}$  are the self-discharge, charge, and discharge efficiencies, respectively. The maximum charge and discharge rate are restricted by the following two constraints:

$$\mathcal{B}_{p,t}^s \leq C^{BESS}, \forall p \in \mathcal{P}, \forall t \in \mathcal{T} \quad (4.27)$$

$$\mathcal{B}_{p,t}^{chs} + \mathcal{B}_{p,t}^{dis} \leq \left(\frac{1}{4}\right) \times C^{BESS}, \forall p, \forall t \quad (4.28)$$

where  $\mathcal{B}_{p,t}^{chs}$  and  $\mathcal{B}_{p,t}^{dis}$  are BESS charge and discharge rates, respectively. To disregard solutions with concurrent charging and discharging, a small cost of  $10^{-3}$  \$/MW is applied to the BESS charge rate,  $\mathcal{B}_{p,t}^{chs}$ , in objective function in the lower level, which does not influence the cost-optimal system.

### 4.2.3 Problem formulation

The objective of the optimization is to minimize annual system costs from Capex and OpEx by utilizing lower-cost PV generation for carbon emissions reduction. The cost function that is to be minimized by the upper-level optimizer:

$$\begin{aligned} \min Cost = & c^{BESS} C^{BESS} \frac{ir(ir+1)^{yrb}}{(1+ir)^{yrb}-1} + [c^{PV} C^{PV} + c^{ITES} C^{ITES} + \sum_{x \in \mathcal{X}, j \in \mathbb{N}} c_x^{chl} Q_{x,j}^{chl,des} + \\ & \sum_{j \in \mathbb{N}} c^{P,FS} C_j^p + c^{P,VSD} C^{sp} + c^{twr} C^{twr}] \frac{ir(ir+1)^{yr}}{(1+ir)^{yr}-1} + c^{PV,O} C^{PV} + OpEx \end{aligned} \quad (4.29)$$

where  $c_x^{chl}$ ,  $c^{PV}$ ,  $c^{BESS}$ ,  $c^{ITES}$ ,  $c^{P,FS}$ ,  $c^{P,VSD}$ ,  $c^{twr}$  are installed chillers, PV, BESS, I-TES, chiller pumps, secondary pumps, and cooling towers Capex, respectively, and  $C^{PV}$ ,  $C_j^p$ ,  $C^{sp}$ ,  $C^{twr}$  are

the installed PV, chiller pumps, secondary pumps, and cooling towers capacities, respectively,  $c^{PV,0}$  is the yearly OpEx for installed PV,  $ir$  is the interest rate,  $yrb$  is the BESS's service life, and  $yr$  is the service life of the remaining equipment. OpEx is the estimated yearly electricity charge determined by solving the scheduling and dispatch problem, which are given by:

$$\min OpEx = c^e \sum_{p \in \mathcal{P}, t \in \mathcal{T}} GT_{p,t} N_p^{days} + c^P \sum_{p \in \mathcal{P}} GT_p^P N_p^{mos} \quad (4.30)$$

$c^e \sum_{p \in \mathcal{P}, t \in \mathcal{T}} GT_{p,t} N_p^{days}$  and  $c^P \sum_{p \in \mathcal{P}, t \in \mathcal{T}} GT_{p,t} N_p^{mos}$  are the electricity charges from energy use and demand charges, respectively,  $GT_{p,t}$  is the electricity consumed from the grid,  $GT_p^P$  is peak electricity demand,  $N_p^{days}$  and  $N_p^{mos}$  are the number of days and months represented by scenario  $p$ , respectively,  $c^e$  and  $c^P$  are electricity price and peak demand charge, respectively,

The pump's installed capacity in Equation (4.29) is the rated power calculated in Section 4.2.2.3. For fixed-speed pumps, the capacities are their rated power as obtained from Equations (3.16) and (3.17), which are given by:

$$C_j^p = P_j^{cp,des} + P_j^{pp,des} \quad (4.31)$$

For variable speed pumps, the rated power is the power when running at the maximum speed ( $VSD^{sp} = 1$ ) as follows:

$$C^{sp} = P^{sp,des} \quad (4.32)$$

The cooling towers are sized to reject the heat given when all chillers are operating at their designed capacity:

$$C^{twr} = \frac{\Delta T^{cond,ref}}{\Delta T^{cond,des}} \sum_{x \in \mathcal{X}, j \in \mathbb{N}} Q_{x,j}^{chl,des} \left( 1 + \frac{1}{COP_{x,j}^{ref}} \right) \quad (4.33)$$

where  $\Delta T^{cw,des}$  is the chiller design condenser temperature differential. The cooling tower's physical size is assumed to vary linearly with the design condenser temperature differential, which correlates with the condenser water flowrate.

The upper-level optimization is only constrained by a minimum and maximum chiller capacity:

$$\underline{Q^{chl,des}} \leq Q_{x,j}^{chl,des} \leq \overline{Q^{chl,des}} \quad (4.34)$$

where  $\underline{Q^{chl,des}}$  and  $\overline{Q^{chl,des}}$  are the lower and upper nominal chiller capacity limits and are taken to be 350 and 900 tons for the examined problem, respectively. The lower limit is based on the current market offering for WC chillers, and the upper limit is set to reduce the risk of loss of service due to downtime and maintenance.

For the lower-level problem, three constraints were applied. The first lower-level constraint balances the building electricity demand with generation as follows:

$$P_{p,t}^{chl} + P_{p,t}^{Aux} + \mathcal{B}_{p,t}^{chs} + PV_{p,t}^{curt} + \mathcal{L}^{Elec} = \eta^I I_{p,t} C^{PV} + \mathcal{B}_{p,t}^{dis} + GT_{p,t}, \quad \forall p \in \mathcal{P}, \forall t \in \mathcal{T} \quad (4.35)$$



where  $PV_{p,t}^{curt}$  is the curtailed PV generation,  $\mathcal{L}^{Elec}$  is the building's non-cooling load, and  $I_{p,t}$  is the incident solar insolation on an inclined surface at the optimal fixed-tilt angle at Qatar latitude of 25°. The second constraint balances chiller loading with building demand and I-TES dispatch amount and is described by:

$$\dot{Q}_{p,t}^{chl} + S_{p,t}^{dis} = \dot{Q}_{p,t}^{\mathcal{D}} + S_{p,t}^{chs}, \forall p \in \mathcal{P}, \forall t \in \mathcal{T} \quad (4.36)$$

Since the first hour of the day is an arbitrary decision, the storage can have a non-zero initial SoC as long as it returns to it at the end of the day in each scenario, which is given by:

$$S_{p,t=1} = S_{p,t=24}, \forall p \in \mathcal{P} \quad (4.37)$$

#### 4.2.4 Model parameters

The considered characteristics parameters in the model are tabulated in Table 4.1. Similar to the utility-scale analysis, a high-efficiency inverter with 98% efficiency is assumed for on-site PV generation [83]. A 4-hour BESS was considered with charge and discharge efficiencies of 92% and a self-discharge efficiency of 99.9% [84], [85]. The charge and discharge efficiencies also account for BESS inverter losses.

**Table 4.1: Assumed characteristics parameters**

Item	Parameter	Symbol	Value
PV	Inverter efficiency	$\eta^I$	98%
	Charge efficiency	$\eta^{BESS,chs}$	92%
BESS	Discharge efficiency	$\eta^{BESS,dis}$	92%
	Self-discharge efficiency	$\eta^{BESS,sdis}$	99.9%
I-TES	Self-discharge efficiency	$\eta^{ITES,sdis}$	99.9%

The considered financial parameters in the model are tabulated in Table 4.2. Installed PV Capex was assumed to be higher than in the utility-scale at \$600/kW<sub>p,dc</sub>, and OpEx to be \$10/kW<sub>p,dc</sub>/yr. for fixed-tilt. Based on current market prices, small-scale 4-hour BESS was taken at \$300/kWh. Benefiting from access to affordable capital, the system was assumed to be financed at a 3.5% interest rate. Service life was taken to be 25 years for I-TES, ice chillers, and PV and 10 years for the BESS. Similarly, based on current market offerings and published figures [85], [88], [91], the cost of I-TES is \$80/TR-hr (\$14/kWh<sub>th</sub>). Centrifugal chillers were at \$400/TR with an additional \$50/TR for a VSD drive. Screw chillers are cheaper but generally less efficient at \$350/TR. The cost for water pumps was \$150/kW and an additional \$50/kW for a VSD. Last, the cost of cooling towers was \$57/kW<sub>th</sub> (\$200/TR) at the standard design 6°C water temperature differential; a larger temperature differential reduces the tower size and cost.

**Table 4.2: Assumed financial parameters**

Item	Unit	Expense	Symbol	Value
PV	Fixed-tilt	Capex	$c^{PV,C}$	\$600/kW <sub>p,dc</sub>
		OpEx	$c^{PV,O}$	\$10/kW <sub>p,dc</sub> /yr.
I-TES	Internal melt	Capex	$c^{ITES}$	\$23/kWh <sub>th</sub> (\$80/TR-hr)
BESS	4-hour Li-ion	Capex	$c^{BESS}$	\$300/kWh
Chiller	Centrifugal w/o VSD	Capex	$c_1^{chl}$	\$115/kW <sub>th</sub> (\$400/TR)
	Centrifugal w/ VSD	Capex	$c_2^{chl}$	\$130/kW <sub>th</sub> (\$450/TR)
	Screw w/o VSD	Capex	$c_3^{chl}$	\$100/kW <sub>th</sub> (\$350/TR)
	Fixed Speed Pumps	Capex	$c^{P,FS}$	\$150/kW
Auxiliary Equipment	Variable Speed Pumps	Capex	$c^{P,VSD}$	\$200/kW
	Cooling Tower	Capex	$c^{twr}$	\$57/kW <sub>th</sub> (\$200/TR)
Misc.	Capital	Interest Rate	$ir$	3.5%
		Service Life	$yr$	25 years
		BESS Service Life	$yrb$	10 years

The electricity rates for non-bulk consumers (peak load less than 5 MW) are subsidized and unsuitable for carbon pricing analysis. Instead, unsubsidized bulk customer electricity rates are used, even though the modeled buildings do not meet the criteria for bulk customers. The tariff structure for bulk customers is tabulated in Table 4.3. The rate is flat during the winter months at \$58/MWh. In the summer month, the rate is \$66/MWh during the off-peak period and raises to \$93/MWh during the on-peak period between 12 and 6 PM. No demand charges are currently implemented in Qatar ( $c^P = \$0/\text{MW}_p$ ).

**Table 4.3: Qatar electricity tariffs for bulk customers**

Period	Electricity Tariff
May 1 – October 31	
12:00 PM – 6:00 PM	\$93/MWh
6:00 PM – 12:00 PM	\$66/MWh
November 1 – April 30	
All day	\$58/MWh

#### 4.2.5 Chillers performance data

Three chillers with a performance representative of the compressor technology are selected from the EnergyPlus WC chillers library. The selected chillers are: 365-tons Carrier 19XR with centrifugal compressor, 383-tons Carrier 19XR with VSD equipped centrifugal compressor, and 340-tons Carrier 23XL with slide valve equipped screw compressor. Details of selected chillers' characteristics can be found in Appendix B. To predict the performance of chillers with different capacities and condenser flowrates needed for the capacity sizing problem, the COP, as described by reformulated Gordon-Ng model in Equation (3.10), is expressed as a function of normalized parameters: chiller loading ( $PLR$ ) and temperature differential ratio

$\left(\frac{\Delta T_x^{cw,ref}}{\Delta T^{cw,des}}\right)$  as follows:

$$\frac{1}{COP_{x,j}^{base}} = \frac{\dot{Q}_{x,j}^{chl}(\dot{Q}_{x,j}^{chl} + \dot{Q}_{x,j}^{leak,eqv} + m_{x,j}^{cw,adj} c_{p,cw} [R_{x,j} \dot{Q}_{x,j}^{chl} - T^{sw}] + T^{sw} [\Delta S_{x,j}^{int} + \Delta S_{x,j}^{intQ} PLR_{x,j}])}{m_{x,j}^{cw,adj} c_{p,cw} (\dot{Q}_{x,j}^{chl} T^{csw} + \dot{Q}_{x,j}^{leak,eqv} [T^{csw} - T^{sw}] + T^{csw} T^{sw} [\Delta S_{x,j}^{int} + \Delta S_{x,j}^{intQ} PLR_{x,j}])} \quad (4.38)$$

where,

$$\dot{Q}_{x,j}^{chl} = PLR_{x,j} \dot{Q}_x^{ref} \quad (4.39)$$

$$m_{x,j}^{cw,adj} = \dot{m}_x^{cw,ref} \left( \frac{\Delta T_x^{cw,ref}}{\Delta T^{cw,des}} \right) \quad (4.40)$$

where  $\dot{Q}_x^{ref}$ ,  $\dot{m}_x^{cw,ref}$  and  $\Delta T_x^{cw,ref}$  are the nominal capacity, condenser mass flowrate, and condenser temperature differential of the reference chiller from EnergyPlus, respectively, and  $m_{x,j}^{cw,adj}$  is the adjusted flowrate based on the decided design chiller temperature differential, which linearly correlates with flowrate. To account for the improvement in cooling performance observed in chillers with larger capacities, the effective chiller COP is linearly adjusted with the capacity relative to the reference chiller COP:

$$COP_{x,j} = COP_{x,j}^{base} + \delta(\dot{Q}_{x,j}^{chl,des} - \dot{Q}_x^{ref}), \forall x \in \mathcal{X}, j \in \mathbb{W} \quad (4.41)$$

$\delta$  is the improvement in chiller performance per increase in cooling capacity and is approximately  $10^{-3} \text{ TR}^{-1}$ , based on Australia's Department of Climate Change, Energy, the Environment, and Water minimum energy performance standard for chiller efficiency [146], which agrees with the market offering. Piecewise linearization is applied to the predicted COP, computed for the pre-determined condenser water temperature in refrigeration and ice-making mode under a range of chiller loading.

#### 4.2.6 Scenarios selection

Five days are selected from the simulated cooling demand for the commercial and residential building. One day represents the peak demand day (design day) and four days capture intra-annual demand and weather variations in each season.

##### 4.2.6.1 Commercial building

The selected five scenarios and the number of days of the year they represent are tabulated in Table 4.4. The five scenarios are arbitrarily labeled from 1 to 5. Scenario 1 represents the peak demand or design day, occurring only ten days out of the year. This scenario dictates the minimum installed cumulative chiller and I-TES capacities. Scenario 2 represents the high cooling demand period between mid-July and mid-September, which lasts for two months and is driven by the high ambient humidity levels. Scenario 3 exemplifies the longest period of the year with a moderate cooling load, and it lasts 148 days, from late April to mid-July and from mid-September to mid-November. This period is dominated by high peak daytime temperatures between 35 and 45°C, which drives the building cooling load. Scenario 4 exemplifies the shoulder season, characterized by moderately warm days with afternoon temperatures between 30 and 35°C. and lasts for about three months in late fall and early spring. Scenario 5 exemplifies the low cooling season in the winter and is described by mild daytime temperatures between 20 and 25°C. The cooling load in this period is driven by occupancy and electric load.

**Table 4.4: Scenarios for the commercial building**

	Scenario	Date	Number of Represented Days
1	Design day	August 15	10
2	High cooling	July 28	57
3	Moderate cooling	July 11	148
4	Shoulder Season	March 13	83
5	Low Cooling	January 30	67

Figure 4.7 below shows the five scenarios' hourly cooling demand, non-cooling load, solar insolation, and ambient wet-bulb temperature.

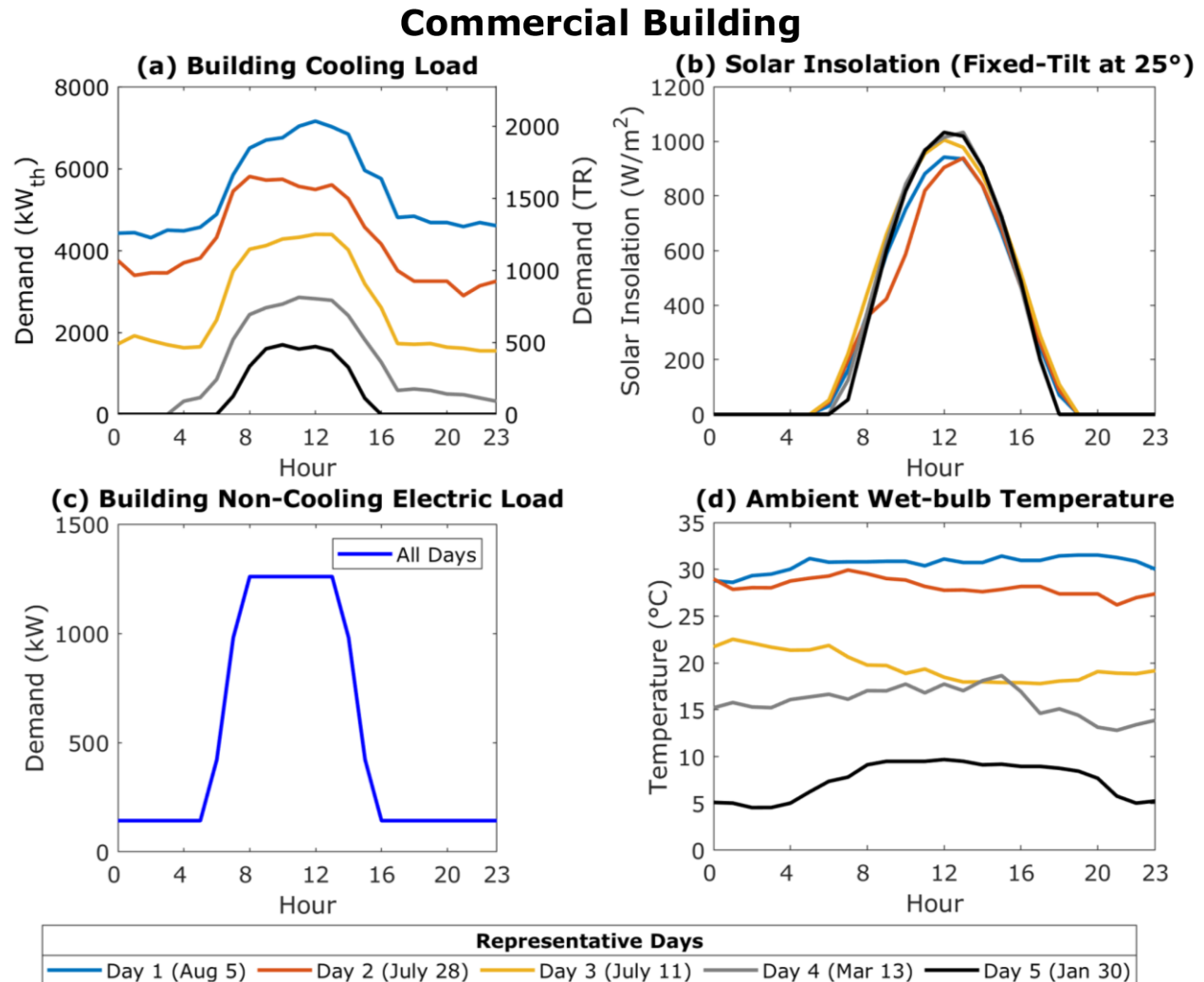


**Figure 4.7: The five scenarios for the commercial building with (a) building thermal cooling demand, (b) solar insolation, (c) non-cooling load, and (d) ambient wet-bulb temperature.**

The non-cooling load is assumed to be fixed year-round and is predominantly during the daytime from assumed higher daytime building occupancy. The building peak cooling demand increases by about a factor of 4 from around 1700 kW<sub>th</sub> in the low cooling demand season to 7200 kW<sub>th</sub> in the peak cooling load day. A small variation in solar insolation with notably extended sunshine hours during the summer is observed. On the other hand, ambient wet-bulb

temperatures drastically increase from an average of 7°C in the low-cooling season to the low 30s in the high-demand season. While intra-daily variations are small, the seasonal variations are large enough for speed modulation in chillers with VSD-equipped compressors.

#### 4.2.6.2 Residential building

The selected five scenarios and the number of days they represent for the residential building are tabulated in Table 4.5. Scenario 1 represents the peak cooling demand day and similarly dictates the required cumulative chillers and I-TES capacities. Scenario 2 is the high cooling demand period between mid-July and mid-September. Scenario 3 is the moderate cooling season and persists for 109 days a year. This scenario has the longest period of the year, from mid-May to mid-July and mid-September to mid-October. Scenario 4 is the second longest period representing 101 days of the year in late fall and early spring. Scenario 5 is the low cooling season in the winter; in this period, the load is driven by occupancy and electric load.

**Table 4.5: Scenario for the residential building**

	Scenario	Date	Number of Represented Days
1	Design day	August 15	10
2	High cooling	July 28	76
3	Moderate cooling	July 11	109
4	Shoulder Season	March 13	101
5	Low Cooling	January 30	69

Figure 4.8 shows the five scenarios' hourly cooling demand, electric demand, solar insolation, and ambient wet-bulb temperature for the residential building. The non-cooling load is assumed to be fixed year-round and is characterized by a morning spike and a generally higher load in the evening correlated with assumed building occupancy. The building peak cooling demand increases by more than a factor of 4 from 1500 kW<sub>th</sub> in the low cooling demand season

to 6550 kW<sub>th</sub> in the peak cooling load day. The daily demand variations are smaller in the residential building than in the commercial building, especially in the cooling seasons.

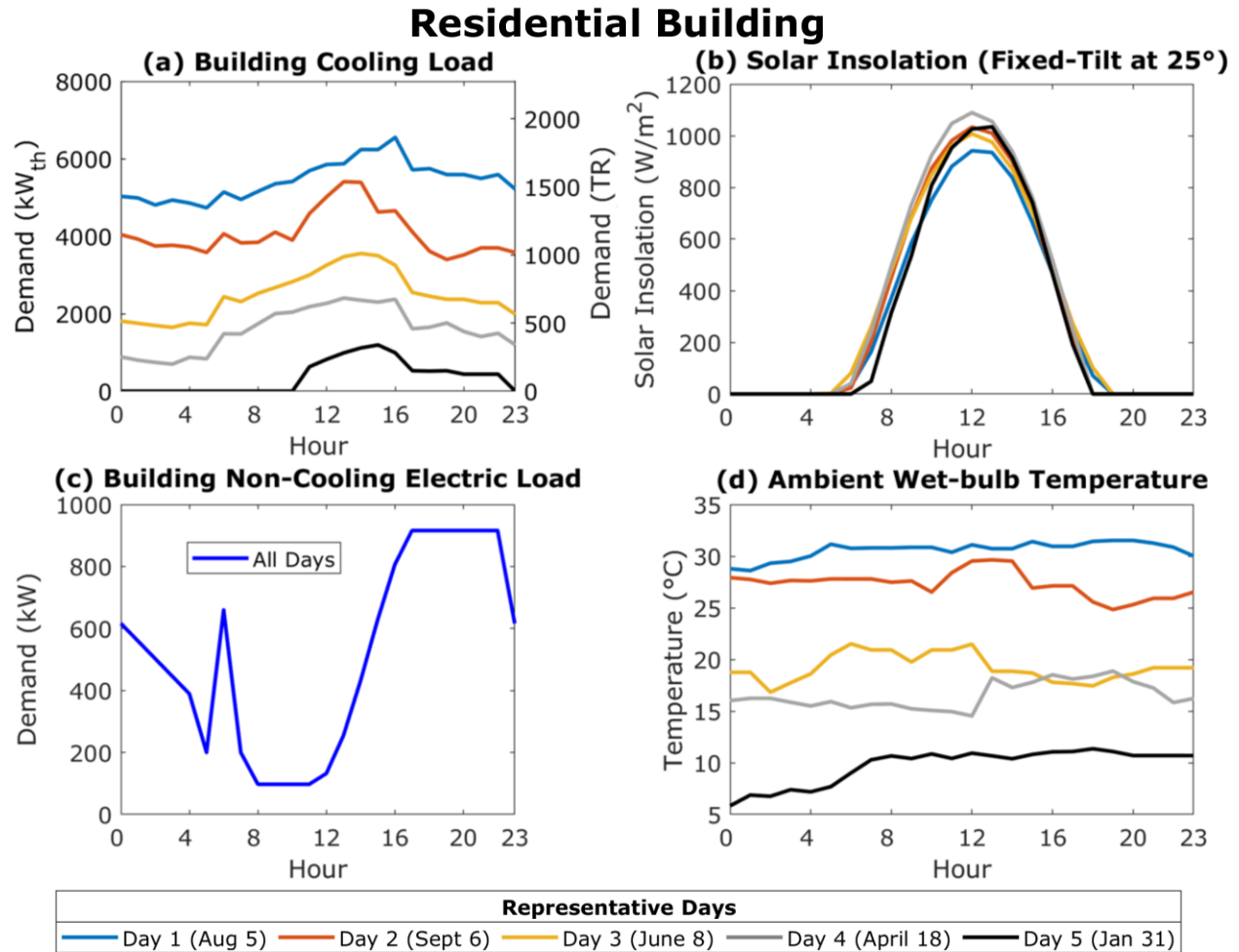


**Figure 4.8:** The five representative days for the residential building with (a) building thermal cooling demand, (b) solar insolation, (c) non-cooling load, and (d) ambient wet-bulb temperature.



## 4.3 Results and discussion

The formulated problem is first solved at the current system structure, where all electricity is from the grid, which was established as the reference case. The model was then exposed to a range of carbon pricing from 0 to \$150/ton of CO<sub>2</sub> to examine the impact of economic incentives on decarbonization efforts.

### 4.3.1 Commercial building

The effects of carbon pricing on the cost-optimal system installed capacities are shown in Figure 4.9, and the corresponding system characteristics are shown in Figure 4.10. The optimal on-site PV capacity is near the building's peak electricity demand of 3000 kW. Higher carbon pricing promotes the installation of an additional 1000 kW of PV for energy storage charging. However, installed I-TES and BESS capacities remain small even as the carbon price increases. Nevertheless, the results show that the excellent alignment of building cooling and electricity need with solar insolation reduces the required energy storage capacity and curtailment. PV generation alone could reduce emissions by about 65%, minimally impacted by carbon pricing. I-TES supplements nighttime cooling needs in the low-demand season, which reduces emissions by a mere 3%. As the carbon price increases, I-TES is increasingly used to meet more of the increased cooling demand in the shoulder season, reducing emissions by 8% from load shifting with an average daily capacity utilization factor of about 70%.

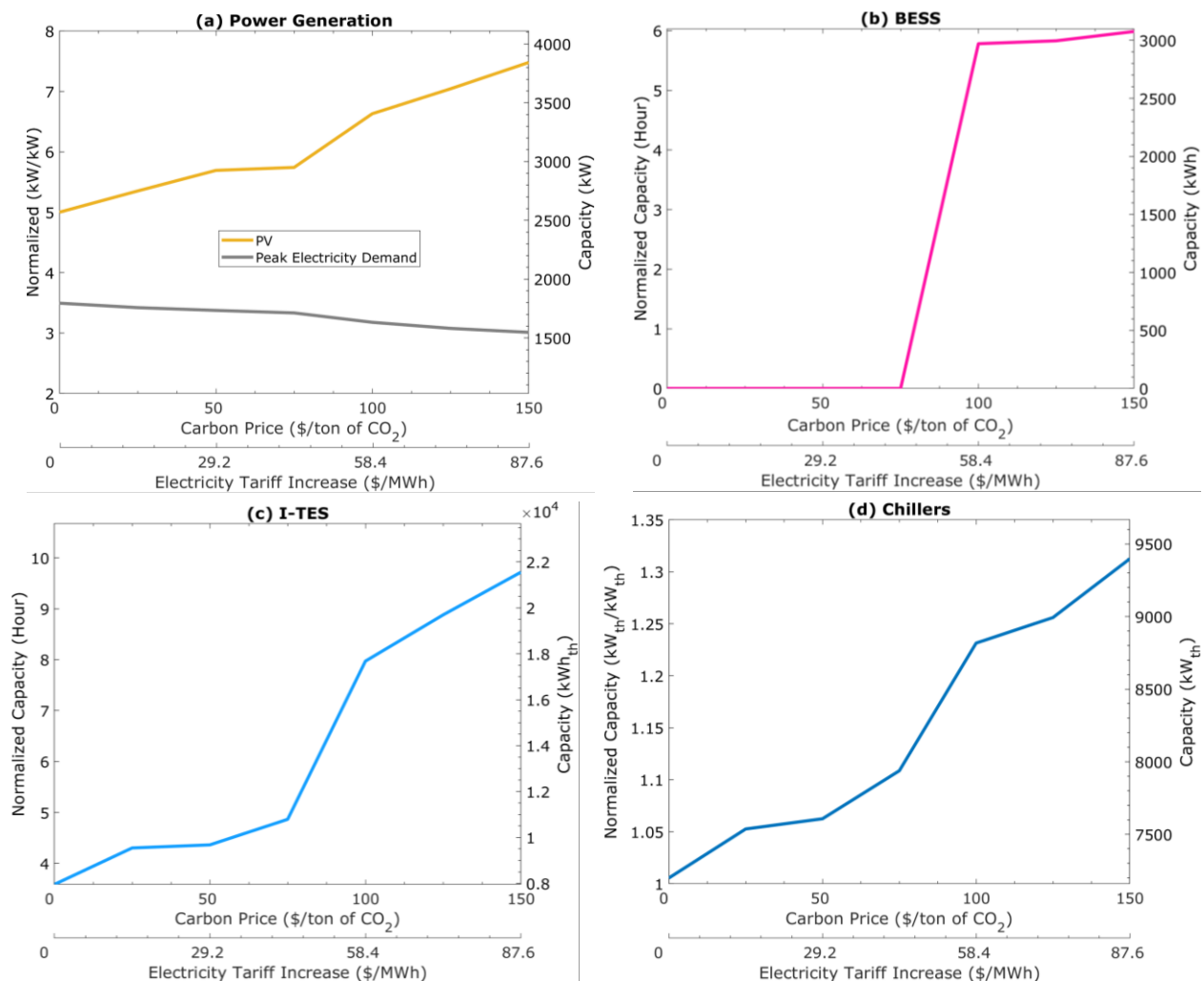


**Figure 4.9: Effect of carbon pricing on the cost-optimal system installed capacities of (a) PV, (b) BESS, (c) I-TES, and (d) chillers for the commercial building. PV and BESS are normalized to the average electric demand of 515 kW, I-TES is normalized to the average cooling load of 2213 kW<sub>th</sub>, and the total capacity of chillers is normalized to the peak cooling demand of 7160 kW<sub>th</sub>. Peak electricity demand is the maximum power drawn from the electricity grid.**

Due to the high seasonality of cooling demand and capacity degradation in ice-making mode, I-TES is not feasible for load shifting in the high-demand season, even as the carbon price is considerably increased, limiting the potential of I-TES for emissions reduction. Furthermore, the optimal chiller capacity was only 30% higher than the peak cooling need because I-TES is not used in the high cooling season and relies on utilizing idle chiller capacity in the lower demand season. This result suggests that buildings with conservatively oversized chillers are

suited for exploiting I-TES for load shifting without additional cooling capacity. BESS becomes cost-effective above a carbon pricing of \$75/ton of CO<sub>2</sub> and is only used to meet the near year-round constant baseload with an average daily capacity utilization rate of 90%. A deep decarbonization rate of about 90% can be achieved in a system with a carbon price above \$100/ton of CO<sub>2</sub>, of which direct PV utilization is responsible for about 70% of emissions reduction.

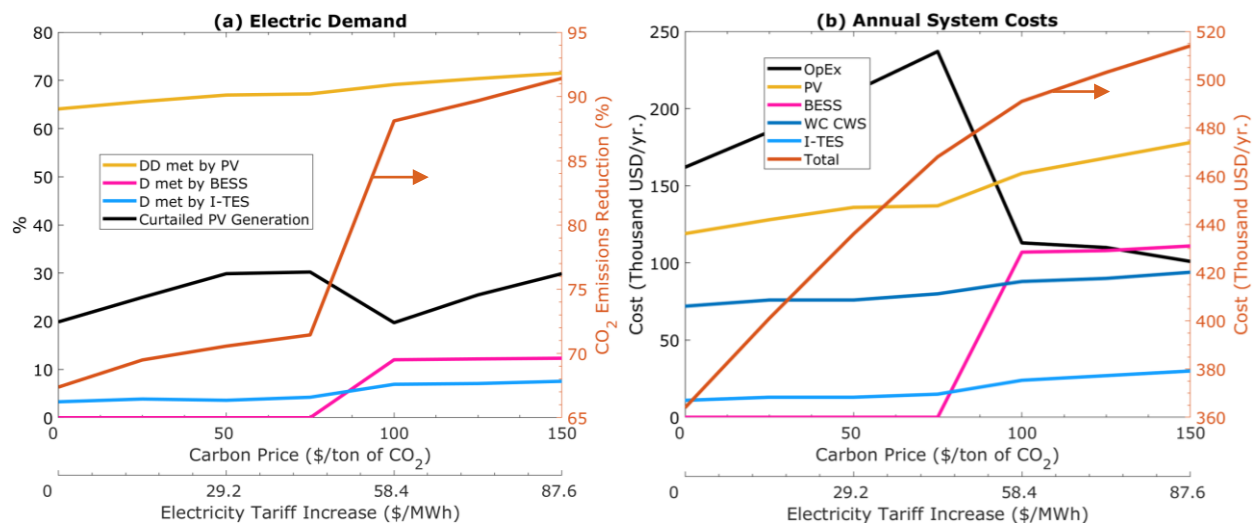


**Figure 4.10: Effect of the carbon price increases on (a) contribution to meeting the electric demand and (b) breakdown of annual system cost for the commercial building.**

Annual system cost in the cost-optimal system with a carbon price below \$100/ton of CO<sub>2</sub> is dominated by OpEx and Capex from installed PV. Once BESS is economical, half of the annual system cost is from BESS and PV. The increase in annual costs is justified to mitigate carbon tax. Despite the increase in the carbon tax, OpEx monotonically decreases above a carbon tax of \$100/ton CO<sub>2</sub> as an increasing amount of demand is met by BESS and I-TES.

The carbon abatement cost for the cost-optimal system as carbon price increases is shown in Figure 4.11. Carbon abatement cost is defined as the yearly cost of mitigating carbon

emissions from carbon-based electricity from the grid. The negative abatement cost indicates that a more sustainable solution can be achieved at a reduced annual system cost compared to the conventional approach of solely using electricity from the grid. The observed negative abatement cost is enabled by well-matched PV generation with building cooling and electricity needs.

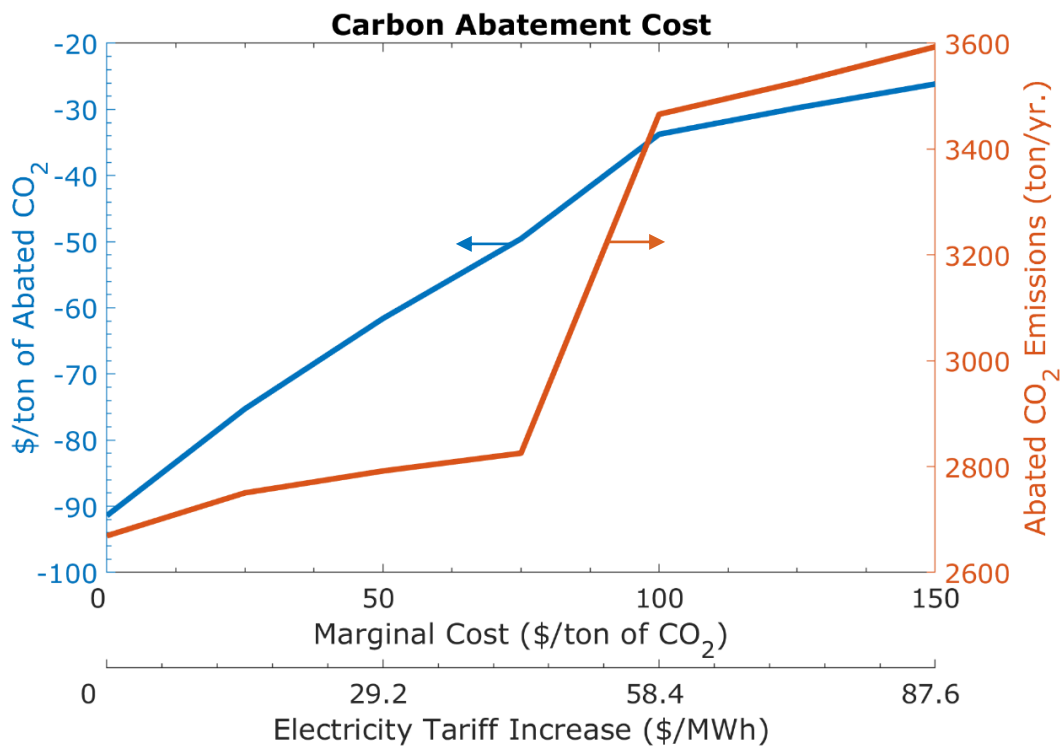


**Figure 4.11: Carbon abatement cost and abated CO<sub>2</sub> for the commercial building.**

Despite the suitability of on-site PV generation for buildings with daytime electricity needs, challenges arise from (i) the required land area, which far exceeds the building-built floor area, (ii) challenges with cleaning the panels to limit soiling on PV, and (iii) unsubsidized electricity tariff for bulk customers do not reflect electricity tariffs for the majority of building stock in Qatar. Using current technology, energy generated by rooftop PV generation can support decarbonizing energy demands in buildings up to three-story high.

Decided chiller capacities and compressor technology types are tabulated in Table 4.6. The base scenario is when all electricity demand is met from the electricity grid, representing

nearly all of Qatar's building stock. The cost-optimal system consists of two chillers with VSD-equipped centrifugal compressors for optimized part load performance. This selection is partly promoted by the large intra-annual variations in wet-bulb temperatures, which permits speed modulations when accompanied by reduced building loads. The unequal capacities of centrifugal chillers with VSD allow for more efficient chiller sequencing and reduced pump power use. This configuration is especially important since chillers are often part-loaded, whereas their associated pumps' power use is constant. The lower-cost screw chiller supports I-TES charging and supplements cooling during the short-lived high-cooling demand season.

The decided design temperature differential in the evaporator for all scenarios is about 8°C, sufficiently high enough to reduce pump power use but not large enough to over-burden the chillers with a reduced supply water temperature setpoint. The decided temperature differential on the condenser side is higher at 10°C, which reduces condenser pump power use and the size of the cooling tower. Although it degrades the chillers' cooling capacity, the oversized cooling capacity compensates for the degradation.

**Table 4.6: Optimal-cost cooling system capacities for the commercial building**

Carbon Price [\$ /ton of CO <sub>2</sub> ]	CWS Cost [\$ /yr.]	I-TES Capacity [kW <sub>th</sub> ]	Chiller 1 (VSD Centrifugal) [kW <sub>th</sub> ]	Chiller 2 (VSD Centrifugal) [kW <sub>th</sub> ]	Chiller 3 (Fixed Speed Screw) [kW <sub>th</sub> ]	Total Chiller Capacity [kW <sub>th</sub> ]
Base	74	0	3,165	2,637	1,441	7,243
0	72	7,955	3,165	1,567	2,468	7,200
25	75	9,543	3,165	1,881	2,492	7,538
50	75	9,677	3,165	1,552	2,892	7,609
75	80	10,791	3,165	2,374	2,399	7,939
100	88	17,679	3,165	2,632	3,020	8,818
125	90	19,695	3,165	3,165	2,664	8,994
150	94	21,554	3,165	3,165	3,067	9,398

Hourly chillers loading and load profile for Scenarios 2-4 (high cooling to shoulder season) for a system without carbon pricing are shown in Figure 4.12, and for a system with a carbon pricing at \$100/ton of CO<sub>2</sub> are shown in Figure 4.13. I-TES was not used in the high cooling demand constrained by the lack of idle chillers capacity. In the shoulder season, sufficient idle capacity allows I-TES to meet all nighttime cooling demands. The additional chillers' cooling capacity in the system with carbon pricing permitted a larger capacity and higher utilization of I-TES in the moderate demand season with little to no impact on the high cooling demand season. BESS utilizes most of the remaining excess PV generation to meet the year-round nighttime baseload of about 150 kW.

## Commercial Building (\$0/ton of CO<sub>2</sub>)

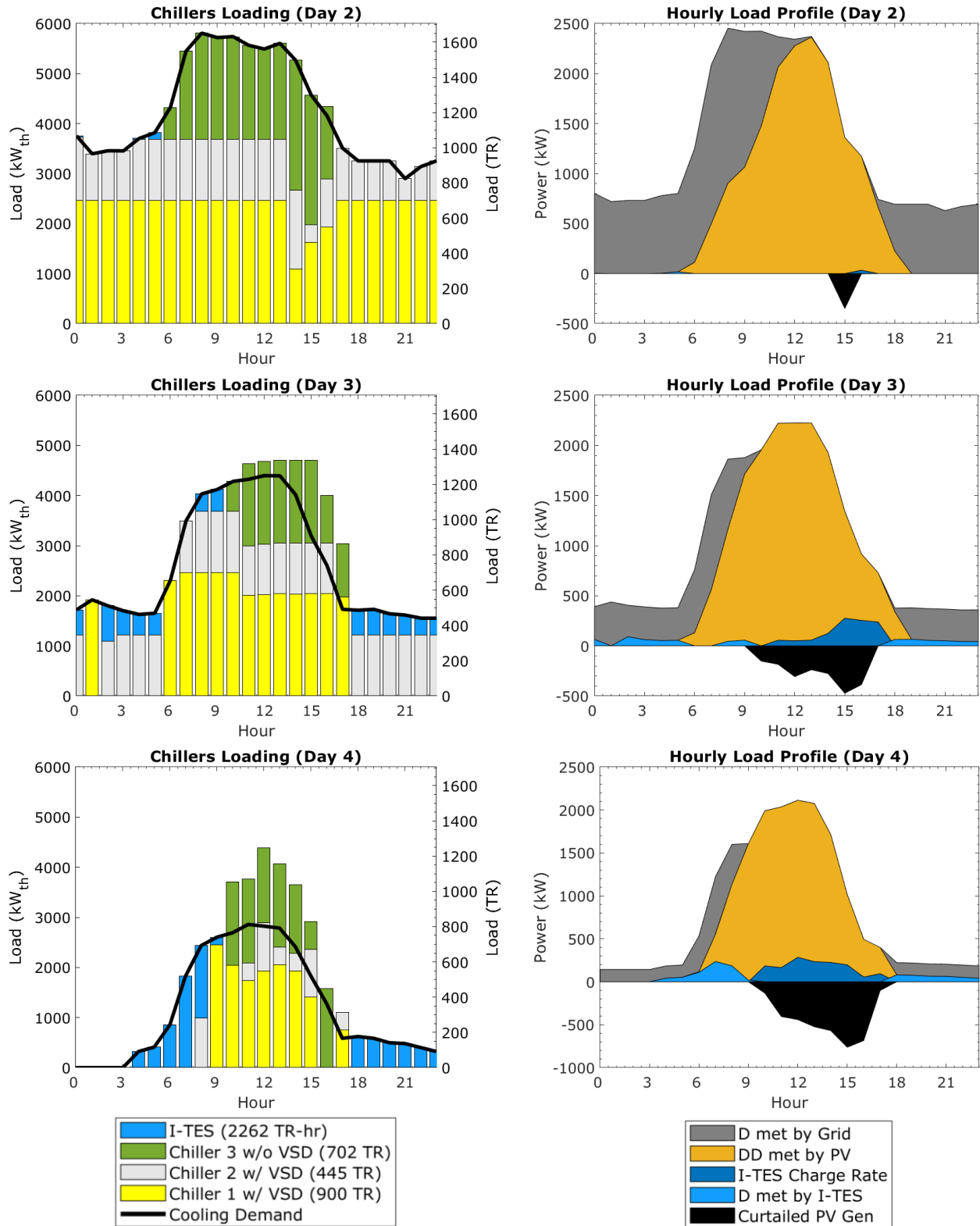


**Figure 4.12: Cost-optimal system with (a) chillers loading and (b) hourly load profile for the commercial building without carbon pricing.**

## Commercial Building (\$100/ton of CO<sub>2</sub>)

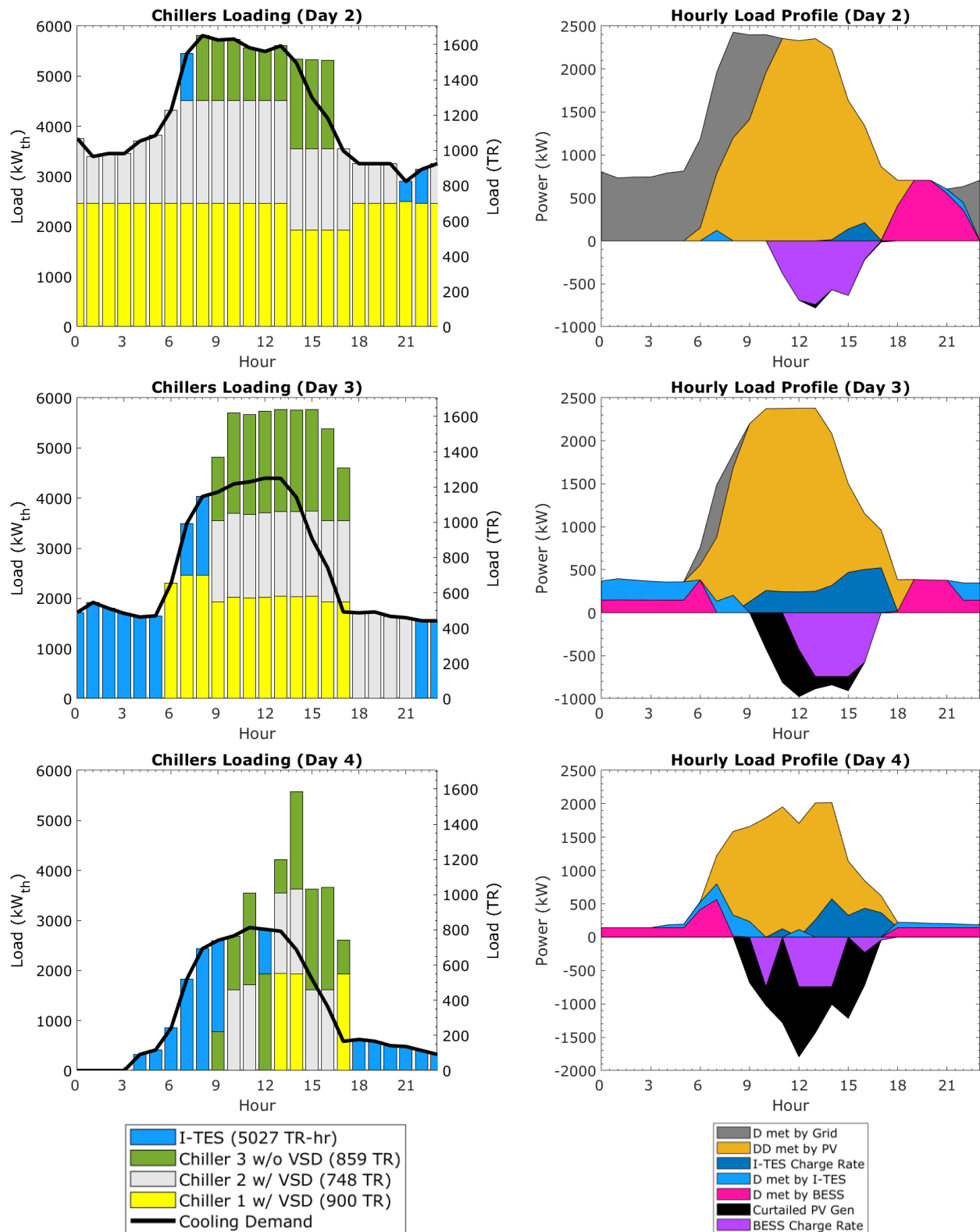


**Figure 4.13: Cost-optimal system with (a) chillers loading and (b) hourly load profile for the commercial building with carbon pricing at \$100/ton of CO<sub>2</sub>.**



### 4.3.2 Residential building

The effect of carbon pricing on the cost-optimal system installed capacities are shown in Figure 4.14, and the corresponding system characteristics are shown in Figure 4.15. Unlike the commercial building, on-site PV capacity is below the building's peak electricity demand of 2300 kW due to multiple reasons: (i) misalignment of building demand peak with solar insolation peak; (ii) without a feed-in tariff, the highly seasonal load leads to low utilization and large curtailments; and (iii) low carbon pricing does not support the use of energy storage.

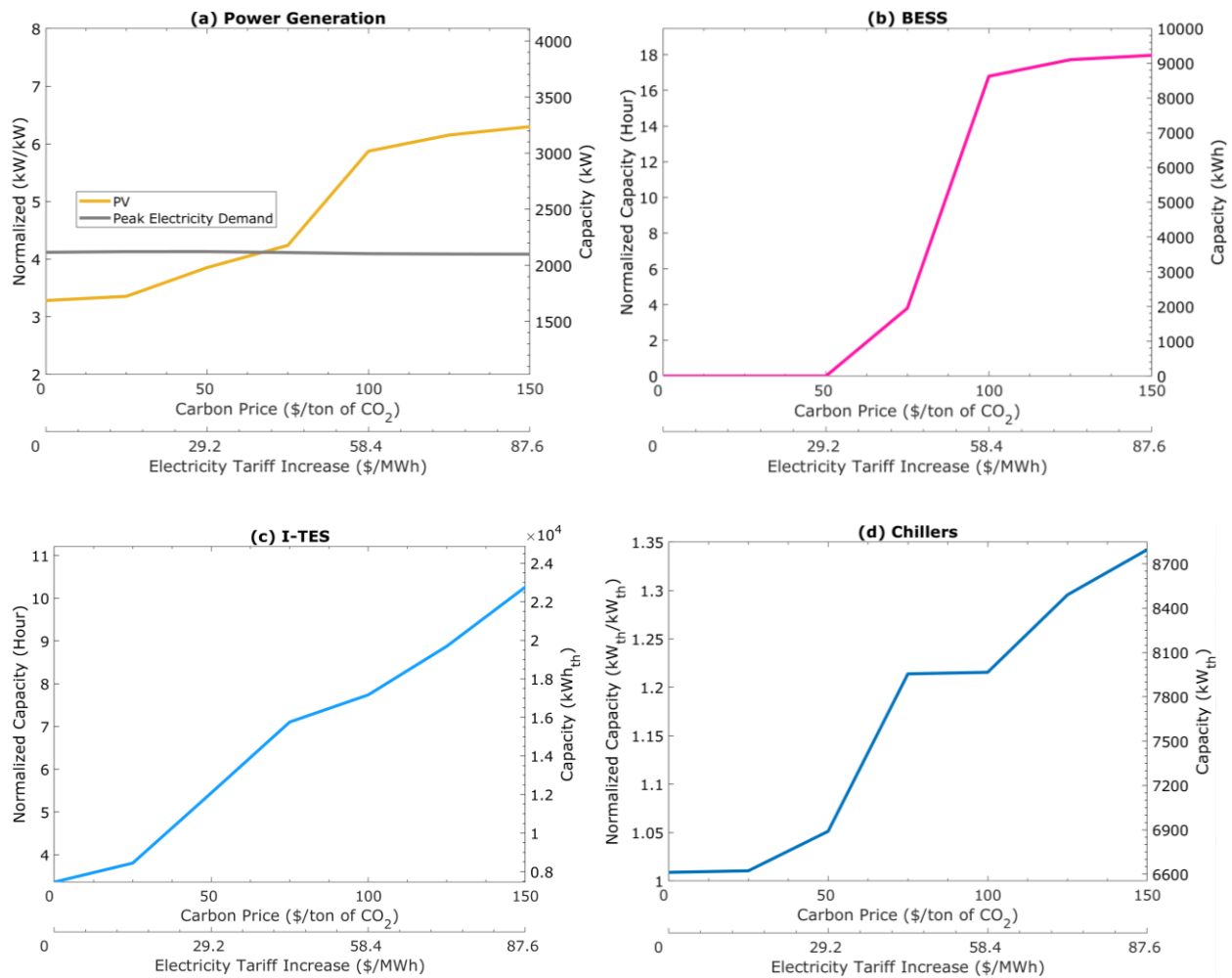


**Figure 4.14: Effect of carbon pricing on the cost-optimal system installed capacities of (a) PV, (b) BESS, (c) I-TES, and (d) chillers for the residential building. PV and BESS are normalized to the average electric demand of 515 kW, I-TES is normalized to the average cooling load of 2213 kW<sub>th</sub>, and the total capacity of chillers is normalized to the peak cooling demand of 7160 kW<sub>th</sub>.**

Carbon pricing above \$75/ton of CO<sub>2</sub> promotes using BESS and larger PV and I-TES capacities. Supported by a larger night-time load, BESS capacity was three times larger in the residential building than in the commercial building. I-TES capacity is nearly identical, primarily constrained by the chillers' cooling capacity and the narrow window of charging. A system with a carbon price at \$100/ton of CO<sub>2</sub> reduces emissions by about 87%, of which PV, BESS, and I-TES contribute 42%, 37%, and 8%, respectively, which matches the commercial building.

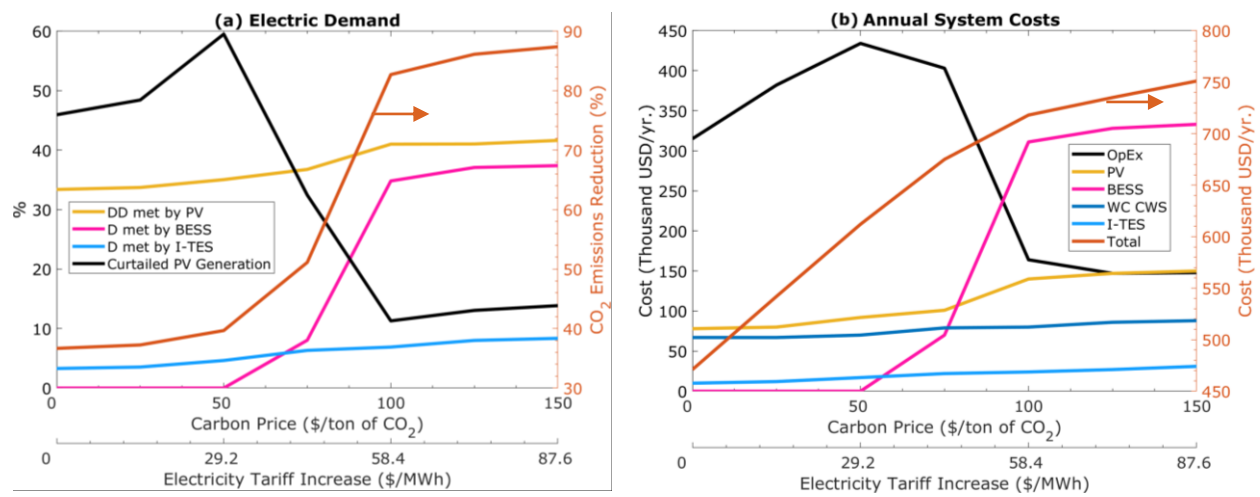


**Figure 4.15: Effect of the carbon price increases on (a) contribution to meeting the electric demand and (b) breakdown of annual system cost for the residential building.**

Annual system cost in the cost-optimal system with a carbon price below \$100/ton of CO<sub>2</sub> is overwhelmingly dominated by OpEx alone. Once BESS becomes economical, the annual system cost becomes predominantly from BESS, accounting for nearly half of the annual system cost. For this system, OpEx is reduced by a factor of 2 relative to a system without carbon pricing. Although both buildings reach a decarbonization rate of about 90% with a carbon price of \$100/ton of CO<sub>2</sub>, the system cost in the commercial building is 30% less due to better integration of PV generation, which reduces the needed costly energy storage capacity. Furthermore, investment in BESS and I-TES increases the annual system cost by 25% from \$600

thousand/yr. to \$750 thousand/yr. while abating nearly 3000 tons of CO<sub>2</sub>/yr. (50% of yearly carbon emissions).

As carbon pricing increases, carbon abatement cost and the abated CO<sub>2</sub> for the residential building are shown in Figure 4.16. Carbon abatement cost is initially negative due to exploiting low-cost PV generation. Unlike the analysis outcome for the commercial building, the mismatch between demand and solar insolation requires energy storage which drives carbon abatement costs to \$40/ton of CO<sub>2</sub>.

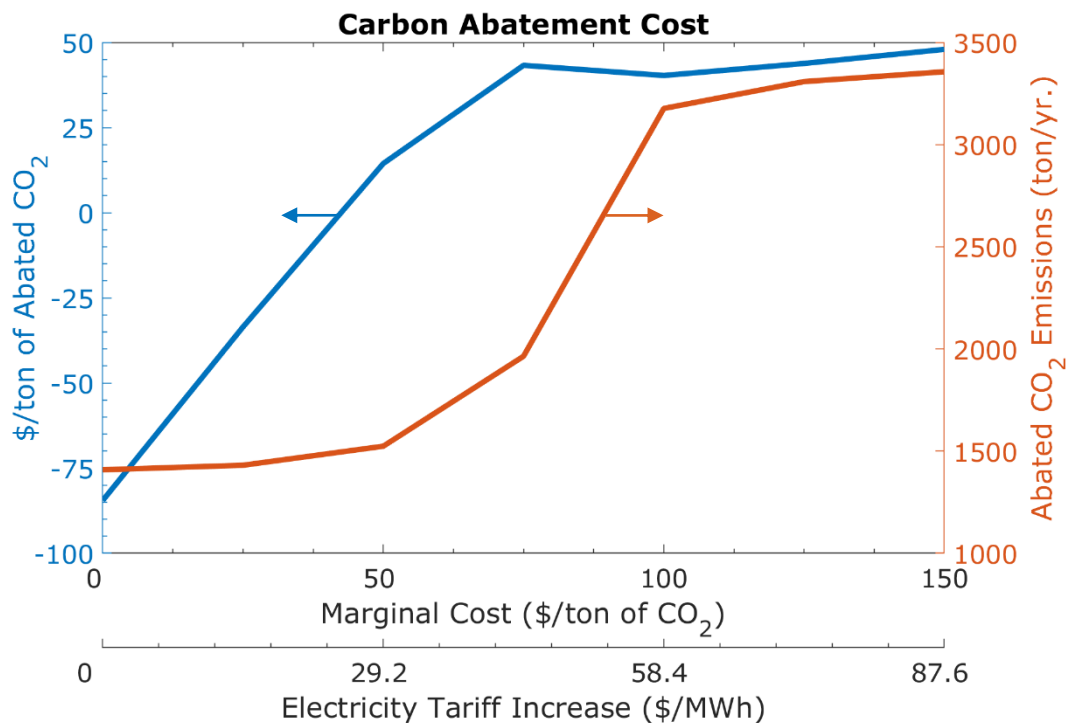


**Figure 4.16: Carbon abatement cost and abated CO<sub>2</sub> for the residential building.**

Decided chiller capacities and compressor technology types are tabulated in Table 4.7. Similar to the commercial building analysis, the cost-optimal system consists of two chillers with VSD-equipped centrifugal compressors for optimized part load performance. This selection is supported by the large intra-annual variations in wet-bulb temperatures, independent of building energy use. The lower-cost screw chiller aids I-TES charging and supplements cooling in the

high-cooling demand season. However, a relatively larger VSD chiller capacity and a relatively smaller screw chiller are selected for the residential building at a low carbon tax. The difference in selection is attributed to the more evenly distributed cooling demand, which a larger VSD chiller capacity could benefit from for optimized part-load performance. Similarly, the decided design temperature differential in the evaporator for all scenarios is about 8°C, which is on par with recommendations by chillers manufacturer Trane [75].

**Table 4.7: Optimal-cost cooling system capacities for the residential building**

Carbon Price (\$/ton of CO <sub>2</sub> )	CWS Cost (Thousand \$/yr.)	I-TES Capacity (kW <sub>th</sub> )	Chiller 1 (VSD Centrifugal) (kW <sub>th</sub> )	Chiller 2 (VSD Centrifugal) (kW <sub>th</sub> )	Chiller 3 (Fixed Speed Screw) (kW <sub>th</sub> )	Total Chiller Capacity (kW <sub>th</sub> )
Base	67	0	3,165	2,269	1,145	6,580
0	67	7,457	3,165	1,925	1,521	6,612
25	68	8,441	3,165	2,065	1,391	6,621
50	70	12,081	3,165	1,963	1,761	6,889
75	79	15,760	3,165	1,721	3,071	7,956
100	80	17,165	3,165	2,051	2,751	7,967
125	86	19,687	3,165	3,127	2,197	8,490
150	88	22,758	3,165	2,922	2,708	8,796

Hourly chillers loading and load profile for Scenarios 2-4 for a system without carbon pricing are shown in Figure 4.17, and for a system with a carbon price at \$100/ton of CO<sub>2</sub> are shown in Figure 4.18. A large amount of PV generation is curtailed, especially in the low cooling demand season compared to the commercial building. However, as carbon pricing increases and BESS becomes cost-effective, most excess of the generation is utilized to meet nighttime electricity needs. Although I-TES's role is slightly more pronounced in the residential building than in the commercial building, the system is dominated by BESS due to a reliable baseload.

## Residential Building (\$0/ton of CO<sub>2</sub>)

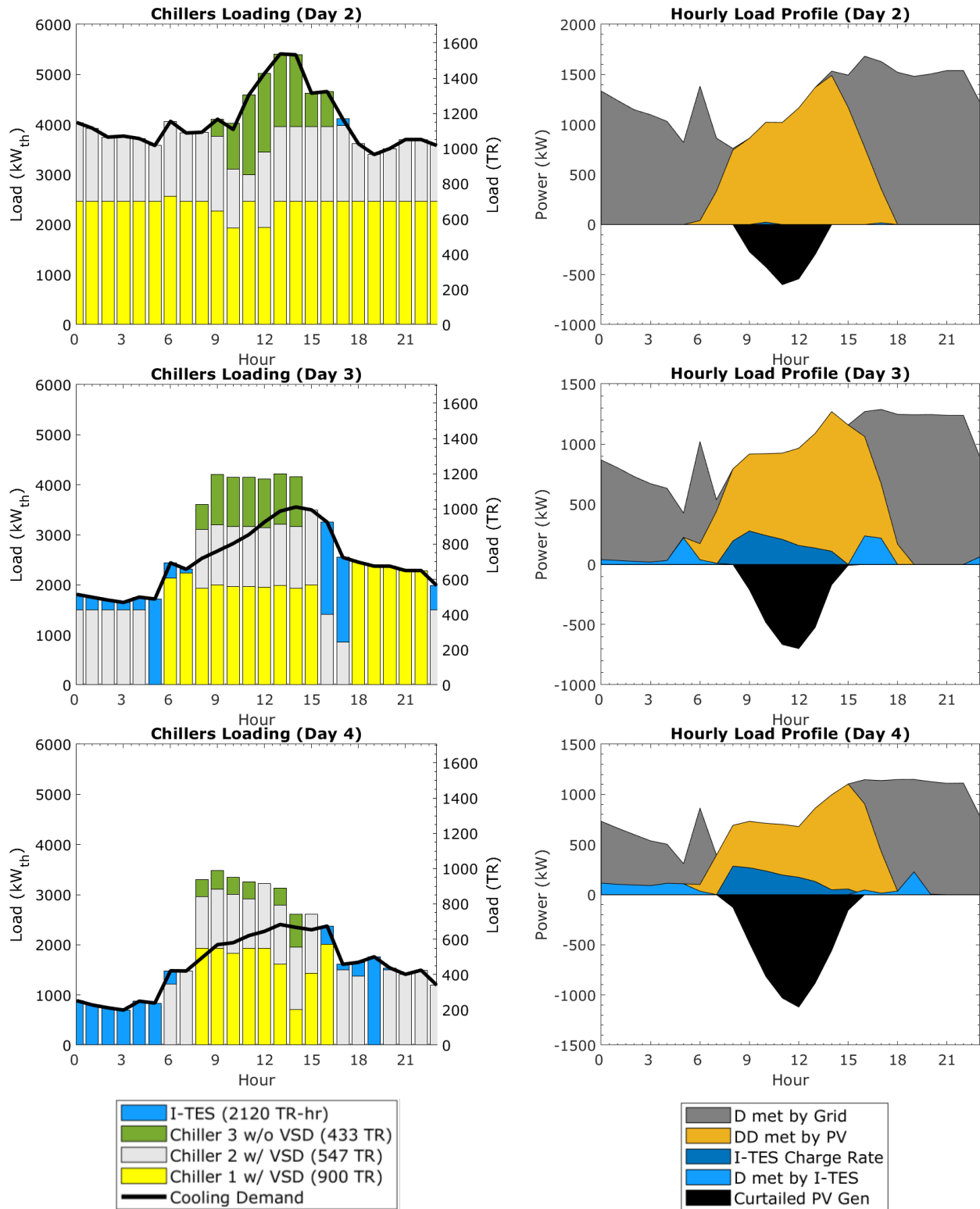


**Figure 4.17: Cost-optimal system with (a) chillers loading and (b) hourly load profile for the residential building without carbon pricing.**

## Residential Building (\$100/ton of CO<sub>2</sub>)

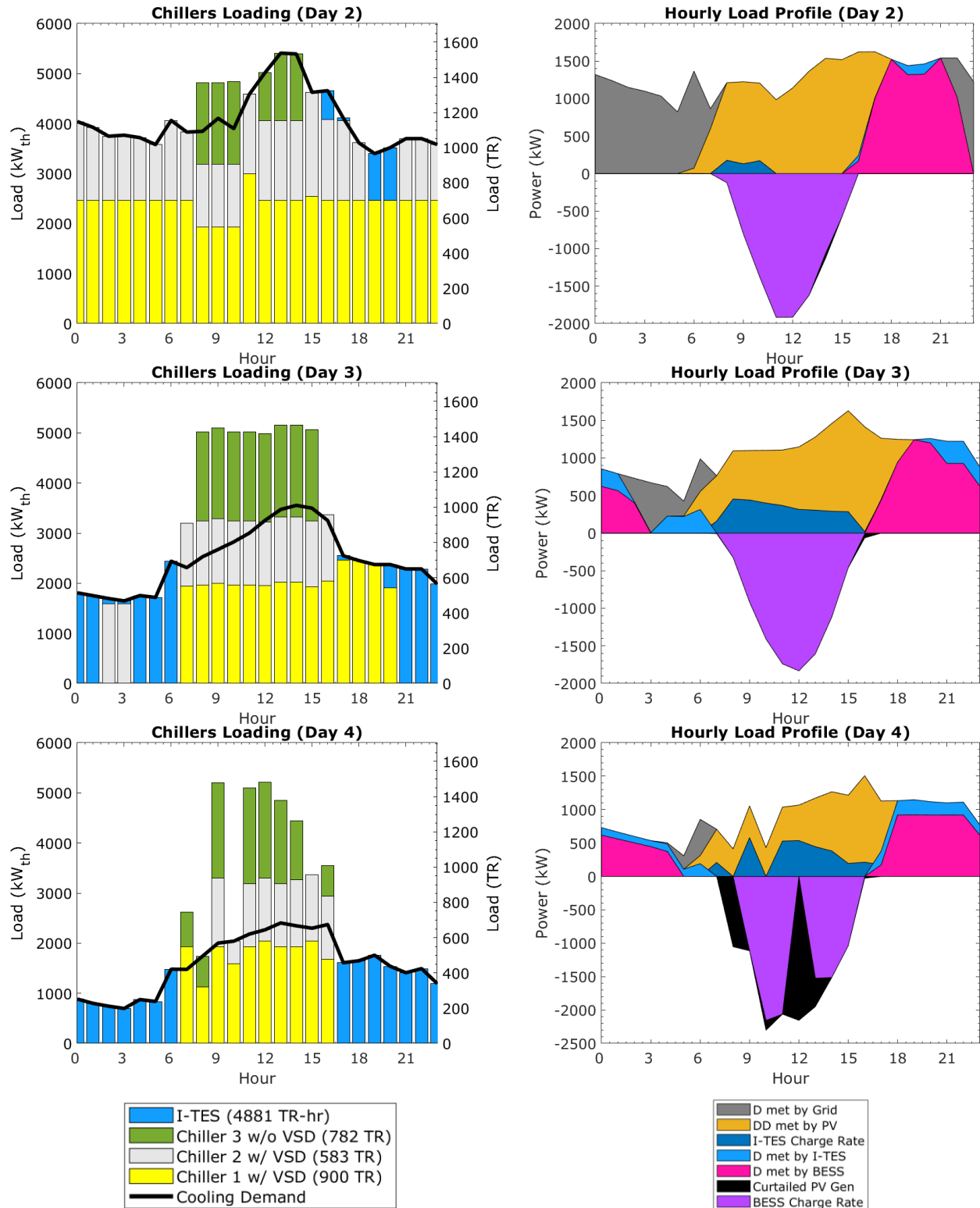


**Figure 4.18: Cost-optimal system with (a) chillers loading and (b) hourly load profile for the residential building with carbon pricing at \$100/ton of CO<sub>2</sub>.**

## 4.4 Conclusion

This chapter examined the decarbonization pathway from a building scale and proposed a solution to the capacity sizing and design problem of an integrated WC CWS with I-TES, BESS, and on-site PV generation for cost and emissions reduction. To combat low electricity rates in Qatar, the model was exposed to a range of carbon pricing. Energy demand profiles were simulated for two buildings that are typical and representative of building stock in Qatar with two uses, business-commercial and residential. These two buildings generally have an inversely related occupancy rate as people move from their workplaces to their residences.

A challenge confronted when sizing equipment is estimating their energy, which requires solving the highly non-linear and complex scheduling and dispatch problem. The approach was to decompose the problem into a bi-level optimization formulation and simplify the components model, particularly the chiller and I-TES models. The upper level minimizes yearly total system costs and decides the installed capacities and design parameters using particle swarm optimization. The decided parameters are passed down to solve the scheduling and dispatch problem in a mixed-integer linear program with piece-wise linearization and return the estimated yearly electricity charges to adjust the guesses for the next iteration.

The developed optimization strategy can be applied to newly constructed buildings for better integration with PV generation from the ground up or buildings with existing cooling systems for energy storage and PV capacity sizing. Furthermore, the strategy can be altered to be compatible with other on-site renewable energy sources or applied to improve renewable integration in the electricity grid communicated via a pricing signal. While the algorithm is applied to buildings in Qatar, the developed strategy can be broadly applied to buildings with different cooling technologies and under different climatic conditions.

The distributed scale analysis affirmed the suitability of decarbonizing the electricity grid using PV-enabled solutions, although at a higher cost than utility-scale. Commercial buildings with diurnal demand synergetic with solar insolation are particularly well suited for exploiting PV generation and can achieve a decarbonization rate above 60% without carbon pricing. I-TES is suitable for utilizing the large idle chiller capacities during the shoulder cooling season for cooling load shifting and could reduce building carbon emissions by 5-10%. Carbon pricing does not make I-TES suitable for load shifting in the high cooling season because of (i) chiller capacity degradation in ice-making mode, (ii) reduced idle chiller capacity from higher cooling demands, and (iii) the narrow window of charging of no more than 8 hours a day. The chillers' cooling capacity must be extraordinarily oversized for I-TES to be used in the high cooling demand season. BESS becomes cost-effective with carbon pricing above \$75/ton of CO<sub>2</sub> and is used to meet the near year-round constant baseload since it requires a high daily capacity utilization rate is around 90%. With carbon pricing above \$100/ton of CO<sub>2</sub>, the cost-optimal system can yield a decarbonization rate of about 90% for either building. Similar to the utility-scale analysis, BESS decarbonizes the base load. Without a feed-in tariff, the aggregate non-cooling load is reliable and steady, which makes the utility-scale implementation of BESS more cost-effective.

Limitations of the outcome of the analysis include (i) the simplified models, which do not fully capture the complex behavior of cooling systems, and (ii) the selected representative performance curves for compressor technologies may not fully represent the magnitude of performances delivered by various manufacturers. Nevertheless, the exploration of additional representative curves, including multiple curves for different compressors of the same type, can be achieved at the expense of an increase in computational time.



## **Chapter 5: Optimal equipment scheduling and dispatch of WC**

### **CWS with I-TES**

#### **5.1 Introduction**

Demand side management is an instrument the electric utility uses to adjust demand to match the power supply better. Demand-side management is essential in low-carbon power grids examined in Chapters 2 and 4 since intermittent renewable generations cannot be dispatched or perfectly predicted. Dynamic pricing, such as time-of-use (TOU) and real-time pricing, are well-explored methods for demand control. They offer cost savings for the utility and the consumers through better management and dispatch of power generations with demand. Cooling is responsible for about half of the electricity demand in Qatar, thereby making cooling systems a crucial target for demand-side management. However, operating CWS to maximize savings from demand side management can be challenging. This challenge stems from operating the system outside its design conditions, which requires careful consideration of chillers' part-load performances and the performances of associated auxiliary equipment.

The literature is rich with attempts to solve the chilled water system's scheduling problems [147]–[156]. Most of the literature neglects the roles of auxiliary components and only considers the problem of loading chillers. They tend to assume a fixed water supply and condenser temperatures. This simplifies the chiller model to a cubic or often a quadratic function of their loading. Various optimization strategies are used to solve these problems, ranging from simple linear to quadratic programming and meta-heuristic optimization strategies like genetic algorithm and particle swarm optimization. The most detailed model found in the literature was developed by Zhang et al. [157]. The formulation captures the complex behavior of chillers and cooling towers using regression-based models and takes supply and condenser water

temperatures as decision variables. The considered solution approach is near-optimal using sequential quadratic programming. In another work, Zhang et al. [158] consider the effect of minimum up/down time constraints on the optimization. Their work suggests that minimum up/down-time significantly increases the complexity of the problem with little return in cost minimization, and it is best-handled post-computation heuristically. Trautman et al. [159] formulated a detailed CWS model to optimize the condenser water pump and tower fan speed. Their model results suggest that optimal tower fan speed can achieve 12-15% energy savings, while condenser pump control has negligible energy savings.

Much attention has been given to the scheduling problem with thermal energy storage [55], [130], [160]–[167]. A more sophisticated model and optimization strategy are often used in these problems. Lee et al. [160] used meta-heuristic particle swarm optimization to minimize the I-TES life cycle cost for a single chiller WC CWS. Chen et al. [162] utilized the dynamic programming method to optimize a CWS with I-TES. Kamal et al. [167] used an evolutionary algorithm to optimize a multi-chiller CWS with I-TES and chilled water storage for load shifting and cost reduction. Storage was found to reduce cost and equipment size.

This chapter proposes a solution to the scheduling and dispatch problem of CWS with I-TES to reduce operating costs. The proposed solution provides a reasonably scalable and robust approach that can be used on highly non-linear space cooling and heating problems, thereby negating the need for simplistic models developed in the literature. CWS operators can use the output of the optimization problem to optimize plant operation.

This chapter is organized as follows: the methodology is presented in Section 5.2. The problem formulation and assumptions are laid out, followed by the optimization strategy. Section 5.3 presents the results with three scenarios of cooling demand under TOU electricity pricing.

The proposed approach is compared to two commonly used heuristic strategies for storage use: chiller and storage priority control. Lastly, the chapter is concluded in Section 5.4.

## 5.2 Methodology

### 5.2.1 Problem formulation

The overall framework is to determine the scheduling of equipment, setpoints, and storage dispatch amount such that the cooling load is met with the least cost, influenced by the cooling load, storage capacity and utilization, and TOU rates. The hybrid steady-state models developed in Chapter 3 for I-TES and the key power-consuming components, including the chillers, cooling towers, water pumps, and cooling coil fans, are used in this chapter with the addition of several operational and balancing constraints derived from mass and energy balance. An illustration of the analyzed system is shown in Figure 5.1 below.

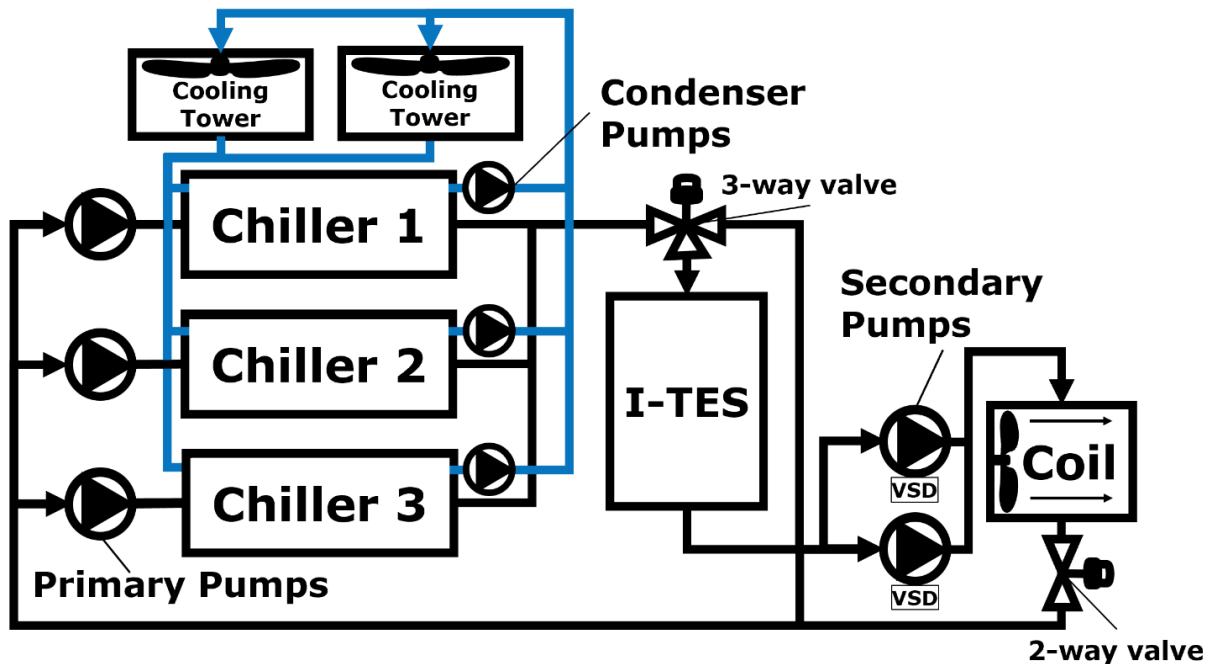


**Figure 5.1: The considered CWS in a primary-secondary configuration with three WC chillers (two 212-tons Carrier 19XR chillers with VSD and one 153-tons Trane RTHB chiller), two shared cooling towers (360 tons each), and I-TES (1600 TR-hr). The building is represented in a single coil with the respective aggregate cooling load.**

The system is comprised of three chillers that were selected from the chillers data library in EnergyPlus: two 212-tons Carrier 19XR with VSD-equipped centrifugal compressor chillers and one 153-tons Trane RTHB screw chiller without VSD, at their reference performance with a cumulative cooling capacity of 570 tons, two 360 tons cooling towers, and 1600 TR-hr internal melt I-TES for a design building cooling demand of 730 tons. The considered model parameters can be found in Appendix C. The plant operating cost, which is to be minimized, is given by  $\sum_t c_t^e P_t^{Sys}$ , where:

$$P_t^{Sys} = \sum_{j \in \mathcal{J}} (P_{t,j}^{chl} + P_{t,j}^{pp} + P_{t,j}^{cp}) + \sum_{n \in \mathcal{N}} P_{t,n}^{twr} + \sum_{g \in \mathcal{G}} P_{t,g}^{sp} + P_t^{cf}, \quad \forall t \in \mathcal{T} \quad (5.1)$$

where the subscripts  $j$  is the chiller index set  $\{1, 2, 3\}$  denoted by  $\mathcal{J}$ ,  $t$  is the time-step index set  $\{1, 2, 3, \dots, 24\}$  denoted by  $\mathcal{T}$  that refers to the hours of the day,  $n$  is the cooling tower index set  $\{1, 2\}$  denoted by  $\mathcal{N}$ , and  $g$  is the secondary pump index set  $\{1, 2\}$  denoted by  $\mathcal{G}$ .  $c_t^e$  is TOU electricity rates,  $P$  is the power consumed of which superscripts  $pp$  refers to primary pumps,  $cp$  to condenser pumps,  $twr$  to cooling tower fans,  $sp$  to secondary pumps,  $cf$  to the cooling coil fan, and  $Sys$  to the total system power use.

The decision variables are: chillers and tower scheduling ( $ON_{t,j}^{chl}$  and  $ON_{t,n}^{twr}$ ), chillers temperatures setpoints ( $T_{t,j}^{sw}$ ), cooling towers temperature setpoints and speed ( $T_t^{csw}$  and  $VSD_t^{twr}$ ), coil fan and pump speeds ( $VSD_t^{sp}$  and  $VSD_t^{cf}$ ), and flowrate to storage ( $\dot{m}_t^{iw}$ ). Designated temperatures and flowrates symbols at various system nodes that appear in the problem formulation are shown in Figure 5.2.

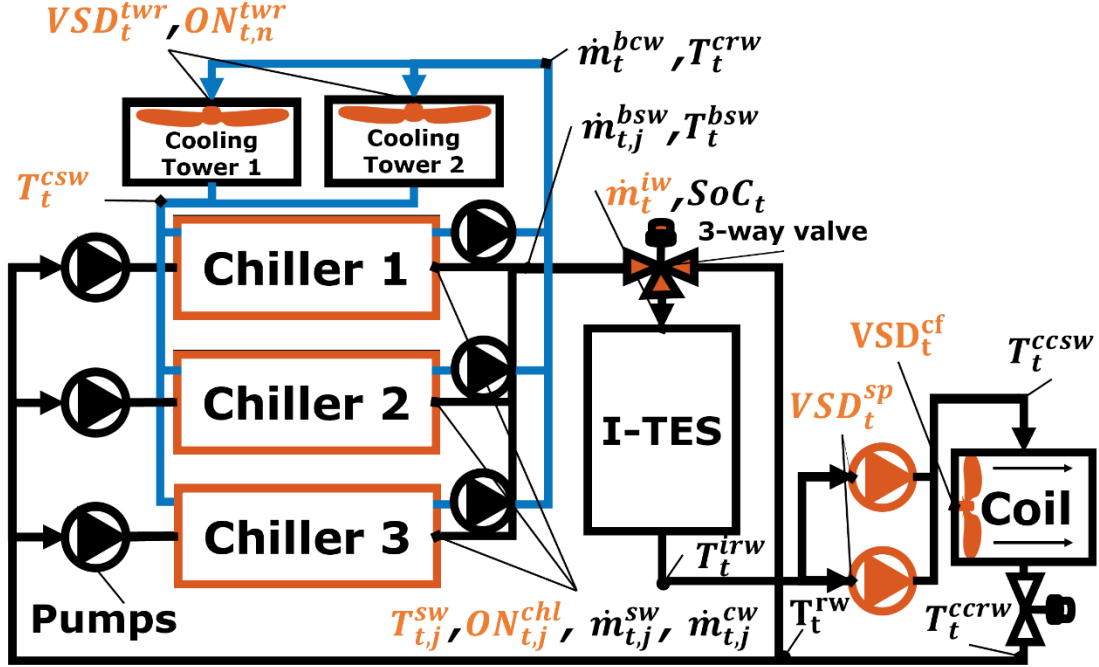


Figure 5.2: The considered CWS with decision variables highlighted in orange and variables in black are consequences of the decision variables.

The first constraint bounds operating chillers to within permitted part-load ratios and is given by:

$$PLR_j^{min} \leq PLR_{t,j} \leq PLR_{t,j}^{max}, \forall t \in \mathcal{T}, \forall j \in \mathcal{J} \quad (5.2)$$

where  $PLR_j^{min}$  is the minimum chiller part-load ratio obtained from EnergyPlus,  $PLR_{t,j} =$

$\dot{Q}_{t,j}^{chl} / \dot{Q}_j^{chl,des}$ , and  $PLR_{t,j}^{max} = \dot{Q}_{t,j}^{chl,max} / \dot{Q}_j^{chl,des}$  from the estimated chillers' cooling capacity in

Equation (3.13). The second and third constraints bound and set the initial storage SoC as

follows:

$$0 \leq SoC_t \leq 1, \forall t \in \mathcal{T} \quad (5.3)$$

$$SoC_0 = 0 \quad (5.4)$$

The storage is assumed to be initially empty. The fourth constraint bounds the fraction of the coil in the dry section as follows:

$$0 \leq f_t^{dry} \leq 1, \quad \forall t \in \mathcal{T} \quad (5.5)$$

Constraints 5-7 are three load balancing constraints given by:

$$\sum_{j \in \mathcal{J}} (PLR_{t,j} \dot{Q}_j^{chl,des}) - \dot{m}_t^{iw} c^{p,sw} (T_t^{irw} - T_t^{bsw}) - \dot{Q}_t^{\mathcal{D}} = 0, \quad \forall t \in \mathcal{T} \quad (5.6)$$

$$VSD_t^{sp} \dot{m}_t^{bsw} c^{p,sw} (T_t^{ccrw} - T_t^{ccsw}) - \dot{Q}_t^{\mathcal{D}} = 0, \quad \forall t \in \mathcal{T} \quad (5.7)$$

$$VSD_t^{cf} \dot{m}_t^{cca,des} (h_t^{ai} - h_t^{ae}) - \dot{Q}_t^{\mathcal{D}} = 0, \quad \forall t \in \mathcal{T} \quad (5.8)$$

The constraints ensure the building demand,  $\dot{Q}_t^{\mathcal{D}}$ , is met by both the chiller and storage in (5.6) and delivered to the coil waterside in (5.7) and the air side in (5.8).  $T_t^{bsw}$  and  $\dot{m}_t^{bsw}$  are the blended supply water temperature and flowrate from mixing streams leaving the chillers,  $T_t^{irw}$  and  $\dot{m}_t^{iw}$  are I-TES leaving water temperature and flowrate,  $T_t^{ccsw}$  and  $T_t^{ccrw}$  are cooling coil supply and return water temperatures, respectively,  $h_t^{ai}$  and  $h_t^{ae}$  are cooling coil entering and leaving enthalpy of moist air, respectively,  $c^{p,sw}$  is the water-glycol mixture specific heat, and  $VSD$  is the non-dimensional rotational speed defined as the actual angular speed normalized by the maximum angular speed. The amount of water delivered to the cooling coils is controlled by modulating the secondary pump speed,  $\dot{m}_t^{ccw} = VSD_t^{sp} \dot{m}_t^{bsw}$ . The fourth balancing constraint balances mass flowrate to storage and available mass flowrate in the primary loop as follows:

$$\dot{m}_t^{bsw} - \dot{m}_t^{iw} \geq 0, \quad \forall t \in \mathcal{T} \quad (5.9)$$

The fifth and last constraint balances the heat rejected by the chillers and cooling towers as follows:

$$\dot{m}_t^{bcw} c^{p,cw} (T_t^{crw} - T_t^{csw}) - \sum_{n \in \mathcal{N}} \dot{Q}_{t,n}^{twr} ON_{t,n}^{twr} = 0, \quad \forall t \in \mathcal{T} \quad (5.10)$$

where  $\dot{Q}_{t,n}^{twr}$  is the heat rejected from the tower,  $\dot{m}_t^{bcw}$  is the condenser blended water flowrate from the mixing of streams,  $T_t^{csw}$  and  $T_t^{crw}$  are blended chillers entering and leaving condenser water temperatures, respectively, and  $c^{p,cw}$  is condenser water specific heat. Each operating cooling tower receives an equivalent fraction of water mass flowrate such that  $\dot{m}_t^{wtwr} = \dot{m}_t^{bcw} / \sum_{n \in \mathcal{N}} ON_{t,n}^{twr}$ , and is controlled at the same speed to maintain the condenser water temperature setpoint. Similarly, secondary pumps are controlled at the same speed to deliver an equal amount of flow. For systems with a more sophisticated secondary pumping configuration, their optimal scheduling and speed configuration can be determined beforehand and represented as a function of flowrate. The optimal scheduling and speed configuration does not depend on chillers' settings upstream.

The total flowrates in the primary and condenser loops are dictated by the design evaporator and condenser flowrates for operating chillers, respectively, which are given by:

$$\dot{m}_t^{bsw} = \sum_{j \in \mathcal{J}} \dot{m}_j^{sw} ON_{t,j}^{chl}, \quad \forall t \in \mathcal{T} \quad (5.11)$$

$$\dot{m}_t^{bcw} = \sum_{j \in \mathcal{J}} \dot{m}_j^{cw} ON_{t,j}^{chl}, \quad \forall t \in \mathcal{T} \quad (5.12)$$

Primary loop blended supply and return temperature are computed from the mixing of streams as follows:

$$T_t^{bsw} = \sum_{j \in \mathcal{J}} \frac{\dot{m}_j^{sw}}{\dot{m}_t^{bsw}} T_{t,j}^{sw} ON_{t,j}^{chl}, \quad \forall t \in \mathcal{T} \quad (5.13)$$

$$T_t^{rw} = VSD_t^{sp} T_t^{ccrw} + (1 - VSD_t^{sp}) T_t^{ccsw}, \quad \forall t \in \mathcal{T} \quad (5.14)$$

The water-glycol mixture temperature at the coil inlet deviates from the supply water temperature based on the storage dispatch amount as described by:

$$T_t^{ccsw} = \left(1 - \frac{\dot{m}_t^{iw}}{\dot{m}_t^{bsw}}\right) T_t^{bsw} + \frac{\dot{m}_t^{iw}}{\dot{m}_t^{bsw}} T_t^{irw}, \quad \forall t \in \mathcal{T} \quad (5.15)$$

The I-TES exit temperature is computed by re-arranging Equation (3.52) in Chapter 3 as follows:

$$T_t^{irw} = T_t^{bsw} - \varepsilon_t^{ITES} (T_t^{bsw} - T_t^{ITES}), \quad \forall t \in \mathcal{T} \quad (5.16)$$

The storage effectiveness,  $\varepsilon_t^{IS}$ , is updated in increments of 10 minutes to capture any change in charge and discharge rates within a time step. The storage temperature is initially 6°C and reaches 0°C when latent charging mode initiates. For all other modes and in discharging, the effectiveness is computed with  $T_t^{ITES}$  at a reference temperature of 0°C. The storage temperature in sensible charging and the storage SoC are updated as follows:

$$T_{t+1}^{ITES} = T_t^{ITES} - \frac{\dot{m}_t^{iw} c_{p,sw} (T_t^{irw} - T_t^{bsw})}{\dot{m}_t^{ITES} c_{p,w}} \Delta t, \quad \forall t \in \mathcal{T} \quad (5.17)$$



and,

$$SoC_{t+1} = SoC_t + \frac{\dot{m}_t^{iw} c^{p,sw} (T_t^{irw} - T_t^{bsw})}{3600 C^{ITES}} \Delta t, \quad \forall t \in \mathcal{T} \quad (5.18)$$

where  $C^{ITES}$  is I-TES capacity,  $m_t^{ITES}$  and  $c^{p,w}$  are the mass and specific heat of the water inside the I-TES tanks, and  $\Delta t$  is the time step in seconds. The temperature of the returning condenser water to the cooling tower is computed from the following expression:

$$T_t^{crw} = T_t^{csw} + \frac{\sum_{j \in \mathcal{J}} (P_{t,j}^{chl} + Q_{t,j}^{chl})}{\dot{m}_t^{bcw} c^{p,cw}}, \quad \forall t \in \mathcal{T} \quad (5.19)$$

## 5.2.2 Optimization strategy

### 5.2.2.1 Bi-level formulation

A prevalent solution strategy in the literature is the genetic algorithm, a meta-heuristic evolutionary optimization strategy inspired by the theory of evolution. The algorithm can work with non-convex and non-continuous problems [168]–[170], typically confronted with equipment scheduling problems. They explore the solution space by using a population of potential solutions. The algorithm selects the fittest individuals to produce the next generation of solutions. Over multiple iterations, the algorithm evolves toward a globally optimal solution.

However, because of the nonlinearity and the large number of degrees of freedom, the problem described above is too cumbersome to be solved using either traditional gradient-based or meta-heuristic optimization strategies. The solution approach, as illustrated in Figure 5.3, is to decompose the problem into a bi-level optimization formulation to decouple the equipment scheduling problem at each hour from the storage dispatch. This simplifies the scheduling

problem sufficiently to allow for the use of the genetic algorithm for both levels. The upper level minimizes daily operation costs and decides the storage dispatch amount over the next 24 hours. The decided dispatch amount is fed to the lower-level optimizer to solve the equipment scheduling problem at each hour sequentially and return the corresponding system power consumption over the next 24 hours.

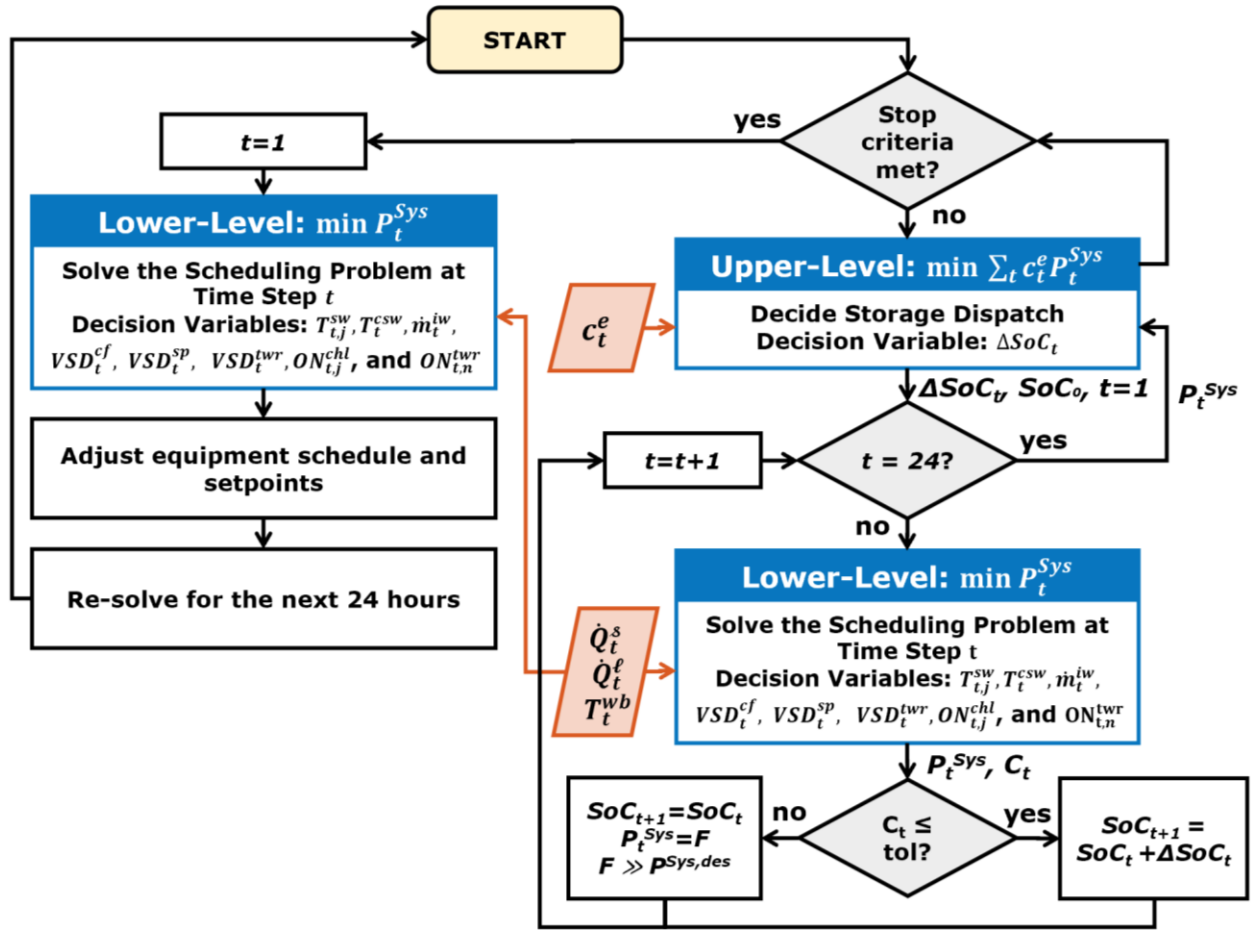


**Figure 5.3: The developed bi-level optimization strategy. The upper-level decided dispatch is passed down to the lower-level optimizer to solve the equipment scheduling problem sequentially. Infeasible storage dispatch at a given hour is rejected and penalized. The upper-level optimizer input is the TOU rates, and lower-level optimizer inputs are the sensible and latent cooling load and ambient wet-bulb temperature. The genetic algorithm is applied to both levels.**

Six constraints derived from mass and energy balance constrain the lower-level problem.

The added sixth constraint ensures that the I-TES dispatched amount in the lower level agrees with the decided dispatch amount by the upper-level optimizer. Storage dispatch amounts decided by the upper-level optimizer that lead to infeasible solutions are penalized. The constraints are handled using the penalty function method, which penalizes constraint violation and turns the problem into unconstrained optimization. The bi-level objective formulation is given by:

$$\min Obj^1 = \sum_{t \in \mathcal{T}} c_t^e P_t^{Sys} \quad (5.20)$$

$$\min Obj_t^2 = \left( \frac{P_t^{Sys}}{P_t^{Sys,des}} \right)^\alpha + C_t, \quad \forall t \in \mathcal{T} \quad (5.21)$$

where

$$C_t = \left[ \begin{array}{l} a_1 \left| 1 - \frac{\dot{m}_t^{iw} c^{p,sw} (T_t^{irw} - T_t^{bsw}) + \dot{Q}_t^{\mathcal{D}}}{\sum_{j \in \mathcal{J}} (PLR_{t,j} \dot{Q}_j^{chl,des})} \right|^{b_1} \\ + a_2 \left| \frac{VSD_t^{sp} \dot{m}_t^{bsw} c^{p,sw} (T_t^{ccrw} - T_t^{ccsw}) + \Delta}{\dot{Q}_t^{\mathcal{D}} + \Delta} - 1 \right|^{b_2} \\ + a_3 \left| \frac{VSD_t^{cf} \dot{m}_t^{cca,des} (h_t^{ai} - h_t^{ae}) + \Delta}{\dot{Q}_t^{\mathcal{D}} + \Delta} - 1 \right|^{b_3} \\ + a_4 \left| 1 - \frac{\dot{m}_t^{iw}}{\dot{m}_t^{bsw}} \right|^{b_4} [\dot{m}_t^{iw} > \dot{m}_t^{bsw}] \\ + a_5 \left| \frac{\dot{m}_t^{bcw} c^{p,cw} (T_t^{crw} - T_t^{csw})}{\sum_{n \in \mathcal{N}} \dot{Q}_{t,n}^{twr} ON_{t,n}^{twr}} - 1 \right|^{b_5} \\ + a_6 |SoC_t - SoC_t^{ulo}|^{b_6} \end{array} \right] \quad (5.22)$$

where  $\alpha$ ,  $a_1$  to  $a_6$ , and  $b_1$  to  $b_6$  are the penalty factors,  $SoC_t^{ulo}$  is the storage dispatch amount decided by the upper level, and  $\Delta$  is an arbitrarily small load ( $<1\%$  of  $\dot{Q}^{des}$ ) with the same unit as

$\dot{Q}_t^D$ . Bound constraints on chillers' part load ratio and storage SoC in Equations (5.2)-(5.3) are enforced by resetting the violating variable to the nearest bound. This inevitably leads to the violation of balancing constraints and thus discourages the genetic algorithm from populating that search space area. Solutions that violate the length of the dry section bound constraint in Equation (5.5) cannot be truncated and are eliminated from the algorithm gene pool.

Constraints are relaxed to allow for a violation of no more than 3%, although they largely fall below 1%. The system power use over the next 24 hours, as determined by the lower-level optimizer, is returned to the upper-level optimizer to update the storage dispatch guess for the next iteration. The input of the upper level is the TOU electricity prices, and the inputs for the lower level are the cooling load (sensible and latent), ambient wet-bulb temperature, and storage current SoC. The decision variable for the upper-level problem is the storage dispatch amount ( $\Delta SoC_t$ ) and the decision variables for the lower-level problem are setpoints

$(T_{t,j}^{sw}, T_t^{csw}, \dot{m}_t^{iw}, VSD_t^{cf}, VSD_t^{sp}, VSD_t^{twr})$  and equipment scheduling ( $ON_{t,j}^{chl}$ , and  $ON_{t,n}^{twr}$ ).

Upon meeting the algorithm stop criteria, the converged storage dispatch amount curve ( $\Delta SoC$  v. time) can be used to adjust equipment scheduling and setpoints while continuously re-solving for the next 24 hours to factor in deviations from forecasted demand and ambient conditions.

### 5.2.2.2 Parameters tuning

Balancing constraints in the lower-level problem are handled using the penalty function method. This method makes the objective function subject to influence by both the system power use and violations of balancing constraints. This poses a challenge for the genetic algorithm to assess the population's fitness effectively. There are 13 penalty factors in Equations (5.21)-(5.22); manual tuning of the 13 penalty factors is difficult and cumbersome, especially considering the impact of the cooling load, ambient wet-bulb temperature, and storage use on the

solution space. In addition to penalty factors, genetic algorithm parameters such as population size, crossover rate, number of generations, number of stall iterations, and elite count, among others, can highly impact the quality of the converged solution. A more systematic and robust approach is to tune the penalty factors and genetic algorithm parameters with training data using an optimizer such as particle swarm optimization.

Training data are manufactured by sampling various operating combinations of cooling load, ambient wet-bulb temperature, and storage SoC and dispatch amount. Feasible solutions, irrespective of optimality, should satisfy the constraints and hence can be used to tune the penalty factors. The intention is to allow the genetic algorithm at the lower level to distinguish apart the contribution of each variable to the objective function, better assess the population fitness and locate a feasible, globally optimal solution. The manufactured training data are shown in Figure 5.4. The dataset contains 237 unique combinations of cooling demand, ambient wet-bulb temperature, storage dispatch amount, and storage SoC. The objective function for the penalty factor tuning optimization is as follows:

$$\min Obj = \sum_{z \in \mathcal{Z}} [P_z + \beta C_z] \quad (5.23)$$

where,

$$P_z = \begin{cases} P_z^{sys} & C_z \leq tol \\ F & Otherwise \end{cases} \quad (5.24)$$

subscript  $z$  is data point index set  $\{1, 2, 3, \dots, 237\}$  denoted by  $\mathcal{Z}$ ,  $\beta$  is a constant that is manually adjusted such that  $\beta C_z$  sufficiently reduces constraints violation but not large enough to meaningfully impact the objective function,  $tol$  is the constraint relaxation tolerance (taken as

3% for the analysis), and  $F$  penalizes ( $F \gg P^{Sys,des}$ ) infeasible solutions ( $C_z > tol$ ). Tuning of the penalty factors eliminated the genetic algorithm problem of premature convergence.

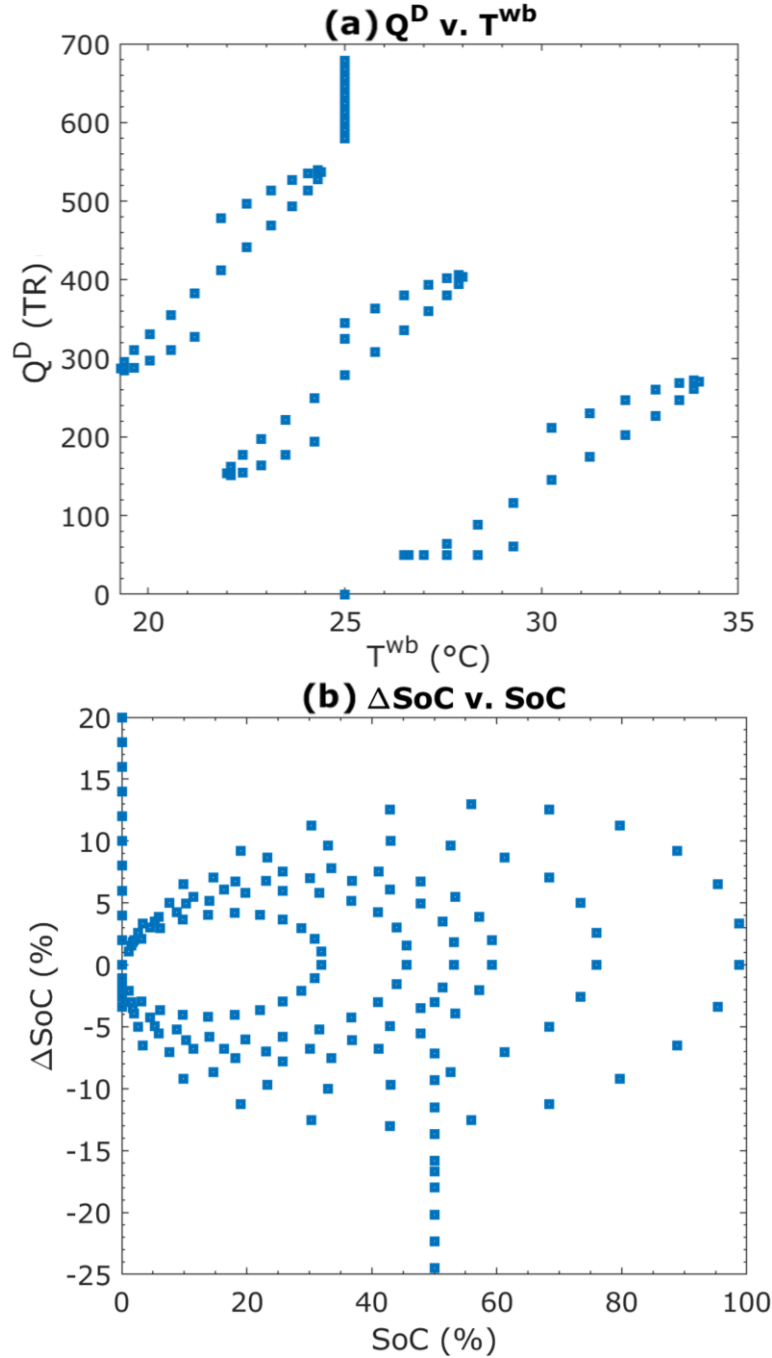


**Figure 5.4: Manufactured Training data with (a) cooling demand v. wet-bulb temperature and (b) storage dispatch amount and SoC. This set has 237 unique data points, each an independent input condition for the scheduling problem. A sensible heat ratio of 0.7 is assumed.**

The optimal system COP for three modes of storage operation (charging, discharging, and idle) generated for the considered system under a range of cooling loads are shown in Figure 5.5 at a design wet-bulb temperature of 25°C. Despite the problem's high nonlinearity and complexity, the tuned penalty factor and genetic algorithm parameters resulted in near-smooth and continuous system performance curves. The curve's shape is a consequence of the three-chillers system. There are two configurations for operating this system when charging at a rate of 160 tons in Figure 5.5 (a) since the smallest chiller cannot provide sufficient cooling on its own. At lower than 300 tons, the system utilizes a more efficient configuration of two centrifugal chillers for charging. When discharging or idling, like in Figures 5.5 (b) and (c), the more complex shape is caused by the operation of the three chillers. At lower loads, it is sufficient to use one chiller to reduce parasitic pump power use. However, as the load increase, more thoughtful consideration is necessary to schedule the remaining chillers. At higher loads, the system is obligated to use all chillers.

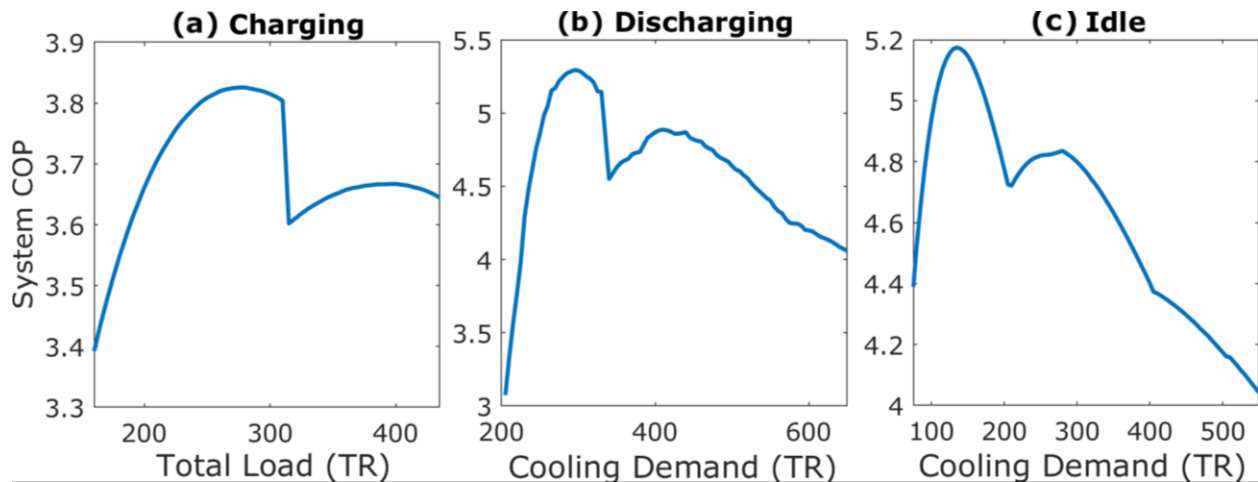


**Figure 5.5: System COP for a range of cooling loads at a wet-bulb temperature of 25°C when (a) charging at a rate of 160 tons, (b) discharging at a rate of 160 tons, and (c) idle I-TES. The total load includes the cooling load and the storage charge amount.**

Meta-heuristic algorithms are computationally demanding as they depend on exploring the solution space to locate the globally optimal solution, especially with the large population needed to solve the examined problem (1000-5000). To tackle the problem of long run time, the lower-level problem is pre-solved under a range of cooling loads, storage use and SoC, and ambient air wet-bulb temperatures. A standard sensible heat ratio of 0.7 is assumed for the cooling load. Tri-linear interpolation is applied between the data points, which reduces the run time to 1-2 minutes.

### **5.3 Results and discussion**

The proposed optimal control strategy is compared to two commonly used heuristic strategies for thermal energy storage dispatch: chiller priority control and storage priority control. In chiller priority control, chillers are loaded at capacity, and storage is used to supplement additional cooling needs. This strategy aims to maximize the efficiency of the chillers. In storage priority control, full storage capacity is utilized, and storage dispatch is prioritized over the chillers. Storage supplies a steady cooling rate while the chillers meet the residual and fluctuating cooling demand. Storage is charged at the maximum rate the chillers allow in both heuristic strategies. For storage and chiller priority controls, the scheduling problem is solved heuristically as follows:

- 212-tons centrifugal chillers with VSD are operated first before the 153-tons screw chiller is started because of the higher efficiency
- Charging at chillers supply temperature setpoint of  $-7^{\circ}\text{C}$
- Discharging at chillers design supply temperature setpoint of  $6^{\circ}\text{C}$ ; temperature is gradually increased if necessary to maintain storage dispatch amount



- Cooling tower condenser water temperature setpoint based on design approach temperature of 3°C (difference between leaving water and ambient air wet-bulb temperatures)
- Operating cooling tower is fully loaded before the second one is started

The three storage dispatch strategies are compared in three scenarios of cooling loads under TOU rates shown in Figure 5.6. I-TES is necessary to satisfy building cooling demand when the load exceeds the design chillers' cooling capacity of 570 tons. Scenario 1 has the highest total cooling needs; the demand for cooling begins at 8 AM and terminates at 6 PM. The load peaks at 600-700 tons and requires 976 TR-hr of stored energy (61% of storage capacity) to satisfy building cooling demand. Scenario 2 has intermediate cooling needs and similarly starts at 8 AM and terminates at 6 PM. The load peaks at 550-650 tons and require 544 TR-hr of stored energy (34% of storage capacity). Scenario 3 has the least cooling needs, starting later at 9 AM and ending earlier at 5 PM. This demand scenario peaks at 500-600 tons and requires only 144 TR-hr of stored energy (9% of storage capacity).

Simple two levels TOU tariffs are considered with an on-peak period lasting 8 hours between 8 AM and 4 PM and an off-peak period otherwise. The TOU tariff doubles from \$0.1/kWh in the off-peak period to \$0.2/kWh in the on-peak period, coinciding with a high building cooling load. For all three scenarios, the ambient wet-bulb temperature is lower during early morning hours and higher during the evening, which overlaps with the cooling load and slightly depresses the chiller cooling capacity.

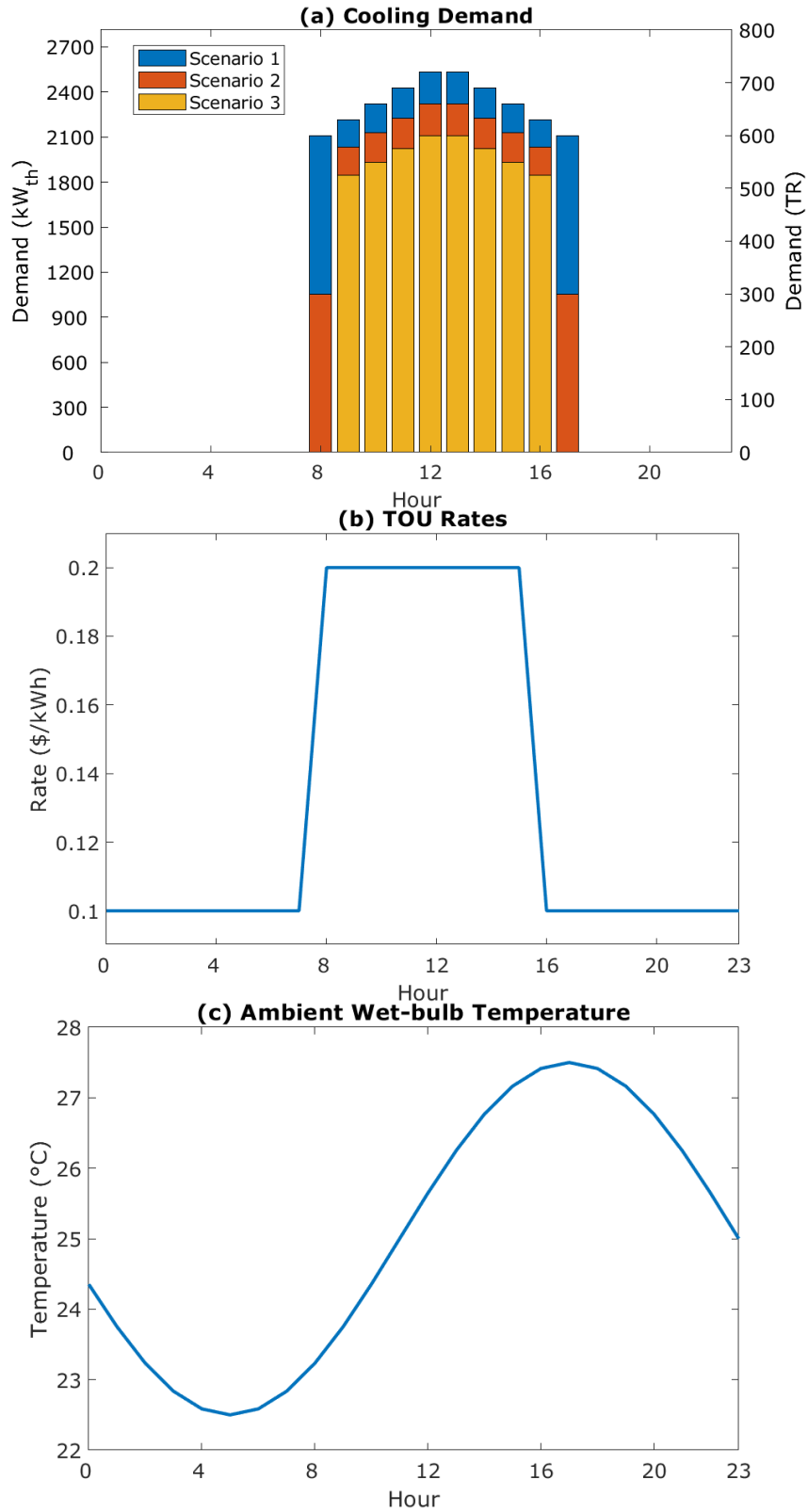


**Figure 5.6: Optimization problem input for three scenarios with hourly (a) cooling demand, (b) TOU rates, and (c) ambient wet-bulb temperature. A sensible heat ratio of 0.7 is assumed.**

The formulated problem is solved for the three scenarios using each of the three considered strategies, and the results are tabulated in Table 5.1. The hourly load contribution from each chiller and the storage to meet the cooling demand is shown in Figure 5.7. The hourly system characteristics for all scenarios are shown in Figure 5.8 with (a) system operation cost, (b) system total energy use, (c) chiller energy use, and (d) auxiliary equipment energy use, and in Figure 5.9 with (a) system COP, (b) blended chillers evaporator leaving temperature, (c) storage dispatch amount, and (d) flowrate to I-TES.

**Table 5.1: Daily cost, energy use, and storage utilization for all scenarios**

	Optimization Strategy	Cost (\$/day)	Energy (kWh/day)	Storage Utilization (% of Capacity)	Cost Difference to Optimal Control (%)
Scenario 1	Chiller Priority Control	1070	6434	61	17
	Storage Priority Control	1045	6610	100	14
	Optimal Control	916	5888	96	-
Scenario 2	Chiller Priority Control	909	5215	34	19
	Storage Priority Control	852	5485	100	11
	Optimal Control	766	4954	96	-
Scenario 3	Chiller Priority Control	746	4068	9	23
	Storage Priority Control	675	4470	100	11
	Optimal Control	606	4013	96	-

Optimal dispatch and equipment scheduling reduce operation costs by 17%, 19%, and 23%, and total energy use by 9%, 5%, and 1% for Scenarios 1, 2, and 3, respectively, relative to chiller priority control. Although chiller priority control attempts to maximize chillers' efficiency, the missed opportunity cost from load shifting combined with sub-optimal chiller

scheduling resulted in a significantly higher system cost. Relative to storage priority control, optimal control reduces operation costs by 14%, 11%, and 11%, and total energy use by 12%, 11%, and 11% for Scenarios 1, 2, and 3, respectively. In addition to the cost reduction, the cost-optimal control system reduced daily energy use, resulting in reduced carbon emissions.

Although auxiliary equipment energy use, shown in Figure 5.8 (d), is small and minimally impacts the overall system energy use compared to chillers' energy use, shown in Figure 5.8 (c), their interaction with the chillers significantly impacts chillers' performance and consequently their energy use.

I-TES is more efficiently charged in optimal control than heuristic strategies; the cost-optimal control system only utilizes the more efficient 212-tons centrifugal chillers with VSD for storage charging. Although it prolongs the charging period by an additional hour compared to storage priority control, it evades running the chillers at a reduced part-load ratio and thus increases overall efficiency. The deterioration of I-TES effectiveness diminishes the utility of the higher flowrate provided by the third chiller. It is worth noting that the storage was not fully charged in optimal control under all scenarios to avoid the increased thermal resistance around the I-TES coils at the end of the charging cycle. For all strategies, storage was charged at a water-glycol mixture inlet supply temperature of  $-7^{\circ}\text{C}$ , as shown in Figure 5.9 (b).

In Scenario 1, the cooling demand far exceeded the design chiller capacity, which required using all three chillers. The higher efficiency attained in the optimal control is primarily due to the optimal loading of the three chillers. The model results suggested loading the screw chiller fully and equally part-loading the 212 tons VSD centrifugal chillers. As the demand is reduced in Scenario 2 and further in Scenario 3, the screw chiller is progressively displaced, and when operated, it is fully loaded. An exception is in Scenario 3 at 3 PM, where a screw chiller

was necessary to provide sufficient water flowrate to discharge the I-TES. Not only that, but the model also attempts to operate the VSD centrifugal chillers at their maximum efficiency point with a part load ratio between 0.8 and 0.9. This is more easily accomplished in Scenario 3 when storage dispatch is less constrained by the cooling demand.

Figure 5.9 (d) shows the supply water-glycol mixture flow rate to I-TES. The reduced flowrate in the optimal control strategy caused by switching off the screw chiller is traded with an increased supply temperature during discharge, enhancing system COP. Compared to heuristic strategies, discharging of storage largely terminates before the end of on-peak electricity pricing, further contributing to cost savings. This was achieved by re-setting the water supply temperature at the outlet of the chillers above the design point by 2-3°C, which enhanced the chillers' cooling capacity, particularly the 153-tons chiller with a positive displacement screw compressor. Other sources of enhanced system COP are lower ambient temperatures combined with reduced chillers loading, specifically during the discharging period, which benefited the VSD chillers.

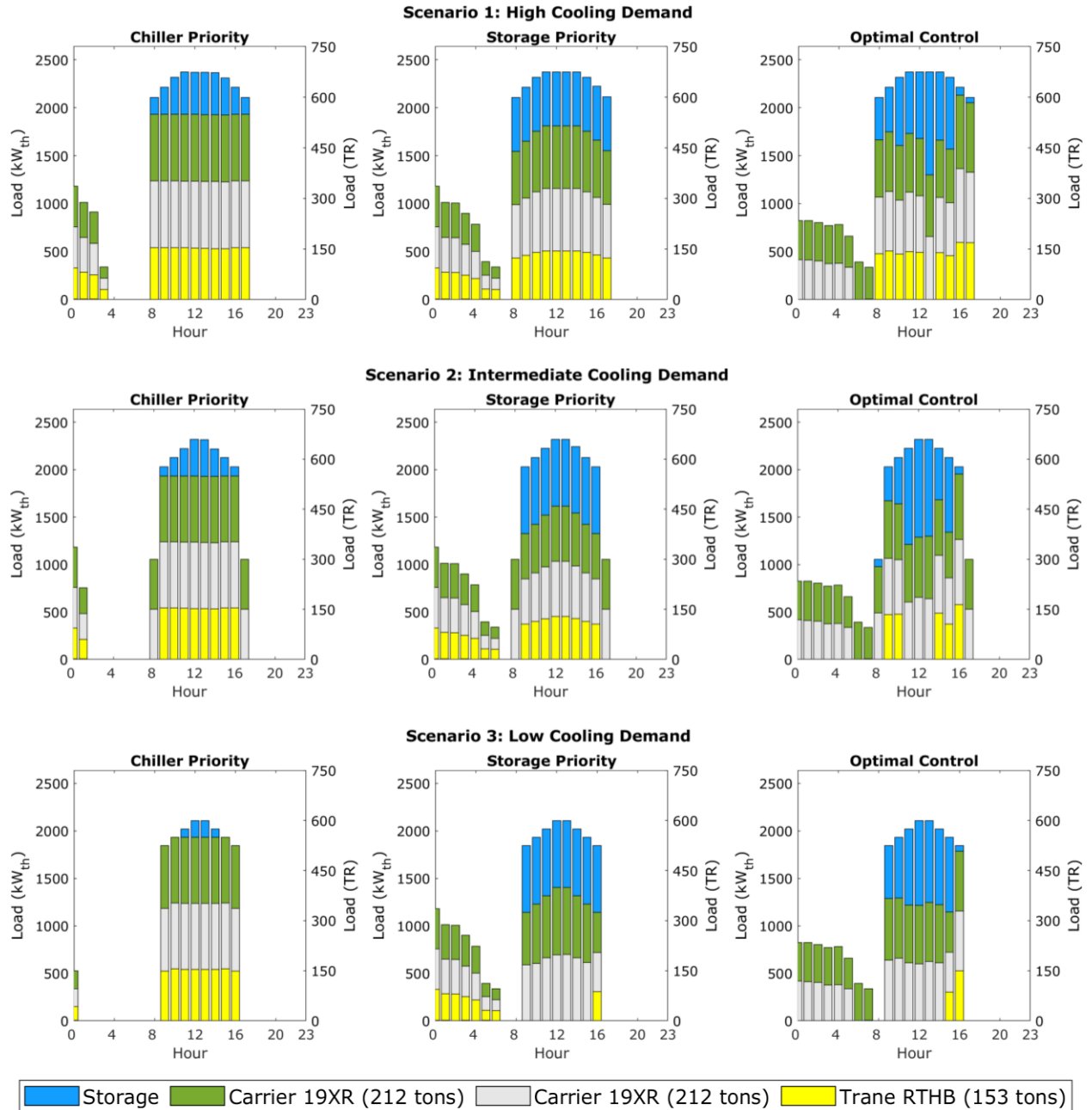


**Figure 5.7: Cooling demand contribution breakdown from each chiller and storage for the three considered control strategies. From left to right: chiller priority control, storage priority control, and optimal storage control. The system comprises two 212-tons chillers with a VSD-equipped centrifugal compressor (Carrier 19XR) and one 153-tons screw chiller without VSD (Trane RTHB).**

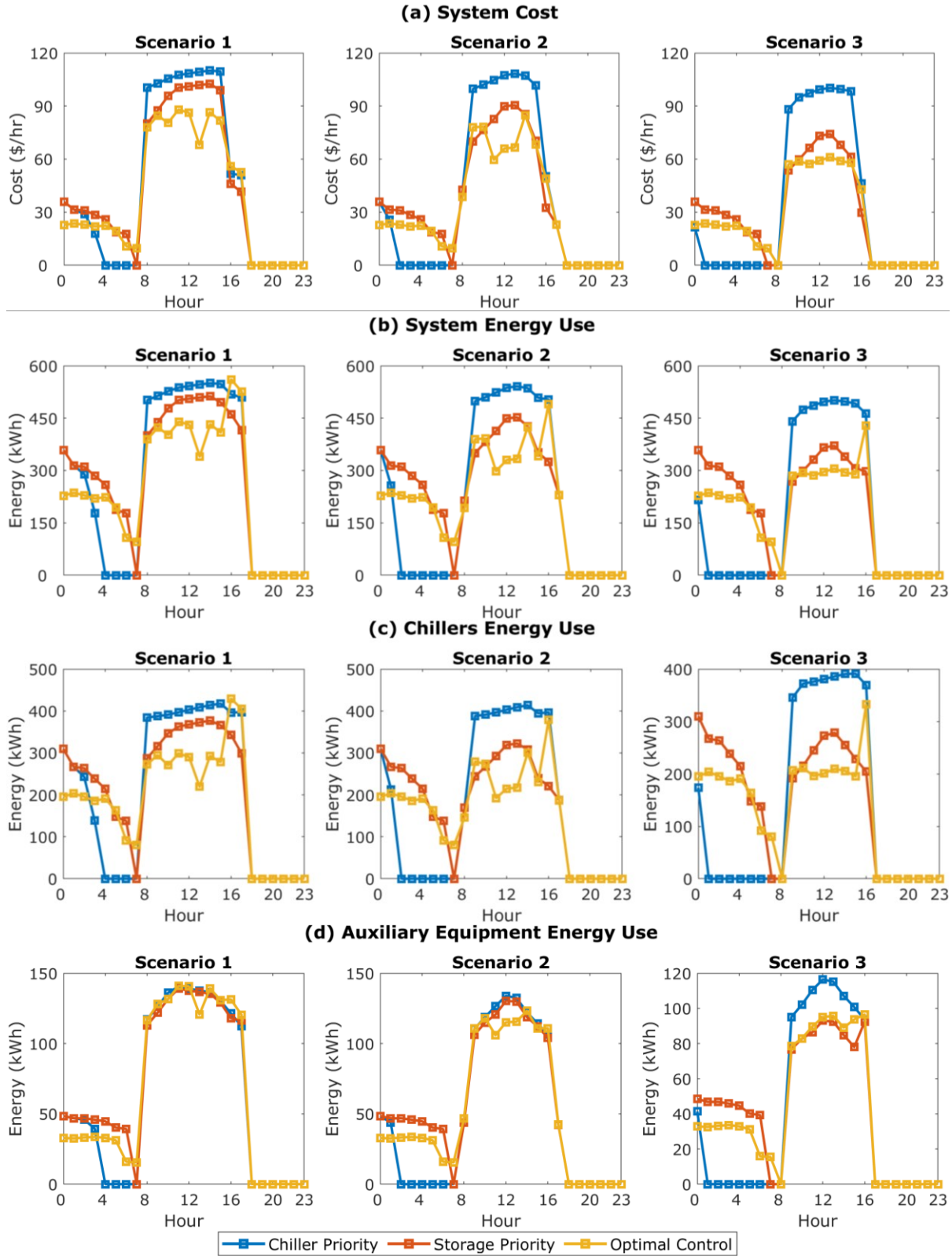


**Figure 5.8:** For the three control strategies, hourly systems profiles with (a) system operation cost; (b) total system electric energy use; (c) total energy use by all chillers excluding auxiliary equipment; (d) auxiliary equipment energy use which includes primary, secondary and condenser pumps, and towers and coil fans.

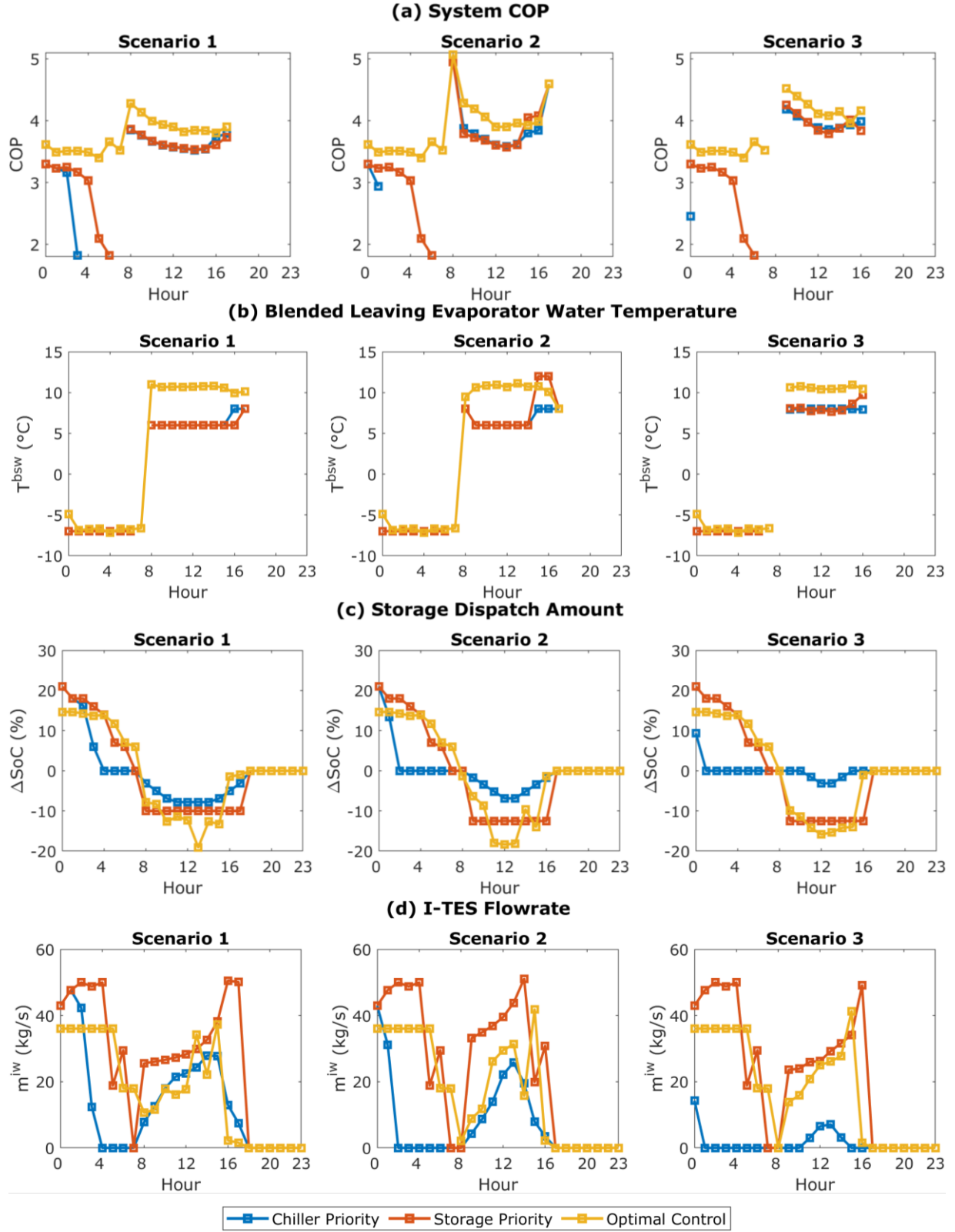


**Figure 5.9:** For the three control strategies, hourly system: (a) COP, (b) blended chillers supply temperature, (c) storage dispatch amount curve, and (d) flowrate to I-TES. System COP is the ratio of total chiller loading to the system's electric load.



In addition to TOU pricing, demand charges are often applied to commercial and industrial customers as a fee to maintain the reliability and infrastructure of the power grid. They are charged based on the highest power used during a billing cycle. The application of demand charges promotes storage use not only for load shifting but also for peak shaving. The formulated problem was solved with a demand charge of \$20/kW applied to Scenario 1, the scenario with the highest cooling demand assuming it repeats for a month. The added monthly charge is given by  $\$20/\text{kW} \times \max_{t \in T} P_t^{\text{Sys}}$ . The analysis suggests that the cost-optimal system can reduce peak electric demand by 75 kW and cost from demand charges by 17% relative to storage priority control and by 113 kW and 26% relative to chiller priority control. However, the inclusion of the demand charge results in an increase in the daily cost of energy use from \$916/day to \$928/day. Despite the increased thermal resistance around the I-TES coils at the end of the charging cycle, the system fully utilizes the storage capacity for load shifting and peak demand reduction. Figure 5.10 shows the cost-optimal system load contribution breakdown in (a) and energy use in (b) when a demand charge of \$20/kW is applied to Scenario 1.

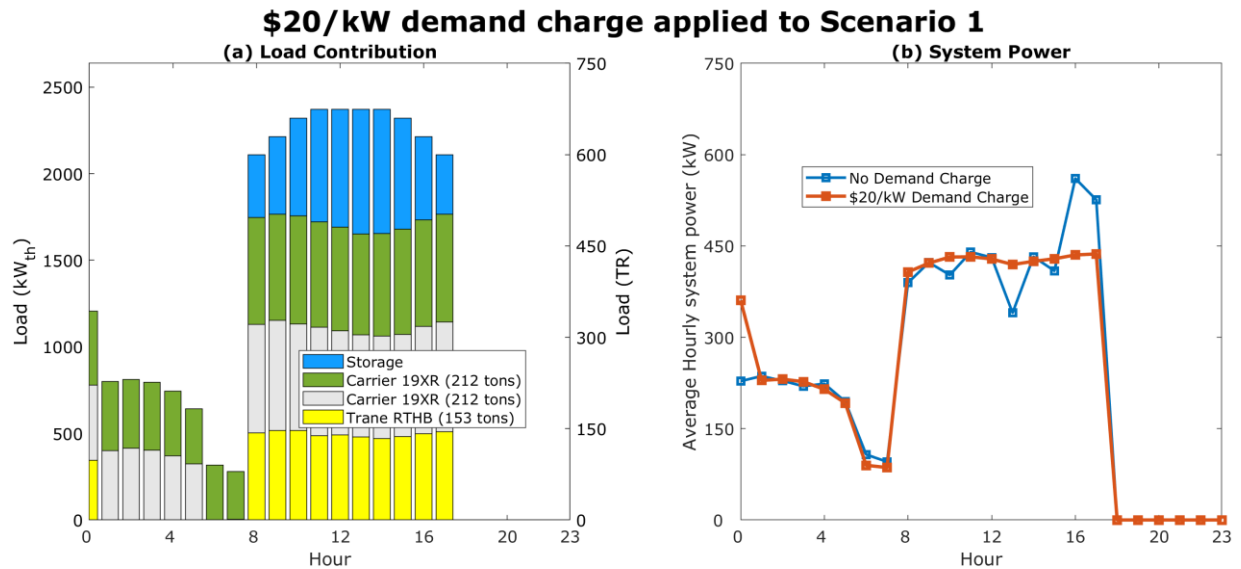


**Figure 5.10: Applying a demand charge of \$20/kW to Scenario 1 with (a) a breakdown of cooling contribution from each chiller and storage and (b) system electric energy use.**

As shown in Figure 5.10 (b), the demand charges oriented storage dispatch around reducing the peak power use, which produced a near-flat power curve. Unlike the scenarios with no demand charge, this system utilized the screw chiller to support a higher I-TES charging rate in the first hour (Hour 0). Furthermore, instead of effectively terminating the discharge process at the end of on-peak pricing at 4 PM, the storage dispatch continues for two additional hours to reduce the peak demand and hence, peak demand charges.

## 5.4 Conclusion

Moving toward a more sustainable power grid based on intermittent renewable energy requires demand-side management to maintain the reliability and stability of the power grid. As opposed to today's power grid which relies on dispatchable power generation, a low-carbon grid reliant on renewables must adjust the demand to match the supply better. This supply matching can be accomplished via demand-side management, which requires energy storage and load adjustment. Cooling is responsible for half of the electricity demand in Qatar, thereby making cooling systems the primary target for demand-side management. However, the operation of CWS tends to be complex from the interaction of its constituent components.

Hybrid steady-state models developed in Chapter 3 for I-TES and the key power-consuming components, including the chillers, cooling towers, water pumps, and cooling coil fans, were used to formulate the scheduling and dispatch problem. The formulated problem is highly non-linear and too cumbersome to solve using traditional optimization methods. The solution strategy is to decompose the problem into bi-level optimization to decouple the equipment scheduling problem from storage dispatch, which sufficiently simplifies the problem. The genetic algorithm is used to solve the simplified problem. The upper level minimizes operation costs and decides the storage dispatch amount fed to the lower-level optimizer to solve

the equipment scheduling problem sequentially and return the subsequent system power consumption to update the guess for the next iteration. Constraints in the lower-level problem are handled using the penalty function method. Tuning the penalty factors and genetic algorithm parameters using an optimizer and training data diminished and eliminated the premature convergence problem. This approach negates the need for simplistic system models for complex space cooling and heating applications. While computationally taxing, the run time for the proposed approach can be reduced to 1-2 minutes by pre-solving the lower-level problem under a range of input conditions and tri-linearly interpolating between them. CWS plant operators can use the developed strategy to optimize plant operation. For CWS without I-TES, the lower level problem can be solved at each time step to determine optimal chillers loading and sequencing. Limitations of the strategy include no considerations for minimum chiller uptime and additional energy savings that could be enabled through better modeling of the air distribution side.

The developed optimal control strategy is compared to two commonly used heuristic storage strategies: chiller priority control and storage priority control, in three scenarios of cooling demand under TOU tariffs. The model results suggest that the optimal control strategy consistently offered cost reduction by 17-23% relative to chiller priority control and 11-12% relative to storage priority control. Furthermore, optimal equipment and scheduling dispatch reduced energy use by 1-9% relative to chiller priority and 11-12% relative to storage priority control. When Scenario 1 is reconsidered with a demand charge of \$20/kW, the optimal system can reduce peak demand power and cost from demand charge by 75 kW and 17%, respectively, relative to storage priority and by 113 kW and 26% relative to chiller priority controls. The benefits of the proposed strategy are amplified when a more sophisticated tariff structure is present. Lastly, the proposed approach can be used to decide storage dispatch over a more extended period than 24 hours at the expense of increased computational time.

## **Chapter 6: Conclusions and recommendations for future works**

### **6.1 Main Conclusion**

Moving to low-carbon electricity grids is necessary to mitigate climate catastrophe and remains humanity's greatest challenge. The pathway to a low-carbon electricity grid will not be universal. Instead, each region must tailor a plan specific to its energy needs, climate, and geology. Qatar is attractive for utilizing solar PV since it has relatively high and predictable solar insolation with a global horizontal irradiance of 2200 kWh/m<sup>2</sup>/yr. synergetic with electricity demand. With a hot desert climate, space cooling drives the electricity demand and is responsible for nearly half the electricity consumed.

The work described in this dissertation aims to examine and analyze a decarbonization pathway for the cooling-driven electricity sector in Qatar using PV generation combined with I-TES and BESS for load shifting from multiple perspectives in a top-down approach, with (i) assessing the potential for large-scale deployment from a utility-scale perspective, (ii) examining the subsequent distributed energy resources capacity sizing problem, and (iii) proposing a solution to the arising demand side management problem. Carbon pricing policy was examined in the form of the carbon tax to facilitate the transition to more sustainable renewable energy sources that otherwise would be challenging with Qatar's access to plentiful and cheap natural gas. Carbon pricing enables renewable energy to compete with carbon-based energy sources and mobilize investments in alternative energy sources for carbon abatement.

The utility-scale perspective in Chapter 2 provided insight into the renewable penetration potential, overall emissions reduction, and the impact on power grid operation for large deployment of PV generation combined with centralized BESS and decentralized building-scale I-TES, which was modeled using a stochastic linear program. Linear programs are also useful for

describing the aggregate behavior and performance of the systems, which tend to exhibit simpler behavior than their constituents. The analysis suggests that BESS is cost-prohibitive under the current gas price of \$3.3/MMBtu and capacity cost of \$250/kWh. Nevertheless, at the current gas price, 8 GW of PV and 28 GWh<sub>th</sub> of I-TES capacity introduced in the national grid can reduce CO<sub>2</sub> emissions by 43% while cutting annual system costs by 20%. Emissions can be reduced by 60% in a system with carbon pricing at \$60/ton of CO<sub>2</sub> with higher investments in PV and I-TES. Several hurdles impede further emissions reduction, including (i) misalignment of electricity demand, which peaks in August, and solar insolation, which peaks in June, producing less when needed, (ii) I-TES cannot outcompete existing gas generation for seasonal cooling needs, (iii) reduced idle chiller capacity in the peak cooling season, and (iv) chiller capacity degradation due to higher ambient temperatures in the high demand season. However, I-TES is well suited to utilize idle chiller capacity that is a consequence of a highly seasonal cooling load for load shifting in the shoulder season. More so in less efficient cooling systems, such as AC systems, due to an equal tank volume corresponding to greater electric load shifting.

BESS becomes cost-effective with a carbon price above \$100/ton of CO<sub>2</sub> at the current capacity cost of \$250/kWh. While BESS does not displace I-TES for cooling load shifting, either at higher carbon pricing or lower capacity cost, it is primarily used to manage non-cooling loads. This is because BESS requires a high daily capacity utilization rate of about 90% to become cost-effective, making it unsuitable for seasonal cooling demands. A system with a carbon price of \$140/ton of CO<sub>2</sub> can achieve a deep decarbonization rate of 92%, supported by BESS. Further emissions reductions realized with higher carbon pricing are limited.

Naturally, decentralized I-TES must ultimately be adopted by individual buildings. While simpler models were used for large-scale deployment analysis, they cannot be applied to

individual systems. Chapter 3 developed more sophisticated models for WC CWS, the conventional way of cooling large buildings in Qatar. Hybrid steady-state models are developed for the major devices in CWS, including chillers, pumps, cooling towers, cooling coils, and I-TES. Hybrid models combine the physical insight of physics-based models with the efficiency of data-driven models in a simpler formulation achieved with empirically obtained parameters. The developed models are used for the site analysis in Chapter 4 and the scheduling and dispatch problem in Chapter 5.

The site analysis performed in Chapter 4 encompassed proposing a solution to the equipment capacity sizing problem and gaining insight into the integration of distributed-scale renewable generation. To overcome the lack of building energy demand profiles in Qatar, demand profiles were simulated for two typical buildings with two uses, business-commercial and residential, which generally have opposing occupancy rates as people move from home to the workplace. The developed strategy formulates the problem into a bi-level optimization with a simplified components model. The upper level minimizes and decides the installed design parameters using particle swarm optimization, and the lower level solves the scheduling and dispatch problem in a mixed-integer linear program with piece-wise linearization. This strategy can be broadly applied to new and existing buildings with different cooling system technologies under different climatic conditions.

The site analysis affirmed the suitability of distributed-scale PV generation. Buildings with diurnal demand synergetic with solar insolation are particularly well suited for exploiting PV generation and can achieve a decarbonization rate above 60% without carbon pricing. I-TES is suitable for utilizing the large idle chiller capacities during the shoulder cooling season for cooling load shifting and could reduce building carbon emissions by 5-10%. Similar challenges

to the utility-scale perspective are confronted when applying carbon pricing to promote I-TES. The chillers' cooling capacity must be remarkably oversized for I-TES to be utilized in the high cooling demand season. BESS becomes cost-effective with carbon pricing above \$75/ton of CO<sub>2</sub> and is used to meet the near year-round constant building baseload. With carbon pricing above \$100/ton of CO<sub>2</sub>, the cost-optimal system can yield a decarbonization rate of about 90% for either building using distributed-scale solutions.

Although buildings are well suited for exploiting PV generation, Qatar is better suited for utility-scale implementation. Utility-scale implementation offers (i) reduced generation cost, (ii) reduced curtailment from demand aggregation, (iii) higher output from solar tracking technology, and (iv) better accessibility for cleaning since soiling on PV is identified as a major challenge in Qatar. BESS, as well, is better suited for utility-scale due to a more reliable aggregate non-cooling loads that can permit high daily capacity utilization needed for BESS to be cost-effective.

Since intermittent renewable generations are not dispatchable, nor can they be perfectly predicted. High penetration of PV generation combined with I-TES and BESS requires demand-side management, a tool the electric utility uses to adjust the demand to match the power supply. A method to control demand is using dynamic pricing in the form of TOU. Due to the high load from space-cooling, cooling systems are a crucial target for demand side management. However, operating CWS to maximize savings from demand-side management can be challenging and requires careful consideration of chillers' staging and part-load performances, as well as the performances of associated auxiliary equipment.

The solution strategy developed in Chapter 5 was to decompose the problem into bi-level optimization to decouple the equipment scheduling problem from storage dispatch, which

sufficiently simplifies the problem. The genetic algorithm is used to solve the simplified formulation. The upper level decides the storage dispatch amount, and the lower-level optimizer solves the equipment scheduling problem at each hour. The constrained optimization in the lower-level problem is turned into an unconstrained optimization using the penalty function method. The genetic algorithm problem of premature convergence was eliminated by tuning the penalty factors and genetic algorithm parameters using an optimizer and training data.

The proposed approach negated the need for simplistic system models often used in complex space cooling and heating applications. Compared to two commonly used heuristic storage dispatch strategies, the model suggests optimal control reduces cost and energy by 11-14% and 10-12%, respectively, relative to storage priority control, and 16-33% and 1-9%, respectively, relative to chiller priority control. In an investigation with a demand charge, optimized control reduces demand charges by 17% relative to storage priority and 26% relative to chiller priority control. The utility of the proposed approach is augmented when a more sophisticated tariff structure is present, which is expected with high penetration of intermittent renewable generations.

There are possible approaches to overcome the challenges identified in this work that would better address future sustainable urban development needs, which include (i) more considerable reliance on WC systems that are more efficient and could reduce the seasonality of cooling and electric loads; (ii) DXS capable of ice charging as standards for better future integration with I-TES; (iii) more energy-efficient buildings with passive design to reduce peak cooling demand; (iv) removing energy subsidies and further promoting energy conservation awareness; (v) reducing urban heat island effect, which impact cooling need and cooling systems performance, by planting more trees and considering lighter colors for sidewalks and home



exterior. Lastly, by using existing decarbonization solutions at current prices, Qatar could substantially reduce its carbon footprint and decrease the reliance on gas generation for cooling and electric loads using solar PV generation, energy storage, and moderate carbon pricing.

## **6.2 Recommendations for future work**

The scope of this work could be expanded to explore the limitations identified during this work.

The recommendations, in no particular order, are as follows:

### **6.2.1 Examining the cost of retrofitting DXS**

Currently sold and installed DXS are not designed for operation with I-TES. The direct expansion cooling systems were charged using additionally installed dedicated ice chillers at a cost in the large-scale deployment problem analyzed from the utility-scale perspective in Chapter 2. Investigating the cost of retrofitting the existing DXS to allow them to be capable of storing ice can unlock the potential for a larger amount of I-TES at a reduced carbon tax.

### **6.2.2 Alternative energy storage technologies**

The low thermal capacity of 0.04 MJ/kg of chilled water storage compared to 0.4 MJ/kg for I-TES, combined with a higher initial cost, makes stratified chilled water storage less economically favorable. However, producing cooling to store ice substantially lowers the chillers' COP and cooling capacity limiting the amount of usable excess energy. Investigating alternative thermal energy storage could yield a more promising storage technology. The desired storage technology must have: (i) thermal energy density comparable to ice, (ii) a melting point higher than ice to reduce the problem of performance and capacity degradation in chillers, and (iii) good thermal properties to maintain comparable charge and discharge rates. This largely remains a challenge with phase change material storage. In addition to thermal energy storage,

long-term energy storage can use a large amount of excess generation from the misalignment of the PV generation peak with the electricity demand peak.

### **6.2.3 Alternative decarbonization pathway**

Excellent climatic conditions in Qatar combined with low-cost PV generation make exploiting solar energy exceptionally attractive. However, the sole use of diurnal PV generation requires sufficiently large energy storage to store a full night's worth of cooling and electricity needs. Energy storage needs can be alleviated by considering alternative energy sources and decarbonization pathways, such as carbon capture and sequestration for gas generation, wind energy, and energy efficiency. However, historical data in Qatar shows wind to be interannually correlated with PV generation, which could limit its benefits. Furthermore, a challenge identified when analyzing the decarbonization pathway for electricity in Qatar is the highly seasonal cooling needs between mid-July to mid-September. Examining the energy efficiency pathway can attenuate the peak cooling demand from better building insulation, higher efficiency cooling systems, and tighter building constructions.

### **6.2.4 Determining the ideal electricity tariffs structure**

The considered tariff structure in Chapter 4 is from bulk customers with a load exceeding 5 MW. The tariff, which lacks subsidies, was used to examine the impact of carbon pricing. In scenarios with high PV adoption, it is likely for the tariff structure to reverse to charge more for nighttime electricity needs. This raises the question of what tariff structure could maximize PV generation utilization at a distributed level.

### **6.2.5 Incorporate BESS in the I-TES dispatch problem**

The CWS equipment scheduling and I-TES dispatch problem examined in Chapter 5 do not incorporate the BESS dispatch problem to maximize renewable penetration in the grid. While

a simple linear BESS model was considered for utility-scale analysis in Chapter 2 and building-scale analysis in Chapter 4, an optimal dispatch of BESS should also consider the impact of capacity degradation from cycling and charge/discharge rates.

### **6.2.6 Inclusion of seawater desalination in the model**

The current approach to meeting Qatar's electricity demand is using gas-powered integrated water and power plants that sometimes are sub-optimally operated to sustain desalination, especially in the winter when the dispatch is concerned with water demand. While other desalination technologies, such as reverse osmosis, are gaining ground due to their higher efficiency, a more accurate analysis should include water demand balance considering desalination plants' energy use, carbon emissions, and impact on the thermal efficiency of power plants.

### **6.2.7 Modeling the impact of electrifying the transportation sector**

The transportation sector in Qatar mainly runs on gasoline and diesel-powered internal combustion engines and electric-powered subway and light rail systems. This dissertation did not address the impact of grid-connected battery electric vehicles expected over the coming decades, which could be used to aid decarbonization efforts by contributing to load shifting.

## References

- [1] R. Heede, “Tracing anthropogenic carbon dioxide and methane emissions to fossil fuel and cement producers, 1854-2010,” *Clim. Change*, vol. 122, no. 1–2, pp. 229–241, 2014, doi: 10.1007/s10584-013-0986-y.
- [2] S. Khatiwala, F. Primeau, and T. Hall, “Reconstruction of the history of anthropogenic CO<sub>2</sub> concentrations in the ocean,” *Nature*, vol. 462, no. 7271, pp. 346–349, 2009, doi: 10.1038/nature08526.
- [3] S. Wang, G. Li, and C. Fang, “Urbanization, economic growth, energy consumption, and CO<sub>2</sub> emissions: Empirical evidence from countries with different income levels,” *Renew. Sustain. Energy Rev.*, vol. 81, no. July 2016, pp. 2144–2159, 2018, doi: 10.1016/j.rser.2017.06.025.
- [4] K. Li and B. Lin, “Impacts of urbanization and industrialization on energy consumption/CO<sub>2</sub> emissions: Does the level of development matter?,” *Renew. Sustain. Energy Rev.*, vol. 52, pp. 1107–1122, 2015, doi: 10.1016/j.rser.2015.07.185.
- [5] K. White *et al.*, “Illuminating the Modern Dance,” *Science (80-. )*, vol. 321, no. September, pp. 19–21, 2008.
- [6] S. A. Montzka, E. J. Dlugokencky, and J. H. Butler, “Non-CO<sub>2</sub> greenhouse gases and climate change,” *Nature*, vol. 476, no. 7358, pp. 43–50, 2011, doi: 10.1038/nature10322.
- [7] S. C. Moser, “Communicating climate change: History, challenges, process and future directions,” *Wiley Interdiscip. Rev. Clim. Chang.*, vol. 1, no. 1, pp. 31–53, 2010, doi: 10.1002/wcc.11.
- [8] J. Gupta, “A history of international climate change policy,” *Wiley Interdiscip. Rev. Clim. Chang.*, vol. 1, no. 5, pp. 636–653, 2010, doi: 10.1002/wcc.67.
- [9] C. Rosenzweig and M. L. Parry, “Potential Impacts of Climate Change on World Food Supply:,” *Agric. Dimens. Glob. Clim. Chang.*, pp. 87–116, 2022, doi: 10.1201/9781315136967-5.
- [10] D. G. Huber and J. Gullede, “Extreme Weather and Climate Change Understanding the Link, Managing the Risk,” *Sci. Impacts Program. Cent. Clim. Energy Solut.*, no. December, pp. 1–13, 2011.
- [11] K. L. Ebi *et al.*, “Extreme Weather and Climate Change: Population Health and Health System Implications,” *Annu. Rev. Public Health*, vol. 42, pp. 293–315, 2020, doi: 10.1146/annurev-publhealth-012420-105026.
- [12] Intergovernmental Panel on Climate Change, *Global warming of 1.5°C*. 2019.

- [13] Intergovernmental Panel on Climate Change, *Climate Change 2014: Mitigation of Climate Change*. 2015.
- [14] S. McCulloch *et al.*, “Energy Technology Perspectives 2017 - Catalysing Energy Technology Transformations,” 2017.
- [15] L. F. Cabeza, D. Urge-Vorsatz, M. A. McNeil, C. Barreneche, and S. Serrano, “Investigating greenhouse challenge from growing trends of electricity consumption through home appliances in buildings,” *Renew. Sustain. Energy Rev.*, vol. 36, pp. 188–193, 2014, doi: 10.1016/j.rser.2014.04.053.
- [16] D. Urge-Vorsatz, K. Petrichenko, M. Staniec, and J. Eom, “Energy use in buildings in a long-term perspective,” *Curr. Opin. Environ. Sustain.*, vol. 5, no. 2, pp. 141–151, 2013, doi: 10.1016/j.cosust.2013.05.004.
- [17] L. Pérez-Lombard, J. Ortiz, and C. Pout, “A review on buildings energy consumption information,” *Energy Build.*, vol. 40, no. 3, pp. 394–398, 2008, doi: 10.1016/j.enbuild.2007.03.007.
- [18] “Qatar - Countries & Regions - IEA,” 2019. [Online]. Available: <https://www.iea.org/countries/qatar>. [Accessed: 25-Jul-2022].
- [19] Kahramaa, “Annual Qatar Statistics Report 2016,” 2016.
- [20] F. Saffouri, I. S. Bayram, and M. Koc, “Quantifying the Cost of Cooling in Qatar,” no. February, pp. 1–9, 2018, doi: 10.1109/ieecgcc.2017.8448269.
- [21] I. S. Bayram, F. Saffouri, and M. Koc, “Generation, analysis, and applications of high resolution electricity load profiles in Qatar,” *J. Clean. Prod.*, vol. 183, pp. 527–543, 2018, doi: 10.1016/j.jclepro.2018.02.084.
- [22] Kahramaa, “Tariff,” *Kahramaa*, 2019. [Online]. Available: <https://www.km.com.qa/CustomerService/Pages/Tariff.aspx>. [Accessed: 03-Oct-2019].
- [23] S. G. Al-Ghamdi and S. K. Al-Thani, “QCCC 2021,” 2021.
- [24] E. S. Fadala and Raffaello, “Sustainable Neighborhoods in the State of Qatar: Msheireb Downtown Doha,” *Saudi J. Eng. Technol.*, vol. 3, no. 7, pp. 446–463, 2018, doi: 10.21276/sjeat.2018.3.7.2.
- [25] “New Qatari Standards for AC Energy Efficiency,” *Kahramaa*, 2013. [Online]. Available: <https://www.km.qa/MediaCenter/Pages/NewsDetails.aspx?itemid=18#:~:text=Qatari energy efficiency system contains,12%25 compared with unclassified appliance.> [Accessed: 25-Jul-2022].
- [26] A. Meier, M. Darwish, and S. Sabeeh, “Complexities of saving energy in Qatar,” *ECEEE*

2013 Summer Study Proc., pp. 41–46, 2013.

- [27] Amjad Khashman, “Qatari utility mulls jump to 800 MW tender as consortia submit bids,” *PV Magazine*, 2019. .
- [28] Tassal Group Limited, “Sustainability Report 2020,” Doha, 2020.
- [29] M. A. Bohra, “Optimising Qatar’s energy transition through model-based analysis,” no. March, 2020.
- [30] M. Bohra and N. Shah, “Optimising the role of solar PV in Qatar’s power sector,” *Energy Reports*, vol. 6, pp. 194–198, 2020, doi: 10.1016/j.egyr.2019.11.062.
- [31] L. Martín-Pomares, D. Martínez, J. Polo, D. Perez-Astudillo, D. Bachour, and A. Sanfilippo, “Analysis of the long-term solar potential for electricity generation in Qatar,” *Renew. Sustain. Energy Rev.*, vol. 73, no. March 2016, pp. 1231–1246, 2017, doi: 10.1016/j.rser.2017.01.125.
- [32] E. C. Okonkwo, I. Wole-Osho, O. Bamisile, M. Abid, and T. Al-Ansari, “Grid integration of renewable energy in Qatar: Potentials and limitations,” *Energy*, vol. 235, p. 121310, 2021, doi: 10.1016/j.energy.2021.121310.
- [33] A. H. Marafia and H. A. Ashour, “Economics of off-shore/on-shore wind energy systems in Qatar,” *Renew. Energy*, vol. 28, no. 12, pp. 1953–1963, 2003, doi: 10.1016/S0960-1481(03)00060-0.
- [34] O. Alrawi, I. S. Bayram, M. Koc, and S. G. Al-Ghamdi, “Economic Viability of Rooftop Photovoltaic Systems and Energy Storage Systems in Qatar,” *Energies*, vol. 15, no. 9, 2022, doi: 10.3390/en15093040.
- [35] N. Elbeheiry, A. Amer, S. Elgazar, S. Shukri, M. Metry, and R. S. Balog, “A Techno-Economic Study of Rooftop Grid-Connected Photovoltaic-Energy Storage Systems in Qatar,” *Conf. Rec. IEEE Photovolt. Spec. Conf.*, vol. 2020-June, pp. 2730–2736, 2020, doi: 10.1109/PVSC45281.2020.9300347.
- [36] O. F. Alrawi, T. Al-Siddiqi, A. Al-Muhannadi, A. Al-Siddiqi, and S. G. Al-Ghamdi, “Determining the influencing factors in the residential rooftop solar photovoltaic systems adoption: Evidence from a survey in Qatar,” *Energy Reports*, vol. 8, pp. 257–262, 2022, doi: 10.1016/j.egyr.2022.01.064.
- [37] E. A. Teshnizi, M. Jahangiri, A. A. Shamsabadi, L. M. Pomares, A. Mostafaeipour, and M. El Haj Assad, “Comprehensive Energy-Econo-Enviro (3E) Analysis of Grid-Connected Household Scale Wind Turbines in Qatar,” *Jordan J. Mech. Ind. Eng.*, vol. 15, no. 2, pp. 215–231, 2021.
- [38] İ. Ş. Bayram and M. Koç, “Demand side management for peak reduction and PV

- integration in Qatar,” *Proc. 2017 IEEE 14th Int. Conf. Networking, Sens. Control. ICNSC 2017*, pp. 251–256, 2017, doi: 10.1109/ICNSC.2017.8000100.
- [39] M. Krarti, F. Ali, A. Alaidroos, and M. Houchati, “Macro-economic benefit analysis of large scale building energy efficiency programs in Qatar,” *Int. J. Sustain. Built Environ.*, vol. 6, no. 2, pp. 597–609, 2017, doi: 10.1016/j.ijsbe.2017.12.006.
  - [40] N. Ayoub, F. Musharavati, S. Pokharel, and H. A. Gabbar, “Energy consumption and conservation practices in Qatar - A case study of a hotel building,” *Energy Build.*, vol. 84, pp. 55–69, 2014, doi: 10.1016/j.enbuild.2014.07.050.
  - [41] A. Kamal, S. G. Al-Ghamdi, and M. Koç, “Role of energy efficiency policies on energy consumption and CO2 emissions for building stock in Qatar,” *J. Clean. Prod.*, vol. 235, pp. 1409–1424, 2019, doi: 10.1016/j.jclepro.2019.06.296.
  - [42] A. Abdallah, D. Martinez, B. Figgis, and O. El Daif, “Performance of Silicon Heterojunction Photovoltaic modules in Qatar climatic conditions,” *Renew. Energy*, vol. 97, pp. 860–865, 2016, doi: 10.1016/j.renene.2016.06.044.
  - [43] D. Martinez-Plaza, A. Abdallah, B. W. Figgis, and T. Mirza, “Performance Improvement Techniques for Photovoltaic Systems in Qatar: Results of First year of Outdoor Exposure,” *Energy Procedia*, vol. 77, pp. 386–396, 2015, doi: 10.1016/j.egypro.2015.07.054.
  - [44] F. Tahir, A. A. B. Baloch, and S. G. Al-Ghamdi, “Impact of climate change on solar monofacial and bifacial Photovoltaics (PV) potential in Qatar,” *Energy Reports*, vol. 8, pp. 518–522, 2022, doi: 10.1016/j.egyr.2022.02.197.
  - [45] Kahramaa, “The Large-Scale Solar PV Power Plant,” 2022. [Online]. Available: <https://www.km.qa/MediaCenter/Publications/solarEngscreen-min.pdf>.
  - [46] C. Carpenter, “QatarEnergy picks Samsung C&T to build solar plants to power its LNG expansion,” *S&P Global*, 2022. [Online]. Available: <https://www.spglobal.com/commodityinsights/en/market-insights/latest-news/electric-power/082322-qatarenergy-picks-samsung-c-t-to-build-solar-plants-to-power-its-lng-expansion>. [Accessed: 22-Aug-2022].
  - [47] E. Campiglio, “Beyond carbon pricing: The role of banking and monetary policy in financing the transition to a low-carbon economy,” *Ecol. Econ.*, vol. 121, pp. 220–230, 2016, doi: 10.1016/j.ecolecon.2015.03.020.
  - [48] E. Tvinnereim and M. Mehling, “Carbon pricing and deep decarbonisation,” *Energy Policy*, vol. 121, no. November 2017, pp. 185–189, 2018, doi: 10.1016/j.enpol.2018.06.020.
  - [49] J. Hirwa, O. Ogunmodede, A. Zolan, and A. M. Newman, “Optimizing design and

- dispatch of a renewable energy system with combined heat and power,” *Optim. Eng.*, 2022, doi: 10.1007/s11081-021-09674-4.
- [50] M. Rabe, Y. Bilan, K. Widera, and L. Vasa, “Application of the Linear Programming Method in the Construction of a Mathematical Model of Optimization Distributed Energy,” *Energies*, vol. 15, no. 5, 2022, doi: 10.3390/en15051872.
  - [51] I. El Kafazi, R. Bannari, E. B. E. I. Adiba, H. Nabil, and T. Dragicevic, “Renewable energies: Modeling and optimization of production cost,” *Energy Procedia*, vol. 136, pp. 380–387, 2017, doi: 10.1016/j.egypro.2017.10.267.
  - [52] X. Luo, C. K. Lee, W. M. Ng, S. Yan, B. Chaudhuri, and S. Y. R. Hui, “Use of adaptive thermal storage system as smart load for voltage control and demand response,” *IEEE Trans. Smart Grid*, vol. 8, no. 3, pp. 1231–1241, 2017, doi: 10.1109/TSG.2015.2513743.
  - [53] S. Al-Hallaj, S. Khateeb, A. Aljehani, and M. Pinar, “Thermal energy storage for smart grid applications,” *AIP Conf. Proc.*, vol. 1924, 2018, doi: 10.1063/1.5020287.
  - [54] M. MacCracken, “Energy storage: Providing for a low-carbon future,” *ASHRAE J.*, vol. 52, no. 9, pp. 28–36, 2010.
  - [55] I. Al-Aali and V. Modi, “Examining Ice Storage and Solar PV As a Potential Push Toward Sustainability for Qatar,” in *ASME International Mechanical Engineering Congress and Exposition, Proceedings (IMECE)*, 2018, vol. 6B-2018, doi: 10.1115/IMECE2018-86709.
  - [56] Y. Ruan, Q. Liu, Z. Li, and J. Wu, “Optimization and analysis of Building Combined Cooling, Heating and Power (BCHP) plants with chilled ice thermal storage system,” *Appl. Energy*, vol. 179, pp. 738–754, 2016, doi: 10.1016/j.apenergy.2016.07.009.
  - [57] Y. Xu *et al.*, “Experimental investigation of solar photovoltaic operated ice thermal storage air-conditioning system,” *Int. J. Refrig.*, vol. 86, pp. 258–272, 2018, doi: 10.1016/j.ijrefrig.2017.11.035.
  - [58] Y. Han, B. Shen, H. Hu, and F. Fan, “Optimizing the performance of ice-storage systems in electricity load management through a credit mechanism: An analytical work for Jiangsu, China,” *Energy Procedia*, vol. 61, pp. 2876–2879, 2014, doi: 10.1016/j.egypro.2014.12.327.
  - [59] S. E. Lenker, “Building for the future,” *Stand. News*, vol. 40, no. 2, pp. 34–37, 2012, doi: 10.1080/0005576x.1949.11750770.
  - [60] T. Deetjen, A. Reimers, and M. E. Webber, “Can storage reduce electricity consumption? A general equation for the grid-wide efficiency impacts of using cooling thermal energy storage for load shifting,” *Environ. Res. Lett.*, 2018, doi: 10.1016/j.pepi.2007.08.007.
  - [61] D. Gräf *et al.*, “What drives capacity degradation in utility-scale battery energy storage



- systems? The impact of operating strategy and temperature in different grid applications,” *J. Energy Storage*, vol. 47, no. March 2021, 2021, doi: 10.1016/j.est.2021.103533.
- [62] A. M. Ershad, F. Ueckerdt, R. C. Pietzcker, A. Giannousakis, and G. Luderer, “A further decline in battery storage costs can pave the way for a solar PV-dominated Indian power system,” *Renew. Sustain. Energy Transit.*, vol. 1, no. May, p. 100006, 2021, doi: 10.1016/j.rset.2021.100006.
  - [63] E. Virguez, X. Wang, and D. Patiño-Echeverri, “Utility-scale photovoltaics and storage: Decarbonizing and reducing greenhouse gases abatement costs,” *Appl. Energy*, vol. 282, no. October 2020, 2021, doi: 10.1016/j.apenergy.2020.116120.
  - [64] A. H. Schleifer, C. A. Murphy, W. J. Cole, and P. L. Denholm, “The evolving energy and capacity values of utility-scale PV-plus-battery hybrid system architectures,” *Adv. Appl. Energy*, vol. 2, no. March, p. 100015, 2021, doi: 10.1016/j.adapen.2021.100015.
  - [65] M. Arbabzadeh, R. Sioshansi, J. X. Johnson, and G. A. Keoleian, “The role of energy storage in deep decarbonization of electricity production,” *Nat. Commun.*, vol. 10, no. 1, 2019, doi: 10.1038/s41467-019-11161-5.
  - [66] N. A. Sepulveda, J. D. Jenkins, F. J. de Sisternes, and R. K. Lester, “The Role of Firm Low-Carbon Electricity Resources in Deep Decarbonization of Power Generation,” *Joule*, vol. 2, no. 11, pp. 2403–2420, 2018, doi: 10.1016/j.joule.2018.08.006.
  - [67] G. Baure and M. Dubarry, “Battery durability and reliability under electric utility grid operations: 20-year forecast under different grid applications,” *J. Energy Storage*, vol. 29, no. April, p. 101391, 2020, doi: 10.1016/j.est.2020.101391.
  - [68] Y. Wu, Z. Liu, J. Liu, H. Xiao, R. Liu, and L. Zhang, “Optimal battery capacity of grid-connected PV-battery systems considering battery degradation,” *Renew. Energy*, vol. 181, pp. 10–23, 2022, doi: 10.1016/j.renene.2021.09.036.
  - [69] X. Han, J. Garrison, and G. Hug, “Techno-economic analysis of PV-battery systems in Switzerland,” *Renew. Sustain. Energy Rev.*, vol. 158, p. 112028, 2022, doi: 10.1016/j.rser.2021.112028.
  - [70] M. S. Ziegler and J. E. Trancik, “Re-examining rates of lithium-ion battery technology improvement and cost decline,” *Energy Environ. Sci.*, vol. 14, no. 4, pp. 1635–1651, 2021, doi: 10.1039/d0ee02681f.
  - [71] T. B. Jekel, “Modeling of ice-storage systems,” 1991.
  - [72] K. H. Drees, “Modeling and Control of Area Constrained Ice Storage Systems,” Purdue University, West Lafayette, 1994.
  - [73] J. E. B. Drees, K. H., “Modeling and Experimental Validation of Area Constrained Ice

- Storage Systems,” *Int. Refrig. Air Cond. Conf.*, 1994.
- [74] T. A. Deetjen, J. S. Vitter, A. S. Reimers, and M. E. Webber, “Optimal dispatch and equipment sizing of a residential central utility plant for improving rooftop solar integration,” *Energy*, vol. 147, pp. 1044–1059, 2018, doi: 10.1016/j.energy.2018.01.110.
  - [75] S. Hanson, M. Schwedler, and B. Bakkum, “Chiller System Design and Control,” 2011.
  - [76] Evapco, “Thermal Ice Storage,” pp. 3–66, 2007.
  - [77] Federal Energy Management Program, “Thermal Energy Storage for Space Cooling Technology for reducing on-peak electricity demand and cost,” 2000.
  - [78] Y. Hida, S. Shibutani, M. Amano, and N. Maehara, “District Cooling Plant with High Efficiency Chiller and Ice Storage System,” *Mitsubishi Heavy Ind. Ltd. Tech. Rev.*, vol. 45, no. 2, pp. 37–44, 2008.
  - [79] B. Silveti, “Application fundamentals of ice-based thermal storage,” *ASHRAE J.*, vol. 44, no. 2, pp. 30–35, 2002.
  - [80] P. Denholm, S. Ong, and C. Booten, “Using Utility Load Data to Estimate Demand for Space Cooling and Potential for Shiftable Loads,” 2012.
  - [81] I. M. Al-Sada, “Towards Cooperative District Cooling Society Role of District Cooling Services Department- Opportunities of DC in Qatar,” 2014.
  - [82] M. Z. Jacobson and V. Jadhav, “World estimates of PV optimal tilt angles and ratios of sunlight incident upon tilted and tracked PV panels relative to horizontal panels,” *Sol. Energy*, vol. 169, no. April, pp. 55–66, 2018, doi: 10.1016/j.solener.2018.04.030.
  - [83] R. Dogga and M. K. Pathak, “Recent trends in solar PV inverter topologies,” *Sol. Energy*, vol. 183, no. March, pp. 57–73, 2019, doi: 10.1016/j.solener.2019.02.065.
  - [84] A. C. Hua and B. Z. Syue, “Charge and Discharge Characteristics of Lead-Acid Battery and LiFePO<sub>4</sub> Battery,” pp. 1478–1483, 2010.
  - [85] K. Mongird, V. Viswanathan, J. Alam, C. Vartanian, V. Sprenkle, and P. Northwest, “2020 Grid Energy Storage Technology Cost and Performance Assessment,” no. December, 2020.
  - [86] D. S. Christian Weber, Ryan Stroupe, “Performance of a Thermal Energy Storage System, 25 Years On,” in *Performance of a Thermal Energy Storage System, 25 Years On*, 2015, p. 27.
  - [87] Pacific Gas & Electric Company, “Thermal Energy Storage Strategies for Commercial HVAC Systems,” 1997.

- [88] FPL, “Water-Cooled Chiller Characteristics,” pp. 1–4, 2012.
- [89] Mark Stehney, “Air- versus water-cooled chilled water plants,” 2020. [Online]. Available: <https://www.csemag.com/articles/air-versus-water-cooled-chilled-water-plants/>. [Accessed: 08-Nov-2022].
- [90] S. Sabihuddin, A. E. Kiprakis, and M. Mueller, “A numerical and graphical review of energy storage technologies,” *Energies*, vol. 8, no. 1, pp. 172–216, 2015, doi: 10.3390/en8010172.
- [91] W. Cole, A. W. Frazier, C. Augustine, W. Cole, A. W. Frazier, and C. Augustine, “Cost Projections for Utility-Scale Battery Storage : 2021 Update Cost Projections for Utility-Scale Battery Storage : 2021 Update,” no. June, 2021.
- [92] D. Feldman *et al.*, “U.S. Solar Photovoltaic System and Energy Storage Cost Benchmark: Q1 2020,” *Natl. Renew. Energy Lab.*, no. September, pp. 1–120, 2021.
- [93] J. H. K. Lai, F. W. H. Yik, and A. K. P. Chan, “Maintenance cost of chiller plants in Hong Kong,” *Build. Serv. Eng. Res. Technol.*, vol. 30, no. 1, pp. 65–78, 2009, doi: 10.1177/0143624408096290.
- [94] “Compare - O&M Costs - Chillers,” *Apogee Interactive Inc.* [Online]. Available: <https://c03.apogee.net/mvc/home/hes/land/el?spc=cel&id=19018&utilityname=northwestern>. [Accessed: 04-Oct-2019].
- [95] R. Carnegie, D. Gotham, D. Nderitu, and P. V. Preckel, “Utility Scale Energy Storage Systems,” 2013.
- [96] J. Ahlen, T. Binet, P. Muhoro, and Brad Seibert, “Battery Energy Storage Overview,” 2019.
- [97] S. T. Taylor, “Chilled Water Plant Design Guide,” *Energy Des. Resour.*, no. December, p. 281, 2009.
- [98] J. McQuiston, F., Parker, J., & Spitler, *Heating, Ventilating and, Air Conditioning*, Sixth. 2005.
- [99] N. DiFonzo and P. Bordia, “Varying Views on Variable-Primary Flow,” *J. Allergy Clin. Immunol.*, vol. 130, no. 2, p. 556, 1998.
- [100] F. Report and E. Peyer, “Variable Primary Flow Chilled Water Systems : Potential,” vol. 2, 2004.
- [101] Y. Yao and Y. Yu, *Modeling and Control in Air- conditioning Systems*. 2017.
- [102] K. C. ; Ng and Jeffrey M. Gordon, “Cool Thermodynamics : The Engineering and Physics

of Predictive, Diagnostic and Optimization Methods for Cooling Systems,” *ProQuest Ebook Central*. 2001.

- [103] J. M. Gordon and K. C. Ng, “Predictive and diagnostic aspects of a universal thermodynamic model for chillers,” *Int. J. Heat Mass Transf.*, vol. 38, no. 5, pp. 807–818, 1995, doi: 10.1016/0017-9310(94)00208-D.
- [104] J. M. Gordon, K. C. Ng, and H. T. Chua, “Centrifugal chillers: Thermodynamic modelling and a diagnostic case study,” *Int. J. Refrig.*, vol. 18, no. 4, pp. 253–257, 1995, doi: 10.1016/0140-7007(95)96863-2.
- [105] J. M. Gordon and K. C. Ng, “Thermodynamic modeling of reciprocating chillers,” *J. Appl. Phys.*, vol. 75, no. 6, pp. 2769–2774, 1994, doi: 10.1063/1.356215.
- [106] K. C. Ng, H. T. Chua, W. Ong, S. S. Lee, and J. M. Gordon, “Diagnostics and Optimization of Reciprocating Chillers: Theory and Experiment,” *Appl. Therm. Eng.*, vol. 17, no. 3, pp. 263–276, 1997.
- [107] W. Jiang and T. A. Reddy, “Reevaluation of the Gordon-Ng performance models for water-cooled chillers,” *ASHRAE Trans.*, vol. 109 PART 2, pp. 272–287, 2003.
- [108] M. Hydeman, N. Webb, P. Sreedharan, and S. Blanc, “Development and testing of a reformulated regression-based electric chiller model,” *ASHRAE Trans.*, vol. 108 PART 2, pp. 1118–1127, 2002.
- [109] P. Haves, “Development and testing of a reformulated regression-based electric chiller model: Discussion,” *ASHRAE Trans.*, vol. 108 PART 2, p. 1127, 2002.
- [110] P. Hanlon, *Compressor Handbook*. 2020.
- [111] ASHRAE, *Chapter 38: Compressors*. ASHRAE, 2020.
- [112] P. N. Bali, M. E. Arsana, and P. N. Bali, “Condenser-Evaporator Approach Temperatures and their Influences on Energy Performance of Water Cooled Chillers,” in *Proceeding of the 14th International Conference on QIR (Quality in Research)*, 2015, no. June 2018.
- [113] C. Y. Chiang, R. Yang, and K. H. Yang, “The development and full-scale experimental validation of an optimal water treatment solution in improving chiller performances,” *Sustain.*, vol. 8, no. 7, pp. 1–21, 2016, doi: 10.3390/su8070615.
- [114] M. A. Bernier and B. Bourret, “Pumping energy and variable frequency drives,” *ASHRAE J.*, vol. 41, no. 12, pp. 37–40, 1999.
- [115] “Understanding the Properties of Glycol Solutions Prevents Design Errors in Pumping and Piping Applications,” Milwaukee, 2001.

- [116] M. F., “Verdunstungskühlung,” *VDI Forschungsarbeit*, vol. 70, pp. 123–128, 1926.
- [117] J. E. Braun, S. A. Klein, and J. W. Mitchell, “Effectiveness Models for Cooling Towers and Cooling Coils,” *ASHRAE Trans.*, vol. 95, no. 2, pp. 164–174, 1989.
- [118] L. Wang, P. Haves, and F. Buhl, “An improved simple chilled water cooling coil model,” in *SimBuild 2012 IBPSA Conference*, 2012.
- [119] M. J. Holmes, “The simulation of heating and cooling coils for performance analysis,” in *1st International Conference on System Simulation in Buildings*, 1982, pp. 245–282.
- [120] D. Erbe *et al.*, “Energy Standard for Buildings Except Low-Rise Residential Buildings,” 2021.
- [121] F. Wang, H. Lin, W. Tu, Y. Wang, and Y. Huang, “Energy Modeling and Chillers Sizing of HVAC System for a Hotel Building,” *Procedia Eng.*, vol. 121, pp. 1812–1818, 2015, doi: 10.1016/j.proeng.2015.09.161.
- [122] Y. Kang, G. Augenbroe, Q. Li, and Q. Wang, “Effects of scenario uncertainty on chiller sizing method,” vol. 123, pp. 187–195, 2017, doi: 10.1016/j.applthermaleng.2017.05.041.
- [123] X. Fang, X. Jin, Z. Du, Y. Wang, and W. Shi, “Evaluation of the design of chilled water system based on the optimal operation performance of equipments,” *Appl. Therm. Eng.*, vol. 113, pp. 435–448, 2017, doi: 10.1016/j.applthermaleng.2016.11.053.
- [124] Q. Cheng, S. Wang, and C. Yan, “Robust optimal design of chilled water systems in buildings with quantified uncertainty and reliability for minimized life-cycle cost,” *Energy Build.*, vol. 126, pp. 159–169, 2016, doi: 10.1016/j.enbuild.2016.05.032.
- [125] S. Bahramara, “Robust Optimization of the Flexibility-constrained Energy Management Problem for a Smart Home with Rooftop Photovoltaic and an Energy Storage,” *J. Energy Storage*, vol. 36, no. August 2020, p. 102358, 2021, doi: 10.1016/j.est.2021.102358.
- [126] C. A. Correa-florez, A. Gerossier, A. Michiorri, and G. Kariniotakis, “Stochastic operation of home energy management systems including battery cycling,” *Appl. Energy*, vol. 225, no. February, pp. 1205–1218, 2018, doi: 10.1016/j.apenergy.2018.04.130.
- [127] N. Holjevac, T. Capuder, N. Zhang, I. Kuzle, and C. Kang, “Corrective receding horizon scheduling of flexible distributed multi- energy microgrids Central control,” *Appl. Energy*, vol. 207, pp. 176–194, 2017, doi: 10.1016/j.apenergy.2017.06.045.
- [128] S. Sanaye and N. Khakpaay, “Innovative combined optimization and modified maximum rectangle method for equipment sizing and operational strategy of an integrated system with cold thermal storage,” *Energy Reports*, vol. 8, pp. 137–160, 2022, doi: 10.1016/j.egyr.2021.11.245.

- [129] B. Mohandes, S. Acharya, and S. Member, "Optimal Design of an Islanded Microgrid With Load Shifting Mechanism Between Electrical," vol. 35, no. 4, pp. 2642–2657, 2020.
- [130] Q. Zhu, Q. Li, B. Zhang, L. Wang, G. Li, and R. Wang, "Capacity optimization for electrical and thermal energy storage in multi-energy building energy system," *Energy Procedia*, vol. 158, pp. 6425–6430, 2019, doi: 10.1016/j.egypro.2019.01.183.
- [131] Z. Xu, X. Guan, Q. S. Jia, J. Wu, D. Wang, and S. Chen, "Performance analysis and comparison on energy storage devices for smart building energy management," *IEEE Trans. Smart Grid*, vol. 3, no. 4, pp. 2136–2147, 2012, doi: 10.1109/TSG.2012.2218836.
- [132] Y. Chen, M. Guo, Z. Chen, Z. Chen, and Y. Ji, "Physical energy and data-driven models in building energy prediction: A review," *Energy Reports*, vol. 8, pp. 2656–2671, 2022, doi: 10.1016/j.egy.2022.01.162.
- [133] N. Fumo, P. Mago, and R. Luck, "Methodology to estimate building energy consumption using EnergyPlus Benchmark Models," *Energy Build.*, vol. 42, no. 12, pp. 2331–2337, 2010, doi: 10.1016/j.enbuild.2010.07.027.
- [134] M. T. Ke, C. H. Yeh, and J. T. Jian, "Analysis of building energy consumption parameters and energy savings measurement and verification by applying eQUEST software," *Energy Build.*, vol. 61, pp. 100–107, 2013, doi: 10.1016/j.enbuild.2013.02.012.
- [135] M. Manfren, P. Ab, and L. Tronchin, "Data-driven building energy modelling – An analysis of the potential for generalisation through interpretable machine learning," *Renew. Sustain. Energy Rev.*, vol. 167, no. December 2021, p. 112686, 2022, doi: 10.1016/j.rser.2022.112686.
- [136] Z. Wang, T. Hong, and M. A. Piette, "Building thermal load prediction through shallow machine learning and deep learning," *Appl. Energy*, vol. 263, no. February, p. 114683, 2020, doi: 10.1016/j.apenergy.2020.114683.
- [137] L. Duanmu, Z. Wang, Z. J. Zhai, and X. Li, "A simplified method to predict hourly building cooling load for urban energy planning," *Energy Build.*, vol. 58, pp. 281–291, 2013, doi: 10.1016/j.enbuild.2012.11.029.
- [138] F. Johari, J. Munkhammar, F. Shadram, and J. Widén, "Evaluation of simplified building energy models for urban-scale energy analysis of buildings," *Build. Environ.*, vol. 211, no. December 2021, p. 108684, 2022, doi: 10.1016/j.buildenv.2021.108684.
- [139] O. Alrawi, I. S. Bayram, and M. Koc, "High-resolution electricity load profiles of selected houses in Qatar," *Proc. - 2018 IEEE 12th Int. Conf. Compat. Power Electron. Power Eng. CPE-POWERENG 2018*, pp. 1–6, 2018, doi: 10.1109/CPE.2018.8372569.
- [140] S. Panda and N. P. Padhy, "Comparison of particle swarm optimization and genetic algorithm for FACTS-based controller design," *Appl. Soft Comput. J.*, vol. 8, no. 4, pp.

- 1418–1427, 2008, doi: 10.1016/j.asoc.2007.10.009.
- [141] M. Karami and L. Wang, “Particle Swarm optimization for control operation of an all-variable speed water-cooled chiller plant,” *Appl. Therm. Eng.*, vol. 130, pp. 962–978, 2018, doi: 10.1016/j.applthermaleng.2017.11.037.
  - [142] D. Jayasekara, “Machine Learning - Particle Swarm Optimization (PSO) and Twitter,” *towards data science*, 2018. [Online]. Available: <https://towardsdatascience.com/machine-learning-particle-swarm-optimization-pso-and-twitter-c952a9ace499>.
  - [143] Y. C. Chang, J. K. Lin, and M. H. Chuang, “Optimal chiller loading by genetic algorithm for reducing energy consumption,” *Energy Build.*, vol. 37, no. 2, pp. 147–155, 2005, doi: 10.1016/j.enbuild.2004.06.002.
  - [144] W. S. Lee, Y. T. Chen, and Y. Kao, “Optimal chiller loading by differential evolution algorithm for reducing energy consumption,” *Energy Build.*, vol. 43, no. 2–3, pp. 599–604, 2011, doi: 10.1016/j.enbuild.2010.10.028.
  - [145] Y. C. Chang, “A novel energy conservation method - Optimal chiller loading,” *Electr. Power Syst. Res.*, vol. 69, no. 2–3, pp. 221–226, 2004, doi: 10.1016/j.epsr.2003.10.012.
  - [146] Department of Climate Change and Energy Efficiency of Australia, “Chiller Efficiency Factsheet,” *J. Am. Soc. Nav. Eng.*, vol. 21, no. 1, pp. 330–335, 2015.
  - [147] F. Jabari, M. Mohammadpourfard, and B. Mohammadi-ivatloo, “Energy efficient hourly scheduling of multi-chiller systems using imperialistic competitive algorithm,” *Comput. Electr. Eng.*, vol. 82, p. 106550, 2020, doi: 10.1016/j.compeleceng.2020.106550.
  - [148] K. M. Powell, W. J. Cole, U. F. Ekarika, and T. F. Edgar, “Optimal chiller loading in a district cooling system with thermal energy storage,” *Energy*, vol. 50, no. 1, pp. 445–453, 2013, doi: 10.1016/j.energy.2012.10.058.
  - [149] J. Deng, S. He, Q. Wei, M. Liang, Z. Hao, and H. Zhang, “Research on systematic optimization methods for chilled water systems in a high-rise office building,” *Energy Build.*, vol. 209, p. 109695, 2020, doi: 10.1016/j.enbuild.2019.109695.
  - [150] K. P. Lee and T. A. Cheng, “A simulation-optimization approach for energy efficiency of chilled water system,” *Energy Build.*, vol. 54, pp. 290–296, 2012, doi: 10.1016/j.enbuild.2012.06.028.
  - [151] M. Ali, V. Vukovic, M. H. Sahir, and G. Fontanella, “Energy analysis of chilled water system configurations using simulation-based optimization,” *Energy Build.*, vol. 59, pp. 111–122, 2013, doi: 10.1016/j.enbuild.2012.12.011.
  - [152] R. Iru *et al.*, “The Optimal Control Strategy for Chilled Water System in Central Air Conditioning Systems,” in *43rd Annual Conference of the IEEE Industrial Electronics*

- Society*, 2017, pp. 8150–8155, doi: 10.1109/IECON.2017.8217430.
- [153] A. J. Ardakani, F. F. Ardakani, and S. H. Hosseinian, “A novel approach for optimal chiller loading using particle swarm optimization,” *Energy Build.*, vol. 40, no. 12, pp. 2177–2187, 2008, doi: 10.1016/j.enbuild.2008.06.010.
  - [154] S. Huang, W. Zuo, and M. D. Sohn, “Amelioration of the cooling load based chiller sequencing control,” *Appl. Energy*, vol. 168, pp. 204–215, 2016, doi: 10.1016/j.apenergy.2016.01.035.
  - [155] S. R. Thangavelu, A. Myat, and A. Khambadkone, “Energy optimization methodology of multi-chiller plant in commercial buildings,” *Energy*, vol. 123, pp. 64–76, 2017, doi: 10.1016/j.energy.2017.01.116.
  - [156] Y. C. Chang, “Genetic algorithm based optimal chiller loading for energy conservation,” *Appl. Therm. Eng.*, vol. 25, no. 17–18, pp. 2800–2815, 2005, doi: 10.1016/j.applthermaleng.2005.02.010.
  - [157] D. Zhang, S. Member, P. B. Luh, L. Fellow, J. Fan, and S. Member, “Chiller Plant Operation Optimization : Primary – Secondary Systems,” *Ieee Trans. Autom. Sci. Eng.*, vol. 15, no. 1, pp. 341–355, 2018.
  - [158] D. Zhang, P. B. Luh, J. Fan, and S. Gupta, “Chiller Plant Operation Optimization with Minimum Up/Down Time Constraints,” *IEEE Robot. Autom. Lett.*, vol. 3, no. 1, pp. 9–15, 2018, doi: 10.1109/LRA.2017.2723467.
  - [159] N. Trautman, A. Razban, and J. Chen, “Overall chilled water system energy consumption modeling and optimization,” *Appl. Energy*, vol. 299, no. April, p. 117166, 2021, doi: 10.1016/j.apenergy.2021.117166.
  - [160] W. S. Lee, Y. T. Chen, and T. H. Wu, “Optimization for ice-storage air-conditioning system using particle swarm algorithm,” *Appl. Energy*, vol. 86, no. 9, pp. 1589–1595, 2009, doi: 10.1016/j.apenergy.2008.12.025.
  - [161] J. A. Candanedo, V. R. Dehkordi, and M. Stylianou, “Model-based predictive control of an ice storage device in a building cooling system,” *Appl. Energy*, vol. 111, pp. 1032–1045, 2013, doi: 10.1016/j.apenergy.2013.05.081.
  - [162] H. J. Chen, D. W. P. Wang, and S. L. Chen, “Optimization of an ice-storage air conditioning system using dynamic programming method,” *Appl. Therm. Eng.*, vol. 25, no. 2–3, pp. 461–472, 2005, doi: 10.1016/j.applthermaleng.2003.12.006.
  - [163] K. Deng *et al.*, “Model Predictive Control of Central Chiller Plant With Thermal Energy Storage Via Dynamic Programming and Mixed-Integer Linear Programming,” *IEEE Trans. Autom. Sci. Eng.*, vol. 12, no. 2, pp. 565–579, 2015, doi: 10.1109/TASE.2014.2352280.



- [164] D. Rohde, B. R. Knudsen, T. Andresen, and N. Nord, “Dynamic optimization of control setpoints for an integrated heating and cooling system with thermal energy storages,” *Energy*, vol. 193, p. 116771, 2020, doi: 10.1016/j.energy.2019.116771.
- [165] S. Sanaye and A. Shirazi, “Thermo-economic optimization of an ice thermal energy storage system for air-conditioning applications,” *Energy Build.*, vol. 60, pp. 100–109, 2013, doi: 10.1016/j.enbuild.2012.12.040.
- [166] J. Yu, X. Yang, A. Zhao, M. Zhou, and Y. Ren, “Research on Optimal Control Algorithm of Ice Thermal-Storage Air-Conditioning System,” in *Advancements in Smart City and Intelligent Building*, 2019, pp. 207–218.
- [167] R. Kamal, F. Moloney, C. Wickramaratne, A. Narasimhan, and D. Y. Goswami, “Strategic control and cost optimization of thermal energy storage in buildings using EnergyPlus,” *Appl. Energy*, vol. 246, no. April, pp. 77–90, 2019, doi: 10.1016/j.apenergy.2019.04.017.
- [168] M. Marghany, “Principles of genetic algorithm,” *Synth. Aperture Radar Imaging Mech. Oil Spills*, pp. 169–185, 2020, doi: 10.1016/b978-0-12-818111-9.00010-0.
- [169] D. A. Coley, “An Introduction to Genetic Algorithms for Scientists and Engineers,” *An Introd. to Genet. Algorithms Sci. Eng.*, 1999, doi: 10.1142/3904.
- [170] P. Bajpai and M. Kumar, “Genetic algorithm—an approach to solve global optimization problems,” *Indian J. Comput. Sci. Eng.*, vol. 1, no. 3, pp. 199–206, 2010.
- [171] ASHRAE, *ASHRAE Fundamental Handbook*. 2001.
- [172] D. G. Stephenson, “Equations for solar heat gain through windows,” *Sol. Energy*, vol. 9, no. 2, pp. 81–86, 1965, doi: 10.1016/0038-092X(65)90207-0.

## **Appendix A: Simulation of buildings' cooling and electric loads**

Simulation of building cooling load can be accomplished by summing heat gains from all major sources. Heat gains sources in buildings can be classified into heat gains from internal sources, including:

- Occupant load
- Electric load from devices, appliances, and lighting

and heat gain from the building envelope, which includes:

- Infiltration and ventilation
- Solar gain through glazing
- Conduction through the building envelope

Several assumptions are made to estimate the heat gain from each source. The aim is to capture generic and non-specific diurnal and interannual demand profiles for the two most common building types in Qatar, residential and commercial buildings, without specific knowledge of building interior zoning, orientation, and construction details that would be required with energy simulation software. The assumptions, in no particular order, are as follows:

### **General:**

- The two buildings have identical total daily electric and cooling needs with different hourly demand profiles.
- The building interior is maintained at 22°C and 50% relative humidity at all times.
- Building occupancy is assumed based on typical working hours in Qatar.
- Building electric load is calculated based on assumed occupancy and typical electric energy consumption in residential and business-commercial (office) settings.

- Occupant activity level is based on resting for the residential and light-office work for the commercial building.

### **Building construction:**

- 30% of the building façade is covered with glazing, which is on par with typical high-rise buildings worldwide and in Qatar.
- No specific building orientation is supposed; instead, a quarter of the building envelope is assumed to be perpendicular to horizontal sun rays at all times when estimating the cooling load from admitted solar insolation.
- Building thermal insulation is on par with Qatar's building code (overall heat transfer coefficients of 0.6 W/m<sup>2</sup>-K for walls, 1.8 W/m<sup>2</sup>-K for windows, and 0.6 W/m<sup>2</sup>-K for the upper-most roof) with exterior surfaces at the ambient temperature.
- The assumed combined infiltration and ventilation rate for the entire building is on par with typical modern construction and Qatar of 1.25 ACH (air change per hour).

The assumed building characteristics are tabulated in Table A.1 below. The building consists of 30 floors with a floor height of 3 m and an area of 2000 m<sup>2</sup> square in shape. The building's gross area is 60,000 m<sup>2</sup> with an envelope opaque surface area of 112,700 m<sup>2</sup> and a glazing surface area of 48,300 m<sup>2</sup>, constituting 30% of the building façade.

**Table A.1: Considered building characteristics**

Parameter	Value	Notes
Number of Floors	30	-
Floor Height	3 m	-
Gross Floor Area	60,000 m <sup>2</sup>	2000 m <sup>2</sup> floor, square
Window-to-Wall Ratio	30%	Building Envelope

## A.1 Occupant load

Buildings' occupants contribute to thermal load from human metabolic heat generation depending on their activity level [171]. Most metabolic heat generation is sensible in an air-conditioned environment and under light work activity. As the work and activity load increases, more metabolic heat generation is latent from perspiration. The metabolic heat generation rate for commercial and residential settings is in Table A.2.

**Table A.2: Occupant heat gain in residential and commercial buildings**

Parameter	Residential	Commercial
Sensible Gain (W/person)	70	75
Latent Gain (W/person)	45	55
Total Heat Gain (W/person)	115	130
Maximum Occupancy Rate (m <sup>2</sup> /person)	50	40

The heat rate for an office setting with light activity levels is a metabolic heat generation rate of 130 W/person, of which 75 W/person is a sensible load and 55 W/person is a latent load. In homes with reduced activity levels, the metabolic heat generation rate is 115 W/person, of which 70 W/person is sensible load and 45 W/person is latent load. Commercial and residential buildings can have an inverse occupancy rate as people transition from their workplace to the place of their residence. Figure A.1 shows the assumed occupancy rate representative of residential and commercial settings. Occupancy is higher in the evening and at night in residential settings and primarily during the day in commercial buildings. The metabolic heat generation rate in moderately occupied buildings minimally impacts the overall thermal load.

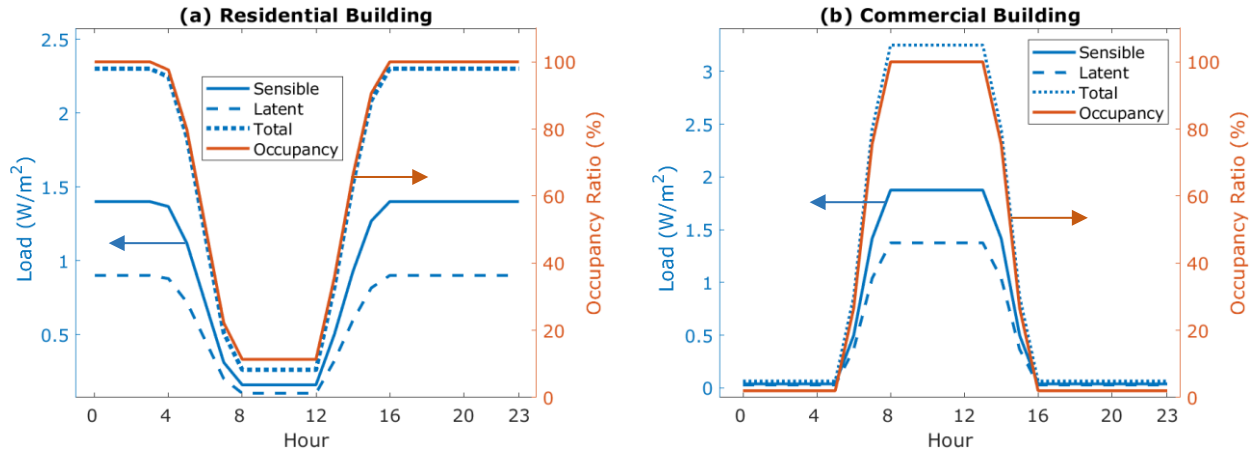


**Figure A.1: Assumed occupant load in (a) residential setting and (b) business-commercial setting. An inverse occupancy relationship is assumed as people move from the workplace to residence.**

## A.2 Electric load

Building electric load from using electric devices, appliances, and lighting contributes to building heat load as the energy consumed in a closed system is ultimately absorbed as heat. The assumed electric load serves two purposes: (i) it measures the contribution to the building's thermal load, and (ii) it represents the building's electricity use. The electric load is influenced by building use, activities, occupancy, and time of day. The assumed electric load is shown in Figure A.2 (a) for the residential setting and (b) for the business-commercial setting. The residential setting load is characterized by a pre-work morning spike, a post-work evening spike, and a generally higher evening load, as observed in demand data published in the literature. For a commercial setting, the load is assumed to be driven by sensible load from electronic devices such as personal computers, printers, and screens. Higher latent load in residential buildings is from appliances such as dishwasher machines, washers and dryers, and food preparation and cooking. The average daily electric load for both buildings is 515 kWh ( $8.6 \text{ W/m}^2$ ).

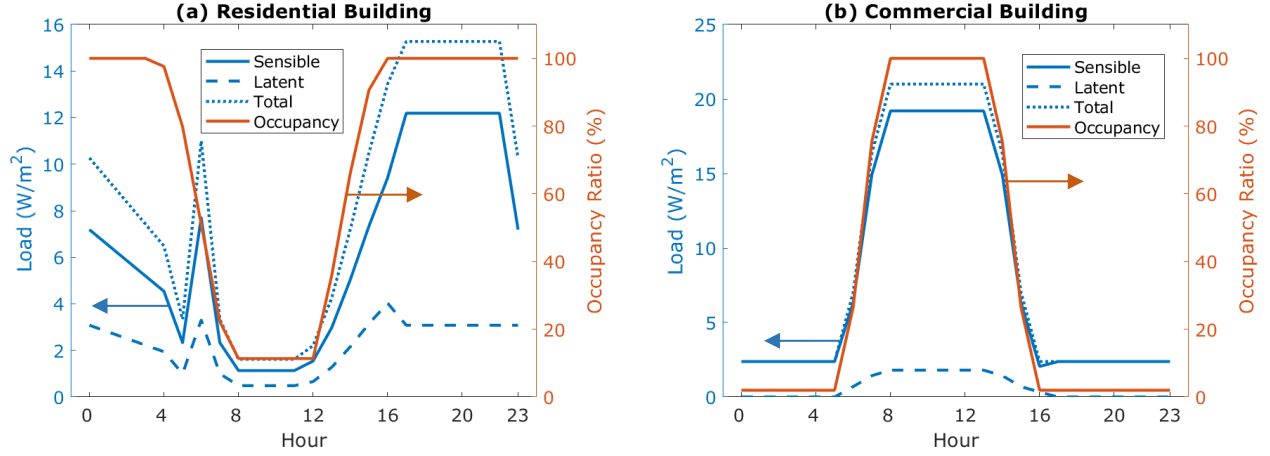


**Figure A.2.: Simulated electric load in (a) residential setting and (b) business-commercial setting. Energy consumed by the electric load ultimately ends up as heat.**

### A.3 Infiltration and ventilation

Building infiltration is the unintentional introduction of outside air into the air condition spaces through the building envelope, contributing to building thermal load. On the other hand, ventilation is the intentional introduction of outside air by mechanical means, such as fans, to maintain indoor air quality. Forced ventilation is typically introduced in kitchens and bathrooms and in densely occupied office buildings, which are needed to maintain healthy indoor air quality. Forced ventilation is typically introduced in kitchens and bathrooms and in densely occupied office buildings, which are required to maintain healthy indoor air quality. The simulated thermal load from infiltration and ventilation is shown in Figure A.3. The thermal load depends on the differences between outdoor and indoor pressure, temperature, and humidity level. The combined infiltration and ventilation rate is assumed to be 1.25 ACH (air change per hour), typical in modern construction and Qatar [39]. The sensible load is given by:

$$\dot{Q}_t^{fresh, sen} = \dot{m}_t^{ACH} c^{p,a} (T^{fresh} - 22) \quad (\text{A.1})$$

and the latent load is given by:

$$\dot{Q}_t^{fresh,lat} = h^{fg} \dot{m}_t^{ACH} (\omega^{fresh} - 0.0087) \quad (A.2)$$

where  $\dot{m}_t^{ACH}$  is air change rate per second,  $c^{p,a}$  is the specific heat of air,  $T^{fresh}$  and  $\omega^{fresh}$  are supplied fresh (ventilation and infiltration) temperature and humidity ratio, respectively, and  $h^{fg}$  is the latent heat of the vaporization of water.

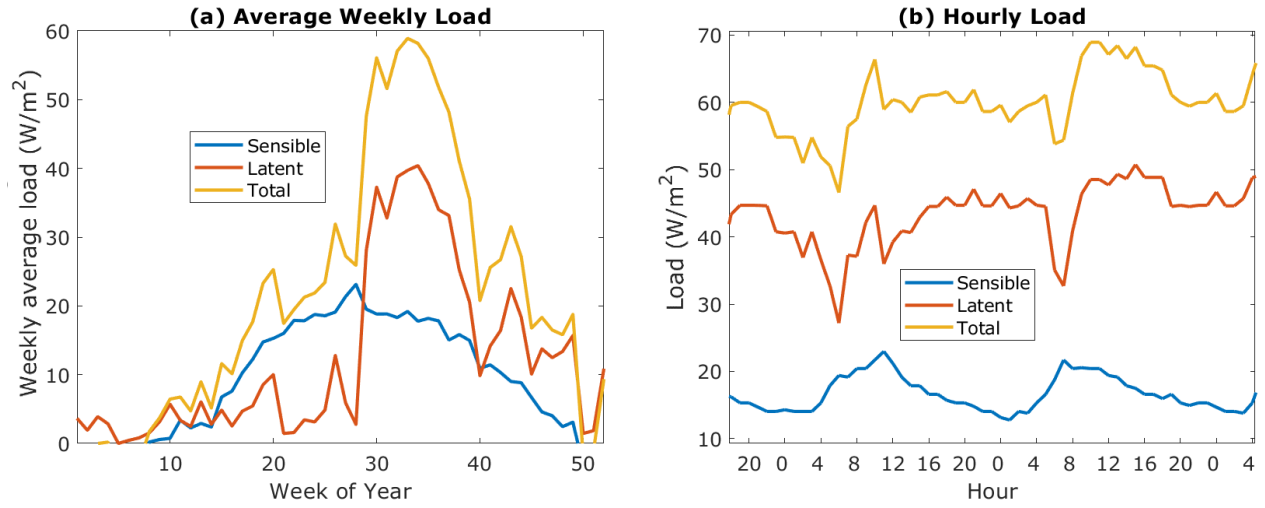


**Figure A.3: Simulated infiltration and ventilation load with (a) average daily load and (b) hourly load during peak demand day. A combined infiltration and ventilation ACH of 1.25 is assumed for residential and commercial buildings.**

#### A.4 Solar gain

Solar gain through fenestration provides the occupants with natural lights. Due to the greenhouse effect, admitted solar radiation is retained inside the building, increasing the thermal load. Windows coating and shading can reduce solar gain. The amount of solar gain is related to the solar angles, building orientation, and windows structure and construction. For simplification, 25% of the building envelope surface area is assumed to receive incident horizontal solar radiation. The solar gain is given by:

$$\dot{Q}_t^{fresh,lat} = SHGC A^{win} (I_t^B \cos(\beta) f + I_t^D Y) \quad (\text{A.3})$$

where  $SHGC$  is the fraction of incident sunlight admitted indoors and is taken to be 0.5,  $A^{win}$  is the total glazing surface area,  $I_t^B$  is beam solar irradiance,  $I_t^D$  is the diffused solar irradiance,  $Y$  is the ratio of diffuse irradiance on a vertical surface to a horizontal surface from reference [172],  $\beta$  is the solar angle, and  $f$  is the fraction of total building glazing surface area exposed to direct sunbeam and is 0.25. Daily and hourly thermal load from solar gains are in Figure A.4.

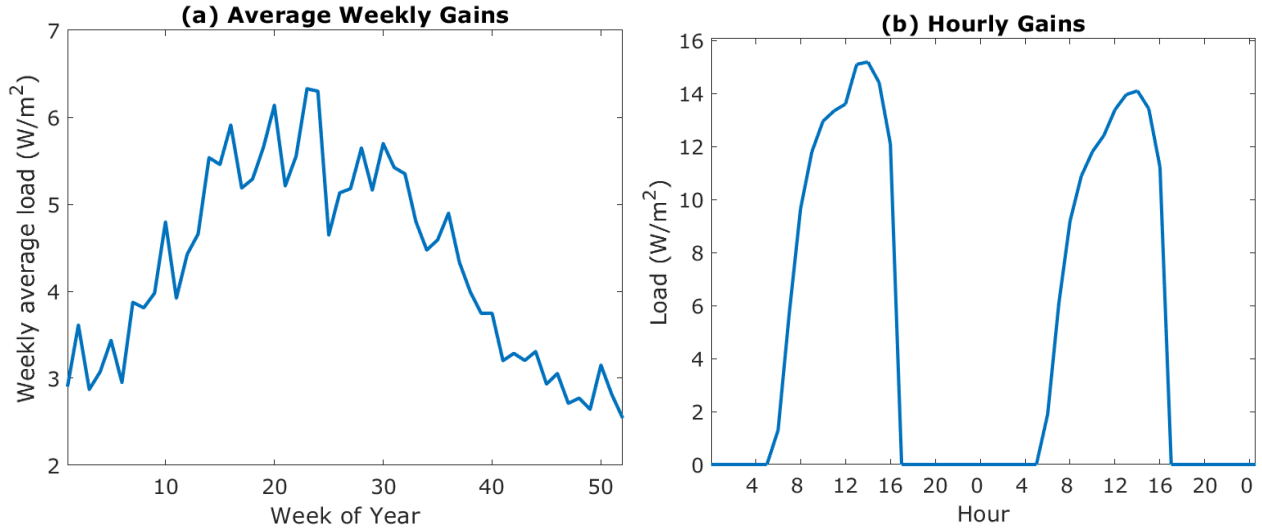


**Figure A.4: Thermal load from solar gain with (a) average daily load and (b) hourly load during peak demand day. 25% of the building envelope is exposed to the sun at each hour of the day.**

### A.5 Shell heat gain

The building envelope experiences a diurnal temperature swing caused by solar insolation and outside temperature fluctuations. The conductive heat gain through transparent and opaque surfaces is proportional to the surface temperature difference between indoor and outdoor and building insulation. The assumed building insulation is on par with Qatar's building code (overall heat transfer coefficients of 0.6 W/m²-K for walls, 1.8 W/m²-K for windows, and 0.6 W/m²-K for the upper-most roof). The heat load from building shell heat gain is given by:



$$\dot{Q}_t^{shell} = [A^{win}U^{win} + A^{roof}U^{roof} + A^{wall}U^{wall}](T_t^{db} - 22^\circ\text{C}) \quad (\text{A.4})$$

Where  $A^{win}$ ,  $A^{roof}$ , and  $A^{wall}$  are windows, roof, and walls surface area, respectively, and  $U^{win}$ ,  $U^{roof}$ , and  $U^{wall}$  are windows, roofs, and walls' overall heat transfer coefficient. Conductive thermal gain through the building shell is shown in Figure A.5.

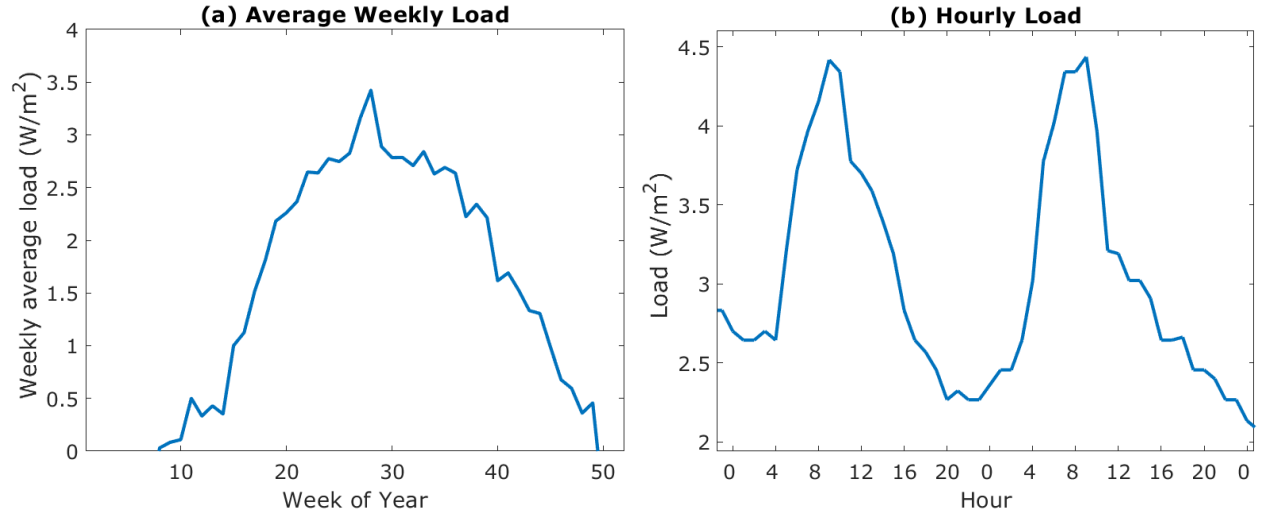


**Figure A.5: Thermal load from envelope heat gain with (a) average weekly load and (b) hourly load during peak demand day. Negative heat gain in the winter was omitted from this figure.**

## A.6 Total heat gain

The simulated load from individual heat gain sources is combined to form the overall building cooling load. The simulated buildings' main heat gain sources are infiltration and ventilation, followed by internal generation from electricity use. Loads from internal sources drive daily variations, while seasonal variations are driven by infiltration and ventilation heat gain, particularly from latent load during the humid period from late July to early September. The average weekly thermal load, identical for both buildings, is shown in Figure A.6, along with ambient dry and wet-bulb temperatures on the right y-axis.

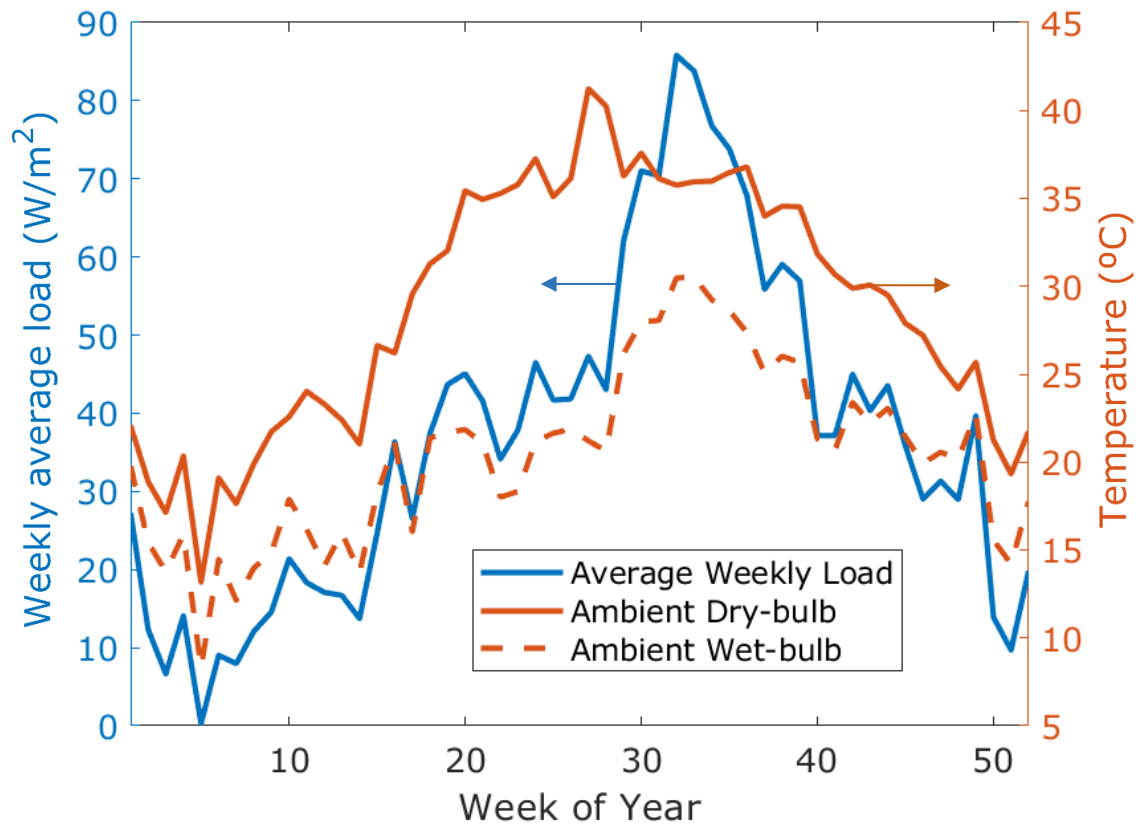
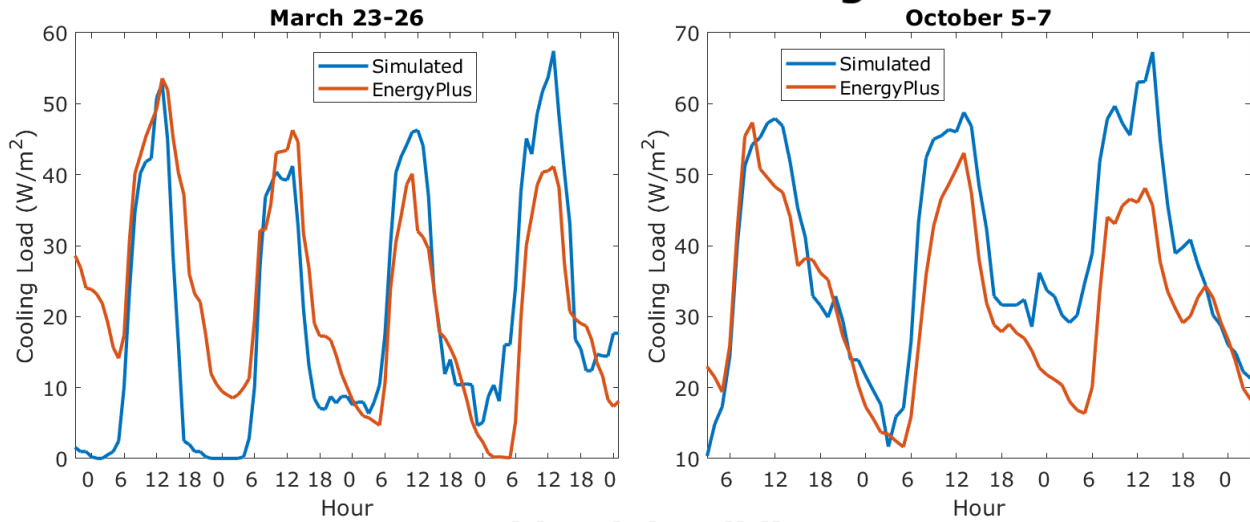


**Figure A.6: Normalized average weekly thermal load from all sources on the left y-axis and ambient temperatures on the right y-axis. While hourly demands differ for residential and commercial buildings, the total daily cooling demand is identical.**

The simulated building loads were validated using EnergyPlus building simulation software with arbitrarily decided building orientation and geometry, producing a comparable estimate. Figure A.7 compares the EnergyPlus model output, which utilizes simulated weather data, with the estimated building cooling and electric demand for three consecutive days in 2016 (March 23-26 and October 5-7) for both buildings.

## Commercial Building



## Residential Building

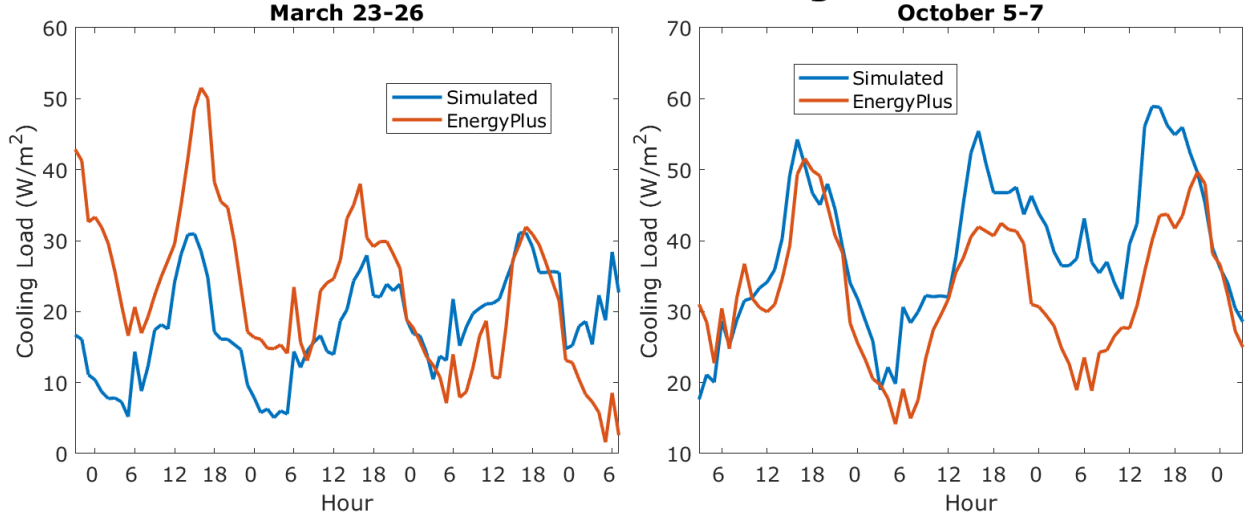


**Figure A.7: Normalized thermal load from the simulated load (blue) compared to the EnergyPlus software output (orange) for the commercial building (top) and the residential building (bottom). EnergyPlus software utilizes simulated weather, which does not perfectly align with 2016 meteorological weather data.**

## Appendix B: Chapter 4 Models Parameters

**Table B.1: Selected WC chillers' characteristics**

Item	WC Chillers		
	Carrier 19XR	Carrier 19XR	Carrier 23XL
Design cooling capacity	1284 kW <sub>th</sub> [365 tons]	1347 kW <sub>th</sub> [383 tons]	1196 kW <sub>th</sub> [340 tons]
Evaporator temperature differential	8.3°C	8.3°C	7.9°C
Condenser temperature differential	6.7°C	6.7°C	7.7°C
Reference COP	6.4*	7.9	6.4
Compressor type	Centrifugal	Centrifugal	Screw
Capacity control	Guide Vanes	VSD	Slide Valve
Evaporator water flowrate	36.84 kg/s	36.84 kg/s	36.53 kg/s
Condenser water flowrate	53.37 kg/s	53.37 kg/s	42.71 kg/s
Refrigerant type	R-134a	R-134a	R-134a

\*Adjusted from 6.2 to better reflect representative centrifugal chiller performance

**Table B.2: Fitted parameters in Gordon-Ng model for the selected chillers**

Item	WC Chillers		
	Carrier 19XR (w/o VSD)	Carrier 19XR (w/ VSD)	Carrier 23XL (w/o VSD)
$\Delta S_t^{int}$	0.1886 kW <sub>th</sub> /K	0.2282 kW <sub>th</sub> /K	0.0540 kW <sub>th</sub> /K
$\Delta S_t^{intQ}$	0.1612 kW <sub>th</sub>	-0.3868 kW <sub>th</sub>	0.1782 kW <sub>th</sub>
$R$	0 K/kW <sub>th</sub>	0.0218 K/kW <sub>th</sub>	0 K/kW <sub>th</sub>
$\dot{Q}_t^{leak,eqv}$	-121.41 kW <sub>th</sub>	-205.7867 kW <sub>th</sub>	134.6552 kW <sub>th</sub>

**Table B.3: Pumps and fans constants**

Item	Chiller	Notes
Primary	0.020 kW/kW <sub>th</sub>	Per cooling capacity
Condenser	0.015 kW/ kW <sub>th</sub>	Per cooling capacity
Variable Speed	0.010 kW/ kW <sub>th</sub>	Per cooling capacity
Tower fan	0.009 kW/ kW <sub>th</sub>	Per heat rejection capacity
Coil fan	0.045 kW/kW <sub>th</sub>	Per cooling capacity

**Table B.4: Cooling tower characteristics**

Item	Symbol	Value	Note
NTU correlation parameters	$c$	3.76	Cooling towers based on Dallas/Fort Worth Airport [117]
	$n$	-0.63	
Design tower approach temperature	$T^{csw} - T^{wb}$	3°C	Difference between leaving water temperature and wet-bulb temperature
Design wet-bulb temperature	$T^{wb}$	25°C	Reference temperature

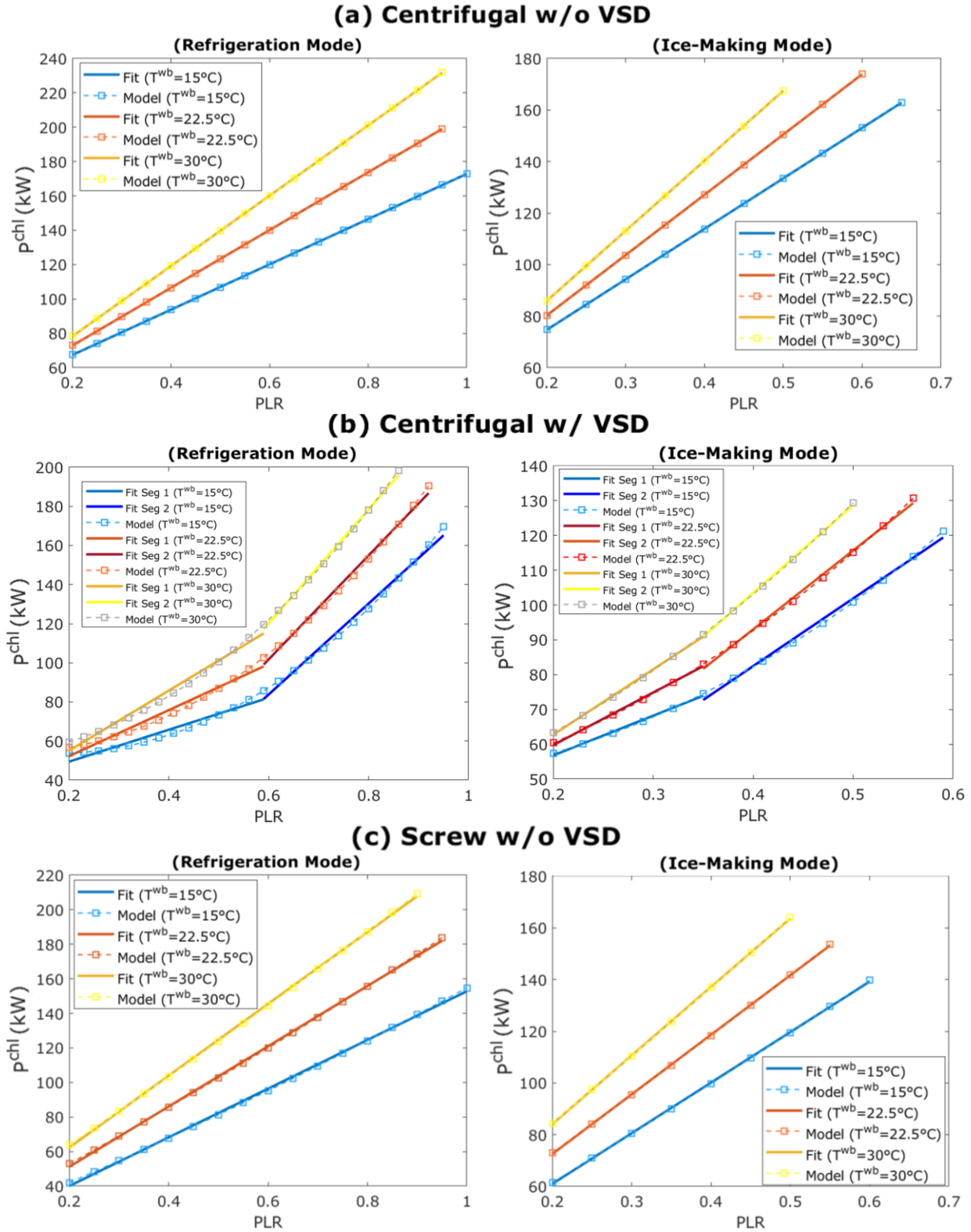


**Figure B.1: Illustration of piecewise linearization for the three chiller types at three inlet condenser temperatures in refrigeration mode with a supply water temperature of 7°C and ice-making mode with a supply water temperature of -6°C. A single segment was sufficient for chillers without VSD.**

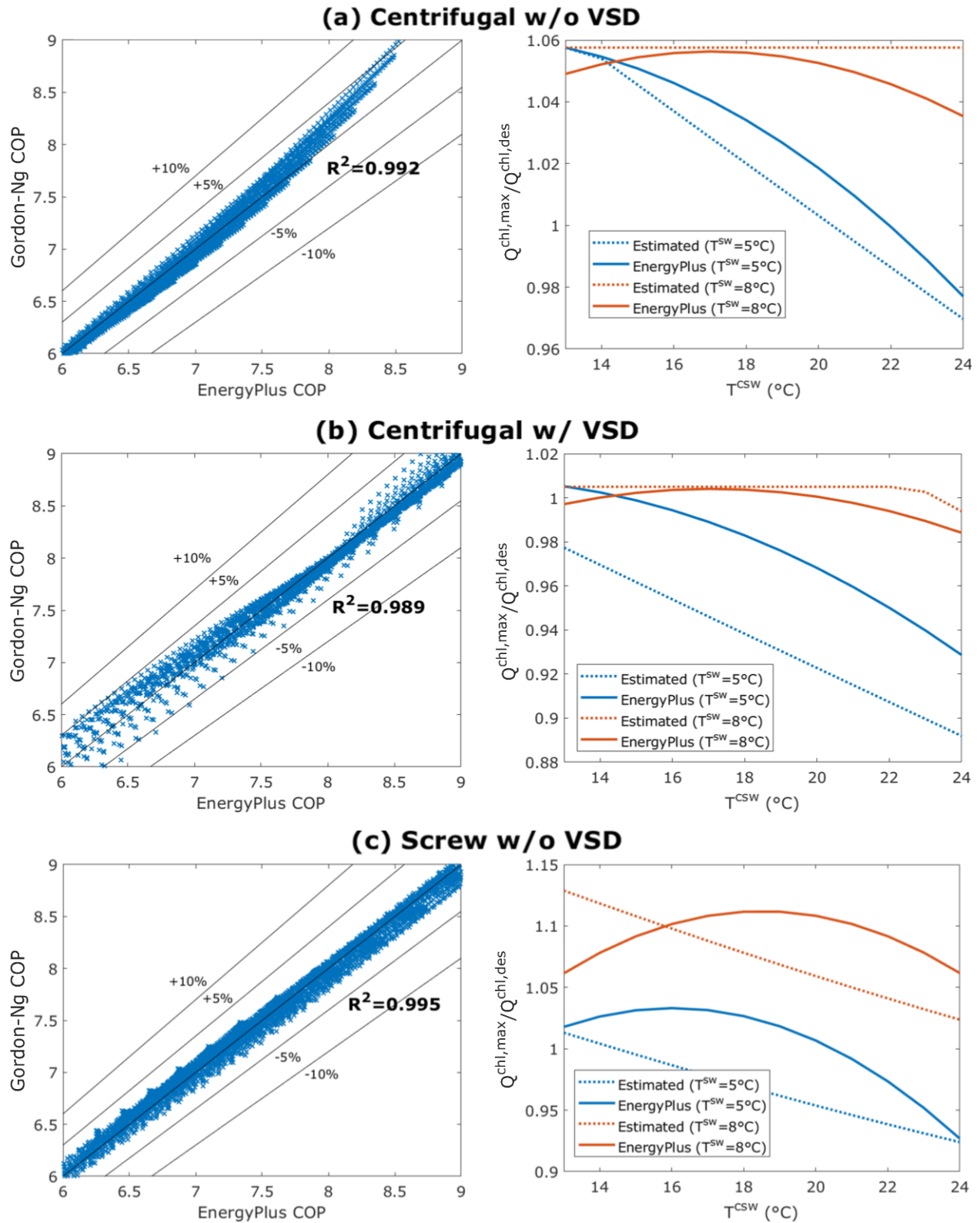


**Figure B.2: Comparison of (a) predicted COP v. COP from EnergyPlus, and (b) Chiller capacity as predicted from thermodynamics v. EnergyPlus for the three selected representative chillers used in Chapter 4.**

## Appendix C: Chapter 5 Models Parameters

**Table C.1: Selected WC chillers' characteristics**

Item	WC Chillers	
	Trane RTHB	Carrier 19XR
Design cooling capacity	531 kW <sub>th</sub> [151 tons]	742 kW <sub>th</sub> [211 tons]
Evaporator temperature differential	9.3°C	9.8°C
Condenser temperature differential	9.4°C	10.8°C
Design COP	4.6	4.7
Compressor type	Screw	Centrifugal
Capacity control	Slide Valve	VSD
Evaporator water flowrate	13.50 kg/s	17.79 kg/s
Condenser water flowrate	15.77 kg/s	19.56 kg/s
Refrigerant type	R-22	R-134A

**Table C.2: Fitted parameters in Gordon-Ng model for the selected chillers**

Item	WC Chillers	
	Trane RTHB	Carrier 19XR
$\Delta S_t^{int}$	0.0432 kW <sub>th</sub> /K	0.0749 kW <sub>th</sub> /K
$\Delta S_t^{intQ}$	0.0001 kW <sub>th</sub>	-0.0002 kW <sub>th</sub>
$R$	0.0292 K/kW <sub>th</sub>	0.0450 K/kW <sub>th</sub>
$\dot{Q}_t^{leak,eqv}$	93.376 kW <sub>th</sub>	132.946 kW <sub>th</sub>

**Table C.3: Pumps and fans constants**

Item	Chiller	
	Trane RTHB	Carrier 19XR
Primary	5 kW	7 kW
Condenser	4 kW	5 kW
Variable Speed		10 kW
Tower fan		10 kW
Coil fan		100 kW



**Table C.4: Cooling tower characteristics**

Item	Symbol	Value	Note
NTU correlation parameters	$c$	3.76	Cooling towers based on Dallas/Fort Worth Airport [117]
	$n$	-0.63	
Design heat rejection capacity	-	1266 kW [360 ton]	Per tower
Design air flowrate	$\dot{m}^{atwr}$	20 kg/s	Maximum fan speed
Design water flowrate	$\dot{m}^{bcw}$	28 kg/s	All chillers are operating (per tower)
Design tower approach temperature	$T^{csw} - T^{wb}$	3°C	Difference between leaving water temperature and wet-bulb temperature
Design wet-bulb temperature	$T^{wb}$	25°C	Reference temperature

**Table C.5: Cooling and dehumidification coil characteristics**

Item	Symbol	Value	Note
	$a_1^{cc}$	$0.596 \times 10^{-3} \text{ K/kg} \cdot \frac{\text{m}^{\frac{5}{2}} \cdot \text{s}^{\frac{15}{4}}}{\text{m}^{\frac{5}{2}} \cdot \text{s}^{\frac{15}{4}}}$	
Coil thermal resistance coefficient	$a_2^{cc}$	$0.217 \times 10^{-3} \text{ K/kg} \cdot \frac{\text{m}^{\frac{5}{2}} \cdot \text{s}^{\frac{15}{4}}}{\text{m}^{\frac{5}{2}} \cdot \text{s}^{\frac{15}{4}}}$	High-performance coils
	$a_3^{cc}$	0.286 K/kW	
Design air flowrate	$\dot{m}^{cca,des}$	120 kg/s	Maximum fan speed
Max air inlet enthalpy	$h^{ai,des}$	55.6 kJ/kg	27°C at 50% RH
Design air outlet enthalpy	$h^{ae,des}$	34.1 kJ/kg	12°C at 100% RH
Design air-side temperature drop	$T^{ai} - T^{ae,des}$	15°C	27°C → 12°C
Design water-side temperature differential	$T^{ccrw} - T^{ccsw}$	13.5°C	3.5°C → 16°C
Coil face area	$A^{face}$	39 m <sup>2</sup>	Normal to air-flow direction
Number of rows	$N^{row}$	5.1	Thickness of the coils
Design water face velocity	$V^{w,des}$	1 m/s	Normal to flow direction
Design air face velocity	$V^{a,des}$	2.5 m/s	Normal to flow direction

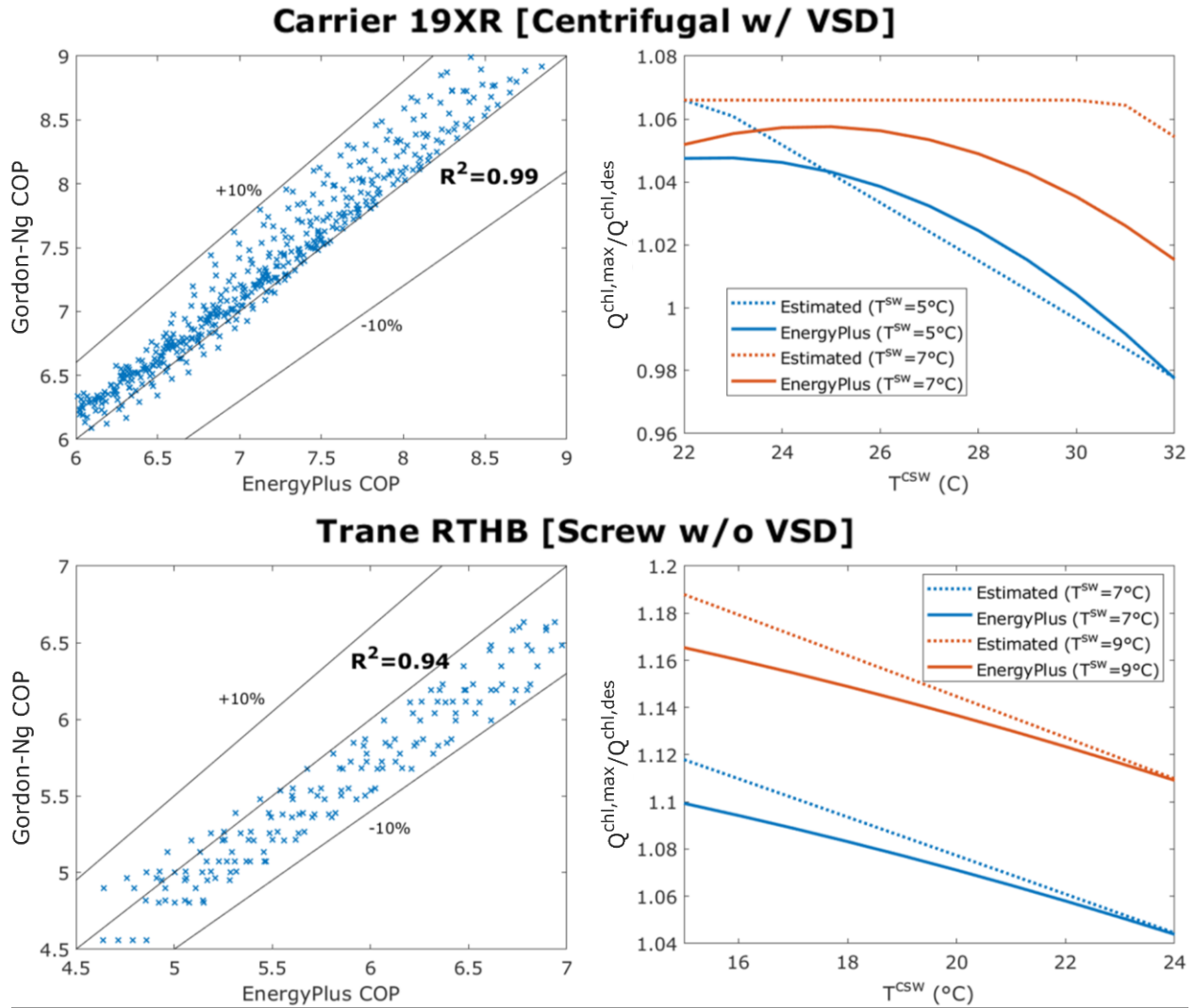


**Figure C.1: Comparison of (a) predicted COP v. COP from EnergyPlus, and (b) chiller capacity as predicted from thermodynamics v. EnergyPlus for the two selected chillers in Chapter 5.**